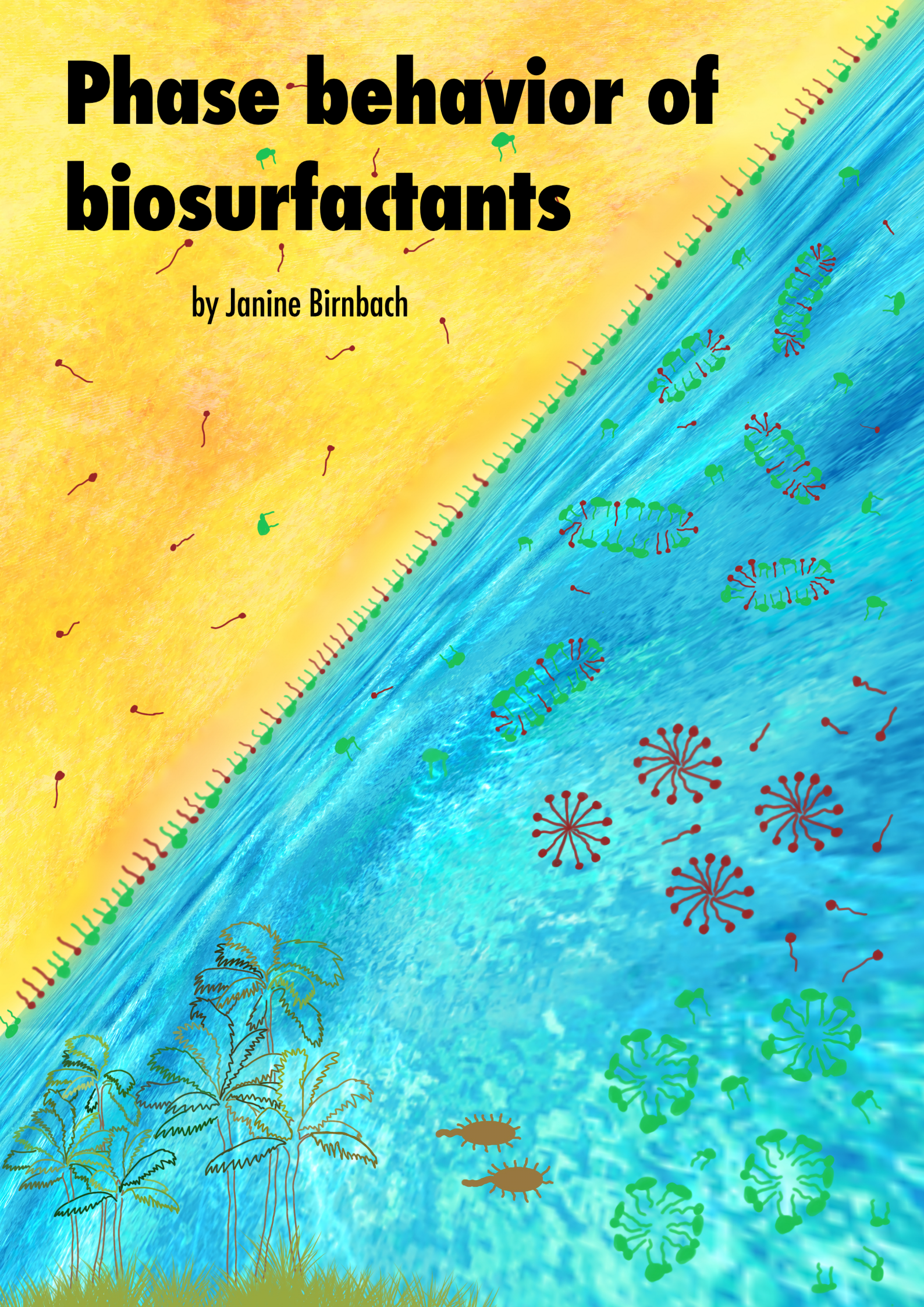


Phase behavior of biosurfactants

by Janine Birnbach





Phase Behavior of Biosurfactants

Inaugural-Dissertation

zur Erlangung des Doktorgrades
der Mathematisch-Naturwissenschaftlichen Fakultät
der Heinrich-Heine-Universität Düsseldorf

vorgelegt von

Janine Birnbach
aus Ratingen

Düsseldorf, May 2025

aus dem Institut für Physikalische Chemie I: Kolloide und Nanooptik
der Heinrich Heine Universität Düsseldorf

Gedruckt mit der Genehmigung der
Mathematisch-Naturwissenschaftlichen Fakultät der
Heinrich-Heine-Universität Düsseldorf

Berichterstatter:

1. Prof. Dr. Matthias Karg

2. Prof. Dr. Guillaume Delaittre

Tag der mündlichen Prüfung: 23.09.2025

For my parents,
my siblings,
and my husband.

To the world.

*Keep thinking big,
for the world is vast,
and its beauty inspires endless possibilities.*

Declaration

I hereby declare under oath that I have produced my thesis independently and without any undue assistance by third parties under consideration of the ‘Principles for the Safeguarding of Good Scientific Practice at Heinrich Heine University Düsseldorf’ and that this work has not been submitted for any other degree or professional qualification. This dissertation is my own work and contains nothing which is the outcome of work done in collaboration with others, except where work which has formed part of joint projects and commissioned experiments has been included. My contribution and those of the other authors to this work have been explicitly indicated in the Acknowledgments and List of Publications. I confirm that appropriate credit has been given within this thesis where reference has been made to the work of others.

Janine Birnbach
Düsseldorf, 2025

Acknowledgements

I would like to thank my supervisor Prof. Matthias Karg for his valuable advice, for always having an open ear for me and for teaching me his broad physico-chemical knowledge. Moreover, I would like to express my deepest gratitude to my supervisor, boss and mentor Dr. Peter Schmiedel. I am grateful for his motivation, his support and I admire his passion for science. In addition, I want to thank my supervisor during the secondment in Paris Dr. Niki Baccile for his great guidance and the broad discussions.

Furthermore, a great thank you is expressed to Prof. Thomas Sottmann for the enlightening discussions. In this context, I want to thank Prof. Cosima Stubenrauch for inviting me to Stuttgart, and also Florian Trummer and Julian Fischer for the discussions about scattering. Moreover, I would like to thank the research director Dr. Thorsten Bastigkeit for the framework conditions to conduct deep science at Henkel.

Moreover, I am grateful for the guidance I received from Dr. François Ribot for the NMR experiments. For the primary NMR experiments, I want to thank the internal NMR team at Henkel, in particular Dr. Oliver Seiler and Verena Schön. I am also grateful for the local contacts at the large scale facilities; including Dr. Petra Pernot from ESRF, Dr. Thomas Bizien and the organizer Dr. François Boué for the beamtime at the SOLEIL synchrotron, and Dr. Sylvain Prévost from ILL. For the chromatography data, I thank Dr. Matthias Frings, Dr. Julian Schwarzkopf, Monika Reinhart, Melanie Wedemeyer and Helmut Beuster from Henkel Corporate Scientific Services who conducted the experiments.

I am grateful to all my colleagues at Henkel. In particular, I would like to thank my team Danuta Bedrunka and Anja von Kather. I also want to thank my students Maria Volk, Moritz Stanek, Cara Kohler and Tristan von Prittwitz und Gaffron. I am thankful to have Caroline Hartwig as my colleague and to be part of such a nice team including especially Yvonne Willemsen, Ines Baranski, Danilo Panzika, Stefan Pahl, Sonja Masuch and Bent Rogge.

In addition, I am grateful to have shared the PhD journey with other students, namely Melanie Slotty, Dr. Nadia Ledermann, Mariola Pawlak, Benjamin Orgis, Bernhard Putz, Julia Sander, Carolin Goy, Angelita Krama, Ayla Yaman, Fabian Junglas, Samuel Lestrat, Leonie Hansen, Rodrigo Sperzel and Michael Monschau. In particular, I want to thank Jörn Optatzi and Christoph Bayer for the nice time at conferences and their help at ILL. Moreover, I want to thank my former office mate Silvia Sauf and the rest of the OC

department, namely Dr. Christian Kropf, Dr. Kira Neubauer, Christian Umbreit, and Janice Mahnke.

Moreover, I want to say thanks to the group of Matthias, in particular Dr. Keumkyung Kuk, Vahan Abgarjan, Julian Ringling and Déborah Feller. I would especially like to thank Jonathan Garthe for his help during my beamtime at ILL.

I also thank all the people at the LCMCP lab and the SMILES team in Paris, in particular, Dr. Marion Merle, Dr. Ieva Goldberga, Claudio Dos Reis Ferreira, Trevys Chanal and Ramanujam Ramanujam. I am also grateful for the nice office mates, especially Valentin Barandard, Elyes Labidi and Pierre Daniel. Apart from mentioning Camille Chareyron, Clara Doisneau, Arthur Hongre, Anna Phan, Thomas Naillon, Natalia Trespacios Villalobos, Kethsovan Var, Daline Akoa, Korin Ozakaya, Maia Ouret and Katsuya Komiyama, I want to thank everyone for making my time in Paris so enjoyable.

Moreover, I am grateful for the organizers of the scientific conferences and scientific facilities which make excellent science possible. For example, I want to thank Dr. Henrich Frielinghaus for his explanations on MuScatt.

Above all, I want to thank my family, including my husband, and my friends. They have been my unwavering support and my greatest source of strength.

Hence, I want to thank everybody that I could have such an amazing time as a PhD student. I am truly honored and privileged to have so many wonderful people around me.

List of Publications

1. Janine Birnbach, Peter Schmiedel, and Matthias Karg. "Multi-component Phase Behavior of Biosurfactants." *Current Opinion in Colloid & Interface Science* (2023): 101765.
2. Janine Birnbach, Peter Schmiedel, and Matthias Karg. "Adsorption Kinetics of Multi-Component Systems Comprising Ethoxylate Surfactants and Anionic Rhamnolipid by Dynamic Interfacial Tension Measurement"
Manuscript in preparation
3. Janine Birnbach, Francois Ribot, Sylvain Prévost, Thomas Bizien, Tanya K. Todorova, Andreas Bick, Xenophon Krokidis, Niki Baccile, Thomas Sottmann Peter Schmiedel, and Matthias Karg. "Phase Behavior and Structure of Microemulsions comprising Rhamnolipid and Ethoxylates"
Manuscript in preparation
Phase behavior of mono-disperse ethoxylates was already investigated in Master thesis. Molecular dynamics simulation were carried out by the company Scienomics after briefing.
4. Janine Birnbach, Francois Ribot, Sylvain Prévost, Petra Pernot, Tanya K. Todorova, Andreas Bick, Xenophon Krokidis, Niki Baccile, Thomas Sottmann Peter Schmiedel, and Matthias Karg. "Structure and Miscibility of Anionic Biosurfactants Mixed with Cationic Surfactants"
Manuscript in preparation
Molecular dynamics simulation were carried out by the company Scienomics after briefing.
5. Janine Birnbach, Peter Schmiedel, and Matthias Karg. "Adsorption of Anionic Biosurfactants Mixed with Cationic Surfactants"
Manuscript in preparation
Maximum bubble pressure measurements and spinning drop measurements were partly done the Bachelor students Cara Kohler and Maria Volk under J.B. supervision.

6. Peter Schmiedel, Janine Birnbach, and Ulrich Pegelow. "Neue Tensidkombination und Wasch- und Reinigungsmittel, welche diese enthalten", DE102021214680A1, June 22, 2023.
Published patent
7. Janine Birnbach, Peter Schmiedel, and Cara Kohler. "Sophorolipid surfactants with surface-active counteranions", DE102022210849A1, April 25, 2024.
Published patent
8. Janine Birnbach, and Peter Schmiedel. "Surfactant mixtures", DE102022210879A1, April 25, 2024.
Published patent
9. Janine Birnbach, Peter Schmiedel, Jörn Phillipp Optatzi, Mahdis Hesami, Susanne Zibeck, Alexander Beck, and Fredy Wsbaldo Baron Nunez. "Surfactant system containing the biosurfactant Mannosylerythritolipid", DE102023205588A1, December 19, 2024.
Published patent
10. Janine Birnbach, Peter Schmiedel, Cara Kohler, and Walter Heberlein. "Synergistic surfactant systems containing Sophorolipids and Glycin betaine", DE102023205204A1, December 5, 2024.
Published patent
11. Janine Birnbach, Peter Schmiedel, and Caroline Hartwig. "Mixture of different nonionics in combination with Rhamnolipid", DE102023205205A1, December 5, 2024.
Published patent
12. Janine Birnbach, Peter Schmiedel, and Caroline Hartwig. "Surfactant system containing rhamnolipid, an ethoxylate and a third anionic surfactant", DE102023205206A1, December 5, 2024.
Published patent

List of Conference Contributions

1. Online attendance at
36th Conference of the European Colloid & Interface Society Crete, 4-9/9/2022.
2. Poster contribution of
Janine Birnbach, Peter Schmiedel, Andrea Wanninger, and Matthias Karg. "Phase Behavior of the Biosurfactant Rhamnolipid with Pure Ethoxylates at Different Temperatures"
18th European Detergents Conference Berlin, 26/10/2022
Poster prize.
3. Attendance at
18th Zsigmondy Colloquium Berlin, 4-8/4/2023.
4. Poster contribution of
Janine Birnbach, Peter Schmiedel, and Matthias Karg. "Structure and adsorption kinetics of rhamnolipid/ sophorolipid and cationic surfactants",
37th Conference of the European Colloid & Interface Society, Naples, 3-8/9/2023,
Poster prize.
5. Oral contribution of
Janine Birnbach, Peter Schmiedel, and Matthias Karg. "Physical-chemical studies of biosurfactants with co-surfactants",
19th European Detergents Conference, Berlin, 25/10/2023.
6. Oral contribution of
Janine Birnbach, Peter Schmiedel, Niki Baccile, and Matthias Karg. "Equilibrium phase behavior & dynamic interfacial properties of rhamnolipid and ethoxylate mixtures",
19th Zsigmondy Colloquium, Düsseldorf, 10-13/4/2024.
7. Poster contribution of
Janine Birnbach, Peter Schmiedel, and Matthias Karg. "How can we formulate green biosurfactants?",
JCF-Frühjahrssymposium, Ulm, 13-16/3/24.

8. Oral contribution of
Janine Birnbach, Peter Schmiedel, Niki Baccile, and Matthias Karg. "Structure of
catanionic micelles containing biosurfactants",
38th Conference of the European Colloid & Interface Society, Copenhagen, 1-
8/9/24.
9. Attendance at
20th European Detergents Conference, Berlin, 16/10/2024.

List of Abbreviations

$\frac{2}{2}$	Winsor I
$\frac{2}{2}$	Winsor II
A	Area
AOT	Sodium dioctyl sulfosuccinate
b	Scattering length
B_0	Strength of the magnetic field
BS	Biosurfactant
c	Concentration, curvature
CAPB	cocoamidopropyl betaine
catanionics	Mixtures of cationic and anionic surfactants
CCD	Charge-coupled device
cmc	Critical micelle concentration
CTAB	Cetyltrimethylammonium bromide
CTAC	Cetyltrimethylammonium chloride
d	Domain size, diameter
D	Diffusion coefficient
DLS	Dynamic light scattering
DST	Dynamic surface tension
E	Energy, strength of the electric field
f	Activity coefficient
F	Free energy
f_a	Amphiphilicity factor
g	Auto-correlation function
G	Gibbs free energy
GSF	Gradient shape factor
H	Mean curvature
H_1	Hexagonal phase
\hbar	Reduced Planck constant
HELDAC	Hydroxyethyl lauryldimethylammonium chloride
HLB	Hydrophilic-lipophilic balance

HSA	Hayter-Penfold Rescales Mean Spherical Approximation
I	Intensity
IFT	Interfacial tension
K	Gaussian curvature
k_B	Boltzmann constant
l	Length
L_1	Micellar phase
L_α	Lamellar phase
LAS	Linear alkyl benzene sulfonate
m	Mass
M_w	Molecular weight
MEL	Mannosylerythritolipid
MD	Molecular Dynamics
MQAS	Multiple quaternary ammonium salts
n	Refractive index
N_A	Avogadro number
NMR	Nuclear magnetic resonance
P	Packing parameter
$P(q)$	Form factor
PGSE	Pulsed Field-Gradient Spin Echo
\vec{q}	Scattering vector
Q	Invariant
R	Radius
R	Gas constant
R_g	Gyration radius
RL	di-Rhamnolipid
S	Crystal phase
$\frac{S}{V}$	Specific interface
$S(q)$	Structure factor
SANS	Small-angle neutron scattering
SAXS	Small-angle X-ray scattering
SF	Surfactin
SL	Acidic unacetylated Sophorolipid
SLD	Scattering length density
SLES	Sodium lauryl ether sulfate
ST	Surface tension
t	Time, smearing factor
T	Temperature
t_0	Contrast thickness
V	Volume

V_1	Cubic phase
W	Pairwise interaction energies
WAXS	Wide-angle X-ray scattering
x	Fraction
\tilde{X}	Point of intersection of all phases
β	Interaction parameter, surfactant concentration
γ	Gyromagnetic ratio, surfactant concentration, surface tension
Γ	Decay rate
Δ	Difference
δ	Amount secondary surfactant in microemulsion
ζ	Zeta-potential
η	Dynamic viscosity
θ	Scattering angle
κ	Bending modulus
$\overline{\kappa}$	Saddle spray modulus
λ	Wavelength
μ	Chemical potential
μE	Microemulsion
ξ	Persistence length
Π	Surface pressure
σ	Surface tension
ϕ	Volume fraction
ω_0	Frequency

Abstract

Biosurfactants are produced by microorganisms from renewable resources and have complex structural formulae. These complex structures result in unknown physico-chemical properties, knowledge of which is essential for the formulation of biosurfactants into industrial products. As these products usually contain several different components, biosurfactants have been studied in mixtures with other surfactants in this thesis. This investigation was conducted in pseudo-binary, ternary and quaternary systems with other surfactants and oil, in order to establish a structure-property relationship. The two most abundant biosurfactants, rhamnolipid and sophorolipid, were combined with cationic and nonionic model surfactants, respectively. Their self-assembled structures in water were analyzed with pulsed field-gradient spin-echo nuclear magnetic resonance spectroscopy (PGSE-NMR), small-angle X-ray (SAXS) and neutron scattering (SANS), wide-angle X-ray scattering (WAXS) and molecular dynamics simulation (MD). In addition, their adsorption dynamics at the air-water and oil-water interfaces were investigated using ring tensiometry, maximum bubble pressure, spinning drop and dynamic light scattering (DLS). The biosurfactants were found to exhibit a pronounced hydrophilic character, as evidenced by the formation of Winsor IV microemulsions of rhamnolipid/ethoxylate/n-decane/water systems in the presence of rather hydrophobic ethoxylates. With sophorolipid, Winsor IV microemulsions disappear even on small addition. Furthermore, the catanionic surfactant systems with biosurfactants do not precipitate at equimolar ratios, nor do they form vesicles. The catanionic surfactant systems form micellar structures, whereas equimolar mixtures with rhamnolipid exhibit rod-like structures, capable of incorporating oil. However, evidence suggests that the biosurfactants are not miscible with other surfactants at the nanoscopic scale, presumably due to strong carbohydrate interactions. Consequently, the biosurfactants manifest properties that are both surfactant and lipid-like. In addition, the biosurfactants demonstrate both a typical ionic and nonionic character depending on the measurement technique employed. The structure and efficiency of the microemulsions containing rhamnolipid/ethoxylate/n-decane/water are analogous to those of ethoxylate/n-decane/water, suggesting minimal influence from rhamnolipid. In contrast, rhamnolipid was found to accelerate the adsorption to interfaces. The research enabled the understanding of the differences between biosurfactants and conventional surfactants, contributing to the development of performing formulations with biosurfactants for applications.

Contents

1	Introduction	1
1.1	Binary Phase Behavior	3
1.2	Pseudo-Binary Phase Behavior	5
1.3	Ternary Phase Behavior	6
1.4	Quaternary Phase Behavior	7
1.5	Mixtures of Cationic and Anionic Surfactants	7
1.6	Mixtures of Anionic and Nonionic Surfactants	8
1.7	Outline of this Thesis	8
2	Theoretical Background	10
2.1	Surfactants	10
2.1.1	Surfactants in Solution	10
2.1.2	Regular Solution Theory of Mixed Micelles	12
2.2	Microemulsions	14
2.2.1	Phase Behavior	14
2.2.2	Microemulsions of Surfactant Mixtures	18
2.2.3	Microstructure	19
2.3	Characterization Methods	21
2.3.1	Pulsed Gradient Spin Echo Nuclear Magnetic Resonance Spec- troscopy	21
2.3.2	Dynamic Light Scattering	23
2.3.3	Static Small-Angle Scattering in General	25
2.3.4	Small-Angle X-ray Scattering	29
2.3.5	Small-Angle Neutron Scattering	29
2.3.6	Spinning Drop Measurements	30
3	Materials and Methods	33
3.1	Materials	33
3.2	Phase Behavior	36
3.3	Pulsed Field-gradient Spin Echo NMR Spectroscopy	37
3.4	Dynamic Light Scattering	39

3.5	Small-Angle X-ray Scattering	39
3.6	Wide-Angle X-ray Scattering	42
3.7	Small-Angle Neutron Scattering	42
3.8	Molecular Dynamics Simulations	44
3.9	Equilibrium Surface Tension	46
3.10	Dynamic Surface Tension	46
3.11	Dynamic Interfacial Tension	47
4	Results and Discussion	48
4.1	Structure of Anionic Biosurfactants with Cationic Surfactants	48
4.1.1	Experiments	48
4.1.2	Miscibility of Cationic and Anionic Surfactants	59
4.1.3	Interactions	61
4.1.4	Shape of the Aggregates	62
4.1.5	Size of the Aggregates	63
4.1.6	Composition of Micelles	64
4.2	Adsorption of Anionic Biosurfactants with Cationic Surfactants	65
4.2.1	Experiments	65
4.2.2	Adsorption Effectiveness	72
4.2.3	Adsorption Dynamics	73
4.2.4	Emulsification	75
4.2.5	(Non)Ionic Nature of Biosurfactants	76
4.3	Phase Behavior of Microemulsions containing Rhamnolipid and Ethoxylates	76
4.3.1	Experiments	79
4.3.2	Optimal Formulation	83
4.3.3	Efficiency	84
4.3.4	Rigidity	85
4.3.5	Effect of Technical Mixture	85
4.3.6	Oxo-Ethoxylates	86
4.3.7	Narrow-Range Ethoxylate	87
4.4	Structure of Microemulsions containing Rhamnolipid and C ₁₂ E ₄	87
4.4.1	Experiments	88
4.4.2	Bulk Structure	96
4.4.3	Structure of the Amphiphilic Film	97
4.5	Adsorption of Rhamnolipid and Ethoxylate	98
4.5.1	Experiments	99
4.5.2	Effect of RL on the Adsorption of Ethoxylates	105
4.5.3	Type of Diffusion	105
4.5.4	Effect of Ethoxylation Degree	106
4.5.5	Effect of Technical Ethoxylates	106
4.5.6	Effect of the Ethoxylate's Polydispersity	107

5 Conclusion and Outlook	109
Supporting Information	130

Chapter 1

Introduction

The contemporary socio-economic system is largely reliant on fossil energy and resources. The combustion of fossil resources or their degradation results in the emission of greenhouse gases, with CO₂ being the most abundant one. This leads to the introduction of greenhouse gases into the atmosphere, which in turn causes global warming. The global warming presents a severe risk to global society, emphasizing the urgent necessity to halt their release.

However, a considerable proportion of the products utilized by society are derived from fossil resources, which are ultimately degraded to CO₂ and H₂O. The only solutions to this linear economy are to reuse the CO₂ or to refrain from extracting fossil resources, thereby establishing a circular economy. It is therefore imperative that the chemical industry and all man-made products undergo a transition from a linear to a circular economy, utilizing renewable resources as raw materials. Moreover, given the current scarcity of renewable energy, it is essential that production processes are energy-efficient [1, 2].

One sector of the chemical industry are products containing surfactants. Surfactants are known to adsorb at interfaces, thereby reducing the interfacial tension (IFT) and facilitating the mixing of hydrophobic and hydrophilic compounds. This is why surfactants are essential for many products, including detergents, shampoos, conditioners, cleaners, paints, inks, coatings, adhesives, paper, petroleum, plastics, fibers, textiles, agricultural agents, food, cosmetics, pharmaceuticals and other applications [3]. As previously discussed, these substances are frequently derived from fossil resources, which is contrary to the principles of a circular economy and green chemistry [4]. Alternatives include surfactants derived from renewable resources, such as fatty alcohols that are ethoxylated with bioethanol or glycosylated with sugars.

They can be chemically synthesized or fermented involving microbes that are cultivated on biomass or even on waste streams [5]. The latter are called microbial biosurfactants (here only biosurfactants, BS). Their renewable origin, their low toxicity and their high biocompatibility make their application desirable [6]. Hence, their application could provide additional benefits in applications, e.g. mildness to skin or care benefits [7]. Examples

of the most common BS (rhamnolipid (RL), sophorolipid (SL), mannosylerythritolipid (MEL), and surfactin (SF)) are displayed in Table 1.1. It is shown that BS typically have a more complex structure compared to conventional surfactants from fossil-resources obtained in a chemical synthesis. Moreover, the microbes often produce a mixture of different molecules resulting in the presence of several structural formulae simultaneously. E.g., RL exists in different chain lengths, one or two chains and one (mono-RL) or two (di-RL) rhamnose groups. Also, SL may have different chain lengths, saturation degrees, acetylation degrees and may exist in an open (acidic) or ring-like (lactonic) structure. This structural complexity results in different and unknown physico-chemical properties. The complexity is even higher in applications where typically surfactant mixtures are used. Probably due to this complexity and unknowns, a one-to-one replacement of traditional surfactants with BS has been found to reduce the performance in today's highly optimized consumer products. This lower performance at higher cost of BS has prevented their widespread use. As mentioned, the reasons for the lower performance are the structural complexity of BS and the lack of knowledge. For example, it is not known what causes this decrease in performance and which physico-chemical parameters are responsible for it. It is even unclear whether BS behave more like a surfactant or like a lipid or whether the substances behave in an either ionic or nonionic way [8–13]. Previous approaches to predict the phase behavior of BS, e.g. using the packing parameter, have not always been successful [14]. In summary, a structure-property relationship for BS has not yet been established.

Therefore, this work addresses this knowledge gap by analyzing the phase behavior of BS with the goal of designing of environmentally friendly formulations which would be a step towards a circular economy. The two BS di-RL and acidic-SL (C18:1, unacetylated) are selected as model BS due to their commercial availability (pK_a values between 5.5 and 6 [15]). Schematic structures and phases of binary, pseudo-binary, ternary and quaternary systems are displayed in Figure 1.1. The following section presents a concise review of the literature on the diverse forms of phase behavior observed for RL and SL [16]. In addition, the typical phase behavior of cationic/anionic and anionic/nonionic conventional surfactant mixture is summarized:

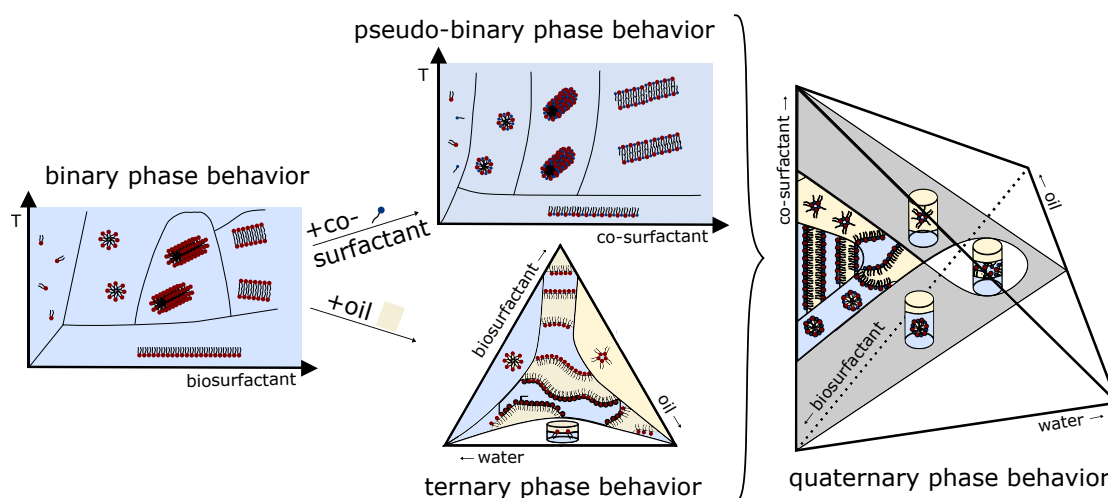


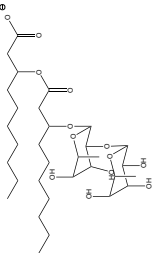
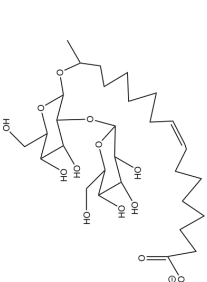
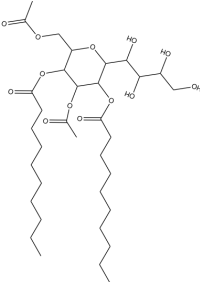
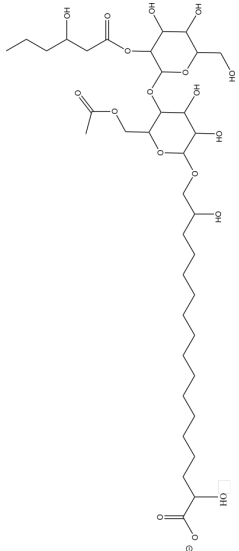
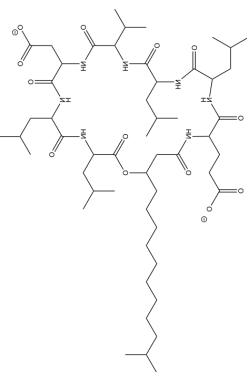
Figure 1.1: Schematic overview of different structures and phases depending on the number and type of components. The binary phase behavior shows the phase boundaries and formed aggregates of one surfactant in water, the pseudo-binary phase behavior of at least two surfactants in water, the ternary phase behavior of one surfactant in an oil-water mixture and the quaternary phase behavior of at least two surfactants in an oil-water mixture (redrawn from [16]).

1.1 Binary Phase Behavior

The binary phase behavior characterizes the structure and phase boundaries of a surfactant in water. This binary behavior of BS has been extensively analyzed and reviewed by Baccile et al. [14]. Simple theories, such as the packing parameter and the HLB concept, often do not provide enough information to fully explain and predict how these molecules assemble. This is due to their complexity of the structural formulas (Table 1.1), e.g. the bola- or gemini-amphiphilic character for the SL or RL, and also due to the presence of impurities, by-products and surfactant mixtures resulting from the production process. The binary phase behavior of BS depends therefore on the composition, but also on concentration, pH (in the presence of a carboxylic group), ionic strength, temperature and pressure. According to these parameters, a BS in water self-assembles into different aggregates (Figure 1.2).

In regard to the binary phase behavior of RL, the formation of micelles ($\text{pH} > 7.5$), vesicles and lamellae (mono-RL and /or $\text{pH} < 7$) has been identified [14]. Moreover, it has been demonstrated that the RL headgroup exhibits conformational flexibility and folding, which results in the shielding of the anionic carboxyl group at high pH and the formation of a large head group area ($38\text{-}114\text{ nm}^2$) when the second alkyl chain of mono-RL is varied

Table 1.1: Examples of BS.

substance	abbe- viation	structural formula	sum mula	for- mula	mole- cular weight [g/mol]	cmc [mmol/l]	ref.
di-rhamnolipid	RL		$C_{32}H_{58}O_{13}$	651	0.16		
acidic sophorolipid	SL		$C_{30}H_{54}O_{13}$	623	0.11		
mannosylerythritol lipid A	MEL		$C_{32}H_{58}O_{13}$	651	0.0066		
cellobiose lipid	CL		$C_{37}H_{65}O_{18}$	798	0.41	[17]	
surfactin	SF		$C_{53}H_{93}N_7O_{13}$	1036	0.0094	[15]	

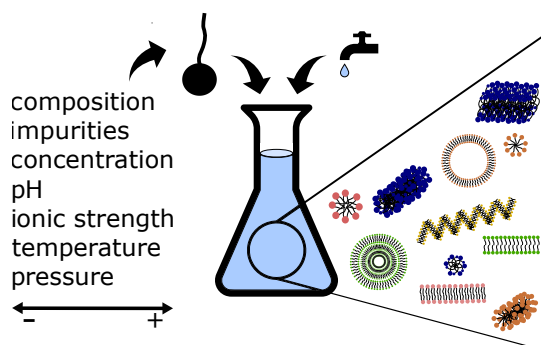


Figure 1.2: Different input parameters influencing the rich binary phase behavior of BS resulting in different aggregates. For a detailed picture, the reader is referred to the text and reference [14]. The pictures only serve as an illustration and do not claim exactness (redrawn from [16]).

[9, 18, 19]. The non-acetylated acidic SL (C18:1 cis) has been observed to self-assemble into spherical or worm-like micelles and nano-platelets [14]. At elevated concentrations, SL forms a lamellar phase, occurring at mass contents exceeding 60-70 wt%. The lamella is characterized by the stretching of SL through it, resulting in the hydrophilic ends being positioned on opposing sides of the lamella. The analogous phenomenon occurs when the carboxylic group of SL is replaced by another sophorose moiety, which molecules self-assembles into a hexagonal phase at high concentrations [20]. Dhar et al. observed that the replacement of a bola-alcoholic group with a bola-carboxylic group in SL results in a lower critical micelle concentration (cmc), a higher equilibrium surface tension (ST), a smaller head group area, and a lower foam height. The presence of a second glucose moiety of SL instead of one moiety leads to a reduction in the cmc, a decrease in the equilibrium ST, a slight increase in the head group area and an increase in the foam volume. [21].

1.2 Pseudo-Binary Phase Behavior

In the context of industrial products, it is uncommon that single surfactants are employed. Mixtures of surfactants frequently demonstrate synergistic properties, such as enhanced surface activity or decreased temperature sensitivity. Hence, at least two surfactants are combined in applications, which, however, results in a completely different phase behavior. When RL is mixed with different anionic surfactants, such as linear alkyl benzene sulfonate (LAS) and sodium lauryl ether sulfate (SLES), micelles and lamellar phases are formed. While RL and LAS mix almost ideally, RL and SLES mix in a manner that is anti-synergistic, as evidenced by results of ST measurements [11, 22]. The addition of cocoamidopropyl betaine (CAPB) to the RL-SLES mixture leads to the formation of

worm-like micelles [23]. The addition of C₁₂E₈ to the RL-SLES-LAS mixture gives rise to a synergistic packing [12, 24, 25]. The addition of anionic surfactants to RL has demonstrated that RL exhibits a rather nonionic character, as evidenced by SANS [11], MD [26] and salt addition studies in ST measurements [9]. Nevertheless, the combination of RL with the nonionic octylphenolethoxylates, comprising approximately 16 ethylene oxide (EO)-units (TX165) or 9.5 EO units (TX100), respectively, revealed the presence of small synergistic effects [27, 28]. Moreover, RL has been combined with the cationic surfactant 1-hexadecyltrimethylammonium chloride (CTAC) and cationic multiple quaternary ammonium salts (MQAS). The formation of nano-vesicles was observed when mono-RL and CTAC are combined, while RL and MQAS demonstrate synergistic properties in equilibrium ST measurements [29, 30]. Furthermore, the combination of different BS is a further possibility. Song et al. investigated the mixed binary system of the nonionic lactonic SL and the anionic di-RL and observed the formation of mixed micelles and large incompact vesicles [31]. A comparison of the surface activity of LAS mixtures with SL or RL revealed that SL exhibits a slightly reduced surface activity. This has been attributed to packing constraints [32]. LAS mixtures with acidic SL form micelles, whereas those with lactonic SL also form lamellar phases, vesicles and bicontinuous structures [13]. Furthermore, favorable interactions of SL were found with choline laurate, sodium dodecylsulfate (SDS) and surfactin [33–35].

1.3 Ternary Phase Behavior

Surfactants are frequently employed in the process of emulsification, whereby two immiscible liquids are combined. Emulsions with RL have been demonstrated to exhibit long stability when exposed to a range of different oils [36, 37]. Switchable emulsions have been developed with RL in which stable emulsions are formed at high pH rather than low pH due to the anionic charge [36]. A comparison of the nonionic and ionic RL in ternary mixtures with n-decane revealed that the ionic variant exhibited a greater number of hydrogen bonds (partly two at the same atom) and a wider distribution of the rhamnose ring than the nonionic RL. Moreover, the ionic RL is observed to segregate from the interface into the bulk at high concentrations, whereas the nonionic variant remains at the interface [38]. Therefore, the nonionic variant appears to be more surface-active, as the same was also demonstrated for mono-RL in comparison to di-RL [39]. Microemulsions (μ E) with 10 wt% RL have been formulated by Nguyen et al., however, with rather hydrophilic oils and high salt contents [40]. The emulsification capacity of SL is found to be inferior to that of RL [41]. Nevertheless, stable emulsions with SL have also been reported [41, 42]. It is noteworthy that the group by Koh and Gross enhanced the interfacial properties and emulsification characteristics of the SL by esterifying the SL carboxylic group with alcohols of varying chain length [43].

1.4 Quaternary Phase Behavior

In technical applications, the use of multiple surfactants is a common practice for the purpose of mixing oil and water. The complexity of at least quaternary systems is a consequence of the multitude of variables inherent to such systems. As a result, the study of quaternary systems is challenging from a scientific perspective. However, their societal relevance necessitates their investigation. Typically, μ Es of anionic or glycoside surfactants are formulated by adding hydrophobic medium-chain alcohols or by establishing a high salinity, which enhances the hydrophobicity of the system [44, 45]. Thus, μ E are observed by adding medium-chained alcohols to RL/oil/water systems [46, 47]. With longer length of the alcohol chain, the existence range of the two-phase region diminishes, while the region of liquid crystals expands [46]. The Winsor III μ E of the system 2% RL/2% lecithin/crude oil/water shows an ultra-low IFT [48]. Alcohol-free μ E were formulated by the group of Nguyen and Sabatini who formulated the systems RL/Sodium dioctyl sulfosuccinate (AOT)/diesel/water with and without oleyl alcohol and RL/SL/lecithin (ratio mono-RL/di-RL=1/1, respectively). The latter system displays superior efficiency compared to the former, achieving ultra-low IFTs [49, 50]. Additionally, other μ E with SL have been reported in which the presence of lactonic SL was found to reduce the existence range of the Winsor IV phase [51] (Figure A1 in SI). Furthermore, non-toxic oil-in-water emulsions of lactonic SL with choline laurate, myristate or oleate were formulated, with the emulsion with choline oleate demonstrating the highest efficiency [35, 52].

1.5 Mixtures of Cationic and Anionic Surfactants

Apart from BS, much research has been conducted on the phase behavior of surfactant mixtures. For example, mixtures of cationic and anionic surfactants (catanionics) were found to have a high surface-activity, a strong synergistic interaction strength and have been extensively studied in literature [53, 54]. These investigations were typically performed with conventional surfactant systems like sulfates, sulfonates and fatty acids as anionic surfactants and quaternary ammonium compounds as cationic surfactants, e.g. sodium dodecyl sulfate and cetyl trimethylammonium bromide [55–57]. All catanionic systems were found to form vesicles and precipitate close to equimolar ratios in water [58, 59]. It was found that asymmetric, i.e. branched, and short surfactant chains decrease the existence range of precipitation [60, 61]. For example, when mixing C_{16} -trimethylammonium and C_{16} -sulfonate, lamellar structures are present at all ratios, while in the mixture C_{16} -trimethylammonium and C_8 -sulfonate, the micellar phase exists up to 30% C_{16} -trimethylammonium [62]. Although asymmetric surfactant systems have been studied, e.g. those with AOT or double-chain surfactants [63–65], no study has reported micelles at equimolar ratios to our best knowledge. In addition, the increase

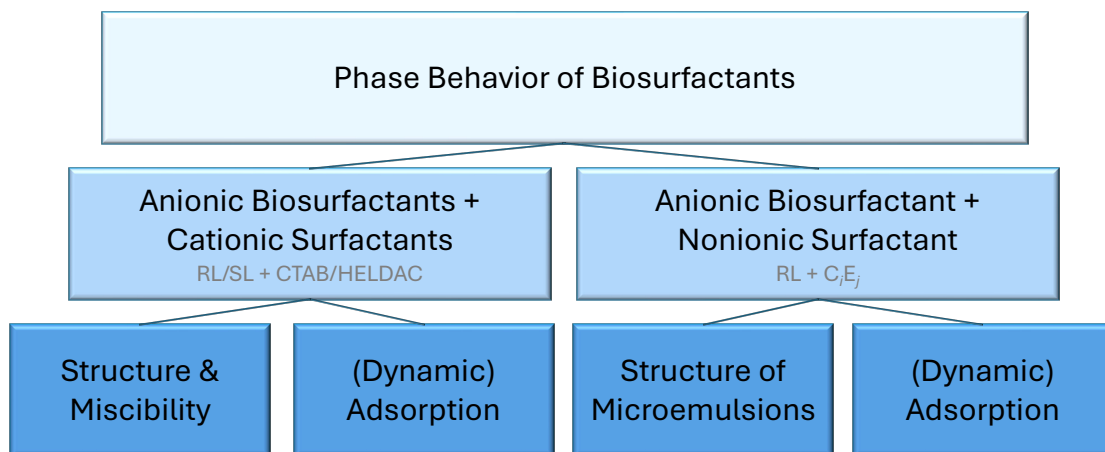


Figure 1.3: Illustration of the scope of this thesis.

of asymmetry, branching degree, and decrease of chain length results in a decrease in synergism [66].

1.6 Mixtures of Anionic and Nonionic Surfactants

Many applications comprise a combination of anionic and nonionic surfactants. A rich phase behavior has been observed, with structures ranging from micelles to vesicles to lamellar phases. The structures and properties of anionic and nonionic surfactant mixtures are frequently associated with those of the individual substances [67, 68]. However, the surfactant mixture often exhibits a lower cmc than the individual surfactants, indicating synergistic interactions. Nevertheless, these interactions are comparatively weaker than those observed in catanionic systems [69, 70]. The majority of research conducted on nonionic surfactants has focused on alkyl ethoxylates C_iE_j , especially in terms of μE [71, 72]. Technical alkyl ethoxylates typically contain a broad mixture of ethoxylates with different chain lengths i , number of ethoxy groups j and fatty alcohol. They are widely used in industry and available from renewable sources (bioethanol and fatty alcohol) [73]. Ethoxylates can be tailored in terms of their hydrophilicity by varying i and j . They are known to reorientate at the surface with increase in surface pressure since they may exist in two different orientations at the surface [74, 75].

1.7 Outline of this Thesis

The investigation of the structure-property relationship of BS and secondary surfactants is conducted on example systems: a cationic-anionic and an anionic-nonionic surfactant

mixture. As the cationic-anionic mixture, two model cationic surfactants cetyl trimethylammonium bromide (CTAB) and alkyl dimethyl hydroxyethyl ammonium chloride (HELDAC) are combined with the anionic di-RL and the anionic acidic-SL. CTAB and HELDAC were used to compare two amine-based cationic surfactants with different counter-ions, which are of industrial relevance [76]. It is noteworthy that synthetic cationic surfactants are combined with renewable and biologically derived anionic surfactants for the purpose of scientific study, with a view to gaining insight into the characteristics of such mixtures.

As the anionic-nonionic mixture, the anionic RL is mixed with alkyl ethoxylates. The reason for selecting alkyl ethoxylates as nonionic surfactants was their straightforward modifiability in hydrophobicity and their substantial relevance in industrial applications [77]. As previously outlined, alkyl ethoxylates can be fully derived from renewable resources.

The two different types of surfactant combinations are examined with regard to the structures which they form in aqueous solutions and in water/oil mixtures, as well as their adsorption properties at interfaces. The self-assembled structures formed in bulk are of significant interest in a number of scientific fields. For instance, the structures may facilitate the solubilization of hydrophobic compounds for emulsification or environmental remediation, function as nanocarriers in drug delivery, or act as templates for the formation of nanomaterials [78]. In addition, the adsorption of surfactants at interfaces is of great significance. For example, adsorbed surfactants reduce the ST for cleaning purposes, improve the wetting of surfaces for coatings and stabilize emulsions and dispersions for pharmaceuticals [79]. The outline of this thesis is illustrated in Figure 1.3.

Chapter 2

Theoretical Background

2.1 Surfactants

2.1.1 Surfactants in Solution

Surfactants (**surface active agents**) are amphiphilic molecules, consisting of both a hydrophobic and hydrophilic part. The former is often a hydrocarbon chain which can be e.g. linear, branched or unsaturated. The charge of the hydrophilic headgroup determines the class of a surfactant, namely cationic, anionic, amphoteric and nonionic surfactants. Usually, a surfactant has one hydrophilic headgroup which is connected to a hydrophobic tail. If two headgroups exist, which are connected by a hydrocarbon chain, the surfactant is categorized as bola surfactant. If two usual surfactants are chemically bonded together through a bridge, the surfactant is called gemini surfactant.

The geometry of surfactants can be described by the concept of the packing parameter P .

$$P = \frac{V}{a_e \cdot l} \quad (2.1)$$

V is the volume and l is the length of the surfactant chains. a_e is the equilibrium area per surfactant molecule at the interface including the hydration shell [80].

Surfactants self-assemble into different structures depending on their concentration, the temperature, the pressure, the salt concentration and the addition of other additives. These factors influence the geometry of the surfactant and therefore P . P hence indicates the structure of the self-assembled aggregates, described in Table 2.1.

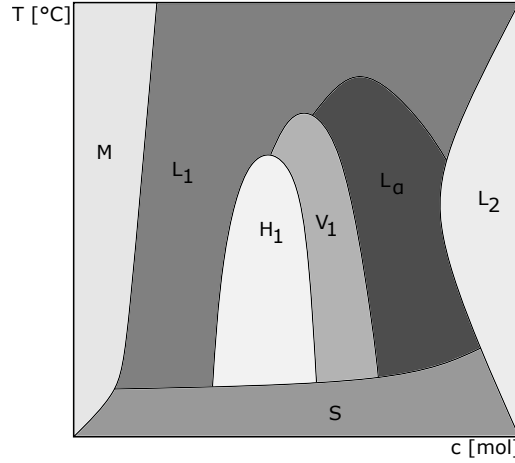


Figure 2.1: Example of self-assembled structures and phase diagram as a function of the packing parameter, here the surfactant concentration c and the temperature T . M is the monomeric, L_1 the micellar, H_1 the hexagonal, V_1 the cubic, L_α the lamellar, L_2 the inverted micellar and S the solid crystal phase.

Table 2.1: Packing parameter P of surfactants and the corresponding shape of the surfactant and self-assembled structures [81].

packing parameter	surfactant shape	structure
0 to $\frac{1}{3}$	cone	spherical micelles
$\frac{1}{3}$ to $\frac{1}{2}$	truncated cone	cylindrical micelles
$\frac{1}{2}$ to 1	truncated cone	flexible bilayers, vesicles
≈ 1	cylinders	planar bilayers
> 1	inverted truncated cone	inverse micelles

A typical phase diagram with examples of self-assembled structures is illustrated in Figure 2.1. The axis of the diagram could be the surfactant concentration, temperature, pressure, salt concentration or other additives, e.g. the surfactant concentration on the x-axis and the temperature on the y-axis. In this latter case, the surfactants exist as free monomers in water at very low surfactant concentration (M).

At a certain temperature and concentration (cmc), typically spherical micelles in water (L_1) are formed due to the hydrophobic effect [82]. The driving force of this hydrophobic effect is the entropy gain due to the liberation of hydration water upon micellization [83].

The Gibbs free energy of micellization dG_m is

$$dG_m = -RT \ln(\text{cmc}) \quad (2.2)$$

with R being the gas constant and T the temperature.

With higher surfactant concentration, the spherical micelles typically become rod-like within the L_1 . At a certain concentration and temperature, the rod-like micelles are densely packed, resulting in a hexagonal phase (H_1). Upon further increase in concentration, the packing parameter changes to flexible and planar bilayers, leading to the formation of cubic (V_1) and lamellar phases (L_α). H_1 , V_1 and L_α are lyotropic liquid crystals which are a state of matter which is thermodynamically situated between liquid and crystalline phases. At very high surfactant concentration, the micelles become inverted (L_2). At low temperature and high concentration, the surfactant appears as a crystal phase (S). The transition from this solid to a liquid phase is called Krafft point. These phase transitions of lyotropic liquid crystals are usually of first order. First order phase transitions are characterized by an abrupt change of the volume, pressure, enthalpy and entropy of a system which occurs since latent heat is released or absorbed.

Since surfactants are surface active agents, they adsorb at interfaces, resulting in a higher concentration at the interface than in the bulk. This surface excess concentration Γ^σ is defined by

$$\Gamma^\sigma = \frac{n^\sigma}{A} \quad (2.3)$$

with n^σ is the surface excess amount and A is the area of the interface. Γ^σ relates to the difference in surface tension σ via the Gibbs adsorption isotherm:

$$\sum_i \Gamma_i^\sigma \mu_i = -d\sigma \quad (2.4)$$

with μ_i being the chemical potential of substance i . In a diluted system of a solvent and solute:

$$\Gamma^\sigma = -\frac{1}{RT} \frac{d\sigma}{d \ln(c/c_0)} \quad (2.5)$$

with c the concentration of the solute and c_0 the standard concentration. Thus, at concentrations just below the cmc, Γ^σ remains constant.

2.1.2 Regular Solution Theory of Mixed Micelles

Mixtures of different surfactants are often used in industrial applications. These different surfactants are likely to have different cmcs. Assuming a mixture of two surfactants, surfactant 1 has the cmc_1 and surfactant 2 the cmc_2 . The chemical potential of the monomeric surfactant 1, μ_1^{mon} , is

$$\mu_1^{\text{mon}} = \mu_1^0 + RT \ln x_1^{\text{mon}} \quad (2.6)$$

with μ_1^0 being the standard chemical potential of surfactant 1, and x_1^{mon} the molar fraction of the surfactant 1 monomer concentration. When surfactant 1 appears in a mixed micelle with surfactant 2, the chemical potential of surfactant 1, μ_1^M , is

$$\mu_1^M = \mu_1^{M0} + RT \ln f_1 x_1 \quad (2.7)$$

with f_1 being the activity coefficient and x_1 the mole fraction of surfactant 1 in the mixed micelle with surfactant 2. μ_1^{M0} is the chemical potential of surfactant 1 in its own micelles:

$$\mu_1^{M0} = \mu_1^0 + RT \ln(\text{cmc}_1) \quad (2.8)$$

Above the cmc, micelles and free monomers are present and in equilibrium, resulting in equal chemical potentials $\mu_1^{mon} = \mu_1^M$. Taking all these considerations into account, the molar fraction of monomeric surfactant 1 is:

$$x_1^{mon} = x_1 f_1 \text{cmc}_1 \quad (2.9)$$

The same thoughts apply to surfactant 2, leading to a molar fraction of monomeric surfactant 2, x_2^{mon} , in a binary mixture when $x_2 = 1 - x_1$:

$$x_2^{mon} = (1 - x_1) f_2 \text{cmc}_2 \quad (2.10)$$

The monomer fraction of surfactant 1 and 2, a_1 and a_2 , at the mixed cmc, cmc_{12} , are

$$x_1^{mon} = a_1 \text{cmc}_{12} \quad (2.11)$$

$$x_2^{mon} = (1 - a_1) \text{cmc}_{12} \quad (2.12)$$

The combination of these equations results in

$$\frac{1}{\text{cmc}_{12}} = \frac{a_1}{f_1 \text{cmc}_1} + \frac{1 - a_1}{f_2 \text{cmc}_2} \quad (2.13)$$

Considering mass balance relationships, the mole fraction of surfactant 1 in the mixed micelle, X_1 , is

$$X_1 = \frac{a_1 x_1 - x_1^{mon}}{x_1 - (x_1^{mon} + x_2^{mon})} \quad (2.14)$$

Therefore, the following equation holds:

$$1 = \frac{X_1^2 \ln \left(\frac{a_1 \text{cmc}_{12}}{X_1 \text{cmc}_1} \right)}{(1 - X_1)^2 \ln \left[\frac{\text{cmc}_{12}(1 - a_1)}{(1 - X_1) \text{cmc}_2} \right]} \quad (2.15)$$

Hence, it becomes possible to determine the mole fraction of surfactants within the micelle, X_1 and X_2 , and calculate the activity coefficients, f_1 and f_2 , and the interaction parameter, β :

$$f_1 = e^{\beta(1-X_1)^2} \quad (2.16)$$

$$f_2 = e^{\beta X_1^2} \quad (2.17)$$

$$\beta = \frac{\ln\left(\frac{\alpha_1 \text{cmc}_{12}}{X_1 \text{cmc}_1}\right)}{(1-X_1)^2} \quad (2.18)$$

β is the net pairwise interactions between the surfactants 1 and 2 in the mixed micelle

$$\beta = \frac{N(W_{11} + W_{22} - 2W_{12})}{RT} \quad (2.19)$$

with N being the Avogadro number in mol^{-1} and W the pairwise interaction energies between the surfactant molecules in mono-component micelles, W_{11} and W_{22} , or bi-component micelles, W_{12} [84, 85]. Hence, negative β values indicate attractive and a positive β repulsive net interactions of the two surfactants. Examples of β with RL and SL are presented in Table 2.2.

The Gibbs free energy can be calculated with

$$\Delta G_{\text{ex}} = RT[X_1 \ln f_1 + (1 - X_1) \ln f_2]. \quad (2.20)$$

If the components mix ideally, their cmc can be expressed as [86]

$$\frac{1}{\text{cmc}_{\text{id}}} = \sum_{i=1}^2 \frac{\alpha_i}{\text{cmc}_i}. \quad (2.21)$$

2.2 Microemulsions

2.2.1 Phase Behavior

μEs are optically isotropic and thermodynamically stable mixtures of oil, water and surfactant(s). They form spontaneously because the surfactant(s) cause a very low IFT [92, 93]. The phase behavior of microemulsions, being at least ternary systems, results from the phase behavior of the binary systems, e.g., oil/water, oil/surfactant and water/surfactant. An example of the phase diagrams using nonionic surfactant and temperature-variation is displayed in Figure 2.2. The phase diagram of the oil/water mixture shows a large two-phase region, whereby small amounts of oil and water are isotropically mixed at high temperature. The ratio of oil and water is defined as

$$\alpha = \frac{m_{\text{oil}}}{m_{\text{oil}} + m_{\text{water}}} \quad (2.22)$$

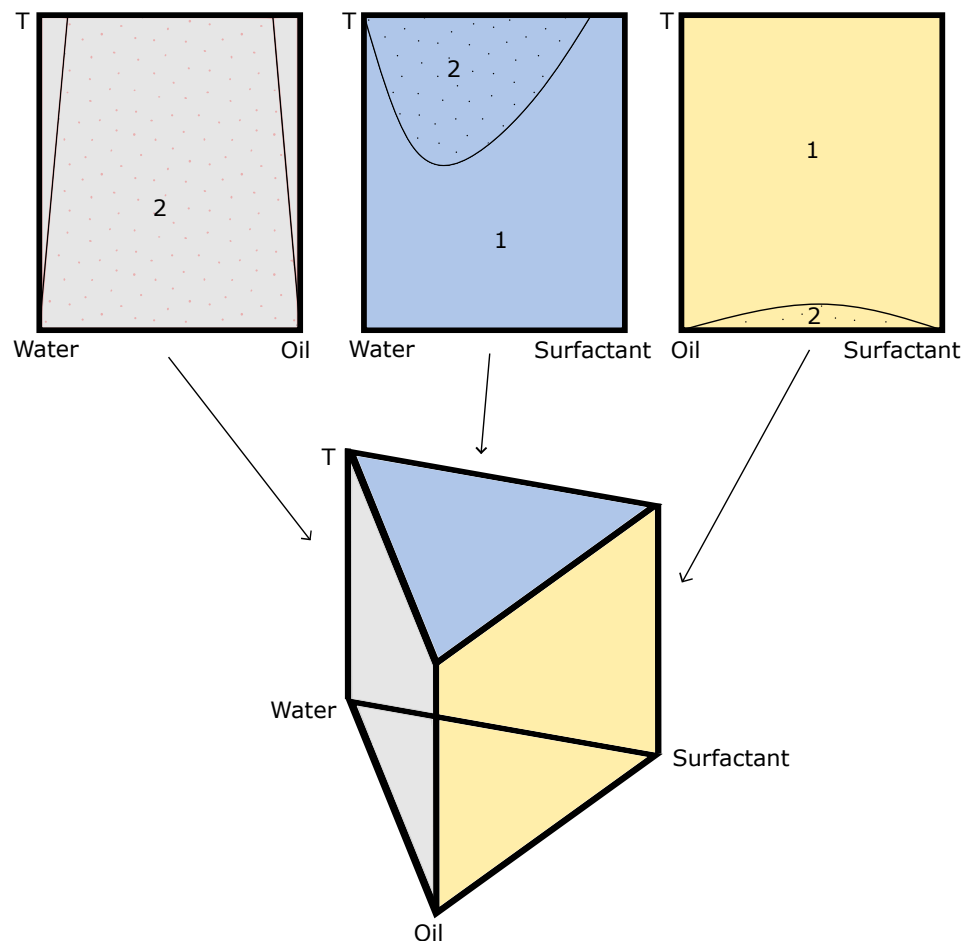


Figure 2.2: Binary phase diagrams of nonionic surfactant, water and oil.

Table 2.2: Comparison of the interaction parameter β of mixed micelles (redrawn from [16]).

type of BS	type of co-surfactant	ratio BS/co-surfactant	pH	β	reference
RL	SDS	0.6 ^a	^d	-5.3	[87]
60% mono- 40% di-RL	SLES	^c	7.1	1.7	[22]
mono-RL	CTAC	0.6 ^a	7.1	-6.7	[29]
RL	SG	0.5 ^a	^d	-8.23	[88]
RL	MQAS	0.5 ^a	^d	-7.06	[30]
RL	TX165	0.6 ^a	^d	-3.3947	[27]
67% mono- 33% di-RL	TX100	0.5 ^b	^d	-0.206	[89]
95% mono-RL	TX100	0.517 ^b	neutral	-0.098	[90]
di-RL	l-SL	0.5 ^a	^d	-0.74	[31]
di-RL	l-SL	0.5 ^a	^d	-0.09	[91]
a-SL	LAS	0.3-0.7 ^a	neutral	\approx -2.0	[32]
l-SL	CHOL	0.6 ^a	^d	-5.674	[35]
l-SL/a-SL	SF	0.5 ^a	^d	-0.413	[34]

^a molar ratio; ^b weight ratio; ^c ratio not indicated; ^d pH not indicated

and surfactant ratio of μ Es is

$$\gamma = \frac{m_{surfactant(s)}}{m_{oil} + m_{water} + m_{surfactant(s)}}. \quad (2.23)$$

The binary phase diagram of surfactant-oil displays a lower miscibility gap. The mixture of surfactant/water also forms a two-phase region at high temperatures [93, 94].

The Gibbs phase prism results from the individual binary phase diagrams (Figure 2.2). The different phases in this prism are hence consequences of the two phase areas of the binary phase behavior. To simplify the analysis of the Gibbs prism, different cuts of the prism can be studied. One cut is the fish or $T(\gamma)$ -cut which occurs at constant oil/water ratio (Figure 2.3). Depending on the ratios of the components and temperature, different phases can be distinguished. The mixture in $\underline{2}$ shows two phases, one oil-in-water emulsion phase and one coexisting excess oil phase (Winsor I). The $\bar{2}$ system contains a water-in-oil emulsion phase and an excess water phase (Winsor II). The system 3 displays a middle phased μ E with an excess water and an excess oil phase (Winsor III). With increasing the surfactant concentration of Winsor III, the excess phases become smaller. When the excess phases disappear and the system contains only one isotropic phase, the Winsor IV system is reached. It is worth noting that the different phases of ternary systems with ionic surfactants emerge in reverse order with temperature compared to systems with nonionic surfactants due to the inverse temperature-dependency of the surfactants [93, 94].

The point of intersection of all phases is known as the \tilde{X} point. It defines the minimal surfactant concentration $\tilde{\gamma}$ and the corresponding temperature \tilde{T} which are capable to form a Winsor IV μ E. Hence, the \tilde{X} point is considered as the efficiency of the μ E. The

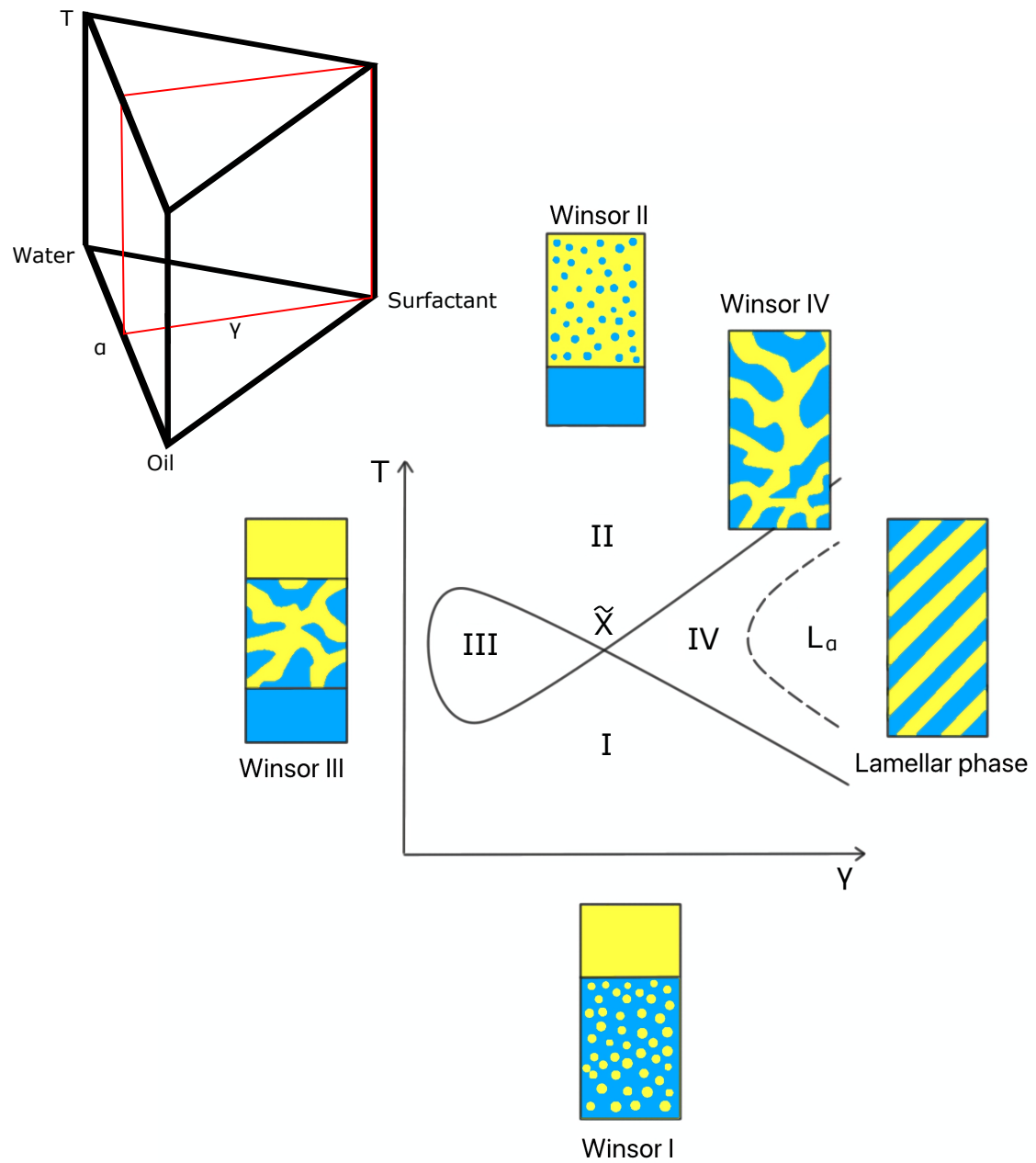


Figure 2.3: Phase behavior of μ Es at constant oil/water ratio (α) and different surfactant concentration (γ).

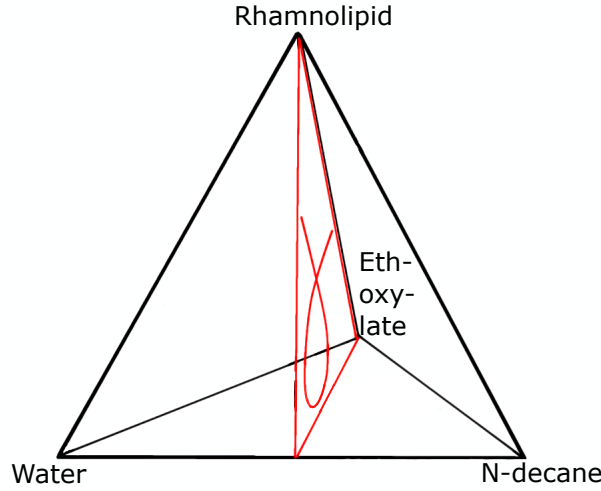


Figure 2.4: Example of a Gibbs prism of quaternary systems with a cut at constant n-decane/water ratio.

monomeric solubility of the surfactant in water and oil has been found to correlate with the efficiency of a μ E in case of ethoxylates. Due to a high monomeric solubility in oil and water, less surfactant is available to adsorb at the interface to create the μ E which reduces the efficiency. The efficiency of μ E increases with longer chain lengths of the surfactant and with shorter chain length of the oil [94, 95].

2.2.2 Microemulsions of Surfactant Mixtures

As discussed earlier, the characteristic curvature of a surfactant not only depends on the temperature, but it also on other factors like the addition of a secondary surfactant or co-surfactant. The change of the characteristic curvature of nonionic sugar-containing surfactants is usually varied by the addition of another surfactant since their phase behavior is hardly temperature or salt-dependent [96]. Hence, the temperature in Figure 2.2 can be replaced with the ratio of another surfactant, e.g. the ethoxylate in a RL/water/n-decane system (Figure 2.4). The mass fraction of the other surfactant is defined as

$$\delta = \frac{m_{surfactant2}}{m_{surfactant1} + m_{surfactant2}} \quad (2.24)$$

When ionic and ethoxylated surfactants are mixed together with oil and water, the μ E becomes less temperature dependent due to the inverse temperature effects of the different surfactant types [97–99]. Technical surfactant systems are per se a mixture of different components. Surface-active components may shift the phase boundaries according to their hydrophilicity and monomeric solubility. μ Es with technical ethoxylates show a strong

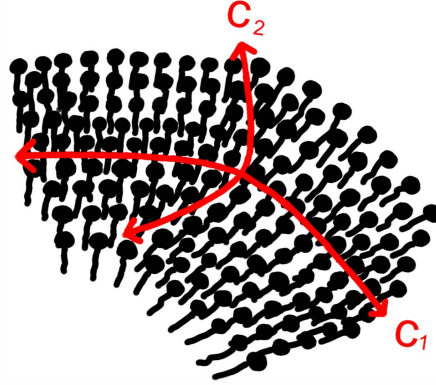


Figure 2.5: Surfaces at different mean curvatures, H , and Gaussian curvatures, K (based on [103]).

deviation at low surfactant concentration due to partitioning of the more hydrophobic compounds within the technical ethoxylate [71, 100–102].

2.2.3 Microstructure

The microstructure of μ Es is schematically shown in Figure 2.3. Whereas droplets are formed in Winsor I and II, a bicontinuous structure exists in Winsor III and IV. The surfaces of the structures can be characterized by the minimum and maximum curvatures of a surface, namely the principle curvatures $c_1 = \frac{1}{R_1}$ and $c_2 = \frac{1}{R_2}$ (Figure 2.5). With these curvatures, it becomes possible to define the mean curvature, H , and the Gaussian curvature, K :

$$H = \frac{c_1 + c_2}{2} \quad (2.25)$$

$$K = c_1 \cdot c_2 \quad (2.26)$$

Depending on H and K , different shapes of surfaces emerge, illustrated in Figure 2.6. The surface is curved to different directions if $H < 0$ or $H > 0$. A change of the temperature, pressure, salt-content, α , or δ will result in a corresponding change in H . This may, for instance, manifest as a transition from Winsor I to Winsor II. When $H = 0$, the surface is flat on average, which is why $H = 0$ in Winsor III and IV. At low surfactant concentrations close to the \tilde{X} -point, $K < 0$. With increasing surfactant concentration γ , K also increases. The free energy per area, F/A , of a surfactant film assuming a negligible thickness and dominant elastic properties has been defined by Helfrich as

$$F/A = 2\kappa(H - H_0)^2 + \bar{\kappa}K. \quad (2.27)$$

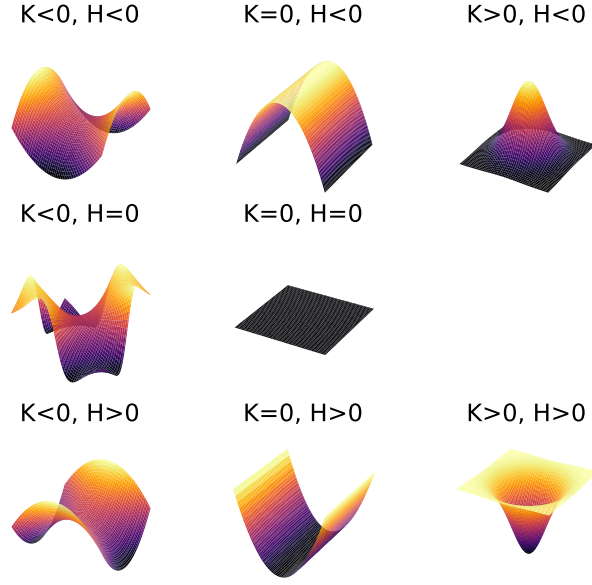


Figure 2.6: Surfaces at different mean curvatures, H , and Gaussian curvatures, K (based on [103]).

H_0 is the equilibrium mean curvature, κ is the bending modulus and $\bar{\kappa}$ is the saddle splay modulus [104]. H_0 and the corresponding spontaneous curvature, c_0 , are adopted by the surfactant film in an optimal environment with optimal hydration of the surfactant. κ quantifies the energy which is required for bending the surfactant film and controls the amplitude of thermal fluctuations. The higher κ , the more ordered is the amphiphilic surfactant layer [105]. $\bar{\kappa}$ rules the preferred interface topology, in the way that $\bar{\kappa} < 0$ for Winsor I and II and $\bar{\kappa} > 0$ for Winsor III and IV. [106, 107]. Hence, the bending rigidity, κ , is closely related to the persistence length, ξ , which describes a length below which the interface is basically flat:

$$\xi = l_s \cdot e^{\frac{2\pi\kappa}{k_B T}} \quad (2.28)$$

l_s is the length of the surfactants chain, k_B is the Boltzmann constant and T is the temperature [108]. It has been found that the persistence length ξ is approximately the half of the domain size d in μEs [109].

2.3 Characterization Methods

2.3.1 Pulsed Gradient Spin Echo Nuclear Magnetic Resonance Spectroscopy

Nuclear magnetic resonance spectroscopy (NMR) is based on the non-zero magnetic nuclear spin of atoms. In an external magnetic field, the possible orientations of the spins demonstrate an energy difference, ΔE , known as the Zeemann effect:

$$\Delta E = \hbar \gamma B_0 = \hbar \omega_0 \quad (2.29)$$

B_0 is the strength of the magnetic field, \hbar is the reduced Planck constant, ω_0 is the resonance or Larmor frequency and γ is the gyromagnetic ratio which depends on the type of atom. ω_0 is contingent upon the particular magnetic field of a nucleus and its environment. When a nucleus is excited by a pulse containing its specific Larmor frequency, the orientation of the spins changes, resulting in an absorption of energy ΔE , which can be detected.

The application of a gradient G to B_0 , $B_0(x)$, $\omega_0(x)$ and $\Delta E(x)$ results in a dependence on position along the gradient. Therefore, when a gradient is applied after the pulse, the phase evolution depends on the location of the spin. When the same gradient is applied in the opposite direction, the phase evolution occurs in a manner analogous to that observed with the initial gradient (Figure 2.7 without diffusion). It is only possible to achieve refocusing if the nuclei are situated at identical points within the gradient. In the event of a change in position due to diffusion, the spins are not fully refocused in one direction, resulting in a reduction in signal intensity [110]. The decline in signal intensity depends on the gradient strength, as postulated by the Stejskal and Tanner formula [111, 112]:

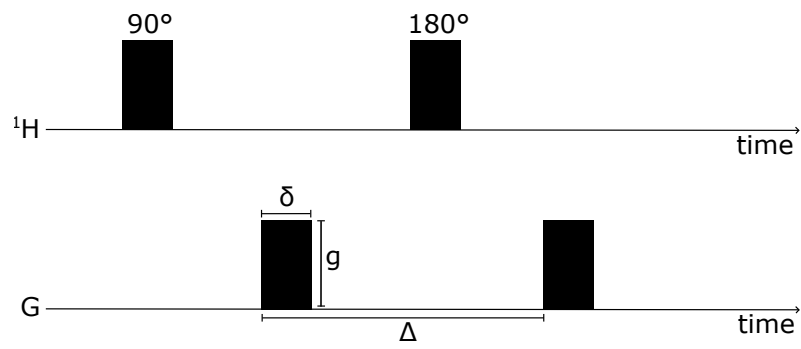
$$I_g = I_0 e^{-D \gamma_{\text{eff}}^2 \delta^2 G S P^2 g^2 \Delta} \quad (2.30)$$

I_g represents the echo intensity for a given gradient, I_0 is the echo intensity which would occur without diffusion, D is the translational diffusion coefficient, γ is the gyromagnetic ratio ($2.675 \cdot 10^8 \text{ rads}^{-1} \text{T}^{-1}$ for ^1H), g is the gradient strength, δ is twice the duration of the gradient pulses, GSP is the gradient shape parameter and Δ is the diffusion delay (time between the coding and decoding gradient blocks) [110].

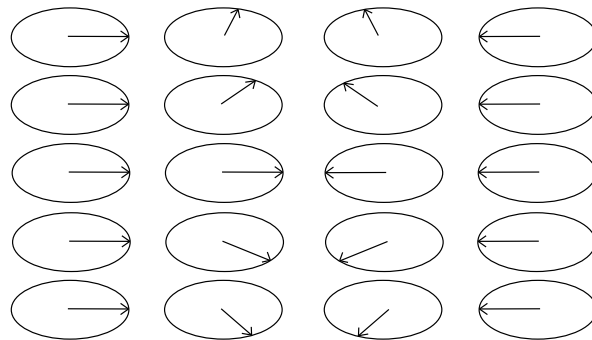
When one signal in NMR contains contributions of two molecules, I_g can be modeled by a sum of two discrete exponential functions:

$$I_g = I_{0A} e^{-D_A \gamma_{\text{eff}}^2 \delta^2 G S P^2 g^2 \Delta} + I_{0B} e^{-D_B \gamma_{\text{eff}}^2 \delta^2 G S P^2 g^2 \Delta} \quad (2.31)$$

I_{0A} , I_{0B} , D_A and D_B are the initial intensities and diffusion coefficients of the components A and B which have their peak at the same chemical shift [113].



Without diffusion:



With diffusion:

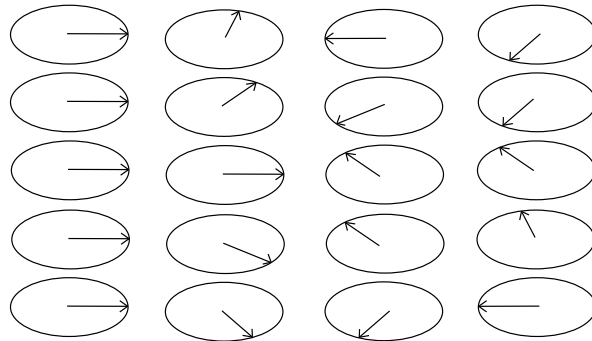


Figure 2.7: Puls sequence and direction of spins of a PGSE-NMR experiment.

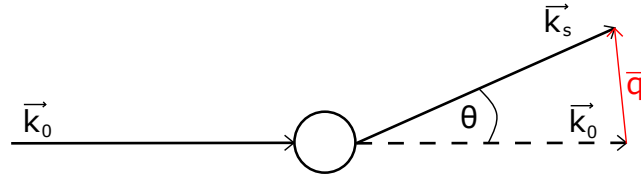


Figure 2.8: Definition of scattering vectors.

2.3.2 Dynamic Light Scattering

Light interacts with colloidal objects in a medium which can result in the scattering of light (\vec{k}_s) from its original path (\vec{k}_0) in a certain angle θ (Figure 2.8) with

$$|\vec{k}_s| = |\vec{k}_0| = \frac{2\pi}{\lambda}. \quad (2.32)$$

\vec{q} is defined as the scattering vector which is the difference between \vec{k}_s and \vec{k}_0 :

$$\vec{q} = \vec{k}_s - \vec{k}_0 \quad (2.33)$$

q is the absolute value of the scattering vector:

$$q = |\vec{q}| = \frac{4\pi n}{\lambda} \cdot \sin \frac{\theta}{2} \quad (2.34)$$

n is the refractive index of the solvent, and λ is the wavelength. Different forms of scattering can be distinguished. In elastic scattering the kinetic energy of the incident light beam is conserved and only the direction of the light beam changes ($\vec{k}_0 = \vec{k}_s$). In inelastic scattering, parts of the kinetic energy of the incident light beam are transferred onto the scattering object, resulting in $\vec{k}_0 > \vec{k}_s$. Elastic scattering can be divided into Rayleigh scattering if the diameter of the scattering object $d < \frac{\lambda}{20}$ and Mie scattering if $d > \frac{\lambda}{20}$.

Dynamic light scattering (DLS) is a quasi-elastic scattering experiment as elastic and inelastic scattering occurs. The technique allows the measurement of diffusion coefficients of colloidal scattering objects in liquid media. Due to the Brownian motion of the scattering objects, the intensity of the scattered light fluctuates with time. This variation in intensity over time can be correlated which auto-correlation function, which then gives the diffusion coefficient of the scattering object. This working principle is illustrated in Figure 2.9.

A typical DLS spectrometer comprises a coherent laser beam that is directed at the sample. After the scattering events, the detector (e.g. a photomultiplier) records the intensity of the scattered light $I(t)$, as a function of the time t , and the intensity $I(t + \tau)$ after the lag

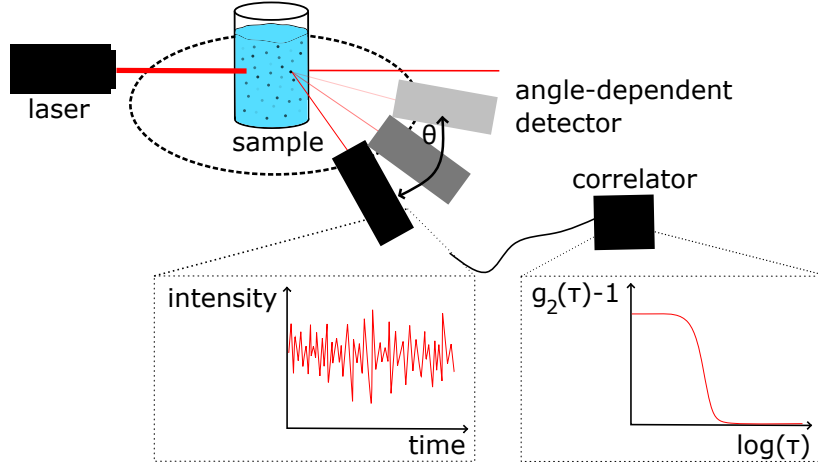


Figure 2.9: Schematic illustration of a dynamic light scattering experiment.

time τ at q . The correlator determines the intensity-time-auto-correlation function $g_2(\tau)$ [114]:

$$g_2(\tau) = \frac{\langle I(t) \cdot I(t + \tau) \rangle}{\langle I \rangle^2} \quad (2.35)$$

For data analysis, $g_2(\tau)$ is transferred into the electric field correlation function $g_1(\tau)$

$$g_2(\tau) = 1 + \beta |g_1(\tau)|^2 \quad (2.36)$$

in which B is the baseline and β is the intercept, which is a measure of the signal-noise ratio (Siegert relation; originally $B = 1$ and $\beta = 1$) [115]. $g_1(\tau)$ is

$$g_1(\tau) = \frac{\langle E(t) \cdot E(t + \tau) \rangle}{\langle I \rangle^2} \quad (2.37)$$

with E being the strength of the electric field. For monomodal and monodisperse samples,

$$g_1(\tau) = e^{-\Gamma\tau} \quad (2.38)$$

with Γ being the decay rate, can be applied. In the cumulant analysis, this equation can be approached by the following Taylor series [116, 117]

$$\ln(g_2(\tau) - B) = \ln\beta + 2(-\Gamma\tau + \frac{k_2}{2!}\tau^2 - \frac{k_3}{3!}\tau^3) \quad (2.39)$$

where k_2 and k_3 are coefficients. The translational diffusion coefficient D_t can be derived from

$$D_t = \frac{\Gamma}{q^2} \quad (2.40)$$

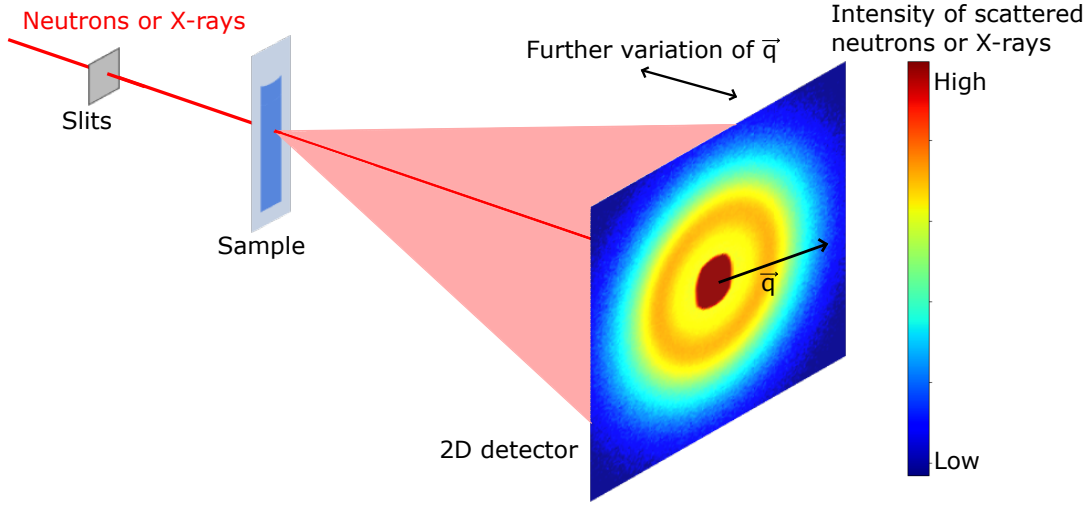


Figure 2.10: Schematic presentation of the principle of small-angle scattering experiments with neutrons or X-rays with isotropic scattering and a 2D area detector.

Assuming spherical scattering objects, the hydrodynamic radius R can be determined by the Stokes-Einstein-equation

$$R = \frac{k_B T}{6\pi\eta D_t} \quad (2.41)$$

with η being the dynamic viscosity of the medium. In case of anisotropic scattering objects, rotational diffusion may exist besides the translational one. This rotational diffusion coefficient D_r can often be quantified in the intercept y of the plot Γ vs. q^2 which is

$$y = 6D_r \quad (2.42)$$

2.3.3 Static Small-Angle Scattering in General

In static scattering, the intensity is taken as an average of time, $I(q) = \langle I(q, t) \rangle_t$. Figure 2.10 displays the typical setup of a static small-angle experiment, where the intensity of the scattered waves (e.g. neutrons or X-rays) $I(q)$ is measured as a function of the scattering vector q . The multitude of different scattering events leads to an interference of the scattered waves. This can be captured in the following formula

$$I(\vec{q}) = \left| \int_{V_j^0} f(\vec{r}') e^{i\vec{q}\vec{r}'} d\vec{r}' \right|^2 \left| \sum_{j=1}^N e^{i\vec{q}\vec{r}_j} \right|^2 \quad (2.43)$$

with V_j^0 being the scattering volume of object j , \vec{r}_j being the vector to the center of the scattering object j and $f(\vec{r}')$ is the scattering ability. $I(\vec{q})$ depends on the distribution of

scattering centers in certain objects (first part of Equation 2.43, form factor $P(\vec{q})$) and on the distribution of these scattering objects in space (first part of Equation 2.43, structure factor $S(\vec{q})$):

$$P(\vec{q}) = \left\langle \left| \frac{\int_{V_j^0} f(\vec{r}') e^{i\vec{q}\vec{r}'} d\vec{r}'}{\int_{V_j^0} f(\vec{r}') d\vec{r}'} \right|^2 \right\rangle \quad (2.44)$$

$$S(\vec{q}) = \frac{1}{N} \left| \sum_{j=1}^N e^{i\vec{q}\vec{r}_j} \right|^2 \quad (2.45)$$

Hence, $I(\vec{q})$ can be described by

$$I(\vec{q}) = V_p \phi (\Delta \text{SLD})^2 P(\vec{q}) S(\vec{q}) \quad (2.46)$$

V_p is the volume of the scattering object, ϕ is the volume fraction, and ΔSLD is the difference of the scattering length densities of the solvent and the scattering object. It should be noted that only elastic coherent scattering is regarded and that inelastic scattering also occurs in reality.

The form factor $P(q)$ describes the distribution of scattering centers within the scattering objects. Spherical (swollen) micelles are usually considered as core-shell spheres with the hydrophobic part as core and hydrophilic part as shells:

$$P(q) = \frac{9}{V_p^3} \left[V_c (\text{SLD}_c - \text{SLD}_s) \frac{\sin(qR_c) - qR_c \cos(qR_c)}{(qR_c)^3} + V_p (\text{SLD}_s - \text{SLD}_{\text{solv}}) \frac{\sin(qR_p) - qR_p \cos(qR_p)}{(qR_p)^3} \right]^2 \quad (2.47)$$

V_p is the volume of the whole scattering object, V_c is the volume of the core, R_p is the radius of the whole scattering object, R_c is the radius of the core, SLD_c is the SLD of the core, SLD_s is the SLD of the shell and SLD_{solv} is the SLD of the solvent.

The availability of appropriate $P(q)$ models for the scattering of the amphiphilic film in bicontinuous μEs (film contrast) is low. The model of Porcar et al. uses randomly oriented disks as form factor [118]

$$P(q) = 4(\pi R_g^2 \Delta \text{SLD})^2 \frac{1 - \cos(qt_0) e^{-q^2 t_0^2 / 32}}{q^2 (q^2 R_g^2 + 2e^{-q^2 R_g^2 / 6})} \quad (2.48)$$

with R_g being the gyration radius of the disks and t_0 being the contrast thickness (hydrophobic core of the surfactant film).

The structure factor $S(q)$ describes the distribution of the scattering objects in space. Micelles with ionic surfactants contain charge which is why a Hayter-Penfold Rescaled Mean Spherical Approximation (HSA) structure factor may be employed [119–121]. For two-component systems, e.g. when oil and water are the main scattering objects in the bulk contrast of bicontinuous μE , the Teubner-Strey model can be used as $S(q)$:

$$S(q) = \frac{8\pi\phi(1-\phi)(\Delta\text{SLD})^2\xi^4}{\xi \left[\left(1 + \left[\frac{2\pi\xi}{d} \right]^2 \right)^2 + q^2(-2\xi^2 \left(\frac{2\pi\xi}{d} \right)^2 + 2\xi^2) + q^4\xi^4 \right]} \quad (2.49)$$

d is the periodicity, e.g. of the oil plus water domains in bicontinuous μE , ξ is the correlation length which is a long-range order, and ϕ is the volume fraction [122, 123]. The amphiphilicity factor f_a is defined as [124]

$$f_a = \frac{\left(\frac{2\pi}{d} \right)^2 - \frac{1}{\xi^2}}{\left(\frac{2\pi}{d} \right)^2 + \frac{1}{\xi^2}}. \quad (2.50)$$

f_a quantifies the amphiphilicity of a surfactant and therefore also the structuring of the μE , with $f_a = -1$ for well structured and $f_a = 1$ for disordered μE s [125]. Furthermore, the bending modulus κ can be derived by [126]

$$\kappa = \frac{10\sqrt{3}\pi\xi k_B T}{64d}. \quad (2.51)$$

For the analysis of the film contrast in μE , a different $S(q)$ was used which has been derived by Lei et al. for a sponge-like structure [127]

$$S(q) = 1 + \frac{A \cdot \arctan(q\xi_{io}/2)}{q} + \frac{B}{1\xi_3^2 + (q - 2\pi/d_f)^2} \quad (2.52)$$

with d_f being the thickness of the amphiphilic film, ξ_{io} being inside-outside correlation length (greater than the pore size of the bicontinuous structure), ξ_3 being the correlation length and q_3 correlates with the average pore size $\xi = \frac{2\pi}{q_3}$.

The total amount of scattering is independent of the shape or size of the scattering object if the relative volume fractions are incompressible. This amount is quantified by the invariant Q^*

$$Q^* = \int_0^\infty I(q)q^2 dq. \quad (2.53)$$

The experimental invariant can be obtained from scattering experiments if extrapolating the data points for the not measured q values. The theoretical invariant of a two-phase system is

$$Q_{th}^* = 2\pi^2(\Delta\text{SLD})^2\phi_1\phi_2. \quad (2.54)$$

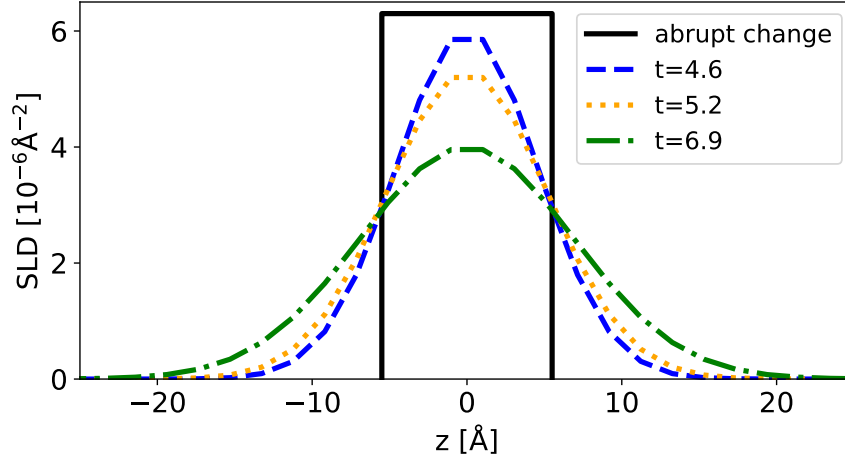


Figure 2.11: Profile of the interface assuming different smearing factors t and a constant scattering amount.

For high q , Porod found

$$\lim_{q \rightarrow \infty} I(q) = 2\pi\phi(\Delta\text{SLD})^2 \frac{S}{V} q^{-4} \quad (2.55)$$

with $\frac{S}{V}$ being the specific interface if the SLD change is abrupt [128, 129]. If the SLD change is not abrupt, i.e. if oil or water penetrates the amphiphilic surfactant film, a smearing function for diffuse interfaces should be employed:

$$\lim_{q \rightarrow \infty} I(q) = 2\pi\phi(\Delta\text{SLD})^2 \frac{S}{V} q^{-4} e^{-q^2 t^2} \quad (2.56)$$

t is the smearing factor of the Gauss profile. As an example, density profiles $\text{SLD}(z)$ for different t is displayed in Figure 2.11, assuming a Gaussian profile and the same amount of total scattering [130]. Theoretically, changes in SLD occur over a fraction of the molecular length of the surfactant molecule [130]:

$$t = \frac{l_s}{\sqrt{2\pi}} = \frac{V_s}{A_s \sqrt{2\pi}} \quad (2.57)$$

l_s is the length, V_s the volume and A_s the surface area of the surfactant molecule. Applying contrast matching experiments for μEs , the contrasts of oil and water can be matched resulting in the sole scattering of the amphiphilic film. In this case Equation 2.56 changes to [130]

$$\lim_{q \rightarrow \infty} I(q) = 2\pi\phi(\Delta\text{SLD})^2 \frac{S}{V} q^{-2} e^{-q^2 t^2}. \quad (2.58)$$

2.3.4 Small-Angle X-ray Scattering

Small-angle X-ray scattering (SAXS) is a technique of static scattering in which the scattered X-rays are quantified at small angles. The fundamental principle is that the photons of X-rays undergo elastic scattering at the electron shell of a scattering object as a function of q . Given that X-rays possess an energy $E \approx 10$ keV and therefore a wavelength $\lambda \approx 0.12$ nm, X-rays have a smaller wavelength than light, and hence larger q (Equation 2.34). In SAXS, Δ SLD correlates with an excess of the electron density. The electron density of a molecule SLD can be calculated with

$$\text{SLD} = \frac{\sum_i b_i(r)}{v} = \frac{\sum_{\text{atom}} \text{atomic number}}{\sum_{\text{atom}} \text{weight}} d \quad (2.59)$$

with d being the mass density, v being the resolution volume and $b_i(r)$ being the scattering length of atom i at location r . It follows that contrast depends on the electron density of a substance and thus on its atomic number. The high energy of X-rays interacts strongly with the electron shells of the atoms, leading to intense scattering, high sensitivities, especially for heavy and dense materials, and typically higher signal intensities. However, the strong interaction of X-rays with the sample and surrounding materials also results in significant background scattering, which often requires subtraction to isolate the true scattering from the sample. The scattered X-rays are detected by a two-dimensional-detector, such as a charge-coupled device (CCD) camera. The high resolution of the CCD camera, in conjunction with the collimation, monochromator and high intensity, ensures excellent precision of q .

2.3.5 Small-Angle Neutron Scattering

Small-angle neutron scattering (SANS) uses neutrons as energy source which interact with atomic nuclei according to its SLD:

$$\text{SLD} = \frac{\sum_i b_i(r)}{v} = \frac{N_A \sum \text{atomic scattering length in molecule}}{\text{molar volume}} \quad (2.60)$$

with N_A being the Avogadro number. The atomic scattering length does not only vary between elements, but also between the isotopes of the same element. For example, the SLD for H_2O is calculated to be $-0.56 \cdot 10^{-10} \text{ cm}^{-2}$ and for D_2O $6.34 \cdot 10^{-10} \text{ cm}^{-2}$. This illustrates the potential for conducting contrast variation experiments using deuterated substances, i.e. to highlight different structural features of multi-component systems. In multi-component systems containing two surfactants in water, the contrast of one surfactant and water could be matched leading to the investigation of the other surfactant. In μE , the oil domains, the amphiphilic film and each surfactant in this film can be studied in this way (Figure 3.3).

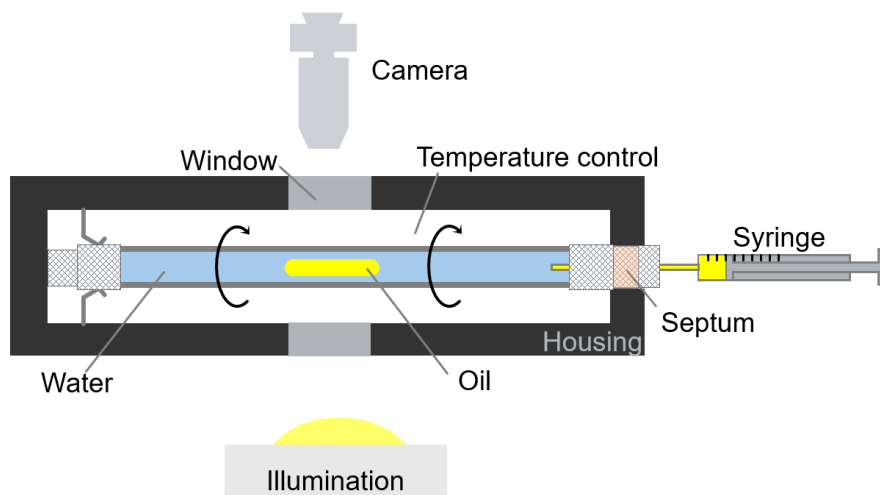


Figure 2.12: Schematic illustration of the spinning drop experiments.

Comparing the Equations 2.59 and 2.60, the SLDs have different values for same substances, resulting in varying contrast effects in SAXS and SANS experiments [131]. A comparison of octyl- β -maltopyranoside micelles revealed that SAXS yielded a larger gyration radius than SANS. This discrepancy can be attributed to the significant contribution of the hydration shell surrounding the micelles to the contrast observed in SAXS, due to the high sensitivity of X-rays to electron density [132].

SANS utilizes neutrons produced from nuclear reactors or spallation sources, which are less readily accessible than X-ray sources. This limitation in availability affects the accessibility of SANS experiments. The interaction of neutrons with a sample is considerably less than that of X-rays, resulting in a reduction in background scattering, diminished sample damage, and the necessity to utilize longer exposure times. In contrast to SAXS, which employs crystal monochromators to select a narrow X-ray wavelength, SANS utilizes velocity selectors as monochromators to filter neutrons by their energy. The utilization of this monochromator, in conjunction with e.g. He-3 isotope tubes as detectors, serves to limit the resolution of SANS.

2.3.6 Spinning Drop Measurements

Spinning drop measurements enable the determination of low IFTs, γ , of two in-miscible liquids. One drop of a liquid having a lower density is inserted into a glass capillary filled with another liquid. The capillary is rotated at a frequency, ω , about a horizontal axis and the drop elongates which shape can be detected by a camera (Figure 2.12). The cylindrical shape of the drop results from an equilibrium of the centrifugal and the interfacial force [133]. In addition, the total energy of the rotating system E of the droplet approaches a

minimum:

$$\frac{dE}{dR} = 0 \quad (2.61)$$

with R being the radius of the drop. E is a sum of its kinetic energy E_k and surface energy E_s . Assuming a cylindrical shape:

$$E = E_k + E_s = \frac{\Delta m r^2 \omega^2}{4} + 2\pi l r \gamma \quad (2.62)$$

Δm is the mass difference, and l is the length of the cylindrical drop. Hence,

$$\frac{\Delta m r \omega^2}{2} + 2\pi l \gamma = 0 \quad (2.63)$$

and

$$\gamma = \frac{\Delta m r \omega^2}{4\pi l} \quad (2.64)$$

With the density difference $\Delta \rho = \frac{\Delta m}{V}$ and the cylindrical volume $V = \pi l r^2$:

$$\gamma = \frac{\Delta \rho r^3 \omega^2}{4} \quad (2.65)$$

This equation is known as the Vonnegut-equation [134].

Originally originated for dynamic surface tension (DST) measurements, Hua and Rosen derived an empirical model for the DST curves. They divided the DST curve into four regions: the induction, rapid fall, meso-equilibrium, and equilibrium region. Furthermore, they derived the following formula for the first three regions

$$\frac{\gamma_0 - \gamma_t}{\gamma_t - \gamma_m} = \left(\frac{t}{t^*} \right)^n \quad (2.66)$$

where γ_0 the ST of the pure solvents, γ_m is the ST of meso-equilibrium, t is the time and t^* and n are constants. t^* denotes the time at which the half of the ST reduction occurs $t^* = t_{1/2}$ and n represents a scaling exponent responsible for the slope of ST reduction. The ST decay rate $R_{1/2}$ at $t_{1/2}$ can be calculated with

$$R_{1/2} = \frac{\Pi_m}{2t_{1/2}} = \frac{\gamma_0 - \gamma_m}{2t^*} \quad (2.67)$$

with Π_m being the surface pressure at meso-equilibrium [135].

Furthermore, DST data can be also explained based on diffusion where a model was developed by Ward and Tordai [136]. Because an analytic solution of their equation cannot be obtained, Fainerman et al. developed approximations for very short- and long-time scales [137]. However, the Ward-Tordai equation was originally derived for the

diffusional transport of monomer surfactants. In fact, there are other processes present if an interface is newly created, such as solvent relaxation, reorientation, adsorption, diffusional transport of micelles as well as their desorption, decay, and conversion [138]. Therefore, it was proposed to consider micelles if dealing with concentrations above the cmc [139]. However, experimentally, the presence of micelles did not affect the DST curves much, presumably due to fast relaxation times which provide monomers from micelles [140]. If that is the case and at short times, the ST can be described by

$$\gamma = \gamma_0 - 2nTRc \left(\frac{D_s t}{\pi} \right)^{1/2} \quad (2.68)$$

where n is 2 for ionic and 1 for nonionic surfactants [136, 141].

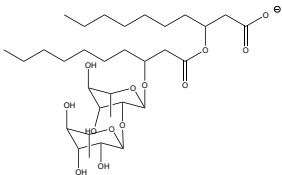
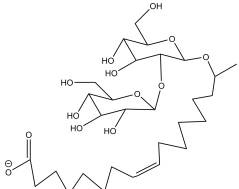
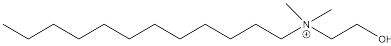
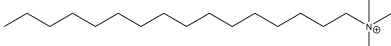
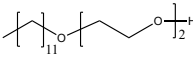
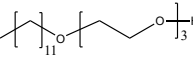
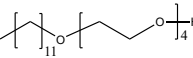
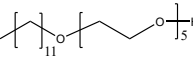
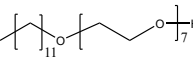
Chapter 3

Materials and Methods

3.1 Materials

As surfactants, Rewoform RL 100 (di-RL dominant, 49.5 wt% water by Karl-Fischer titration) from Evonik Industries AG was used as rhamnolipid (RL). For the acidic sophorolipid (SL), Rewoform SL ONE (42 wt% acidic sophorolipid and 58 wt% lactonic sophorolipid) was hydrolyzed. Therefore, three times the amount of stoichiometric sodium hydroxide with 20 wt% excess over the lactonic SL content was added to Rewoform SL ONE and stirred overnight at room temperature. Liquid chromatography revealed a residual amount of 7 wt% lactonic sophorolipid and Karl-Fischer titration showed a water content of 62.7 wt%. The detailed composition of SL is shown in Table A1 in the Appendix. Alkyl dimethyl hydroxyethyl ammonium chloride (HELDAC) was obtained from Clariant. The chain length distribution was 68 area-% C₁₂, 27% C₁₄ and 5% C₁₆ as determined by liquid chromatography electrospray ionization mass spectrometry. Cetyltrimethylammonium bromide (CTAB, 99 wt% pure) was obtained from VWR. As the technical ethoxylates C₁₂C₁₄E₂, C₁₂C₁₄E₃, C₁₂C₁₄E₄ and narrow-range (NRE) C₁₂C₁₄E₃, Rhodasurf L2 and Rhodasurf L4 from Solvay GmbH, Genapol LA 030 SG Vita from Clariant International Ltd and Novel 1412-3 from Sasol Germany GmbH were used, respectively. They are a mixture of ethoxylates with different chain lengths, mostly C₁₂ and C₁₄. As branched surfactants Lutensol TO3 and Lutensol AO3 from BASF SE were used. Lutensol AO3 had a branching degree of approximately 0.5 and Lutensol TO3 of 2.3 [142]. The exact ethoxylation degrees and chain lengths are displayed in Figure 3.1 and the one of the mono-dispersed ethoxylates of one single chain length in Table A2 in the Appendix. Unlike mono-disperse substances, technical variants consist of many different mono-disperse ethoxylates and fatty alcohol. Normal technical ethoxylates show a broad-range of different ethoxylation degrees (Figure 3.1 A), while narrow-range ethoxylates (NRE) have a narrower distribution of ethoxylates (Figure 3.1 B). Their composition was analyzed using gas chromatography electrospray

Table 3.1: Overview of all surfactants in this study, their structural formulas, their molecular weight (M_w), their critical micelle concentration (cmc) and their hydrophilic-lipophilic balance (HLB) values.

name	structure	M_w [g/mol]	cmc [mg/l]	HLB
RL		650.8	105.8	13.1
SL		622.7	65.4	16.4
HELDAC		307	603	9.0
CTAB		364.5	27	7.7
C ₁₂ E ₂		274.4	9.1	7.7
C ₁₂ E ₃		318.5	16.6	9.4
C ₁₂ E ₄		362.5	23.2	10.7
C ₁₂ E ₅		406.6	26.0	11.7
C ₁₂ E ₇		494.7	40.6	13.2

ionization mass spectroscopy (GC-MS), with the samples dissolved in methanol. Citrate and sodium hydroxide were purchased from Merck KGaA. N-decane with a purity >99 % from Merck KGaA was used as oil.

An overview of the surfactants, their molecular weight (M_w), their cmc and their hydrophilic-lipophilic balance (HLB) values are displayed in Table 3.1. The cmc data of the pure ethoxylates were taken from [143]. The HLB values in Table 3.1 were calculated according to Griffin, assuming two C_8 chains for RL and a C_{18} chain for SL [144].

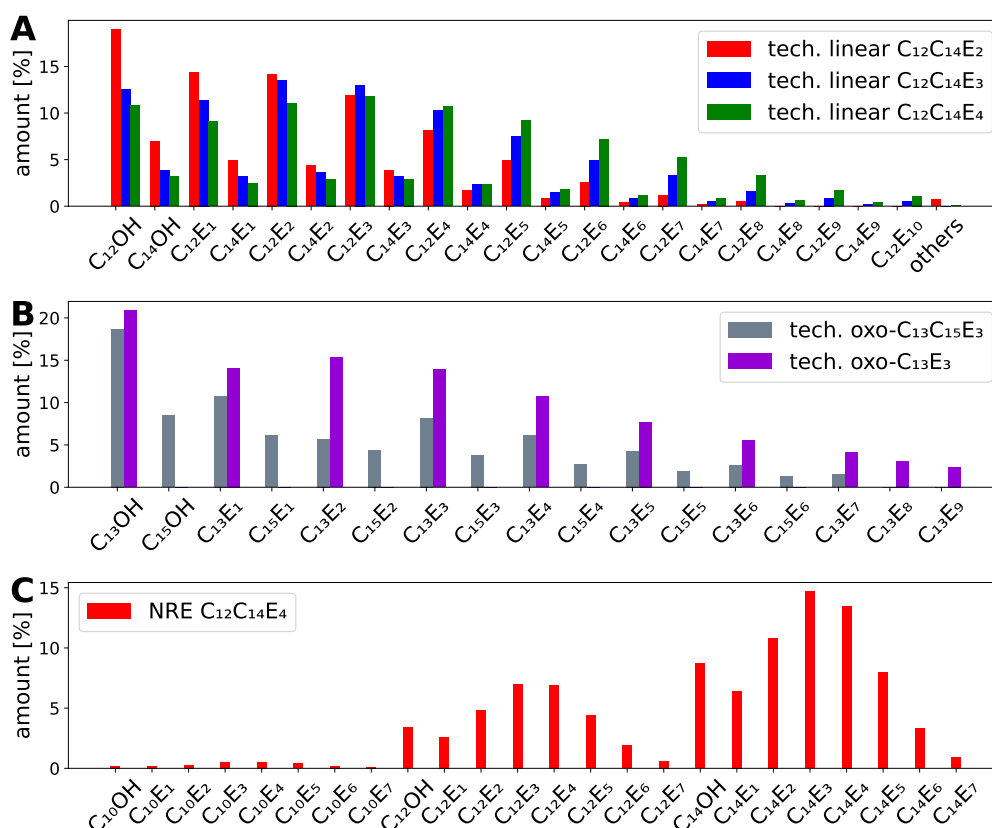


Figure 3.1: A) Composition of the linear technical ethoxylates, and B) the branched ethoxylates, and C) the narrow range ethoxylate (NRE) determined by GC-MS.

All experiments were conducted in 0.33 wt% sodium citrate at pH 8 which is largely above the pK_a of RL (5.5) and SL (4.6) [145, 146]. The pH of each composition was measured before each measurement and adjusted to pH 8 with sodium hydroxide if necessary. All percentages in this thesis are weight percentages because often technical substances are employed, which do not have an explicit molar mass. An exception is the ratio of anionic

to cationic surfactant because here the molar ratio strongly influences the properties of this system.

3.2 Phase Behavior

The apparatus utilized for the phase behavior experiments is illustrated in Figure A12 in the Appendix. For determining the phase diagram, the phase boundaries were identified by titration (Figure 3.2) [147]. The surfactant RL, the citrate buffer at pH 8 and the oil phase were weighted into flat bottom test tubes with a magnetic stirring bar ($\Delta m = 0.0001$ g). The test tubes were placed in a water bath at 30 °C to control the temperature, which was monitored with the high precision thermometer GMH3700 Pt100 ($\Delta T = 0.01$ K). Once the ingredients were completely mixed, the ethoxylate was added using a 1-10 μ l pipette. The sample was subsequently homogenized, after which it was allowed to rest for a period of 1-2 minutes. Then, observation of the sample was conducted through the utilization of crossed polarization filters. When a phase transition was observed, the quantity of added ethoxylate was weighted back. If no phase transition occurred, an additional quantity of ethoxylate was added.

Furthermore, the polarization microscope Zeiss Axio Imager M1 with the peltier system LTS-120 from Linkam Scientific Instruments Ltd ($\Delta T = 0.1$ K) and the conductivity meter Seven Compact S230 from Mettler Toledo (calibrated at 84 μ S/cm) were used to determine the type of μ E. The data was visualized using the python-ternary library [148, 149].

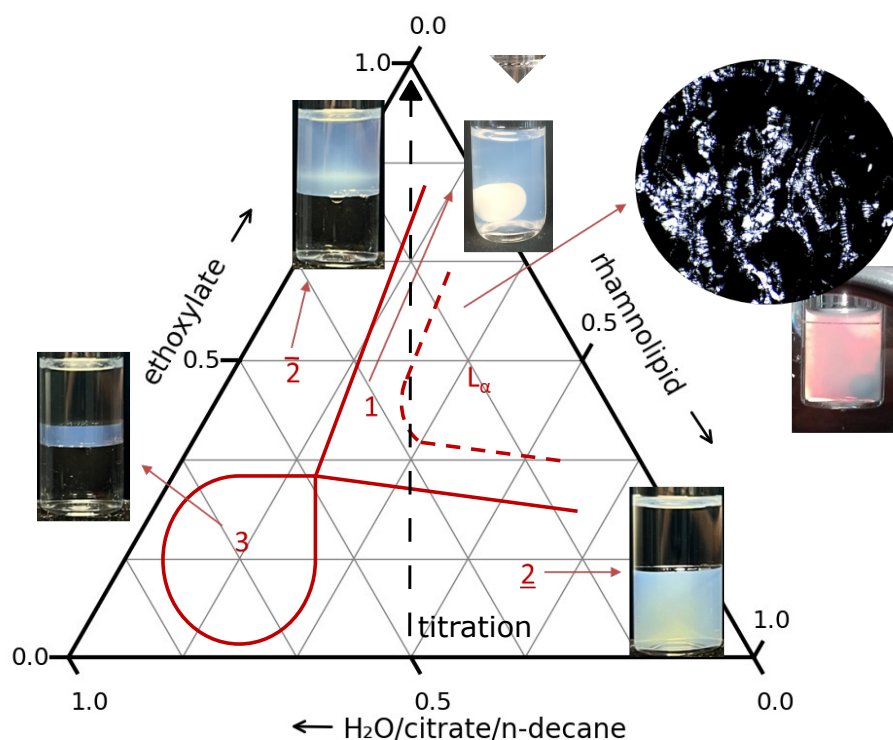


Figure 3.2: Schematically description of the methodology of the determination of the phase behavior by titration, with accompanying images illustrating the different phases.

3.3 Pulsed Field-gradient Spin Echo NMR Spectroscopy

Pulsed Field-Gradient Spin Echo (PGSE) NMR spectroscopy experiments have been performed on a Bruker AVIII 300 NMR spectrometer (300.13 MHz for ^1H) with a 5 mm BBFO probe equipped with a z-gradient coil providing a maximum gradient strength of 50.8 Gcm^{-1} . Samples were prepared with deuterated water (D_2O). Their pH was set at 8 with citrate. A stimulated echo sequence with longitudinal eddy current delay (5 ms), bipolar gradient pulses and water pre-saturation (ledbpgppr2s in Bruker's pulses library) was chosen. Indeed, despite the use of D_2O , the water related signal at 4.7 ppm was still strong for most of the samples. Smooth square-shaped gradient pulses were selected (SMSQ10.100, Integral factor = 0.90). At least 16 gradient increments, from 2% to 90% of the maximal gradient strength, were used for each measurement. Diffusion delays (Δ) of approximately 200 ms were chosen. For each sample, the duration of the gradient pulses ($\delta/2$) was optimized to obtain a residual intensity of 5% for the peak of interest at the higher gradient (90% of the maximum strength), relatively to the intensity

Table 3.2: Chemical shifts and corresponding H-atoms of the different substances analyzed [159–161].

chemical shift [ppm]	corresponding groups and substances
0.8	CH ₃ in RL, HELDAC, CTAB
0.9	-CH ₂ - in RL, C ₁₂ E ₄ , n-decane
1.3	-CH ₂ - in RL, C ₁₂ E ₄ , n-decane
3.1	N-CH ₃ in HELDAC, CTAB
3.6	0-CH ₂ - in C ₁₂ E ₄
4.7	H ₂ O in water
5.2	CH in RL, SL

measured at the lower gradient (2% of the maximum strength).

The data was analyzed with TopSpin 3.6.5. by fitting the attenuation profiles with the classical Stejskal and Tanner formula (Equation 2.30) when only one component contributed to a peak at a specific chemical shift. However, some the peaks are affected by more than one component (see Table 3.2). This is why biexponential fitting was employed using Equation 2.31 and the SciPy package in Python for the non-linear least square fit of the bi-exponential curves [150].

With regard to the error associated with PGSE-NMR experiments, it was assumed that signals which were not overlapping would have a relative error of 2%, as observed for instance in the case of water signals [151]. Such error increases if the signal is overlapped by two different species. In general, a factor of 2 to 3 is considered to be sufficient to distinguish between two diffusion coefficients reliably in the case of a good signal-to-noise ratio [113].

For the experiments with the catanionics, the concentration of all samples was 3 wt%, except for the 100% CTAB sample which was 1 wt% due to turbidity of the sample. Characteristic peaks, which do not overlap with others, were used to independently monitor the diffusive behavior of each compound in the binary mixtures. The peaks and corresponding chemical groups of the different surfactants are displayed in Table 3.2 and in Figure A2 in the Appendix [152–155].

For the μ Es, the chemical shifts of the components is also displayed in Table 3.2. Only the signal of water does not overlap with other peaks, which is why Equation 2.31 were employed to determine the diffusion coefficients of the surfactants and n-decane. Reduced diffusion coefficients were calculated by dividing the measured diffusion coefficient D by the diffusion coefficient of the substance in its pure form D_0 . The values of D_0 for water and n-decane were taken from literature [156, 157]. The one for C₁₂E₄ was measured at 3% solution in water, yielding results that align with the PGSE-NMR data of C₆E₄ [158].

3.4 Dynamic Light Scattering

Angle-dependent 2D DLS measurements were performed with the LS Spectrometer from LS Instruments with the laser Cobolt Flamenco 100 with 660 nm and 100 mW. Four measurements were recorded at 50, 60, 70, 80, 90, 100, 110, 120, and 130 ° for 20 s. The analyzed samples had a concentration of 20 mM, pH 8, 25 °C (30 °C with the apparatus not possible) and were prepared with Milli-q water. The usual count rate was about 50-60 kHz at full laser power. To avoid dust, each sample was filtered through the 450 nm-filter Chromafil Xtra H-PTFE-45/25 before each measurement. The autocorrelation functions of the intensity of scattered light $g^{(2)}(\tau)$ were fitted with the cumulant analysis following the method of Frisken to directly fit the baseline B (Equation 2.39) [116].

3.5 Small-Angle X-ray Scattering

SAXS measurements were performed at the European Synchrotron Radiation Facility (ESRF, Grenoble, France) for the catanionic systems or using the apparatus Xeuss (Xenocs) at Sorbonne University (Paris, France) for the μ Es.

For the measurement of the catanionic systems at ESRF, the experiments were performed at the BioSAXS beamline BM29. A flow-through 1 mm diameter quartz capillary with an automatic sample changer was used at 20 °C. The sample was irradiated 10 times at 12.5 keV for 1 s for the experiments in water (Figure 4.3), while 45 times for 2 s for the experiments with added oil (Figure 4.11). The detector Pilatus3 2M was situated at a distance of 2827 mm. The data was acquired in absolute scale by subtracting the scattering profile of the capillary including the aqueous buffer without surfactants [162]. The scattering curves were fitted with the model of core_shell_ellipsoid as $P(q)$ including the hayter_MSA (HSA) as $S(q)$ in SasView 5.0.6. [120, 163]. As fitting strategy, the temperature was fixed to 298 K, citrate concentration to 0.0426 M, dielectric constant to 80.82, the volume fraction to the total volume of the surfactants in solution, the SLD of the core to $7.8\text{-}7.9\cdot 10^{-6} \text{ \AA}^{-2}$ depending on the chain length of the surfactant, the SLD of water to $9.4\cdot 10^{-6} \text{ \AA}^{-2}$, the axial ratio of the shell to 1 and the polydispersity to 0.1. Hence, the core radius, the shell thickness, the axial ratio of the core, the SLD of the shell, the background and the charge were varied. To account for the uncertainty of the fit, a 10% error of the fit parameters were assumed.

For the measurement of the μ Es with the Xeuss, a GenX Cu HFVL X-ray source, a detector distance of 2300 mm and a measurement time of 250 s in high resolution mode was employed. The sample was measured in 1.5 mm quartz glass capillaries from Capillary Tube Supplies Ltd, UK, at 30 °C. The data was treated in XSCAT analysis software and fit with the Teubner-Strey Fit (Equation 2.49) in SasView 5.0.6, in which the volume fraction and SLDs were fixed and the domain size d and persistence length ξ varied.

The calculated SLDs for the used substances are summarized in Table 3.3, together with

the molecular volumes of the substances. To estimate the molecular volume of SL, twice the volume of glucose was used as the head group and the Tanford formula was used for the hydrophobic part [164]. For HELDAC, the molecular volumes of methanol and dodecyltrimethylammonium chloride were taken [131, 165]. The molecular volumes of the alkyl chain ($C_iH_{2i}CH_3$) were calculated by extrapolation at 25 °C of Reiss-Husson data on molten paraffins: $v^{298K}[\text{nm}^3] = 0.02699i + 0.02721$ [131, 166].

Table 3.3: The scattering length densities (SLDs) and molar volumes for all surfactants and its chains are shown for X-rays and neutron. For neutrons, the SLDs are displayed for the hydrogenated and deuterated molecules. The SLDs of hydrogenated RL, SL and C₁₂E₄ have labile hydrogen which is considered in the presented value.

substance	volume [Å ³]		SLD [10 ⁻⁶ /Å ²]				reference		
			X-rays		neutrons				
	chain	surfactant	chain	surfactant	hydrogenated chains	hydrogenated surfactant		deuterated chains	deuterated surfactant
H ₂ O		30		9.44		-0.56		6.40	[10]
RL	243	1052	7.54	9.52	-0.43	1.16			[10]
SL	513	866	7.97	11.06	-0.37	2.08			[164]
HELDAC	351	550	7.79	8.24					[131, 165]
CTAB	459	601	7.93	9.19	-0.37	-0.24	7.12	5.86	[167]
n-decane		324		7.16		-0.49		6.19	[168]
C ₁₂ E ₄	351	630	7.79	9.06	-0.39	0.08	6.12	6.28	[169]

3.6 Wide-Angle X-ray Scattering

Wide-angle x-ray scattering (WAXS) was performed at the SWING beamline at the Synchrotron SOLEIL, France (2023/446). The energy was set at 16 keV and the detector distance at 0.53 m. The data was treated with the Foxtrot 3.5.10. The samples were measured in 1 mm quartz glass capillaries from Capillary Tube Supplies Ltd, UK. The Winsor I phase was measured at 30 °C and the Winsor IV phases at 55 °C. The scattering profile of the empty capillary was subtracted from the measured sample profile.

3.7 Small-Angle Neutron Scattering

SANS data were acquired on D22 at the Institut Laue-Langevin, the European Neutron Source (ILL, Grenoble, France) [170]. A de Broglie wavelength of 0.60 nm (relative full width half-maximum 10%) was selected. The rear detector was centered on and perpendicular to the direct beam, at a distance of 17.6 m from the sample. The front detector was tilted at 20 ° and at 1.4 m from the sample to provide a continuous angular coverage of the detection. A semi-transparent attenuator (perforated cadmium) was used to measure simultaneously the transmission. The beam was collimated over 17.6 m, with a circular source aperture of 30 mm diameter and a sample aperture of 7 (horizontal) x 10 (vertical) mm². This setup allowed data to be obtained simultaneously over the q -range of $2.7 \cdot 10^{-2} - 6.4 \text{ nm}^{-1}$. Samples were contained in quartz cuvettes of 1 mm pathway (110-QS and 120-QS, Hellma GmbH & Co. KG, Müllheim, Germany), installed in a thermalized copper sample changer. The data were processed with the program Grasp V.10.24d [171], taking into account the detector background (measurement of sintered $^{10}\text{B}_4\text{C}$), empty container, sample thickness, transmission as measured within the direct beam, parallax, normalizing with monitor and correcting with a flat field, using experimental beam centers for both detectors. Absolute scale was obtained from the measurement of the empty beam flux ($1.05 \cdot 10^6$ neutrons per second), as measured on the rear detector with a chopper having a known attenuation coefficient. The data were binned according to q -resolution with 5 bins per standard deviation. This resolution was calculated from the direct beam profile.

All SLD of the substances are displayed in Table 3.3. The labile hydrogen of the OH-groups of the carbohydrate are readily exchangeable with deuterium [172]. Accordingly, RL was treated as deuterated sugar hydrogen ($\text{C}_{32}\text{H}_{58}\text{O}_{13}$ in H_2O as $\text{C}_{32}\text{H}_{53}\text{O}_{13}\text{D}_5$) in D_2O for an accurate SLD calculation.

For the catanionic samples, the sample preparation was done in deuterated water with hydrogenated sodium citrate and sodium hydroxide. The impact of these hydrogenated substances on the SLD of D_2O was calculated to be negligible. In order to match the contrasts between CTAB and water, deuterated CTAB was used and 0.074 v% H_2O was added to the D_2O . The data were fitted according to the procedure described in Section

3.5 with the SLDs for neutrons (Table 3.3). The background was estimated and pre-subtracted prior to each fit. By fitting the experimental curves with the different models described subsequently, the exact background was determined and then subtracted from the pre-subtracted data to remove the incoherent background and calculate the invariant.

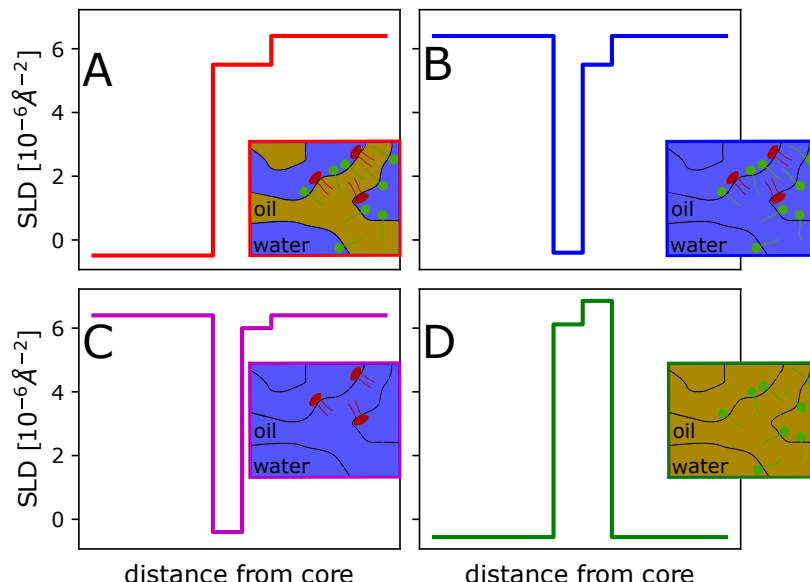


Figure 3.3: Representation of the contrasts analyzed in this study. A) bulk, B) film, C) RL and D) EO contrast in Winsor I. The inset pictures show schematically the microscopic image which the neutrons detect where the red surfactant is the RL and the green one is the $C_{12}E_4$. The exact values of the contrasts are stated in Table 3.3.

For the μ Es, the samples were prepared with partly deuterated substances according to their contrast in Figure 3.3. The Winsor I μ E contained 5 v% $C_{12}E_4$ and 6 v% RL. The Winsor IV μ E was measured at two different ratios, (1) 7 v% $C_{12}E_4$ and 2 v% RL and (2) 9 v% $C_{12}E_4$ and 2 v% RL. The used SLDs are displayed in Table 3.3. The temperature was controlled and changed for the Winsor IV samples until a isotropic phase could be observed. Given that the scattering of the bulk contrast was so high that multiple scattering occurred significantly, the scattering data for the bulk contrasts was rescaled using MuScatt by Henrich Frielinghaus [173]. The fitting was also performed using SasView 5.0.6. The Winsor I samples were fitted with the onion model for spheres as form factor and a HSA structure factor [120]. The volume fraction (0.37), the charge (60 e), the polydispersity (0.25), the SLDs of the core and solvent, the number (2) and decay rate (0) of the shell were fixed, whereas the radius, shell thicknesses and SLD of the shell were varied. The bulk contrasts of Winsor IV were fitted with the Teubner-Strey

model, as previously described in the SAXS experiments [122]. The fits of the film, RL and EO contrasts of Winsor IV were performed with an oblate model according to the model in Ref. [118] (Equations 2.48 and 2.52)). The inside-outside correlation length ξ_{io} , the domain size d , the persistence length ξ , the volume fraction ϕ_m and the SLD were held constant. Accordingly, the contrast length t_0 , the diameter of the membrane d_m , the gyration radius σ , and the coefficients A and B were varied. However, the contrast length t_0 and the diameter of the membrane d_m were fixed for C₁₂E₄ due to the availability of literature data [174]. Furthermore, the following sequence of sizes was required $\sigma > d_m > t_0$. The calculations of the invariant and specific interface were performed using SASFit (version 240115091150).

A further objective of the SANS studies of μ Es was to analyze the quantity of RL and C₁₂E₄ which is incorporated into the amphiphilic film. This can be achieved by comparing the scattering intensities of the RL and EO contrasts with that of the film contrast, respectively [175]. As the SANS curves of the different contrasts do not exhibit the same shape, the invariants of each curve were determined and displayed in Table A3 in the Appendix. From the ratio of the invariants, a factor f can be preserved. By relating this factor to the scattering length derived difference of the different contrasts $f = \frac{\Delta\text{SLD}_{\text{film}}}{\Delta\text{SLD}_{\text{RLorEO}}}$, the expected scattering length density difference for the contrast of the individual contrasts $\Delta\text{SLD}_{\text{RLorEO}}$ can be deduced. By knowing the scattering length densities of the different phases, the amount of the component RL or EO can be derived. An example of this calculation is provided in the Appendix. It is worth mentioning that the calculation was performed taking into account that approximately 2% of monomeric C₁₂E₄ solubilizes in n-decane, that the solubility of RL in water (cmc \approx 0.1%) was neglected and that up to 5% of the deuterated water was already hydrogenated [71]. Another approach was the determination of a factor f by shifting the contrasted matched scattering curve to the non-contrast matched one, as previously described in literature [175]. The factors and shifted curves can be observed in Figure A18 in the Appendix.

3.8 Molecular Dynamics Simulations

The simulations were commissioned to the research partner Scienomics SAS, Paris. All the Molecular Dynamics (MD) simulations were performed at the mesoscopic level employing the Martini force field [176]. The model uses a four-to-one mapping, i.e., on average four heavy atoms and associated hydrogens are represented by a single interaction center. The simulations were performed using the Large-scale Atomic/Molecular Massively Parallel Simulator (LAMMPS) within the Scienomics Materials and Process Simulation package suite (MAPS) [177, 178]. The model employs a four-to-one mapping, whereby, on average four heavy atoms and their associated hydrogens are represented by a single interaction center. The initial configurations were random, with all molecules randomly placed in a box in a way that large overlaps are avoided. The systems were

first energy minimized and then run in an NPT (constant pressure and temperature) ensemble simulation followed by an NVT (constant volume and temperature) ensemble. A short-range van der Waals cutoff at 1.5 nm and switching at 1.2 nm (force-switch) was used. For the Coulomb interactions, a cutoff at 1.5 nm and potential-shift-Verlet were used as Coulomb modifier. The relative dielectric constant of the medium was set to 15. The time step was 10 fs, the thermostat was damped every 500 fs and the barostat every 1000 fs. The NVT simulations were run for at least 1000 ns to ensure evolution to equilibrium configurations. Long runs were necessary due to the size of the system, the low surfactant concentration and the charged species that slow down the dynamics.

For the calculation of the IFT, the systems were energy minimized followed by an NPT dynamics (constant composition, pressure and temperature) for at least 100 ns until equilibrium density and morphologies were reached. Of particular importance was the convergence of the area per molecule in the interface. Then, the IFT was determined by performing MD calculations for 300-500 ns in a NPzzAT ensemble where in addition the interfacial area A was kept constant (equivalently keeping the L_x and L_y fixed). The IFT was calculated by using two different approaches over the diagonal element of the pressure tensor $\langle P_{xx}(z) \rangle$, $\langle P_{yy}(z) \rangle$, and $\langle P_{zz}(z) \rangle$. The first approach evaluates these elements as an ensemble average of the pressure tensor over the whole volume of the simulation cell, during the simulation and then performs a time average, whereas the second approach calculates them by using an ensemble average of the pressure tensor along discrete slabs in the z direction [179]. We have used rectangular simulation boxes where the L_z dimension was larger than the other two. By employing this geometry, one forces the appearance of slabs of liquid-liquid sandwiched side by side. The system spontaneously forms the interfaces spanning the minimal area, parallel to the xy plane. Due to the periodic boundary conditions, each bulk phase is bounded by two independent interfaces. The periodic boundary conditions in xy directions allow for conditions representative of essentially infinite interfaces.

The mesoscopic representations of the surfactants are shown in Figure 3.4. It should be noted that pure substances and water are used in the simulations, as opposed to the partial mixture of components and presence of citrate described in Section 3.1. For the catanionic systems in water, all systems in the simulations were composed of 100 cations and 100 anions in pure water so that the concentration of the surfactant was 15 g/l. The corresponding density was approximately 1 g/ml. For the RL & ethoxylate system, the systems composed of 100 molecules at the water/n-decane interface, resulting in a surfactant concentration of 15 g/l. The corresponding density was also approximately 1 g/ml.

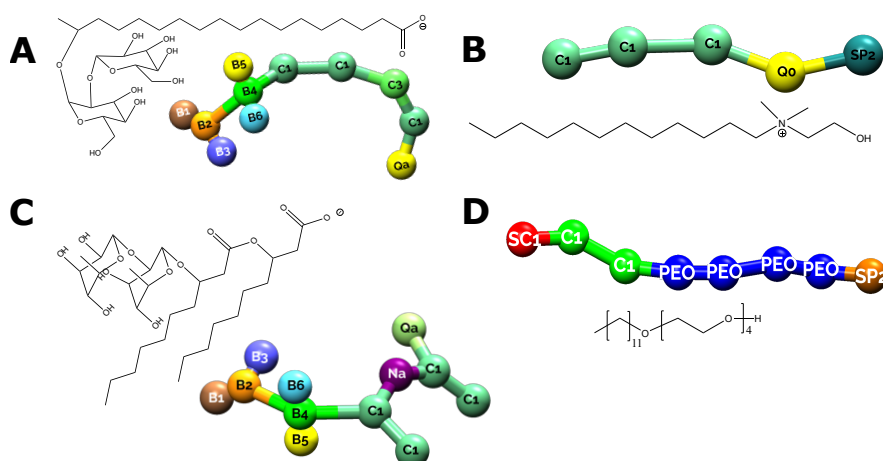


Figure 3.4: Representation of the structural formula of A) SL, B) HELDAC, C) RL and D) mono-disperse C₁₂E₄ and its beads with labels for the MD simulations.

3.9 Equilibrium Surface Tension

Du Noüy ring tensiometry was performed as a function of the concentration. DCAT25 apparatuses from DataPhysics Instruments GmbH were used at 25 °C with the software DCAT Version 4.1.96176. The concentration was varied by concentrating the aqueous solution with an increasing amount of surfactant. Each concentration step included an addition of a more concentrated surfactant solution. Afterwards it was stirred for 300 s with 20 r.p.m., the agitation was stopped and the measurement started after a delay of 10 s. The value for the ST was taken when the variation of the values was below ± 0.1 mN/m. Each concentration was measured in triplicate. To obtain the cmc values, ISO 4311:1979 was applied [180]. Essentially, the cmc is determined from the intersection of two regression curves. The error of the cmc is thus obtained from the two regression curves. In cases where a minimum existed, corresponding to more surface-active components within the surfactant system used, the cmc was taken at this minimum. In this case, the difference to the next concentration was chosen as the error of the cmc. However, due to these surface-active impurities, the surface excess concentration was not calculated [181].

3.10 Dynamic Surface Tension

DST measurements were made using a maximum bubble pressure apparatus from SITA Messtechnik GmbH, Germany. 1 g/l of surfactant solution was prepared and measured in triplicates at the room temperature (23 ± 1) °C (25 or 30 °C with the apparatus not

possible). The mean values were fitted by linear regression with the Equations 2.66 and 2.68.

3.11 Dynamic Interfacial Tension

Dynamic IFT measurements were performed using the spinning drop tensiometer SVT25 from DataPhysics Instruments GmbH, Germany, and a thermostat for holding the temperature at (25.0 ± 0.5) °C for the catanionic systems and (30.0 ± 0.5) °C for the μ Es. 1 g/l of surfactants was dissolved in the aqueous citrate buffer and then this solution was placed into the glass capillary. A drop of approximately 3 μ l of n-decane was inserted into the capillary and accelerated to $\omega = 6.000$ r.p.m. When this rotation speed was achieved, time was set to zero and the optical contour analysis of the drop was performed using the software SVTS 20 from DataPhysics Instruments GmbH. The IFT was then calculated with Equation 2.65 and averaged over three replicates.

Chapter 4

Results and Discussion

4.1 Structure of Anionic Biosurfactants with Cationic Surfactants

Starting with the analysis of catanionic model systems containing BSs, the self-assembled structures of these catanionic systems are studied.

4.1.1 Experiments

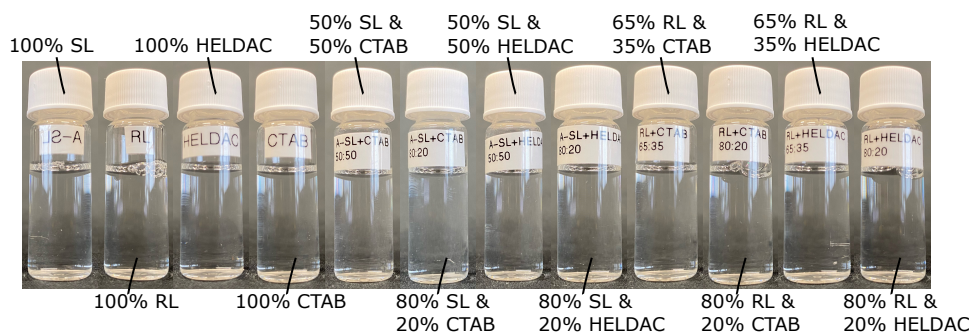


Figure 4.1: Photographs of aqueous dispersions containing 3 wt% surfactants. All percentages in the photograph are in molar shares of the respective surfactant in the surfactant mixture.

Catanionic mixtures usually precipitate at equimolar ratios [60, 61]. Interestingly, when using the BSs RL and SL, we did not observe any precipitation as shown in Figure 4.1. This finding leads to a more detailed study looking at the structure in micelles and at interfaces of catanionic systems in adsorption studies, their surface activity and their emulsification properties.

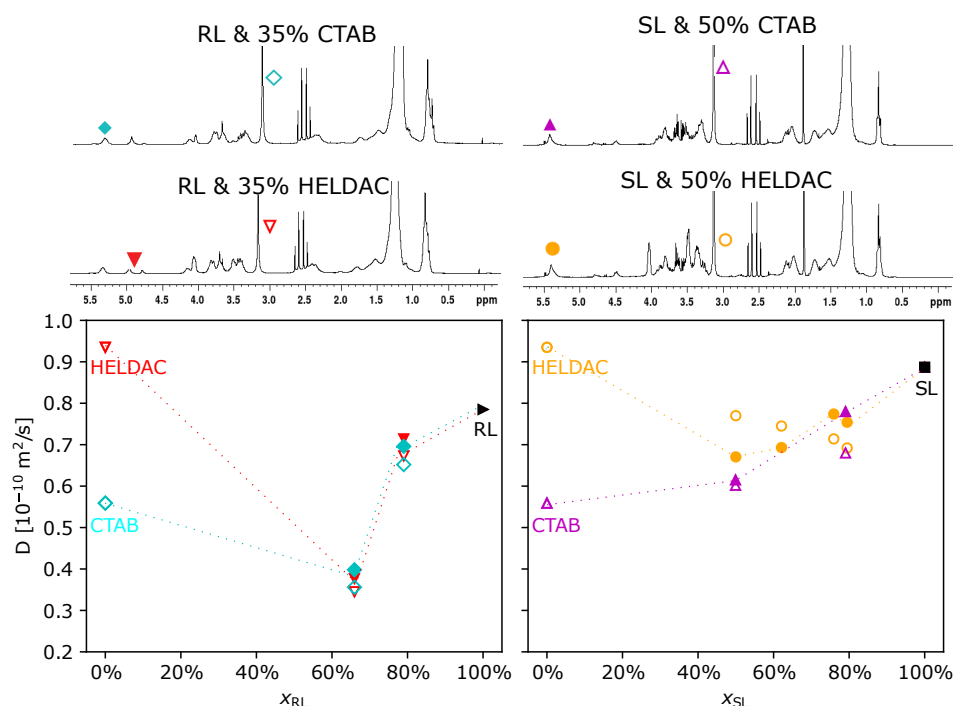


Figure 4.2: Pulsed field-gradient spin echo NMR spectroscopy of catanionics at 3 wt% of RL (left) and SL (right) mixtures with the catanionic surfactants. The diffusion coefficient of the BS is displayed in filled and the one of the cationic surfactant in open symbols as a function of the molar ratio of the BS in the surfactant mixture. The diffusion coefficients of the RL & CTAB system are displayed in cyan diamonds, the one of RL & HELDAC in red inverted triangles, the one of SL & CTAB in magenta pyramids and the one of SL & HELDAC in orange circles. Examples of the spectra are displayed above the diagrams. The errors of the diffusion coefficients are estimated to be 2%. The lines serve only as guide for the eye. The exact values of the diffusion coefficients are displayed in Table 4.6

The fact that all samples in Figure 4.1 are clear and do not scatter light indicates that no precipitation occurs, and no vesicles are formed, which is atypical for conventional catanionic surfactant systems. Instead, other aggregates must form whose self-assembled structures are elucidated subsequently.

PGSE-NMR measurements allow the access to the diffusion coefficients for the anionic BSs and the cationic surfactants in mixtures, due to the spectroscopic resolution of NMR. Consequently, it is possible to assess the presence of monomers, micelles or other aggregates. The application of the Stokes-Einstein equation to the obtained diffusion coefficients in Figure 4.2 yields hydrodynamic radii between 2 and 5 nm. This size is incompatible with the size of monomers, indicating that aggregates have been formed. Radii between 2 and 5 nm are typical sizes of micelles.

In addition to the assessment of the type of aggregate, PGSE-NMR allows the *individual*

diffusion coefficients for the different surfactant species to be determined. Hence, the objective of the PGSE-NMR measurements was to ascertain whether cationic and anionic surfactants form mixed micelles. The left plot in Figure 4.2 displays the diffusion coefficients of mixtures of RL and HELDAC (red) or CTAB (cyan). In the case of the RL & HELDAC mixture, the diffusion coefficients of both the RL and HELDAC decrease and converge to a similar value. The same trend was observed for the mixture of RL & CTAB. The 50% RL & 50% HELDAC/CTAB mixture reaches lower values than the individual components. However, the diffusion coefficient of RL is consistently slightly higher (<10%) than the one of HELDAC or CTAB.

The right plot in Figure 4.2 shows the diffusion coefficients of SL and HELDAC (yellow) or CTAB (magenta). The diffusion coefficients of SL and CTAB are similar in the 50% SL & 50% CTAB mixture. In the case of the other ratio and the SL & HELDAC system, the diffusion coefficients of SL and the cationic species vary. Nevertheless, the diffusion coefficients of the anionic and cationic surfactant species differ from those of the pure surfactants.

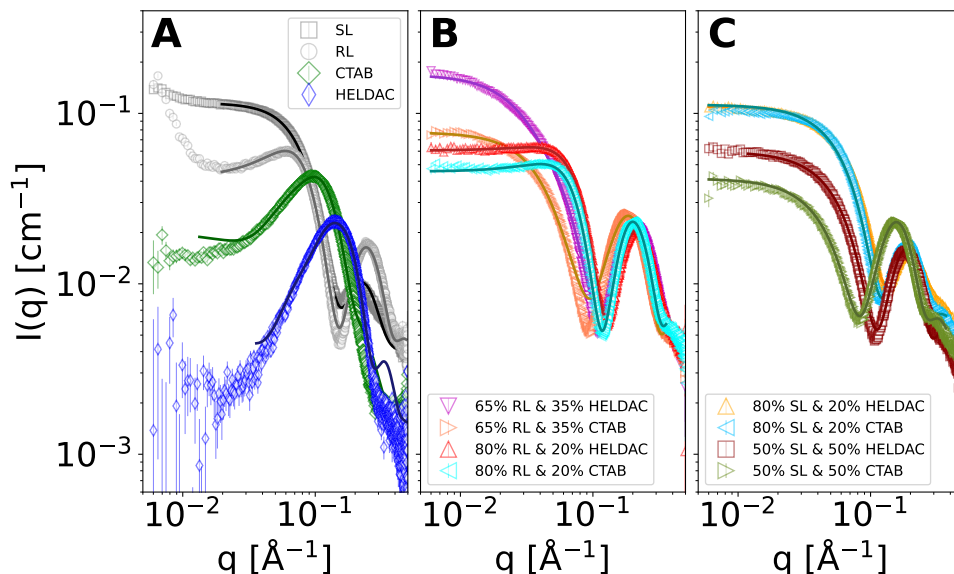


Figure 4.3: Measured SAXS profiles (symbols) including fits for core-shell ellipsoids as form factor and HSA as structure factor. A) Profiles for pure surfactants, B) profiles for cationics with RL and C) profiles for cationics with SL.

To ascertain the explicit size and shape of the aggregates, SAXS measurements were performed. Figure 4.3 shows the measured SAXS profiles for the pure surfactants in A, the RL mixtures in B and the SL mixtures in C. The solid lines correspond to fits to the data using the HSA + core-shell ellipsoid model. The resulting fit parameters are summarized in Table 4.1. The scattering data shows a typical pattern of micellar

structures with an electron-poor core and an electron-rich shell. This is consistent with the total surfactant concentration of 3 wt% in this measurement which is above the cmc (Figure 4.8).

The profile of the scattering curves of pure RL, SL and CTAB in Figure 4.3 A are similar to those in literature [182–184]. The radius of the SL micelle is notably small considering its long C₁₈ chain. Nevertheless, the observed values are in accordance with those reported in literature, where the typical size of a micelle of a bola-surfactant corresponds to the length of one molecule and where a "coffee-bean" model has been proposed for the SL micelle [182, 185]. RL has two C₈ chains. Despite the small chain length, RL contains two hydrophobic chains which is why its hydrophobic volume should be considerably high. Nevertheless, RL forms the smallest micelles, indicating the penetration of water to a certain extent. The fit parameters of the RL profile exhibit a slightly larger core (11.2 vs. 8.0 Å), a more spherical shape (core ratio: 1.7 vs. 2.5) and a higher charge (14.7 vs. 6.4 e) than reported in literature at a pH of 7.5 [184]. The dominance of the structure factor decreases from HELDAC > CTAB > RL > SL, presumably due to an decrease in charge (Table 4.1 A).

Figure 4.3 B illustrates the scattering curves of the catanionic micelles with RL. The structure factor is dominant for the micelles containing 80% RL, rather than the 65% RL ones, due to a greater excess of negative charge (see Figure A3 in the Appendix). Furthermore, an increase in the amount of cationic surfactant results in a corresponding increase in the core radius. This is attributable to the larger core size of cationic surfactant in comparison to anionic BSs as a consequence of the longer C-chains. All systems containing RL have a slope of -1 at low q , resulting in an ellipsoidal shape of the micelles. The axial ratio is higher for ratios closer to equimolarity.

It is worth noting that the samples with 65% RL & 35% HELDAC or CTAB may exhibit an axial ratio of the shell that differs from 1. The reason is that the minimum of the oscillation cannot be fitted with sufficient precision. As shown in Figure A4 in the Appendix, the ratio of the shell thickness varies within the micelle. This may indicate that the shell exhibits a different thickness at the end-caps and in the center of the rod-like micelle.

Figure 4.3 C displays the scattering curves of the catanionic complexes with SL. All data could be fitted without a structure factor, i.e. the catanionic aggregates with SL possess only weak interactions. The size of the core of the catanionics with SL is similar to the ones of RL. The zero slope at low q demonstrate spherical micelles, with the exception of the micelle of 50% SL and 50% CTAB which shows a slight rod-like character at low q (Table 4.1).

In conclusion, the SAXS data suggest the existence of rod-like micelles for the catanionics with RL and spherical micelles for the catanionics with SL. The sizes of the catanionic micelles are between the sizes of the micelles of the pure surfactants. Slight indications were found that the micelles with 65% RL & 35% HELDAC or CTAB have a different

shell thickness along the rod, which will be further analyzed in the following SANS measurements.

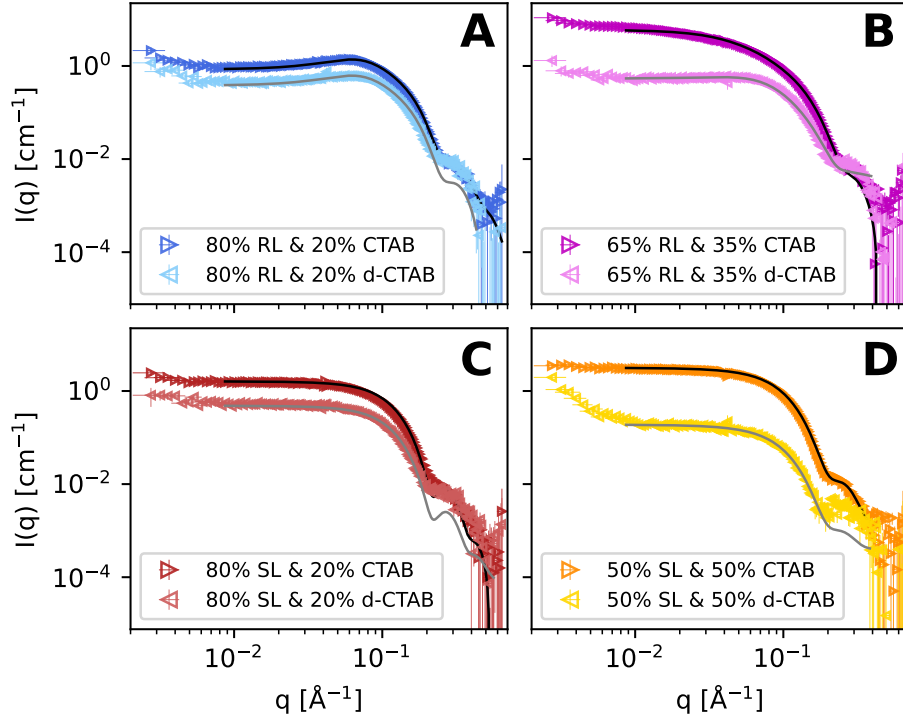


Figure 4.4: Measured SANS profiles (symbols) and fits (solid lines) using models of HSA + core-shell ellipsoids. The two different curves in the respective graphs show a combination with h-CTAB (dark color, \triangleright) and the contrast-matched sample with d-CTAB (light color, \triangleleft). A) Profiles of 80 molar-% RL & 20% h-/d-CTAB, B) of 65% RL & 35% h-/d-CTAB, C) of 80% SL & 20% h-/d-CTAB and D) of 50% SL & 50% h-/d-CTAB.

Contrast variation experiments were performed by SANS with the goal of understanding the distribution of BSs and cationic surfactants within the micellar aggregates. By using d-CTAB instead of h-CTAB, the contrast of CTAB and the solvent can be reduced. Since the SLDs of d-CTAB is $6.8\text{--}7\cdot 10^{-6} \text{ \AA}^{-2}$ [186–188] and the one of D_2O $6.4\cdot 10^{-6} \text{ \AA}^{-2}$, d-CTAB cannot be matched. Nevertheless, the intensity of d-CTAB in Figure A6 is approximately 1.5 orders of magnitude lower than the one of h-CTAB (Figure A6 in the Appendix). As a result, the contrast in the contrast-matched samples with d-CTAB is mostly due to the scattering of BSs within the micelle.

Figure 4.4 depicts the scattering curves of the contrast-matched (in light color, \triangleleft) and non-contrast-matched (in dark color, \triangleright) samples. The profiles of the samples with h-CTAB and d-CTAB are similar in Figure 4.4 A, C and D. The samples with d-CTAB have a lower intensity I_0 compared to the ones with h-CTAB. Samples containing a higher

Table 4.1: Fitting parameters of the scattering data of the SAXS in A) and SANS experiments in B). The data was fitted with the model HSA + core-shell-ellipsoids. The core radius is the equatorial radius of the hydrophobic core of the micelles, the axial ratio of the core is a measure for the anisotropy of the micelles core $\left(\frac{r_{\text{polar}}}{r_{\text{equatorial}}}\right)$, the shell thickness is the thickness of the hydrophilic headgroups including hydration, the total radius is the mean radius of the whole aggregate, the SLD shell is the SLD of the hydrophilic headgroups including hydration and the charge is the charge on the micelles in electrons. The error of the scattering data is estimated to be approximately 10%.

A) SAXS							
system	core radius [Å]	axial ratio of core	shell thickness [Å]	total radius [Å]	SLD shell [10 ⁻⁶ /Å ²]	charge [e]	comment
100% RL	11.2	1.7	6.1	19.6	11.8	14.7	polydispersity: 0.2
100% SL	7.8	2.4	12.9	23.8	10.6	4.8	
100% HELDAC	17.1	3.7	5.5	32.7	11.5	25.0	
100% CTAB	20.4	3.2	11.0	42.2	10.6	20	
65% RL & 35% HELDAC	13.6	6.4	3.7	30.0	14.0	4.3	
65% RL & 35% CTAB	15.1	4.2	4.2	29.4	13.4	10.0	
80% RL & 20% HELDAC	12.7	2.0	6.6	22.7	11.6	10.7	
80% RL & 20% CTAB	13.5	1.8	7.3	23.8	11.2	13.0	
50% SL & 50% HELDAC	14.6	1.0	11.8	26.4	10.3	0.0	
50% SL & 50% CTAB	16.2	1.6	9.2	28.2	10.6	0.0	
80% SL & 20% HELDAC	12.1	1.0	12.1	24.2	10.5	0.0	
80% SL & 20% CTAB	13.2	1.0	13.8	27.0	10.4	0.0	
B) SANS							
system	core radius [Å]	axial ratio of core	shell thickness [Å]	total radius [Å]	SLD shell [10 ⁻⁶ /Å ²]	charge [e]	comment
100% RL	11.3	1.7	6.0	19.6	5.0	14.7	volume fraction: 0.017 volume fraction=0.00045
100% SL	9.7	2.4	9.0	22.4	4.9	4.8	
100% CTAB	20.1	2.1	4.2	30.2	1.3	5.0	
100% d-CTAB	20.1	2.1	4.2	30.2	1.3	5.0	
50% RL & 50% CTAB	15.5	5.2	6.3	34.6	5.0	10.0	scale=0.2783
50% RL & 50% d-CTAB	15.5	2.1	6.3	26.4	5.0	10.0	
80% RL & 20% CTAB	16.0	1.5	4.5	22.9	6.3	15.0	
80% RL & 20% d-CTAB	16.0	1.5	4.5	22.9	6.3	15.0	
50% SL & 50% CTAB	19.0	1.6	5.3	27.6	5.0	1.0	scale=0.45
50% SL & 50% d-CTAB	19.0	1.6	5.3	27.6	5.0	1.0	
80% SL & 20% CTAB	20.0	1.0	7.0	27.0	6.0	1.0	
80% SL & 20% d-CTAB	20.0	1.0	7.0	27.0	6.0	1.0	

percentage of CTAB exhibit a stronger decrease in the intensity of the d-CTAB sample compared to the samples with 20% CTAB. The reduced intensity can be attributed to a diminished number of scattering events, which is a consequence of the CTAB being partially matched with the solvent. Furthermore, the structure factor exerts a similar influence on both the contrast- and non-contrast-matched samples, which suggests that the pronounced structure factor is attributable to the BSs. In the case of 50% SL & 50% CTAB in Figure 4.4 D, an increase in intensity is visible at low q which is also evident in the scattering of pure SL in Figure A7 in the Appendix. However, in the case of 65% RL and 35% CTAB in Figure 4.4 B, the shapes of the scattering profile with h-CTAB and d-CTAB are different. While the sample with h-CTAB can be interpreted as a typical scattering profile for elongated micelles, the scattering curve with d-CTAB resembles the scattering curve of pure RL (Figure A7 in the Appendix). Hence, this may indicate a peculiar arrangement of RL and CTAB in the micelle which will be discussed later.

Table 4.2: Comparison of the fraction of the BSs RL or SL in the micelles X_{BS} derived from SANS measurements (Figure 4.4) and surface tension measurements (Figure 4.8), discussed below).

System	X_{BS} from ST (Figure 4.8)	X_{BS} from SANS
65% RL & 35% HELDAC	0.63±0.07	
65% RL & 35% CTAB	0.49±0.08	0.73±0.02
80% RL & 20% HELDAC	0.68±0.14	
80% RL & 20% CTAB	0.53±0.10	0.82±0.02
50% SL & 50% HELDAC	0.66±0.10	
50% SL & 50% CTAB	0.48±0.07	0.43±0.02
80% SL & 20% HELDAC	0.68±0.07	
80% SL & 20% CTAB	0.58±0.12	0.79±0.02

Another goal of the SANS experiments was to access the molar percentage of BS in the micelle, where the experimental molar percentage can be compared to the theoretical one. Thus, to estimate the amount of CTAB or BS present within the micelle, the total scattering of the non-contrast-matched and contrast-matched sample were compared. An explanation and example of the calculation can be found in the the Appendix [175]. The resulting compositions of the micelles, X_{BS} , are displayed in Table 4.2. In the 80% RL & 20% CTAB system, 82±2% RL is in the micelle which is nearly identical to the molar percentage of the solution. The micelle of the 65% RL & 35% CTAB contains 72±2% RL. Therefore, the micelle contains a greater proportion of RL than the theoretical value of 65%. With regard to the catanionic micelle comprising 80% SL & 20% CTAB, it is constituted of 79±2% SL which is once more in agreement with the theoretical value of 80%. The 50% SL & 50% CTAB micelle incorporates 43±2% SL. The discussion of the

error will be conducted at a later point.

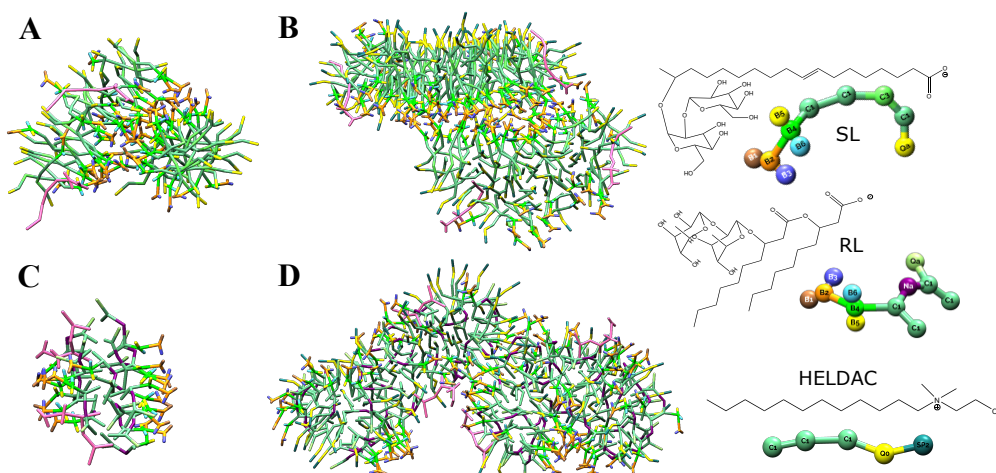


Figure 4.5: Shape of micelles and conformation of individual surfactants from the MD simulations. The dominant conformations in all cases are illustrated by molecules marked in pink. A) SL, B) SL & HELDAC, C) RL and D) RL & HELDAC system.

To obtain more insights into the internal structure and composition of aggregates, MD simulations were performed. The aim was to unravel what occurs on a molecular level when the anionic BSs and cationic surfactants are mixed. The simulations were conducted for the BSs RL and SL, as well as their 50% mixture with HELDAC, since HELDAC is more industrial relevant than CTAB. Figure 4.5 shows that micelles are formed for all aggregates. SL, SL & HELDAC and RL form slightly elongated micelles, whereas the RL & HELDAC mixture forms rod-like micelles. The dimensions of the micelle are provided in Table 4.1. The conformation of the SL in the SL and SL & HELDAC micelles is stretched, with the acidic group and sugar groups of the SL situated on opposite sides of the micelle. This composition is consistent with the findings reported in the literature. Manet et al. found a difference on the head-group composition depending on the location in the micelles, so that a "coffee-bean"-model has been proposed for SL [182]. The acidic and sugar group of the RL in the RL and RL & HELDAC micelles have a bent conformation. Further observations can be made regarding the distribution of the individual surfactants within the micelles. The SL micelle in Figure 4.5 A shows that the acidic groups are pointing outwards towards the water solution. The sugar groups are situated close to each other in a stacked manner. In fact, a bilayer of sugar groups seems to attach two micelles with each other which do not separate during the whole simulation. In combination of SL with HELDAC in Figure 4.5 B, the two surfactant types SL and HELDAC appear to be inhomogeneously distributed. The sugar groups of SL and the hydroxyethyl ammonium ends of HELDAC are located at the end-caps

of the micelle facing the water solution. Moreover, the sugar domains of two elongated micelles aggregate forming a bilayer structure. The RL micelle is illustrated in Figure 4.5 C. The sugar groups are also distributed in a non-uniform manner, so that domains of the sugar group and the acidic group become evident on the outer layer of the micelle. The RL & HELDAC micelle in Figure 4.5 D illustrates a less pronounced formation of sugar domains. Notwithstanding, the sugar groups are rather situated in the shell of the middle of the elongated micelle, while clusters of HELDAC molecules can be observed at the end-caps. Similar to SL & HELDAC, the aggregate appears to be an assembly of two distinct elongated micelles. Once formed, these dimer structures remain intact throughout the simulations.

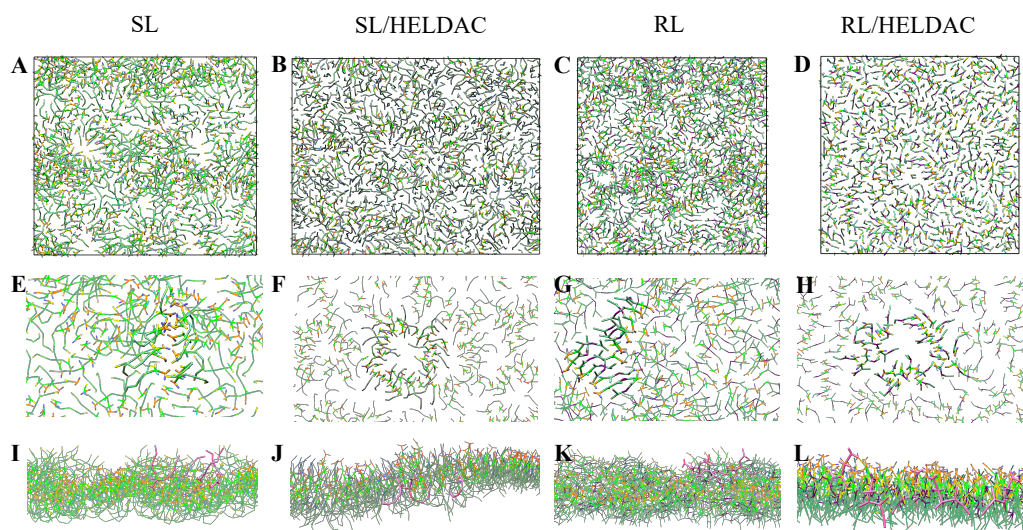


Figure 4.6: Snapshots of the MD simulations of the different surfactant systems at the n-decane/water interface. The first row (A, B, C, D) displays the top view of the amphiphilic layer. The second row (E, F, G, H) shows just the anionic BS without the cationic surfactants in a zoom top view while some surfactants are highlighted. The last row (I, J, K, L) depicts an in-layer side view where the n-decane is located below and water above the layer and some molecules are highlighted.

Since the analysis of the internal structure of the micelles is difficult, the self-assembly at the oil/water interface was modeled using MD simulations. The goal was to validate the nanoscopic phase separations and to create pair-correlation functions.

Figure 4.6 illustrates the molecules at the interface of the systems with 100% SL (first column). In Figure 4.6 A, the on-top view of the interface demonstrates an inhomogeneous distribution of the molecules. Upon closer examination of the magnified image in Figure 4.6 E, the sugar beads appear to be arranged in a stacked manner, which presumably leads to the formation of nanodomains (Figure 4.6 A). Figure 4.6 I shows a side view

of the surfactant film which demonstrates the bend conformation of SL in contact with the n-decane phase, and their linear conformations in contact with the water phase. The oil/water interface of 50% SL & 50% HELDAC is displayed in the second column of Figure 4.6. The molecules in Figure 4.6 B appear to be arranged in a denser manner. This is in accordance with the findings of Zhou et al. who discovered that as the catanionic mixture becomes more equimolar, the interface exhibits a denser packing and a reduction in interface formation energy [189]. However, the sugar groups are still arranged in a stacked configuration, as demonstrated in Figure 4.6 F and the SL molecules in the 50% SL & 50% HELDAC mixture also exhibit a bend conformation. The third column of Figure 4.6 depicts the interface comprising 100% RL. The distribution of RL molecules in Figure 4.6 C appears to be less homogeneous than the SL alone but more homogeneous than the SL & HELDAC system. Furthermore, the sugar groups of the RL are arranged in a stacked manner (Figure 4.6 G). The interface of 50% RL & 50% HELDAC is displayed in the fourth column. The interface of the 50% RL & 50% HELDAC system appears to be the most homogeneous of the analyzed systems (Figure 4.6 D). The formation of domains by the sugar groups is still present (Figure 4.6 H) but less pronounced. The RL molecules are observed to adopt a bend conformation (Figure 4.6 K and L).

The density profile analysis of the mixtures in the interface are presented in Figure 4.7. Figure 4.7 A illustrates the number of molecules of the mixture 50% RL & 50% HELDAC along of the z-axis through the interface (Figure 4.6 L). The RL and HELDAC surfactants are heterogeneously distributed, with a difference between the two peaks of approximately 8 Å. This indicates that, on average, RL is situated at disparate positions along the z-axis of the interface in relation to HELDAC. Similarly, Figure 4.7 D shows that SL and HELDAC are more homogeneously situated within the z-direction of the interface, with a maximum peak difference of approximately 4 Å. In addition, the RL and SL molecules at the interface are positioned closer to the water phase, while the HELDAC molecules are located closer to the n-decane phase. It is worth mentioning that the calculated IFTs from this simulation are presented and discussed in Section 4.2.

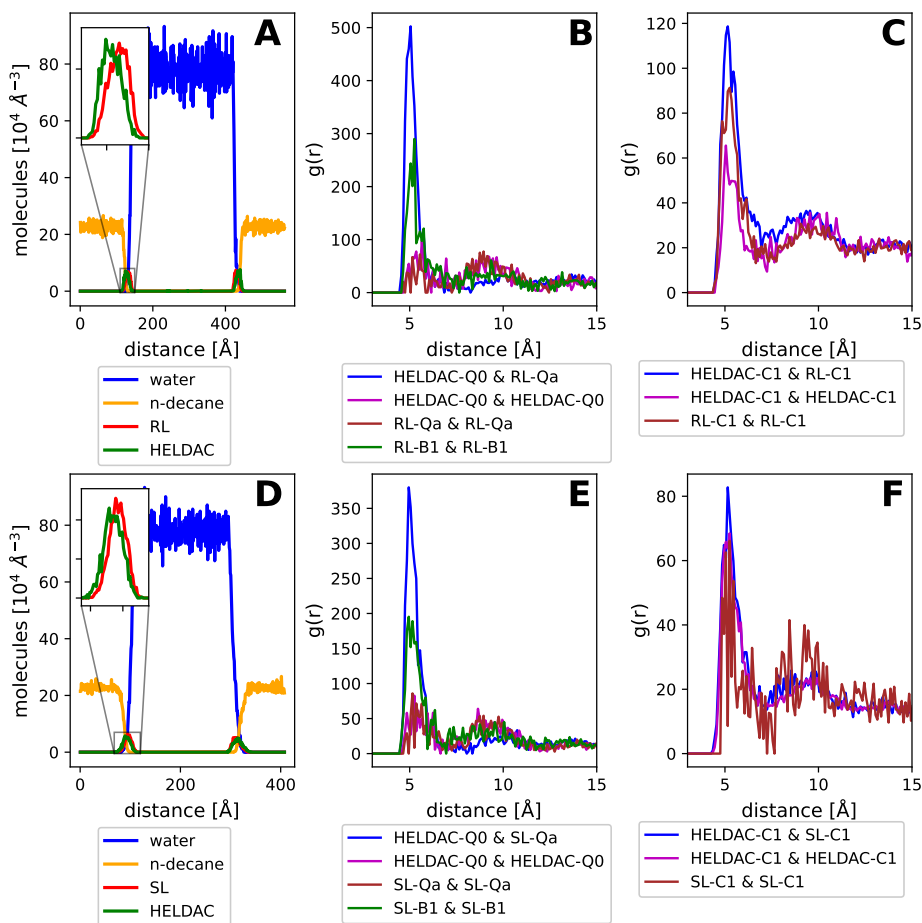


Figure 4.7: Density profiles (A, D) and pair correlation functions of the hydrophilic (B, E) and hydrophobic parts (C, F) of the surfactant molecules (see Figure 4.5 for the labeling).

To gain insights into the interaction of the individual surfactants, the pair correlation functions of the interface in Figure 4.6 are displayed in Figure 4.7. Figure 4.7 B shows the pair correlation functions of the hydrophilic interactions between the RL & HELDAC molecules. The beads of the cationic quaternary ammonium group of HELDAC (bead Q0, illustrated in Figure 4.5) do not interact strongly with each other, like the anionic carboxylic groups of RL (bead Qa) with each other. However, there are very strong interactions between the sugar groups of RL (bead B1) and between the anionic carboxylic bead of RL (bead Qa) and the cationic ammonium bead of HELDAC (bead Q0) with a peak maximum at ca 5 Å. The latter is expected, given that anionic and cationic charges exert an influence on one another. Similar results were observed in the case of the mixture of dodecyltrimethylammonium and dodecylsulfate [190]. The hydrophobic interactions of the RL & HELDAC mixture are displayed in Figure 4.7 C. The alkyl chains of all RL

and HELDAC chain interact strongly with each other, showing two maxima at ca. 5 and ca. 9 Å. The pair correlation functions of the hydrophilic and hydrophobic beads of the SL & HELDAC mixture in Figure 4.7 E and F are strongly similar to those of the mixture RL & HELDAC.

In the following, the results of the structure will be discussed in terms of the miscibility of cationic and anionic surfactants on a macroscopic and nanoscopic scale, their interaction, their shape and size. The discussion of the composition of the micelles can be found in the Appendix.

4.1.2 Miscibility of Cationic and Anionic Surfactants

The formation of mixed aggregates is anticipated when anionic and cationic surfactants are combined, e.g. sodium octyl sulfate and CTAB [191, 192]. Are mixtures of anionic BSs and cationic surfactants also forming mixed aggregates on a macroscopic and nanoscopic scale?

PGSE-NMR measurements showed that the diffusion coefficients of the BSs and cationic surfactants do not exhibit the same value, namely they deviate approximately 10% (Table 4.6 and Figure 4.2). Taking the 2-3% error of the PGSE-NMR measurements into account [151], the differences of the diffusion coefficients of BS and cationic surfactant might be significant. One potential explanation for this deviation in the RL & CTAB system is that RL has a higher cmc than CTAB (Table 4.4). Assuming rapid micellar kinetics and given that the decay of the fitted PGSE-NMR data is attributed to a single contribution, the greater quantity of RL monomers may result in a slightly elevated mean diffusion coefficient for the RL species. In the case of RL & HELDAC, it is challenging to determine a reliable cmc due to the presence of impurities, as discussed later. The determined cmc for HELDAC is higher than the one of RL, rendering the aforementioned explanation invalid due to the higher diffusion coefficient of RL in PGSE-NMR. Furthermore, with regard to the SL & HELDAC system, the diffusion coefficient of SL is observed to be higher than the diffusion coefficient of HELDAC at high SL ratios, but to be lower at higher HELDAC ratios. An alternative explanation assumes a limited nanoscopic miscibility of the BSs and cationic surfactants. As a consequence of this miscibility gap, it is possible that different micelles may have different compositions. It can therefore be postulated that a distribution of compositions is likely associated with a distribution of sizes. The average diffusion coefficient will appear to be higher if a micelle contains a greater proportion of BS and is of a smaller overall size. Due to the rapid exchange occurring through the free monomers, the observed average diffusion coefficients are different for aggregates enriched in BSs or cationic surfactants.

This hypothesis of limited miscibility of RL and SL and cationic surfactants is corroborated by MD simulations, presented in the Figures 4.5 and 4.6. The RL/SL and HELDAC molecules appear to be distributed in an inhomogeneous manner within the micelle or

interface, forming domain-like structures of BS or cationic surfactant molecules. In particular, the sugar groups are aggregated, which results in the anionic carboxylic groups or the cationic ammonium groups of the HELDAC being grouped together. This is surprising, given that ionic charges of the same kind repulse each other. As discussed later, this phenomenon is likely attributable to the strong carbohydrate interactions. However, the domains are more dominant when the micelles and interfaces of pure micelles are considered in comparison to the catanionic mixtures. Despite that a number of simulation studies has been conducted with BSs, only those carried out by Xu et al. have described similar domains. A comparison of the di-RL at varying pH values with dissipative particle dynamics revealed that the micellar surface pattern is exclusive to high pH levels with deprotonated di-RL. Interestingly, they were able to tune the pattern formation by reducing the packing parameter to a certain extent (large number of rhamnose groups and long alkyl chain), increasing the solution polarity and reducing the compatibility between the rhamnose and alkyl chain moieties [193]. This suggests that the asymmetric gemini- and bola-shape structures of the RL and SL are likely the underlying cause of the domain structures.

In order to corroborate the results of the simulations at the experimental level, contrast variation experiments have been conducted via SANS measurements. As previously stated, the contrast-matched curves in Figure 4.4 still contain a contribution from CTAB, but its intensity is 1.5 orders of magnitude below the original intensity. Hence, the impact of the individual surfactants on the mixture can be observed. A comparison of the contrast-matched curves with the non-contrast-matched ones reveals that both curves have the same shape. This does not suggest limited miscibility of the surfactants. An exception is the mixture of 65% RL & 35% CTAB. The contrast-matched curve indicates a more spherical shape than the non-contrast-matched curve. This suggests that the HELDAC is rather situated at the end-caps of the micelle, while RL is rather located in the middle. A comparable pattern is observed in the case of the mixture of 50% RL & 50% HELDAC in the MD simulations, displayed in Figure 4.5 D. Moreover, this pattern can explain the improved fit of the SAXS data when the shell thickness differs between the middle and end-caps of the micelle, as demonstrated in Figure A4 in the Appendix. Similar patterns have been reported by Zemb et al. for nanodiscs, formed by the salt-free catanionic system myristic acid and CTAC in excess of cationic charge, with CTAC being accumulated at the end-caps [194]. In the science of biological membranes, which are constituted of amphiphilic lipids, the formation of domains has been discussed for years. The domains, or rafts, are divided into a liquid ordered and liquid disordered phase [195, 196]. This phase separation is believed to occur due to different intermolecular interactions, for example hydrogen bonds [197, 198]. As discussed later, the BSs exert strong hydrogen bondings between the sugar groups and di-RL was reported to preferentially inset into ganglioside-enriched membranes [199]. Hence, our findings demonstrate that the different intermolecular interactions could lead to differences in the bending rigidity

between the BSs and cationic surfactants which results in nanoscopic phase separation.

4.1.3 Interactions

Intra- and intermolecular non-covalent interactions, e.g. hydrogen bonds or electrostatic interactions, are one cause for the self-assembly. To understand the reason for the particular self-assembly of catanionics with BSs, the intermolecular interactions of the anionic BSs with cationic surfactants is discussed.

One result of intermolecular interactions among others is precipitation in catanionic surfactant systems at specific ratios driven by electrostatic interaction [60, 61]. However, no precipitation was observed for the catanionics with the BSs RL and SL leading to clear solutions (Figure 4.1). A possible explanation is the asymmetric, complex and hydrophilic structure of RL and SL and the short hydrophobic chain (C_{10} for RL and bend chain conformation for SL; Table 4.1 and Figure 4.5). Due to the asymmetry and molecular mismatch, a crystallization of the chains may be prevented, and, especially, the hydrophilicity of the BSs ensures a high solubility in water [60, 61]. Interestingly, it has been found in literature that a narrow precipitation region corresponds to a weak surfactant interaction [200, 201].

The interaction strength between two molecules can be estimated from the MD simulations (Figure 4.7). As expected, the anionic carboxylic groups of RL and SL demonstrate a strong correlation with the cationic ammonium group of the HELDAC. However, the carboxylic groups of RL and SL display a comparatively weaker correlation with one another than the sugar groups. The correlation between the sugar beads is notably strong, subceeding the correlation between the anionic and cationic charges by a factor of 0.5. This correlation of the sugar groups is evident in the Figures 4.5 and 4.6 in which agglomerations of sugar beads are observed. Furthermore, strong carbohydrate interactions have been identified as the driving force for the insertion of di-RL into ganglioside-enriched membranes [199]. This shows the importance of the presence of hydrogen bonds.

Illustrated in the pair correlation functions of MD simulations (Figure 4.7), carbohydrate interactions are the most prominent interactions, with the exception of those between opposing charges. Furthermore, the structure factor in SANS can give hints about the interactions between the aggregates. The pronounced structural factor observed in the catanionic mixtures can be attributed to the presence of BSs in the contrast-matching experiments, which shows that the interaction mostly comes from the BS molecules (Figure 4.4). The structure factor was also assessed in the analysis of mono-RL and CTAB by Esposito et al., who observed a less pronounced structure factor than that displayed in Figure 4.4 [29]. This can be attributed to the single rhamnose group observed in mono-RL as opposed to the two rhamnose groups allowing for the formation of a greater number of carbohydrate interactions than it would be possible with a single rhamnose group. In summary, indications have been found that strong carbohydrate interactions are likely a

reason for the nanoscopic phase separation.

4.1.4 Shape of the Aggregates

Catanionic surfactant systems are known to typically form vesicles at specific ratios [202, 203]. The reason is an increase in the packing parameter, which results in the spontaneous transformation of curved micelles into vesicles with less curvature [80]. However, vesicles were not observed in the case of the catanionics with RL and SL. This is different to conventional surfactants since the mixture of anionic BSs and cationic surfactants results in a neutralization of charge (Figure A3 in the Appendix). As a consequence of this neutralization, the surfactants lose hydration water, as evidenced by the alteration of the SLD, and subsequently, the packing parameter increases. Nevertheless, micelles are formed in the case of catanionics with BSs which means that the packing parameter remains below 0.5. One reason could be the large sugar headgroups of the BSs, which could keep the packing parameter low. The smaller sugar headgroup of mono-RL has previously been found to form nanovesicles when combined with CTAC [29].

The observed mixed micelles in SAXS and SANS adopt a spherical or rod-like shape depending on the surfactant system (Figure 4.3 and 4.4). All catanionics with RL exhibit a rod-like shape, which becomes increasingly pronounced with increasing equimolar ratios. The reason is that the hydrophilic headgroups become increasingly hydrophobic with more equimolar ratios, which consequently increases the packing parameter. Furthermore, the increased hydrophobicity is evident in the increasing SLDs observed at more equimolar ratios, as glucose has a SLD of $14.2 \cdot 10^{-6} \text{ \AA}^{-2}$ while water has a SLD of $9.44 \cdot 10^{-6} \text{ \AA}^{-2}$ [204]. In MD simulations, the mixtures of RL/SL & HELDAC were observed to form two micelles, which are attached to each other (Figure 4.5). This dimer may also account for the failure of the SAXS fits with a constant shell ratio to align with the observed data (see Figures 4.3 and A4 in the Appendix). Nevertheless, the pair correlation function of the SAXS data depicted in Figure A5 in the Appendix does not evidence the formation of these dimers.

The micelles of the catanionics with SL have a rather spherical character. As illustrated in Figure 4.5, the SL molecules are stretched analogous to the SL molecules in the pure SL micelle. Therefore, the shape of the mixed SL & HELDAC or CTAB systems is predominantly influenced by the SL micelle, rather than by the HELDAC or CTAB micelle. Furthermore, the SLDs of the shell of the SL aggregates are smaller than the ones of RL (Table 4.1). This indicates that a greater quantity of water penetrates into the SL aggregates than into the RL aggregates [164, 205]. However, the core of the SL aggregates is larger and more spherical and the shell is smaller than that for the SL micelle alone.

In addition to the investigation of the aggregate's morphology, the shape of the oil/water interface was examined in MD simulations (Figures 4.6 and 4.7). The BSs are found to be situated in proximity to the aqueous phase, while HELDAC was positioned in the vicinity

of the oil phase. These findings indicate that the BSs possess a more hydrophilic character in comparison to HELDAC, thereby suggesting the existence of stronger interactions between RL/SL and water, as well as HELDAC and oil. This configuration at the oil/water interface is analogous to the combined linker concept, in which a hydrophobic and hydrophilic linker are combined, resulting in a structure that resembles an extended surfactant [206].

Table 4.3: Comparison of the sizes from SAXS in Figure 4.3, SANS in Figure 4.4 and MD in Figure 4.5. R_1 and R_2 are the radii of the aggregates perpendicular to each other. The error of the scattering data is estimated to be approximately 10%.

system	SAXS [\AA]		SANS [\AA]		MD [\AA]	
	R_1	R_2	R_1	R_2	R_1	R_2
100% RL	17.3	25.1	17.3	25.2	23.5	
100% SL	20.7	31.4	18.7	32.3	16.5	33.0
100% HELDAC	22.6	68.8			22.0	
100% CTAB	31.4	76.3	24.3	46.5		
50% RL & 50% HELDAC					25.0	66.0
65% RL & 35% HELDAC	17.3	90.2				
65% RL & 35% CTAB	19.3	68.1	21.8	38.9		
80% RL & 20% HELDAC	19.3	31.7				
80% RL & 20% CTAB	20.8	31.3	20.5	28.5		
50% SL & 50% HELDAC	26.4				17.0	36.5
50% SL & 50% CTAB	25.3	34.9	24.3	35.7		
80% SL & 20% HELDAC	24.2					
80% SL & 20% CTAB	27.0		27.0			

4.1.5 Size of the Aggregates

In literature, the micellar dimensions of SL, RL and CTAB have already been studied. The radii, R_1 and R_2 (perpendicular to R_1), are approximately 20 and 44 \AA for SL, 20 and 37 \AA for RL and 27 and 47 \AA for CTAB [184, 207, 208]. On the basis of the diffusion coefficients derived from DLS and PGSE-NMR, a radius in the range of 19.5 to 64.7 \AA can be estimated (Figures A10 and 4.2). Indeed, the scattering data by SAXS and SANS in the Figures 4.3 and 4.4 and MD simulations in Figure 4.5 show similar dimensions. Table 4.3 presents a comparison of the micellar sizes obtained by SAXS, SANS and MD, the sizes of which are in close agreement. It should be noted that the 100% CTAB sample exhibits a smaller and more spherical morphology in SANS than in SAXS. This discrepancy is likely attributed to the lower concentration employed for the CTAB sample in SANS and due to different contrasts in SAXS and SANS. Moreover, the structural

parameters vary around 10 Å comparing different articles in literature [208, 209]. The size of the SL micelle is small compared to its long alkyl chain. This is due to the fact that the SL molecules are stretched throughout the micelle as discussed before. This stretched configuration results in a diameter of the micelle which equals one SL molecule, as expected for bola-shaped amphiphiles, and not two surfactant molecules which is expected for non-bola surfactants [185].

In general, the sizes of the micelles containing mixtures of BS & cationic surfactant are in-between the ones of the micelles of the individual surfactants (Table 4.3). An exception is the sample of 50% RL & 50% HELDAC which is slightly larger due to strong anisotropy. This increase in size is thus typical for catanionic systems [210, 211], since the neutralization of charge likely causes a change in the packing parameter and hence in the curvature of the amphiphilic film which leads to rod-like micelles. However, other authors have also found that micellar sizes and aggregation numbers of surfactant mixtures with BSs are in-between the ones of the pure surfactants, such as mixtures of RL/SL with LAS, mixtures of RL with multiple quaternary ammonium salts and mixtures of mono-RL with CTAC [11, 13, 29, 30]. Conversely, the aggregates of the mixture RL and SLES have smaller sizes than the micelles of the pure surfactants [22].

The scattering data show that the increase of intensity at low q is a feature of the RL and SL aggregates (Figure 4.3 A and A7 in the Appendix). This feature is also present in mixtures, originating from RL and SL (Figure 4.4). This indicates that RL and SL form large structures besides the micelles. The same increase in intensity has been observed by other researchers, which provides evidence for these superstructures, as exemplified by platelets [13, 14, 212].

4.1.6 Composition of Micelles

Based on the cmc and SANS measurements, the amount of BS and cationic surfactant incorporated into the micelles was calculated compared to the amount of surfactants in solution (Appendix and Table 4.2). It was found that the amount of surfactant in solution differs from that in the micelles, especially for more equimolar mixtures. The results indicate that CTAB is more likely to integrate into micelles with BSs compared to HELDAC, where the same is true for RL compared to SL. This suggests that CTAB and RL have a stronger affinity for micelle formation than HELDAC and SL. The latter is in agreement with literature where RL was found to be more surface active than SL [16]. The results of the cmc and SANS measurements in the composition of the micelles display strong discrepancies (Table 4.2), which have already been mentioned. They have been attributed to the high error of the cmc measurements which will be discussed later [213–215]. Hence, the micellar composition from the SANS measurements may be more reliable. However, further studies comparing the ST and SANS results are needed to draw comprehensive conclusions.

4.2 Adsorption of Anionic Biosurfactants with Cationic Surfactants

Following the determination of the structure of catanionic surfactant systems with BSs in bulk, an analysis of their adsorption at interfaces have been conducted. To study the surface activity of the systems, equilibrium IFT measurements have been performed. Furthermore, dynamic IFT measurements have been employed to determine the time dependency of the adsorption. The emulsification studies have demonstrated the capacity of the systems to take up oil, which can be elucidated by the investigation of the structural characteristics and adsorption properties of the examined catanionic systems.

4.2.1 Experiments

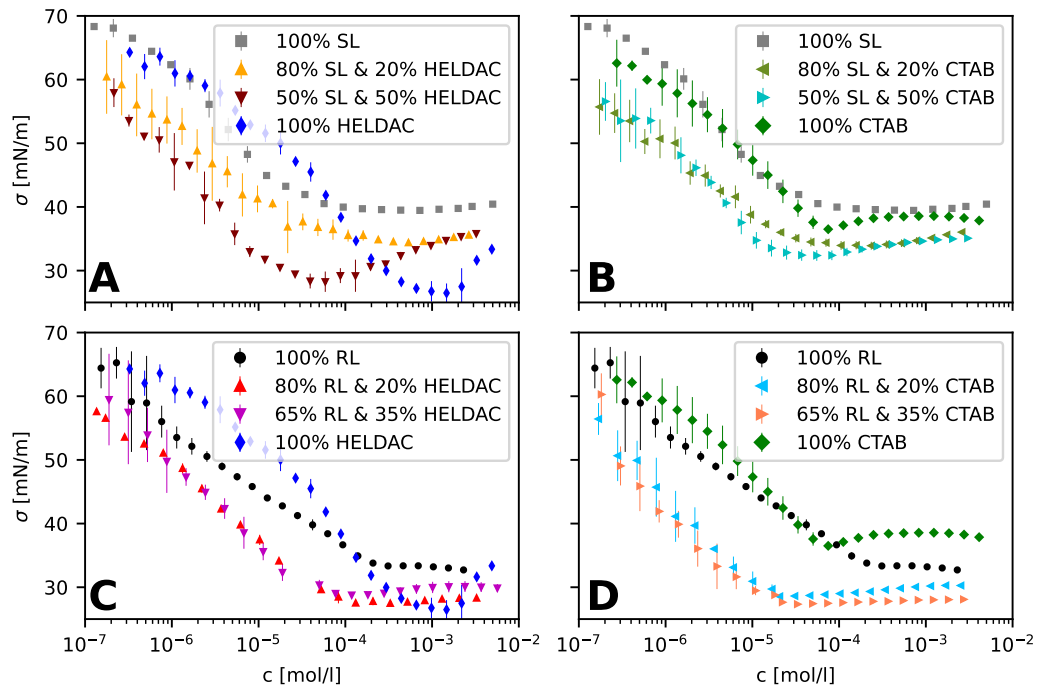


Figure 4.8: Equilibrium surface tension σ as a function of the surfactant concentration c . A) SL & HELDAC, B) SL & CTAB, C) RL & HELDAC and D) RL & CTAB. The error bars are the average of three repetitions.

In order to gain insights into the surface-activity of catanionic surfactant systems compared to the pure surfactants, equilibrium ST measurements were performed. Figure 4.8 shows the equilibrium ST as a function of the concentration. As expected, the ST, σ ,

Table 4.4: Fitting parameters from equilibrium surface tension measurements with Equations 2.18, 2.15, 2.20 and 2.21. cmc_{id} is the cmc of a ideal mixture, β is the net interaction parameter, G_{ex} is the excess Gibbs energy of mixed micelles and σ is the surface tension.

System	cmc_{id} [10 ⁻² mmol/l]	cmc [10 ⁻² mmol/l]	β	G_{ex} [kJ/mol]	σ [mN/m]
100% RL		16±8.2			33.8±1.5
100% SL		10.5±1.1			39.3±1.9
100% HELDAC		196.6±16.3			26.5±3.8
100% CTAB		7.5±6.2			36.5±0.6
65% RL & 35% HELDAC	23.9	3.7±1.2	-10.3±10.6	-6.0±24.0	28.6±1.5
65% RL & 35% CTAB	11.5	1.3±1.0	-8.6±8.2	-5.3±13.3	27.3±3.2
80% RL & 20% HELDAC	19.9	5.7±2.9	-8.6±19.5	-4.7±50.2	27.7±2.0
80% RL & 20% CTAB	13.2	1.7±1.2	-8.4±9.7	-5.2±17.4	28.3±3.3
50% SL & 50% HELDAC	20.0	5.7±5.1	-10.0±13.9	-4.1±31.8	31.9±8.0
50% SL & 50% CTAB	8.7	1.7±1.1	-6.5±5.0	-4.0±8.0	28.3±3.5
80% SL & 20% HELDAC	13.0	3.2±2.5	-7.4±13.7	-5.4±34.4	34.1±2.1
80% SL & 20% CTAB	9.7	3.5±2.4	-4.4±8.0	-2.7±15.7	36.1±2.0

declines until it reaches the cmc (Table 4.4). Above the cmc, the ST remains constant. The found cmcs of RL (0.160±0.082 mM) and SL (0.105±0.011 mM) in the water-citrate-background are similar to those reported in literature (0.23 and 0.04-0.1 mM, respectively) [216, 217]. Nevertheless, it is worth mentioning that a whole range of cmcs have been reported for the BSs (0.004-0.360 mM for RL and 0.009-0.970 mM for SL) [14]. The cmc of CTAB (0.075±0.062 mM) is approximately one tenth of the value observed in the literature for measurements in pure water (0.884 mM) [218]. This may be attributed to the presence of fatty alcohol as impurity and of citrate in water in our experiments. Another evidence for the presence of fatty alcohol is the presence of a small minimum in the CTAB curve at the cmc. The observation of a minimum is typical in presence of hydrophobic impurities when plotting the ST as a function of the concentration ([180]). The reason is the initial adsorption of the impurities within the surfactant samples at the surface due to higher surface activity of the impurity, here the fatty alcohol, compared to the surfactant. At the cmc, the impurities are solubilized within the micelles (composition of HELDAC is described in Chapter 3.1). Consequently, the ST increases with increasing surfactant concentrations [181]. Furthermore, this minimum is particularly evident in the ST curve of HELDAC. Despite the presence of impurities, the cmc of HELDAC is similar compared to the ones obtained through absorbance, fluorescence and specific conductivity (2.7-9.8 mM) [219]. The mixtures of anionic and cationic surfactants exhibit lower cmcs compared to the pure surfactants. Table 4.4 demonstrates that the decrease in cmc is approximately one order of magnitude. This is in accordance with literature in which the decrease of cmc was observed to be of one or two orders of magnitude for

catanionic surfactant systems [220, 221]. Furthermore, the ST at high concentration (equilibrium ST) are lower compared to individual surfactants.

To quantify the reduction in cmcs, the net pairwise interaction strength β of the binary mixtures was determined. The attractive force between the anionic and cationic surfactants can be estimated by calculating β with the Equations 2.15 and 2.18. In addition, the excess Gibbs free energy of mixed micelles can be calculated using Equation 2.20 and the fraction of BSs in the micelle, X_{BS} . Illustrated in Table 4.4, β of the catanionics varies between -4 and -10. These findings are consistent with existing literature, particularly the work of Mei et al., who determined that an equimolar mixture of RL (unknown composition) and a gemini sulfonate surfactant exhibited $\beta = -8.5$ [30]. Moreover, Esposito et al. identified $\beta = -6.7$ in case of mono-RL and cetyl trimethylammonium chloride at pH 7.1 and at a molar ratio of 0.6 [29].

It is worth mentioning that the error displayed in Table 4.4 is very high. Its origin was found to lay in the high error of the cmc determination with two regression curves, which becomes very high due to error propagation. This high error has already been reported in literature, especially for non-equimolar mixtures [213, 215]. Due to this high error and other considerations by Letellier et al., caution must be paid regarding the appropriate applicability of the regular solution theory to our measurement setup [222].

Considering X_{BS} in Table 4.2, the values indicate that the fraction of BSs in micelles is comparable to the fraction which was initially introduced to the system. For instance, when 65% RL & 35% HELDAC were introduced in the mixture, $63 \pm 7\%$ of RL are incorporated in micelles. However, regarding the catanionic systems with CTAB, less molecules of BSs constitute the micelles. For instance, when the surfactant system contains 65% RL & 35% CTAB, $49 \pm 8\%$ of RL constitute the micelles. No significant differences can be found between the catanionics of RL and the ones of SL. The errors in Table 4.4 are considerably high due to the high error of the cmc and its error propagation. This high error is in accordance with various discussions in literature [213, 215, 222].

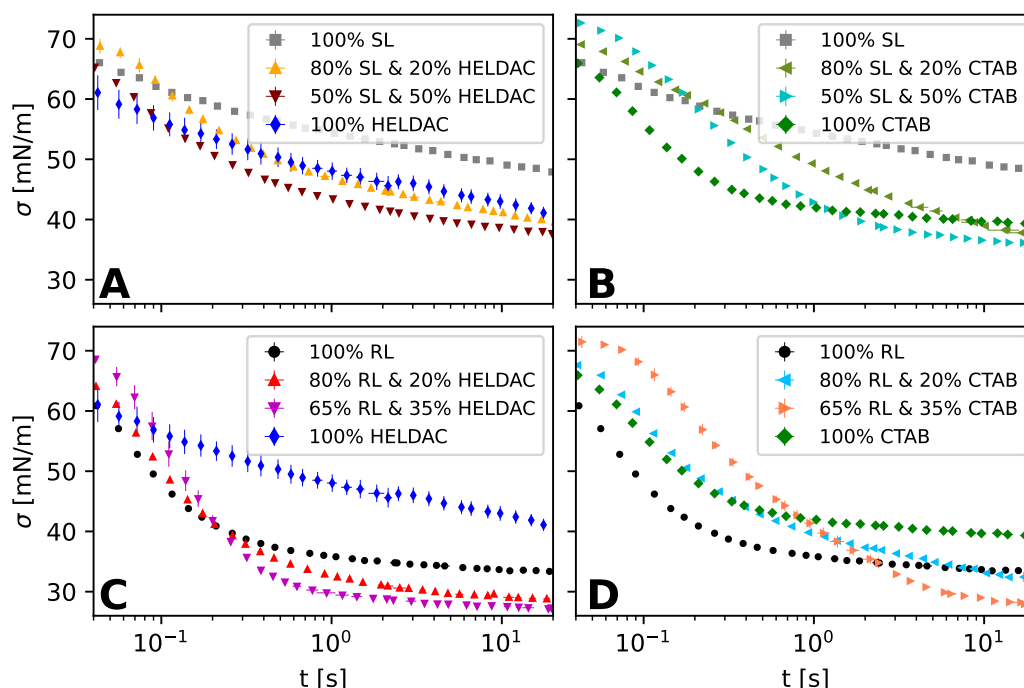


Figure 4.9: Dynamic surface tension σ measurements of different catanionic systems at 1 g/l as a function of time t by maximum bubble pressure tensiometry. A) shows the dynamic surface tensions of the catanionics SL & HELDAC, B) SL & CTAB, C) RL & HELDAC and D) RL & CTAB. The error bar describes the standard deviation of three measurements.

The adsorption of surfactants at interfaces is a dynamic process. Therefore, the ST as a function of time is shown in Figure 4.9. As expected, the ST declines over time for all single and mixed systems. The reason is the diffusion of surfactants to the subsurface, where they adsorb from the subsurface to the surface. The adsorption of RL and CTAB is completed within seconds, whereas the adsorption of SL and HELDAC takes over 10 s. The long adsorption time of SL is in accordance to previous results on SL [223] and the curve of CTAB is similar to previous measurements by Phan et al. [224]. One notable distinction between pure and mixed systems is that the ST is higher for the mixtures at short time scales. For example, the SL & CTAB mixtures have higher STs than SL and CTAB alone below 0.2 s. Conversely at longer time scales, the ST of the mixtures is lower than the one of the pure surfactants. For instance, the ST of 50% SL & 50% CTAB is lower than the one of CTAB for times exceeding 1 s. The crossover times, at which the mixtures have a lower ST than their pure analogues, depend on the surfactant system and are shorter for catanionics with HELDAC. Catanionics with RL achieve lower STs at meso-equilibrium than their SL analogues.

Furthermore, DST measurements can indicate the mode of adsorption, specifically whether it is diffusion or kinetic-diffusion controlled [225]. This procedure is based on the Ward-Tordai equation for very short times scales [136, 141]. Consequently, the ST is plotted against the square root of time and the data is fitted with Equation 2.68, with the ST of water fixed at 72 mN/m. Figure A11 in the Appendix illustrates the agreement between the data points and the fits. The fit is acceptable for pure substances compared to the surfactant mixtures, among which systems with equimolar ratios exhibit the poorest fit. Due to the poor fits, the diffusion coefficients were not derived from Equation 2.68. This quality of the fits indicate that the adsorption is rather diffusion controlled for the pure surfactants, but rather kinetic-diffusion controlled for the catanionics if the Ward-Tordai model can be correctly applied.

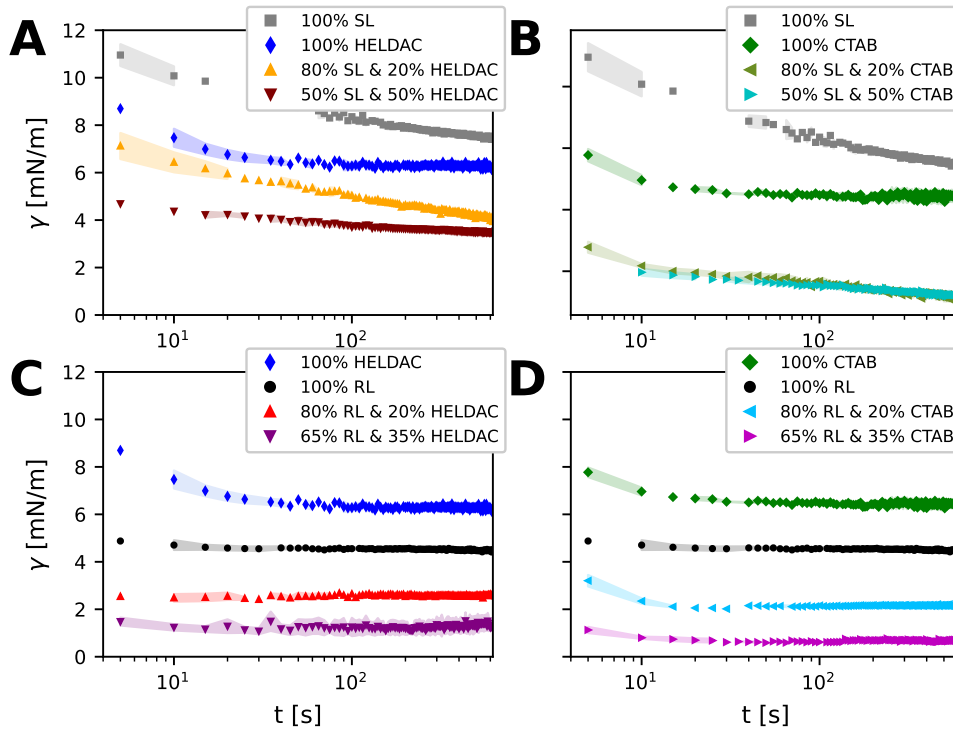


Figure 4.10: Interfacial tension (IFT, γ) of catanionic systems at n-decane/water interface as a function of time t . A) is the SL & HELDAC, B) SL & CTAB, C) RL & HELDAC and D) RL & CTAB combination.

A considerable number of applications in the household and cosmetics industries involve oil/water interfaces. However, it is not possible to directly transfer the results obtained from the air/water interface to those obtained from the oil/water interface. The underlying reasons for this discrepancy can be attributed to partitioning and surfactant/oil interactions

[226]. Hence, it is important to study adsorption at the oil/water interface. N-decane was chosen as oil because of its hydrophobic nature, stability, chemical accuracy and the absence of impurities.

Consequently, spinning drop measurements of the pure surfactants and their mixtures were performed at the n-decane/water interface. Figure 4.10 illustrates the IFTs of the different surfactant systems as a function of time. The following observations can be made: 1) The catanionic mixtures have a lower equilibrium (long time) IFT than their pure analogues. 2) The catanionic mixtures of RL exhibit lower IFTs than those with SL, a phenomenon that is also observed in the case of CTAB compared to HELDAC. 3) The closer the catanionic surfactant system is to equimolarity, the lower is the IFT. 4) Based on the aforementioned observations, the lowest IFT was achieved with a surfactant composition of 65% RL & 35% CTAB. Hence, this composition exhibited the highest adsorption efficacy at the n-decane/water interface.

Furthermore, the time required to achieve a constant IFT was investigated. This time is proportional to the adsorption time of the surfactants and therefore provides insight into the efficiency of the surfactant system. Figure 4.10 can thus also be analyzed in terms of these adsorption kinetics. 5) The pure surfactants SL, CTAB and HELDAC show a reduction of ST with time. Consequently, the rate of adsorption at the oil/water interface is slower for these surfactants than for RL. 6) By mixing anionic and cationic surfactants, the equilibrium IFT value is reached faster which is why the mixtures adsorb faster than the individual surfactants (at the observed time scales). 7) The closer the mixture to equimolarity, the faster does the IFT reach its equilibrium value. Table 4.5 presents the equilibrium IFT values, also in comparison to the simulated IFT values from Figure 4.6. These results will be discussed in detail in the discussion section.

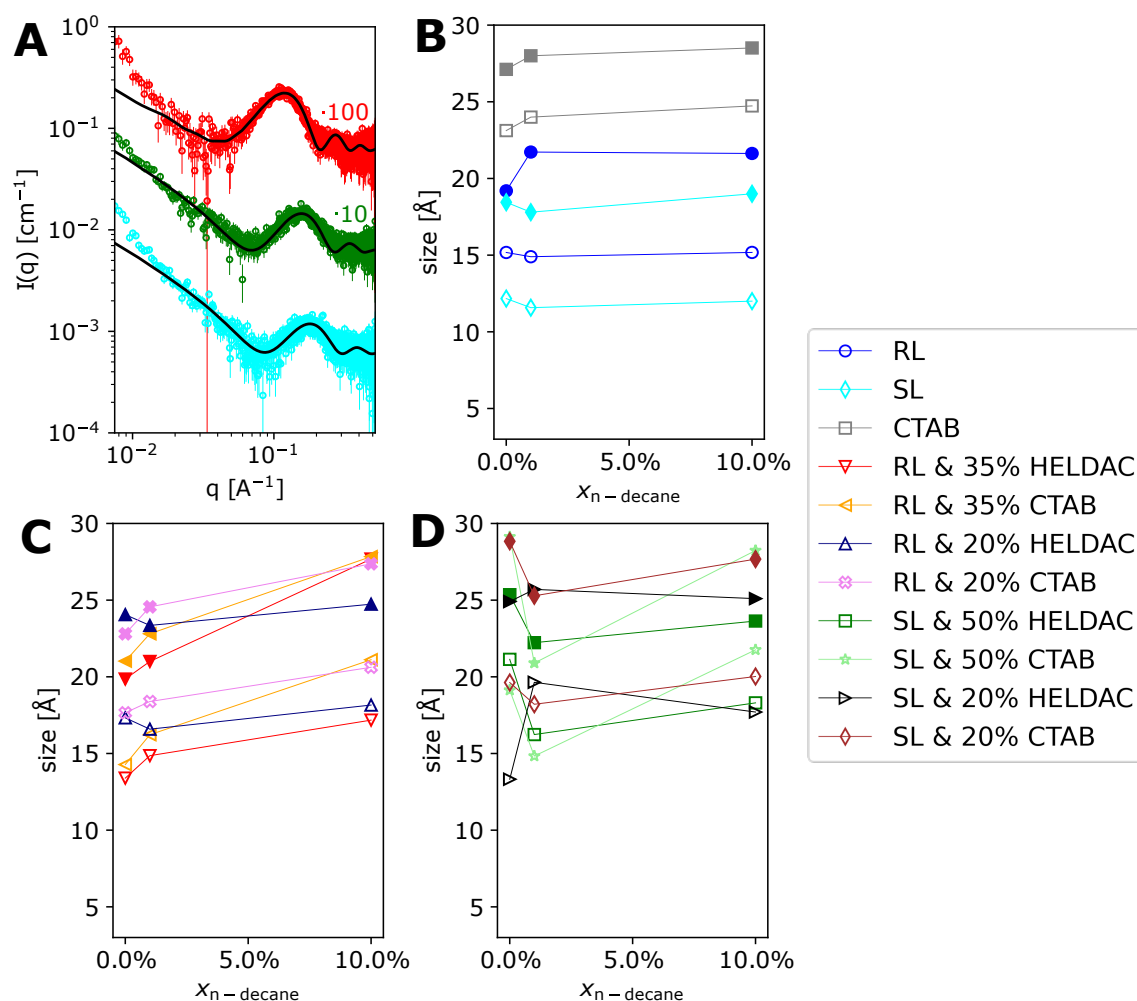


Figure 4.11: SAXS measurements of cationic complexes with addition of different amounts of n-decane. A) SAXS curves of the 65% RL & 35% CTAB system with 0 wt% of oil \circ , 1 wt% of oil \circ , and 10 wt% of oil \circ . The black lines are fits with the core-shell-ellipsoid-model. B) The increase in size of the pure surfactants, C) the RL-mixtures and D) the SL-mixtures. The corresponding fitted SAXS curve are displayed in Figure A9. The open symbols display the core-radius and the filled symbols the core-radius + thickness. The lines serve just as guide for the eye.

Emulsification, especially at low surfactant concentrations, is a crucial process in numerous applications, including detergents, food science, bioremediation or personal care [227, 228]. This is why the capacity of the cationic surfactant systems to incorporate oil is studied by SAXS. The Figures 4.11 A and A9 in the Appendix show the scattering curves of the cationic systems after the addition of 0 wt%, 1 wt% and 10 wt% of oil. The curves at higher surfactant concentration can be seen for the cationics without the

Table 4.5: Equilibrium values of interfacial tension of experimental data IFT_{exp} from Figure 4.10 and MD simulations IFT_{sim} from Figure 4.6. The mixtures are equimolar except for the experimental value of the RL/HELDAC system.

system	IFT_{exp} [mN/m]	IFT_{sim} [mN/m]
SL	7.3 ± 0.1	6.5 ± 2.0
SL/HELDAC	3.3 ± 0.1	2.3 ± 2.0
RL	4.4 ± 0.1	4.0 ± 2.5
RL/HELDAC	$1.0 (65\% \text{ RL}) \pm 0.1$	1.9 ± 2.0

addition of oil in Figure 4.3. The data was fitted and the sizes of the core and the total radius is displayed in Figure 4.11 B-D. Figure 4.11 B illustrates the impact of oil addition on the micelle size of pure surfactants. The addition of oil does not result in a significant change in the size of the micelles. Therefore, it can be concluded that the micelles of the pure surfactants do not incorporate oil. Figure 4.11 C displays the dimensions of the catanionic micelles containing RL. Similarly, the 80% RL & 20% HELDAC mixture does not exhibit a change in size upon the addition of oil, indicating that no oil is incorporated. However, the 80% RL & 20% CTAB mixture exhibits a slight increase in core size. Furthermore, the mixtures of 65% RL & 35% HELDAC and CTAB also exhibit a more pronounced increase in the core size of the micelle in comparison to the 80% RL & 20% CTAB mixture. The thickness of the shell remains constant, which is why the size of the micelles increases due to an increase of the core size. This increase in core size can be attributed to the uptake of oil, which results in micelle swelling. Figure 4.11 D shows the micellar sizes of the catanionics with SL as a function of the oil content. No significant alteration in the sizes was observed.

The results of the adsorption of catanionic systems with BSs will be discussed in terms of their adsorption effectiveness (how low is the IFT?), the adsorption efficiency (how fast is the low IFT reached?), emulsification, and the nonionic or ionic nature of the catanionics with BSs.

4.2.2 Adsorption Effectiveness

Beginning with the adsorption effectiveness, the IFTs of the mixed catanionic systems are lower than those of the individual surfactants at the air/water and the oil/water interface, respectively. This reduction in IFT indicates that the catanionic species are more surface-active and thus exhibit greater adsorption effectiveness than the individual surfactants (Figure 4.8 and Figure 4.10). However, caution must be paid for the systems with HELDAC due to its impurities [181].

This reduction in IFTs was also seen in the MD simulations, presented in Table 4.5.

The values obtained for the IFTs from experiment and simulations are found to be in close agreement. The IFTs are reduced when approaching equimolarity of the anionic and cationic surfactant mixture. This indicates that equimolar systems exhibit a greater adsorption effectiveness than non-equimolar systems. Similarly, the catanionic mixtures of RL are more effective in terms of adsorption than those with SL, and that with CTAB are more effective than those with HELDAC. Nevertheless, the equilibrium IFT is not as low as in other catanionic systems, where even ultra-low IFTs have been observed [229, 230] . In addition, a comparable mixture of C_{12/14}-alkyl polyglycoside sodium hydroxypropylsulfonate (structurally similar to RL/SL) and CTAB reached an IFT of 0.02 mN/m at a surfactant concentration of 1 g/l, however, crude oil was used [231, 232].

Table 4.6: Diffusion coefficients D of DLS (Figure A10 in the Appendix) and PGSE-NMR (Figure 4.2) measurements. The errors are estimated to be approximately 2%. The diffusion coefficient of the BSs D_{BS} was taken from the chemical shift at 5.2 ppm and the one of the cationic surfactants D_{Cat} at 3.1 ppm.

system	DLS	PGSE-NMR	
	D [10^{-11} m ² /s]	D_{BS} [10^{-11} m ² /s]	D_{Cat} [10^{-11} m ² /s]
100% RL	12.6	7.9	
100% SL	8.9	8.9	
100% HELDAC	5.5		9.4
100% CTAB	8.0		5.6
65% RL & 35% HELDAC	5.1	3.8	3.5
65% RL & 35% CTAB	7.2	4.0	3.6
80% RL & 20% HELDAC	10.2	7.1	6.7
80% RL & 20% CTAB	10.6	7.0	6.5
50% SL & 50% HELDAC	6.9	6.7	7.8
50% SL & 50% CTAB	6.8	6.7	7.7
80% SL & 20% HELDAC	8.9	7.5	6.9
80% SL & 20% CTAB	8.9	7.5	6.9

4.2.3 Adsorption Dynamics

As illustrated in the Figures 4.9 and 4.10, SL and HELDAC exhibit slow adsorption kinetics. To understand the reason of this slow adsorption kinetics, it is worth noting that there is no indication in a slow bulk diffusion (PGSE-NMR in Figure 4.2 and DLS in Figure A10 in the Appendix), low cmc (Figure 4.8), differences in the size and shape of the aggregates (SAXS in Table 4.1), or a strong electrostatic barrier which could hinder the adsorption from the subsurface to the surface (ζ -potential in Figure A3 in the Appendix). Hence, the reasons for the slow adsorption kinetics of SL and HELDAC

could be their strong hydration, the stretched conformation of the SL through the micelle (Figure 4.5 and [182]), and impurities of HELDAC which could hinder the adsorption from the subsurface to the surface (equilibrium ST measurements in Figure 4.8).

The DST measurements of the catanionic mixture in Figure 4.9 demonstrate that their adsorption is slower than the ones of the pure surfactants when evaluated over short time scales. The initial adsorption rate at short times is inversely proportional to the distance from equimolarity of the mixtures of anionic and cationic surfactants. This finding is in accordance with the results reported by other research groups [225, 233]. One potential explanation is that the cationic species exhibit lower cmc values, as illustrated in Figure 4.8. Consequently, the number of monomers, which diffuse to the interface, is reduced. Considering the IFT measurements as a function of time in Figure 4.10, the mixed catanionic systems achieve equilibrium IFT at a faster rate than pure surfactants. In addition, it was observed that as the mixture approached equimolarity, the IFT was reached at a faster rate, despite the lower cmc. This is in contrast to the findings of the DST measurements presented in Figure 4.9 at short time scales. However, the spinning drop technique is unable to resolve time scales of the order of those probed by the maximum bubble pressure. It is therefore necessary to compare the spinning drop data (IFT, Figure 4.10) with the maximum bubble pressure (DST, Figure 4.9) data at long time scales. After 10 seconds, which represents the minimum detection period of the spinning drop apparatus, the trends of the spinning drop measurements are analogous to the ones of maximum bubble pressure.

The DST data presented in Figure 4.9 was also evaluated in order to ascertain the prevalent adsorption mechanism. As displayed in Figure A11 in the Appendix, the DST data of the pure surfactants cannot be fitted with the Ward-Tordai equation (Equation 2.68) at low time scales. This indicates that the adsorption mechanism of the surfactant species is less controlled by diffusion. Instead, an adsorption barrier is present, suggesting that the rate-determining step for the adsorption process is likely the transfer from the subsurface to the surface [140]. However, the coefficient of determination of the fit is lower for the catanionic mixtures than for the pure surfactants. According to the Ward-Tordai model, the adsorption of the pure surfactants is hence controlled by diffusion to a greater degree than the adsorption of the catanionic mixtures, where an adsorption barrier must be present. This finding has also been reported by Li et al. who observed a diffusion-controlled mechanism for pure surfactants and a mixed kinetic-diffusion controlled mechanism for their mixtures [225]. This results in a higher adsorption barrier for the catanionic species than for the pure ionic surfactants. However, the electrostatic barrier should be higher for the pure ionic surfactants, given that they exhibit a stronger charge (seen in Figure A3 in the Appendix). Hence, it can be concluded that an additional barrier must be present, which impedes the adsorption process from the subsurface to the surface, but the reason is unclear to our knowledge [234]. Another possibility is the non-applicability of the Ward-Tordai model for this system.

In order to ascertain whether the underlying cause resides in the translational diffusion in the bulk, DLS (Figure A10 in the Appendix) and PGSE-NMR (Figure 4.2) measurements were performed (Table 4.6). No clear differences between the diffusion coefficients of the pure and mixed surfactant systems can be found. The diffusion coefficients obtained from the two techniques exhibited a discrepancy, from 0 to 48%. The diffusion coefficients derived from the DLS measurements consistently exceed those obtained from the PGSE-NMR measurements, except for 100% HELDAC. This may be due to the interparticle interactions which show a stronger contribution to the diffusion coefficient extracted from PGSE-NMR [235, 236].

4.2.4 Emulsification

The analysis of the oil uptake capability in relation to different catanionic systems demonstrated that the pure surfactants and catanionics with SL were unable to solubilize oil. One potential explanation for this phenomenon is the stretched conformation of SL within the micelle, which may impede the micelle's ability to swell. In contrast, catanionics with RL, particularly at higher equimolar ratios, could incorporate oil. They also exhibit the lowest IFT (Figure 4.10 and Table 4.5) and the fastest adsorption dynamics (Figure 4.9). Additionally, catanionics with RL have been observed to form rod-like micelles rather than spherical ones (Figure 4.3). Indeed, previous research has demonstrated that rod-like micelles are capable of incorporating a greater quantity of oil than their spherical counterparts [237, 238]. In conclusion, catanionics with RL are able to emulsify oil, likely due to their low IFT and rod-like micellar structures.

Table 4.7: Comparison of the features of catanionic and nonionic + cationic surfactant system in literature with the features of the studied anionic BSs (RL & SL) and cationic surfactants (HELDAC & CTAB).

feature	literature			this work
	catanionic surfactant system	nonionic + cationic surfactant	ref.	anionic BS + cationic surfactant
ζ -potential	$-\infty$ to $+\infty$ 0 for 1:1 ratio	0 to $+\infty$		-30 to 40 0 for 1:1 ratio
precipitation	yes	no	[85]	no
vesicle formation	yes	no	[85]	no
β parameter	-10 to -25	-1.5 to -3.0	[239, 240]	-4 to -10
adsorption velocity to the surface at short time scales	slower than pure surfactants	in-between pure surfactants	[225, 233, 241]	slower than pure surfactants

4.2.5 (Non)Ionic Nature of Biosurfactants

The structures of the BSs RL and SL comprise different two hydrophilic groups, one anionic carboxylic and one nonionic sugar group at pH 8. Hence, the ionic or nonionic character of the BSs remains an open question in the community [9–13]. Typical features of anionic and nonionic surfactants in mixtures with cationic surfactants are presented in Table 4.7.

Beginning with the ζ -potential, the BSs possess a negative charge which is neutralized first, and then becomes linearly more positive with the addition of cationic surfactant (Figure A3 in the Appendix). This is consistent with a typical behavior of ionic surfactants. Catanionic systems with BSs do not precipitate or form vesicles (Figure 4.1 and Figure 4.3). The lack of precipitation and the formation of micelles is rather typical for nonionic & cationic mixtures than for catanionics at equimolar mixtures [85]. Hence, the ionic effects may be covered by the large sugar groups of the BSs. The β -parameters of the catanionics with BSs range from -4 to -10 (Table 4.4). This is neither typical for ionic nor nonionic surfactants [239, 240]. The β values of catanionic surfactants systems with the same chain length are characterized by markedly negative values. For instance, $\beta = -25.5$ for the $C_{12}SO_4/C_{12}TAB$ system, which points to a strong interaction [239]. Upon increase of the chain length of alkyl trimethylammonium bromide to C_{16} , β decreases to -5/-6 [242]. In a separate study, sulfonation was performed on a $C_{12/14}$ -alkyl polyglycoside and then combined with $C_{16}TAB$, resulting in $\beta = -12$ [231]. It is thus difficult to connect the β -parameter of the catanionics with BS to asymmetric catanionic or nonionic & cationic surfactant systems. Regarding the adsorption velocity to the surface at short time scales, the studied catanionics with BSs are slower than the pure surfactants (Figure 4.9). This behavior is typical for catanionic mixtures [225, 233], whereas mixtures containing an ionic and nonionic surfactant typically adsorb with a velocity between the pure ionic and nonionic surfactants at short times [241]. In summary, our experiments demonstrate that RL and SL exhibit both ionic and nonionic character, depending on the measurement method. The reason may be that the ionic charge of the carboxylic group may be shielded by the flexible sugar group [18].

4.3 Phase Behavior of Microemulsions containing Rhamnolipid and Ethoxylates

Following the investigation of anionic BSs combined with cationic surfactants, the subsequent section studies the combination of anionic BSs with nonionic surfactants. Nonionic surfactants are one of the most important surfactants in laundry and detergency products. Ethoxylates were selected as model nonionic surfactants due to their tunability in hydrophilicity by temperature, their broad availability, their practical relevance and their renewable origin (via fatty alcohols and bioethanol). The following paragraph

presents a study of the phase behavior of μ Es containing RL and ethoxylates, which facilitates an understanding of BSs and their interfaces.

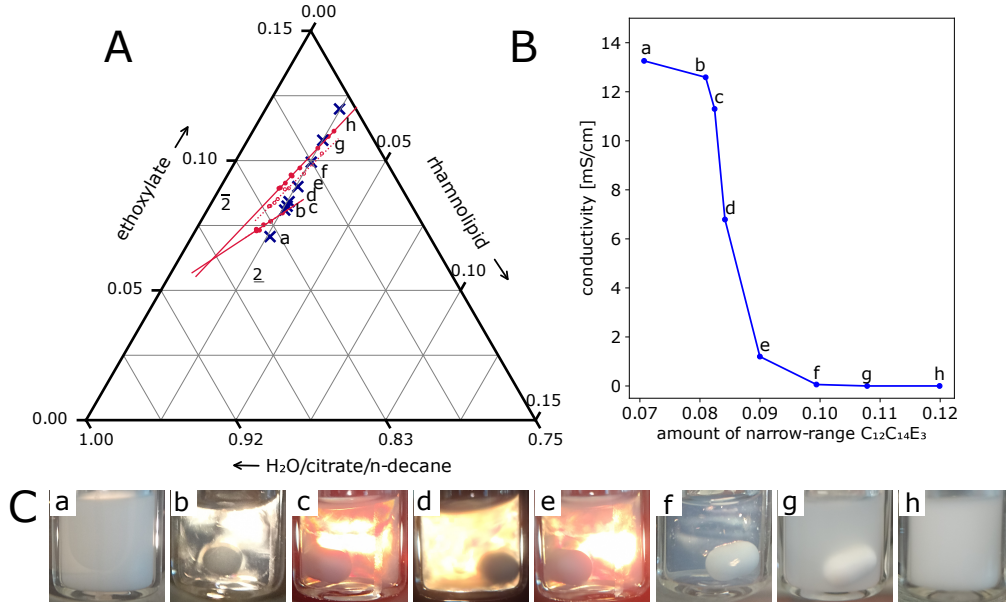


Figure 4.12: A) Phase diagram for the μ E containing RL, narrow-range C₁₂C₁₄E₃, n-decane and water at pH 8 and 30 °C. The blue markers indicate the measured compositions for the two following images. B) Conductivity of different phases as a function of the fraction of ethoxylate at a constant RL concentration of 2.5-2.6 %. C) Images of the samples through two crossed polarization filters. The lines just serve as guidance for the eye.

When RL, ethoxylate, n-decane and water are mixed at $\alpha = 0.5$, 30 °C and pH 8, different types of μ E emerge. Figure 4.12 A illustrates an example of different phases that can be observed along a titration line. The phases are arranged analogous to typical μ Es, according to the Kahlweit-fish or the T(γ)-cut [72]. The conductivity of the points along the titration line are displayed in Figure 4.12 B. Points (a) and (b) have a high conductivity, which suggests that water is the continuous phase. Indeed, the view through two crossed polarization filters (Figure 4.12 C) illustrates a turbid sample, that undergoes phase separation over time, with the turbid phase becoming the bottom phase. Hence, the observed conductivity and optical appearance suggest that sample (a) is an oil-in-water- μ E with an excess oil phase (2, Winsor type I). Sample (b) in Figure 4.12 C is transparent and displays birefringence when subjected to shear forces. This suggests the presence of an isotropic one-phase region with a bicontinuous structure (1, Winsor type IV). Samples (d)

and (e) show a high degree of birefringence in absence of shearing, indicating the presence of a lamellar phase. Sample (g) is turbid and exhibits a low conductivity, indicating a water-in-oil- μ E with an excess water phase ($\bar{2}$, Winsor type II). The intersection point between the Winsor I and Winsor II regions is the \tilde{X} -point. This point characterizes the minimal amount of surfactants necessary to completely micro-emulsify oil and water (reaching Winsor IV), thereby indicating the efficiency of the μ E [93]. The lower the surfactant concentration at \tilde{X} , the higher is the efficiency of the μ E.

In the following phase behavior experiments, we aim to (i) find the phase boundaries of RL and ethoxylate μ Es, (ii) to estimate their efficiency and (iii) to understand the differences in the phase behavior if we use different types of ethoxylates [243]. Thus, first, the quaternary system of RL, pure mono-disperse ethoxylates, n-decane and water is studied. The effect of the chain length, chain configuration and number of ethoxy groups is investigated. These μ Es were then compared to μ E with technical ethoxylates, since technical ethoxylates are used in applications rather than mono-disperse ones. These differences were then understood by mimicking the technical ethoxylates with mixtures of different pure substances. The results of these studies indicated efficient μ Es using long chain narrow-range ethoxylates, which were then further investigated.

4.3.1 Experiments

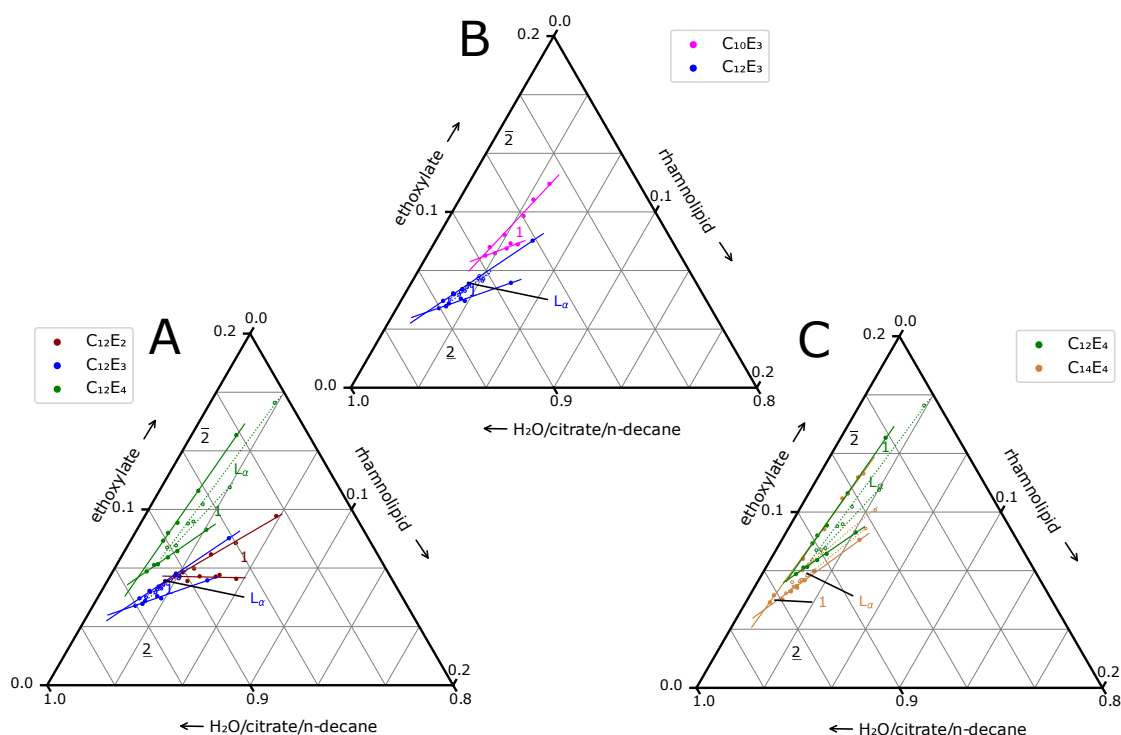


Figure 4.13: Variation of A) the number of ethoxy groups and B) & C) the chain lengths of mono-disperse ethoxylates as second surfactants in a μ E containing RL, n-decane and water at pH 8 and 30 °C. The lines just serve as guidance for the eye. The continuous lines display the phase boundaries of the two- and one-phase regions, whereas the dotted lines show the transitions of the one-phase region and the L_α phase.

Mono-Disperse Ethoxylates

Mono-disperse ethoxylates were first studied as second surfactants in a μ E with RL, n-decane, and water. The chemical properties of the ethoxylate were varied by changing the number of ethoxy groups or the chain length. Figure 4.13 displays the phase diagram of RL, n-decane, water and ethoxylates with different numbers of ethoxy groups. Winsor IV phases could be found the μ E of RL with the ethoxylates C₁₂E₂₋₄ (Figure 4.13 A). For forming Winsor IV μ Es with C₁₂E₄, a higher proportion of the ethoxylate is required than with C₁₂E₂ and C₁₂E₃. The ethoxylate/RL ratio of C₁₂E₂ and C₁₂E₃ is similar at the studied concentrations. Overall, more ethoxylate than RL is needed to form Winsor IV μ Es. Winsor IV phases could not be found with RL/C₁₂E_{>5}/n-decane/water. Subsequently, the effect of RL on the efficiency of the μ Es formed by ethoxylates was

examined. The μE of C_{12}E_3 and RL has its \tilde{X} point at the lowest surfactant concentration ($\tilde{\gamma} = 5.9\%$). Therefore, the μE RL/n-decane/water is more efficient with the following order of the second surfactant: $\text{C}_{12}\text{E}_3 > \text{C}_{12}\text{E}_4 > \text{C}_{12}\text{E}_2$.

Regarding the lamellar phases ($L\alpha$) of the different μE , their existence range decreases from C_{12}E_4 over C_{12}E_3 to C_{12}E_2 . In the μE with C_{12}E_2 no $L\alpha$ phase could be detected. This indicates different rigidities κ and therefore different persistence lengths ξ of the different amphiphilic films [107, 244].

Having studied the influence of the head group, variations in the chain length of the ethoxylate were conducted. The ternary plots are presented in Figure 4.13 B and C. The phase boundaries of the μE RL/n-decane/water with C_{10}E_3 and C_{12}E_4 are shifted to higher ratios of the ethoxylate compared to the μE s with C_{12}E_3 and C_{14}E_4 , respectively.

The reason is that as the head group and the chain length of the ethoxylate decreases, the originally high packing parameter of the ethoxylates becomes lower and the curvature of the amphiphilic film thus decreases. Given that the RL has a very low packing parameter, the minimum amount of the ethoxylate required to generate the zero curvature of a Winsor type IV μE increases.

Furthermore, the \tilde{X} -points of μE s with C_{10}E_3 and C_{12}E_4 are lower compared to μE s with C_{12}E_3 and C_{14}E_4 , respectively. Hence, the efficiency of a μE can be enhanced by using surfactants with longer chains, which has been reported in literature [94, 100, 245].

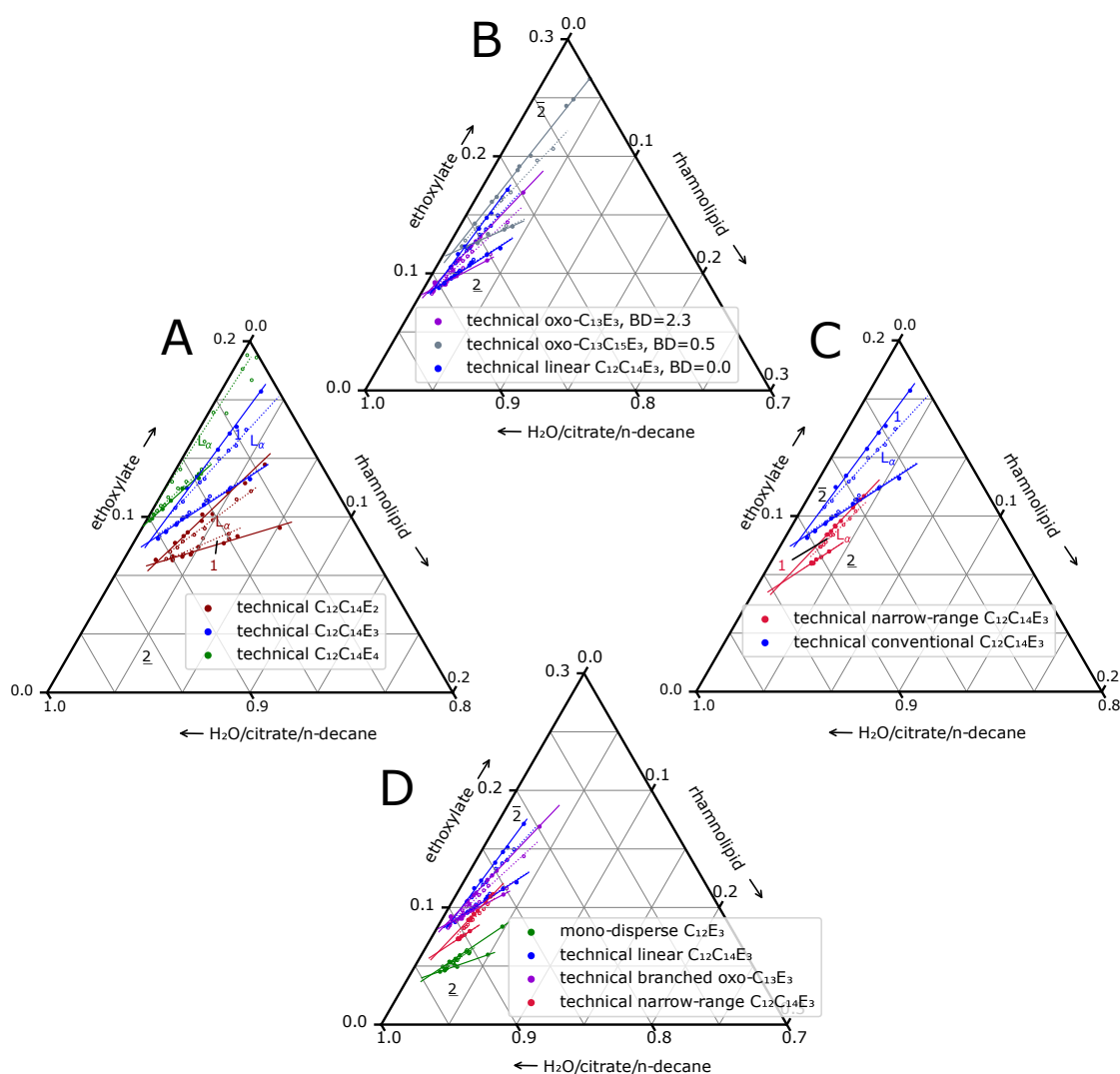


Figure 4.14: Variation of the A) number of ethoxy groups, B) the chain's configuration of ethoxylates of technical ethoxylates with BD being the branching degree, C) comparison of a linear standard technical ethoxylate and its narrow-range variant as second surfactants, and D) comparison between the different $C_{12}E_3$ in a μE containing RL, n-decane and a water at pH 8 and 30 °C. The lines just serve as guidance for the eye. The continuous lines display the phase boundaries of the two- and one-phase regions, whereas the dotted lines show the transitions of the one-phase region and the $L\alpha$ phase.

Technical Ethoxylates

Commercial products use technical ethoxylates rather than mono-disperse ethoxylates. Technical ethoxylates have a wide range of different ethoxylation degrees, including significant amounts of unreacted fatty alcohol, and ethoxylates of different chain lengths,

as shown in Figure 3.1. Figure 4.14 A displays the phase diagrams of the μ E of RL, n-decane, water and various linear technical ethoxylates. The phase boundaries are shifted to higher proportions of the ethoxylate from C₁₂C₁₄E₂ through C₁₂C₁₄E₃ to C₁₂C₁₄E₄. For the μ E with C₁₂C₁₄E₄, the phase boundary Winsor IV/Winsor II cannot be detected. It is also not possible to identify μ E with higher ethoxylation degree, e.g. C₁₂C₁₄E₅. The efficiencies of the μ Es RL/C₁₂C₁₄E₂₋₄/n-decane/water are similar. The lamellar phase is markedly evident within all μ Es.

Subsequently, the effect of the ethoxylate's chain configuration was investigated. Three different degrees of branching were analyzed ranging from the linear C₁₂C₁₄E₃ to oxo-C₁₃C₁₅E₃ with a branching degree of approximately 0.5 to oxo-C₁₃E₃ with a branching degree of approximately 2.3 [142]. Figure 4.14 B displays the phase boundaries of the branched surfactants. The phase boundaries and \tilde{X} -points are similar for μ Es with technical linear C₁₂C₁₄E₃ and oxo-C₁₃E₃. The phase boundaries of μ Es with technical oxo-C₁₃C₁₅E₃ are shifted to higher proportions of the ethoxylate.

Another class of technical surfactants are narrow-range ethoxylates, in which the ethoxylation distribution is narrowed by special catalysts, as shown in Figure 3.1. Figure 4.14 C displays the phase boundaries of technical narrow-range C₁₂C₁₄E₃ compared to technical conventional "broad-range" C₁₂C₁₄E₃. The phase boundaries of the narrow-range ethoxylate are shifted to higher proportions of the ethoxylate. In addition, the existence range of the lamellar phase is shifted to higher concentrations. Regarding the existence range between the two ethoxylates, indicating similarities.

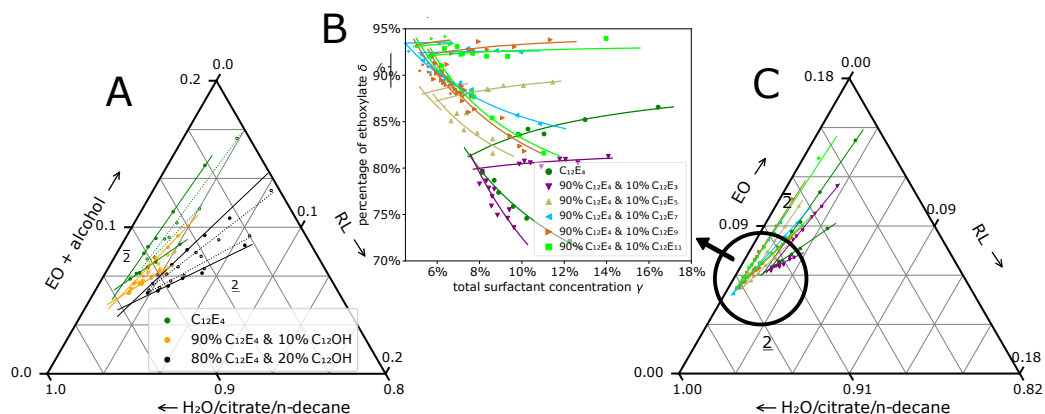


Figure 4.15: A) Addition of the fatty alcohol C₁₂OH, B) and C) of C₁₂E_x to a μ E containing RL, mono-disperse C₁₂E₄, n-decane and water at pH 8 and 30 °C. The lines just serve as guidance for the eye. The continuous lines display the phase boundaries of the two- and one-phase regions, whereas the dotted lines show the transitions of the one-phase region and the L α phase. (EO: ethoxylate)

Mixtures of Mono-Disperse Ethoxylates

The next objective is to understand and explain the differences between the μ Es of mono-disperse and technical ethoxylates. Therefore, well-defined mixtures of mono-disperse ethoxylates and fatty alcohol are used as second surfactant to mimic the technical distribution of ethoxylates shown in Figure 3.1 in a simplified but well-defined way. Hence, the effect of 1-dodecanol ($C_{12}OH$) on the μ E of RL, mono-disperse $C_{12}E_4$, n-decane and water is studied. Figure 4.15 A depicts the phase boundaries of different μ Es, in which $C_{12}E_4$ is partly replaced by $C_{12}OH$. The replace of $C_{12}OH$ shifts the phase boundaries to higher ratios of RL. One explanation is that the alcohol dissolves in n-decane making the oil less hydrophobic [102]. Therefore, less hydrophilic RL is required to reach the one-phase region. Additionally, the total amount of the amphiphiles (RL, $C_{12}E_4$ and $C_{12}OH$ and thus the efficiency) remains constant. Furthermore, the lamellar phase widens with addition of $C_{12}OH$ which implies a higher rigidity of the amphiphilic film.

The Figures 4.15 B and C display the phase boundaries of the μ E RL/ $C_{12}E_4$ /n-decane/water, in which 10 wt% of $C_{12}E_4$ is replaced by $C_{12}E_{3-11}$ (see Equations 2.23 and 2.24 for the axis in Figure 4.15 B). The partial replacement of $C_{12}E_4$ with $C_{12}E_3$ results in a shift of the phase boundaries to higher RL ratios and in a decrease in efficiency. Conversely, replacing $C_{12}E_4$ with $C_{12}E_{5-11}$ shifts the phase boundaries to higher ethoxylate ratios and increases the efficiency. However, when replaced with $C_{12}E_7$, $C_{12}E_9$ and $C_{12}E_{11}$, the phase boundaries and efficiency do not change.

The following section will present the findings of the phase behavior experiments, with a particular focus on the optimal formulation of μ Es, their efficiency, and the rigidity of the amphiphilic layers. Subsequently, the impact of utilizing technical, oxo- or narrow-range ethoxylates in lieu of mono-disperse ethoxylates will be assessed.

4.3.2 Optimal Formulation

As the curvature of the amphiphilic film approaches zero, the μ E is close to the optimal formulation. In this optimal formulation, the Winsor III or IV phase is present, the surfactant interacts equally with the oil and the water and the IFT is at its minimum [246]. This is why optimal formulations are often demanded for applications.

As shown in Figure 4.13, optimal formulations of RL and ethoxylates are found with RL and $C_{10-14}E_{2-4}$ at high ethoxylate ratios with n-decane as oil. $C_{12}E_5$ did not achieve a Winsor type IV μ Es at 30 °C with RL, although alone, it forms μ Es without RL [95]. $C_{12}E_2$, $C_{12}E_3$ and $C_{12}E_4$ are reported to form μ E below 12 °C [71]. Hence, RL rather bends the curvature of the ethoxylate-containing surfactant system due to its low packing parameter. Thus, the ethoxylate with a higher packing parameter, i.e. the longer the chain and the fewer the ethoxy groups, is required to achieve a zero curvature in an optimal formulation.

Mixing a hydrophobic and a hydrophilic component with a low and high packing pa-

parameter is the usual approach to formulating μ Es. Typically, optimal formulated μ Es of anionic or glycoside surfactants are achieved by formulating hydrophobic medium-chain alcohols or a high salinity for the hydrophobicity [44, 45, 247]. This is also true for μ Es with RL which could also be obtained by formulating RL at high salinity or with alcohols [48, 49, 248]. Thereby, alcohols of the chain length C_7 and C_8 were found to form Winsor IV phases with RL at all RL/alcohol ratios [46]. The μ Es with $C_{7-8}OH$ have a greater existence range of Winsor IV than the studied μ Es with ethoxylates or those with lecithin [50]. Thus, the μ E of RL with $C_{7-8}OH$ are likely to be more robust than those with ethoxylates.

On the other hand, alcohols may be undesired in some applications, e.g. due to a malodorous smell, which is why alcohol-free μ Es are demanded, e.g. by formulating with sodium soaps or ethoxylates [249, 250]. Another example is the μ E of the RL-like sucrose mono-laurate formulated with 20 mol-ethoxylated mono-di-glyceride (stearate and palmitate), for which the Winsor IV phase region approaches its maximum if the surfactants are used in equal amounts [251].

4.3.3 Efficiency

For technical applications, the efficiency of a μ E, more specifically of the surfactant system, is of great importance. The efficiency is given by the minimum amount of surfactant required to form a one-phase μ E (the \tilde{X} -point) [95]. The less surfactant is needed for the μ E, the more efficient it is.

As shown in Figures 4.13 B and C, the efficiency of the μ E RL/ethoxylate/n-decane/water increases when a long chain ethoxylate is used as the second surfactant. Hence, a longer alkyl chain of the surfactant can increase the efficiency of the μ E and also the solubilization capacity, which has previously been reported for μ Es of technical and mono-disperse ethoxylates without co-surfactants [94, 100]. Since a higher efficiency indicates a lower monomer solubility, the monomer solubility is lower for the longer chain lengths [71]. Regarding the variation of the number of ethoxy groups, shown in Figure 4.13 A, the μ E with $C_{12}E_3$ is found to be the most efficient one. The μ E with $C_{12}E_4$ has a lower efficiency, which is expected due to a higher monomer solubility of $C_{12}E_4$ than $C_{12}E_3$ in oil (at different temperatures) [71]. Interestingly, the μ E with $C_{12}E_2$ is less efficient than the one of $C_{12}E_3$, likely due to segregation effects of the very hydrophobic $C_{12}E_2$ which partitions into the oil [102].

The efficiency of μ E of ethoxylates alone (ethoxylate/n-decane/water) has been intensively studied and the \tilde{X} -points of $C_{12}E_4$ alone ($\tilde{\gamma} \approx 4.5\%$ and $\tilde{T} \approx 18\text{ }^\circ\text{C}$) and $C_{12}E_5$ alone ($\tilde{\gamma} \approx 7.5\%$ and $\tilde{T} \approx 38\text{ }^\circ\text{C}$) were found [94]. The comparison of these values with the \tilde{X} of our experiments (e.g., $C_{12}E_4$ & RL: $\tilde{\gamma} = 7.6\%$ and $\tilde{T} = 30\text{ }^\circ\text{C}$) is rather difficult because of the \tilde{T} . However, the \tilde{X} -points of μ E and ethoxylate are in the same range as μ E of ethoxylates alone. There may be a slight indication of a decrease in the efficiency of μ E with the addition of RL, as evidenced by a slight increase in $\tilde{\gamma}$. This decrease of efficiency

was also observed when C₁₀E₄ was partially replaced by n-octyl-D-maltopyranoside in a μ E in n-decane/water. For example, replacing 10 wt% of the ethoxylate with the glycoside resulted in an increase in the $\tilde{\gamma}$ -point of approximately 2 wt% and in different \tilde{T} -points of approximately 9 °C [252]. The low efficiency of sugar surfactants (alkyl polyglycosides C_iG_j, RL, etc.) has been reported in the literature, where 15 % surfactants was required to achieve an one-phase μ Es of C₁₂G₁/geraniol/n-octane/water or 28 % for C₁₂₋₁₄G_{1.3}/pentanol/rapeseed methyl ester/water [45, 50, 247]. Taking these values into account, the studied μ E RL/ethoxylate/n-decane/water shows a high efficiency compared to the μ Es of other sugar-based surfactants. μ Es of pure RL were obtained in toluene with a mixture of 50% mono-RL & 50% di-RL at neutral pH and 11 wt% NaCl. The efficiency was considerably high with $\tilde{\gamma} \approx 10\%$, although the different surfactant system, (lower molecular weight and interfacial area of mono-RL) and lower molecular weight of the oil have a positive effect on the efficiency [253].

4.3.4 Rigidity

The existence region of the lamellar phase increases with an increase in the surfactant's chain length and number of ethoxy groups (Figure 4.13). This is expected and reasonable since the longer molecule is able to exert more intermolecular interactions. The increase of the existence range of the lamellar phase indicates an enhanced persistence length of the amphiphilic film [107, 244]. The persistence lengths ξ in m is proportionally connected with the rigidity of the amphiphilic film (Equation 2.28) [108]. Hence, the increase of the ethoxylate's chain length and number of ethoxy groups results in an increase of the rigidity of the amphiphilic film.

4.3.5 Effect of Technical Mixture

Technical ethoxylates consist of a wide range of substances, namely ethoxylates with different ethoxylation degrees and fatty alcohol (Figure 3.1). The phase boundaries of μ E with technical ethoxylates are shifted to higher ethoxylate ratios compared to the μ E with mono-disperse ethoxylate (Figure 4.14 A vs. Figure 4.13 A). This means that the technical ethoxylates with a specific average ethoxylation degree behave overall more hydrophilic than their mono-disperse analogues. One reason could be the higher ethoxylated species C₁₂E₅₋₇, which shift the phase boundaries to higher ratios of the ethoxylate (Figure 4.15 B and C). A possible explanation is that the more hydrophilic ethoxylates, having a lower packing parameter, with a high ethoxylation degree, need a higher ratio of the more hydrophobic ethoxylates, having a higher packing parameter, to achieve a zero curvature. A second reason for this is that the hydrophobic components segregate into the oil to a considerable degree [102, 254]. Thus, higher ethoxylated species rather accumulate at the interface, making the technical ethoxylate appear more hydrophilic than its average ethoxylation degree. C₁₂E₇ was identified by Acosta et al. as the boundary

between partitioning and non-partitioning species [102]. Hence, partitioning may also be the reason why the addition of C₁₂E_{>7} does not lead to a further increase in efficiency (Figure 4.15 B). Therefore, in terms of optimal formulation, evidence was found that the ethoxylates with a high ethoxylation degree exert a dominant effect compared to the ethoxylates with low ethoxylation degrees and fatty alcohol.

In terms of efficiency, the total amount of surfactant at \tilde{X} is higher for C₁₂C₁₄E₃ for the technical mixtures and similar for C₁₂C₁₄E₂ compared to the pure analogs C₁₂E₃ and C₁₂E₂. One explanation is the presence of the longer C₁₄ chains in the technical mixtures. Another explanation of the increase in efficiency may also be due to the highly ethoxylated species (Figures 4.15 B and C). This is an unexpected result because ethoxylates with a higher number of ethoxy groups are known to have a higher monomeric solubility in oil at their respective \tilde{T} and therefore a lower efficiency at the \tilde{X} point [71]. To draw further conclusions, the monomeric solubilities need to be determined at 30 °C.

The existence range of the lamellar phase is more pronounced in the case of the technical substances. One reason is probably the presence of longer chain lengths of the ethoxylate as formerly explained. Another reason may be the presence of fatty alcohol, the addition of which leads to an increase in the existence range of the lamellar phase (Figure 4.15 A). Hence, the alcohol seems to increase the rigidity of the amphiphilic film. This is unexpected, as it has been reported that middle-chain alcohols, such as butanol or pentanol, decrease the order of the amphiphilic film, thereby decreasing the rigidity [255, 256]. One explanation is that the chain lengths of C₁₂OH and C₁₂E₄ are the same which could increase the crystalline character of the amphiphilic film. Moreover, dodecanol has been reported to increase the interfacial rigidity when used as a lipophilic linker [206]. The phase diagram of μ Es with technical ethoxylates is largely analogous to that with mono-disperse ethoxylates, as it has been reported in the literature for μ Es formed by ethoxylates without RL [101]. However, it has been found that the technical ethoxylate has a more hydrophobic character due to segregation effects, resulting in the formation of unsymmetrical phase boundaries [101, 257]. This is not the case for the RL/technical ethoxylate/n-decane/water μ Es.

4.3.6 Oxo-Ethoxylates

The phase boundaries and efficiencies of μ Es with technical linear C₁₂C₁₄E₃ are similar to those of oxo-C₁₃E₃, whereas those of technical oxo-C₁₃C₁₅E₃ are shifted to higher ethoxylate ratios. Hence, the branching degree of technical ethoxylates has little effect on the optimal formulation and efficiency of the μ E RL/ethoxylate/n-decane/water (Figure 4.14 B). The differences in the phase boundaries are more likely due to the differences in the ethoxylation degree (Figure 3.1) since the mean ethoxylation degree is 1.7 for oxo-C₁₃C₁₅E₃ and 2.8 for oxo-C₁₃E₃ and linear C₁₂C₁₄E₃, respectively. Therefore, the phase boundaries of μ E with oxo-C₁₃C₁₅E₃ are at higher levels of the ethoxylate due to its lower average ethoxylation degree and therefore higher hydrophilicity. Thus, higher

amounts of the ethoxylate are required to compensate for the high hydrophilicity of the RL. Hence, the studied ethoxylates with methyl and ethyl branches do not reduce the μ E's efficiency to a considerable degree as reported by Frank et al. [258]. In conclusion, the evidence obtained in this work suggests that the (methyl, ethyl) branching of the surfactant chains has a minor effect compared to differences in the number of ethoxylation groups.

4.3.7 Narrow-Range Ethoxylate

Another type of ethoxylates are narrow-range ethoxylates, in which the ethoxylation distribution is narrowed by special catalysts. The phase boundaries of the μ E with narrow-range $C_{12}C_{14}E_3$ are shifted to lower ethoxylate ratios and higher efficiencies compared to those with "standard-range" $C_{12}C_{14}E_3$. One reason may be the lower proportion of hydrophobic compounds. However, a more important reason is likely due to the higher proportion of longer chains in the narrow-range ethoxylate, C_{14} (Figure 3.1). The longer chains reduce the ethoxylate fraction and increase the efficiency, as shown in Figure 4.13 B and C.

4.4 Structure of Microemulsions containing Rhamno-lipid and $C_{12}E_4$

After understanding the phase behavior of μ Es containing RL and different ethoxylates, the μ E of RL & mono-disperse $C_{12}E_4$ was selected and their structure investigated.

4.4.1 Experiments

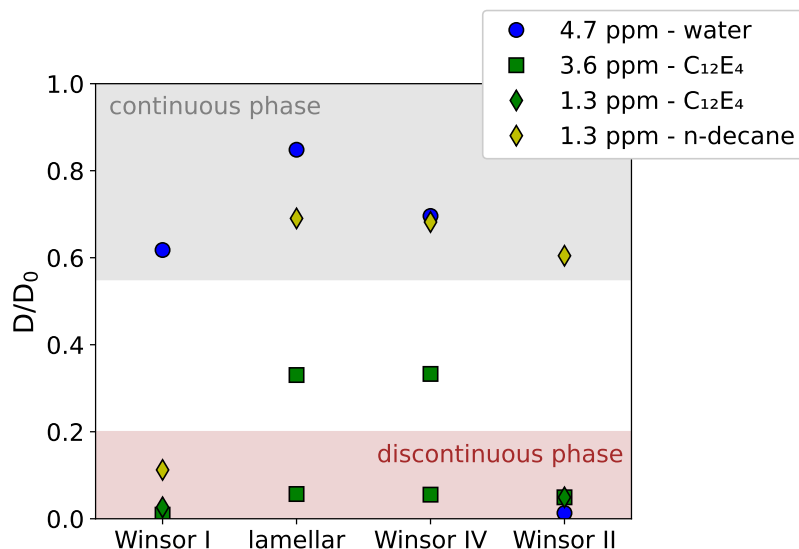


Figure 4.16: Normalized diffusion coefficients from PGSE-NMR of the μ E containing RL and mono-disperse C₁₂E₄. The diffusion coefficients at 0.9 ppm equal the ones at 1.3 ppm and have therefore been removed from this figure for the sake of clarity.

PGSE-NMR measurements were performed to determine the individual diffusion coefficients for water, n-decane and C₁₂E₄ [107, 259]. The corresponding peaks of these compounds are displayed in Table 3.2 and Figure A14 in the Appendix. Figure 4.16 shows the diffusion coefficients D of the various components in the different states of μ Es, normalized to their monomeric diffusion coefficients D_0 of the surfactants or unconfined n-decane and water, respectively. Since the D/D_0 of 1.3 and 0.9 ppm were identical, only the chemical shifts at 1.3 ppm are displayed in Figure 4.16. It was found that the contribution of the alkyl chain of RL to the peaks at 1.3 and 0.9 ppm can be neglected due to the small amount of RL compared to water or n-decane. Despite, the contribution of the alkyl chain of C₁₂E₄ to the peaks at 1.3 and 0.9 ppm is approximately <5%, the attenuation curve cannot be fitted with one single diffusion coefficient for 1.3 ppm in Winsor I and II and for 3.6 ppm in the lamellar and Winsor IV μ E. Therefore, a biexponential analysis (Equation 2.31) is used, resulting in two diffusion coefficients.

For Winsor I, the diffusion coefficient at 4.7 ppm (water) is higher than the diffusion coefficient at 1.3 ppm (n-decane). This indicates that water is the continuous phase and thus confirms the existence of an o/w μ E (Winsor I). The attenuation curve at 1.3 ppm shows two contributions, one at $1.7 \cdot 10^{-10}$ m²/s (75%) and one at $4.1 \cdot 10^{-11}$ m²/s (25%). A possible explanation is that the high diffusion coefficient $1.7 \cdot 10^{-10}$ m²/s corresponds to the diffusion of the oil droplet and the lower diffusion coefficient of $4.1 \cdot 10^{-11}$ m²/s to the

diffusion of C₁₂E₄. The fraction of 25% is similar to the amount of C₁₂E₄ in the sample. Moreover, this lower diffusion coefficient at 1.3 ppm is within the measurement error compared to the diffusion coefficient of $1.5 \cdot 10^{-11}$ m²/s at 3.6 ppm which corresponds to the diffusion of C₁₂E₄. Thus, the diffusion of C₁₂E₄ is probably slightly slower than that of the oil droplets. However, the results obtained for the signal at 3.6 ppm should be treated with caution as the maximum attenuation was only 70%. Also, the oil may appear faster if the excess free oil phase is not completely phase separated.

In the Winsor II μ E, the peak at 1.3 ppm contains two contributions, one at $9.4 \cdot 10^{-10}$ m²/s and one at $6.2 \cdot 10^{-11}$ m²/s. The one at $9.4 \cdot 10^{-10}$ m²/s likely corresponds to the continuous oil phase. Water, which has a slower diffusion coefficient of $3.0 \cdot 10^{-11}$ m²/s, is therefore slower. Consequently, a w/o- μ E (Winsor II) is present. The other diffusion coefficient $6.2 \cdot 10^{-11}$ m²/s of 1.3 ppm is similar to that of C₁₂E₄ at 3.6 ppm and to that of water at 4.7 ppm. Hence, the diffusion coefficient is probably that of C₁₂E₄. Since the diffusion of the water droplets and C₁₂E₄ are similar, C₁₂E₄ is likely attached to the water droplets. The diffusion coefficient of C₁₂E₄ may be slightly faster than that of the water droplet due to the rapid exchange of C₁₂E₄ in the water droplets and free C₁₂E₄ in the continuous n-decane phase.

In the case of the lamellar and Winsor IV phases, the diffusion coefficients of water and n-decane are high. This means that both water and n-decane are continuous phases, which is consistent with their bicontinuous and lamellar structure. In the case of the lamellar structures, Pake peaks were observed in ²H NMR (Figure A15 in the Appendix). The reason is that quadrupol splitting is present, since the D₂O molecules weakly align [260, 261]. Hence, the lamellae orient along the magnetic field, as they do in the C₁₂E₄/water system [262]. The peaks at 3.6 ppm for the lamellar and bicontinuous structures show two contributions. Thus, there are two different species of C₁₂E₄ with different diffusion coefficients. This is not expected since previous PGSE-NMR studies have shown a rather constant diffusion of C₁₂E₄, regardless of the different μ E types [259]. However, the attenuation curves at 3.6 ppm are noisy, its signals are weak and its maximum attenuation is only approximately 30%. In addition, the error in the diffusion of C₁₂E₄ is relatively high due to the two-component fit. However, the existence of two different diffusion coefficients suggests that there are two different types of diffusion present, namely lateral diffusion within the membrane and translational diffusion of free C₁₂E₄ monomers in the continuous phase. Since approximately 2.2 wt% of monomeric C₁₂E₄ is solubilized in n-decane and 0.002 wt% in water [109, 263], the amount of free C₁₂E₄ can probably be neglected.

To estimate the sizes of the μ E, the diffusion coefficients of Figure 4.16 were converted into radii using the Stokes-Einstein equation, assuming a viscosity of D₂O. The result is displayed in Figure A16 in the Appendix. The hydrodynamic radii of the oil droplets in Winsor I are 10-50 Å and those of the water droplets in Winsor II 20 Å.

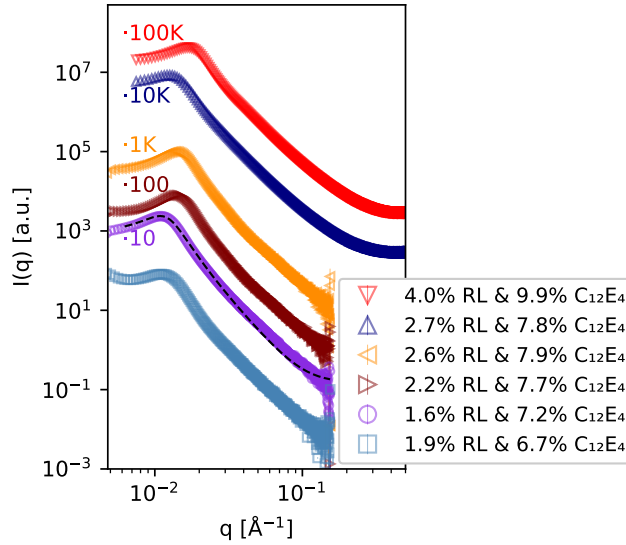


Figure 4.17: SAXS curves of μ Es containing different amounts of RL and mono-disperse $C_{12}E_4$ in Winsor IV. The most efficient μ E was fitted with the Teubner-Strey model with $d=543$ Å and $\xi=279$ Å.

The structure of the μ E is mainly influenced by the persistence length ξ of the amphiphilic film, resulting from its local fluctuations. The higher the persistence length, the higher is the bending modulus, the lower is the IFT and the more efficient is the μ E [125, 264]. Hence, the maximum persistence length ξ and the highest periodicity of the structure d of the μ E RL/mono-disperse $C_{12}E_4$ /n-decane/water were determined by SAXS. Figure 4.17 illustrates the scattering curves of different μ E compositions near the \tilde{X} -point. The scattered compositions are illustrated in a triangle diagram in Figure A17 in the Appendix.

All scattering curves show a similar profile. They have a characteristic peak whose appearance at q is related to the periodicity of the structure d and whose width corresponds to the persistence length ξ . The magenta curve, corresponding to 1.6% RL and 7.2% $C_{12}E_4$, has its peak at the lowest q and the sharpest profile. Therefore, it has the largest domain size and persistence length. Thus, the curve was fitted with the Teubner-Strey model which gives a domain size of 543 Å and a persistence length of 279 Å. Knowing these two values, the amphiphilicity factor f_a and the bending modulus κ were calculated to be -0.83 and $1.01 \cdot 10^{-21}$ J, respectively (Equations 2.50 and 2.51) [124, 126]. This will be further discussed later.

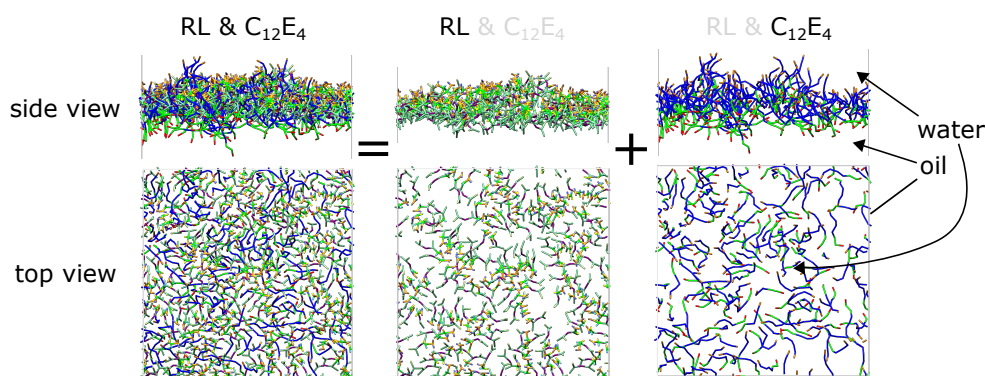


Figure 4.18: Top and side view of the oil/water interface containing RL and mono-disperse $C_{12}E_4$ as obtained from mesoscopic MD simulations. All surfactant species are shown left, the RL and $C_{12}E_4$ molecules are highlighted in center and right.

In order to gain insights into the arrangement of the different surfactant molecules RL and mono-disperse $C_{12}E_4$ within this amphiphilic film, MD simulations were performed. The oily and aqueous parts of the μE are separated by the amphiphilic film composed of surfactant molecules. Figure 4.18 illustrates the amphiphilic layer of the μE . The side view in Figure 4.18 displays a vertical section through the amphiphilic film. The hydrophobic chains of the surfactants are oriented inwards towards the oil phase, while the hydrophilic headgroups are oriented outwards towards the water phase. Comparing the RL and $C_{12}E_4$ molecules separately at the interface, the $C_{12}E_4$ molecules occupy vertically more space, resulting in a thicker layer. Conversely, the RL molecules appear to be more densely packed compared to the $C_{12}E_4$. As revealed in the top view in Figure 4.18, the surfactant molecules are inhomogeneously distributed within the amphiphilic film. The surfactants accumulate locally which results in a domain-like distribution of the surfactant species. Notably, the sugar groups of RL are arranged in a stacked manner.

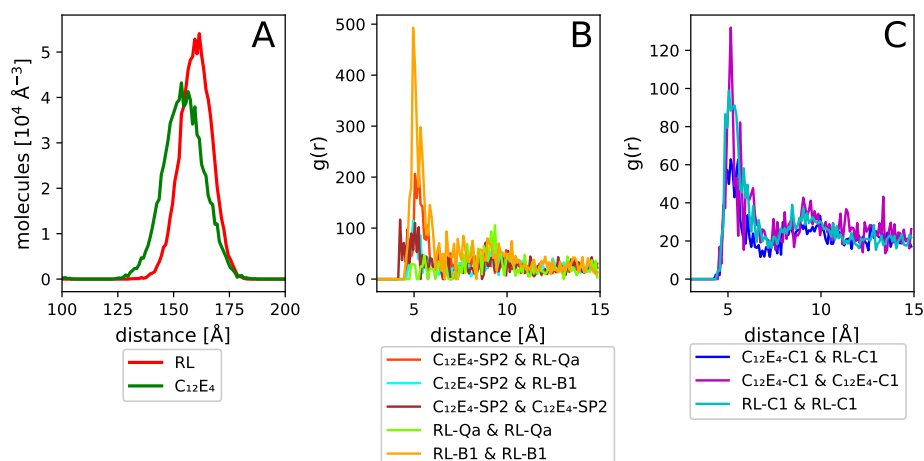


Figure 4.19: A) Density profile of RL and mono-disperse C₁₂E₄ in the amphiphilic film in z-direction. Radial distribution functions of different hydrophilic and hydrophobic beads, in B) and C), respectively (see Figure 3.4 for labelling of the beads).

The RL/C₁₂E₄ interface was further analyzed to obtain more information about the arrangement of the surfactant molecules in the amphiphilic film. Figure 4.19 A displays the amount of molecules at different positions within the film. The RL molecules are rather located towards the aqueous phase, whereas the C₁₂E₄ molecules are rather located towards the oil phase. The peaks have a separation of approximately 6 Å.

Figure 4.19 B illustrates the pair correlation functions of different beads of the molecules. The sugar groups of the RL (e.g. bead B1 of coarse-grained modeling) show the strongest interaction with each other at approximately 5 Å. There are weaker interactions between the ethylene oxide of C₁₂E₄ (bead SP2) and the carboxyl group of RL (bead Qa) as well as between the sugar beads of RL (bead B1) and the ethylene oxide groups of C₁₂E₄ (bead SP2) and between the ethylene oxide groups of C₁₂E₄. A very small maximum appears at approximately 9.5 Å, which might correspond to the second sphere of the neighboring molecules.

Figure 4.19 C shows the correlation of the hydrophobic alkyl chains of the surfactants. Two peaks emerge which appear at approximately 5.1 and 9.5 Å, similar to the correlation of the hydrophilic beads. The peak at 5.1 Å is higher for the interactions between the same type of molecules, RL & RL and C₁₂E₄ & C₁₂E₄, compared to that of the different surfactants with each other, RL & C₁₂E₄, suggesting antisynnergistic effects.

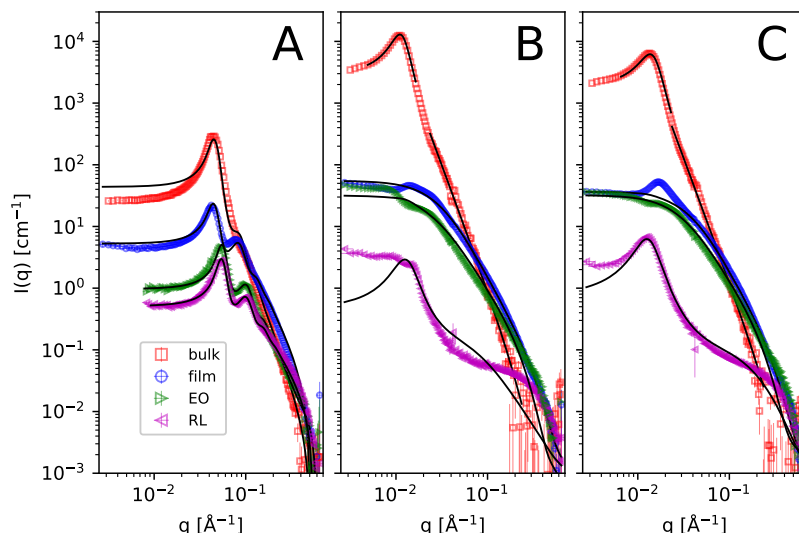


Figure 4.20: SANS curves of μ Es RL/mono-disperse $C_{12}E_4$ /n-decane/water in A) Winsor I and B) and C) Winsor IV at different RL and $C_{12}E_4$ concentrations. The temperature was set to 30 °C although the RL and EO contrast in B) and C) were measured at 55 °C. The different colors display different contrasts which are illustrated in Figure 3.3. The solid lines present fits of A) the core-shell(-shell) sphere form & HSA structure factor, and B) and C) the oblate model, described by Equations 2.48 and 2.52, with parameters shown in Table A3 in the Appendix.

To validate the simulation data, in particular the presence of inhomogeneities, SANS contrast matching experiments were conducted. Four different contrasts were tested, namely the bulk contrast (oil vs. water), the film contrast (RL/ $C_{12}E_4$ vs. oil/water, the RL contrast (RL vs. oil/water/ $C_{12}E_4$) and the EO contrast ($C_{12}E_4$ vs. RL/oil/water, see also Figure 3.3). Figure 4.20 A displays the scattering curves of the Winsor I phase. The bulk contrasts show a typical profile with a pronounced structure peak, while the other contrasts display typical profiles for film contrasts [125]. As expected, the intensity follows the order bulk > film > EO > RL contrast due to the decreasing amount of volume fraction in the sample. The bulk contrast is fitted with core-shell sphere model (core=n-decane=surfactant chain, shell=headgroups), whereas in the film, EO and RL contrasts the scattering curves are fitted with a core-shell-shell sphere model, as the contrast of n-decane has to be distinguished from that of the surfactant chains. The fitting parameters are given in Table A3 in the Appendix. The interaction radii of the bulk and film contrasts exhibit the same value. In addition, the shell thickness 2, which corresponds to the thickness of the headgroups, is similar. Hence, shell thickness 1 probably represents the surfactant chains. Using the Tanford formula, a length of 11 Å corresponds to a chain length of 8 carbon atoms [265]. This is in agreement with the hydrophobic part of the

RL molecule (see Figure 3.4). The thickness of the surfactant chains is smaller in the EO and RL contrasts than in the film contrast and therefore the surfactant chains are shorter than expected from the Tanford formula.

The scattering profiles of the EO and RL contrasts are similar to those of the film contrast in Winsor I. However, the peaks of the EO and RL contrasts are shifted to higher q (Figure 4.20 A). Thus, the interaction radius is smaller in the EO and RL contrast than in the bulk and film contrast (Table A3 in the Appendix). In addition, the samples of the EO and RL contrasts intended for Winsor IV (Figures 4.20 B and C) showed a Winsor I μ E at 30 °C. When these samples were heated to 55 °C, they became Winsor IV. The reason of these findings are probably the use of d-C₁₂E₄ in the EO and RL contrast and use of h-C₁₂E₄ in the bulk and film contrasts. Deuterated surfactants are known to shift the phase boundaries since they may change molecular solubilities and contrasts [266]. Other reasons may be slightly different compositions due to the small sample volume and differences in the incoherent background of the different contrasts.

The scattering curves of the Winsor IV μ Es in two different ratios are illustrated in Figure 4.20 B and C. The intensities of the scattering curves are higher than those of Winsor I. One reason may be a higher structure factor due to a larger surface area of the bicontinuous structure [109]. The profile of the RL contrast scattering curve is not similar to the other scattering curves and atypical for film contrasts. In particular, the high slope at mid- q is atypical and remains if taking possible residual bulk contrast into account. A shoulder appears at approximately 2.8 \AA^{-1} , corresponding to a distance of 22 \AA . The scattering curve of the bulk contrast is fitted using the Teubner-Strey model and Porod decay for diffusive interfaces [122, 130] and curves of the film, RL and EO contrasts are fitted with the oblate model (Equations 2.48 and 2.52) [118]. The fitting parameters are given in Table A3 in the Appendix. The smearing factor t , which is more specifically the standard deviation of a Gaussian scattering profile of the interface, is $t = 4 \text{ \AA}$ and $t = 3 \text{ \AA}$ for the Winsor IV phases, respectively. This is slightly lower than the theoretical $t = 5 \text{ \AA}$ for RL and C₁₂E₄.

Figure 4.20 B and C show that the fits are not optimal, likely due to the suitability of the model and residual bulk contrast. A scattering model for the expected inhomogeneous surfactant film is not available to our knowledge. The residual bulk contrast can be particularly seen in the shoulder of the EO and RL contrast at small q in Figure 4.20 B and in the peak of the RL and film contrast in Figure 4.20 C.

Table A3 in the Appendix illustrates that the radii of gyration σ , the scattering contrast thickness t_0 and membrane thickness d of RL are smaller than of C₁₂E₄, which are in accordance with the smaller chain of RL [174]. As expected, the values for σ , t_0 and d of the film are between those of RL and EO.

Table 4.8: Composition of the amphiphilic film calculated by determining the factor, f , in two different ways in the different analyzed contrasts. Explanations on their calculation are displayed in the Appendix.

		theoretical composition		composition out of invari- ants		composition out of curve shift	
		v% RL	v% EO	v% RL	v% EO	v% RL	v% EO
Winsor I	film contrast	0.54	0.46				
	RL contrast			0.79		0.4	
	EO contrast				0.51		0.36
Winsor IV (1)	film contrast	0.20	0.80				
	RL contrast			0.58		0.39	
	EO contrast				0.82		0.68
Winsor IV (2)	film contrast	0.19	0.81				
	RL contrast			0.61		0.32	
	EO contrast				0.70		0.73

Another goal of the SANS studies was to investigate the amount of RL and C₁₂E₄ which is incorporated in the amphiphilic film. Table 4.8 hence shows the compositions of the amphiphilic film calculated by two different methods (see Section 3.7). Both RL and C₁₂E₄ constitute the amphiphilic film. The amount of RL in the amphiphilic film is higher than the theoretical composition. This is in agreement with the literature where Liley et al. found that RL has a higher surface activity than C₁₂E₈ in the mono-RL/RL/LAS/C₁₂E₈ mixture [25]. Moreover, C₁₂E₄ solubilizes to ≈ 2.2 wt% in n-decane, which amount is no longer available to adsorb at the interface [109, 263].

Nevertheless, the sum of the percentages of the individual components does not equal 100%. When examining the various error possibilities, the main difficulty was the determination of the invariant. The reason was that the value for the invariant constituted up to 40% from the high q Porod approximation. Other reasons were the phase shift from C₁₂E₄. In the original paper of Strey et al. deuterated alcohol was used which barely change the phase boundaries. In this study however, the main surfactant was changed, resulting in a mayor shift of the phase boundaries (30 \rightarrow 55 °C, see previous paragraph).

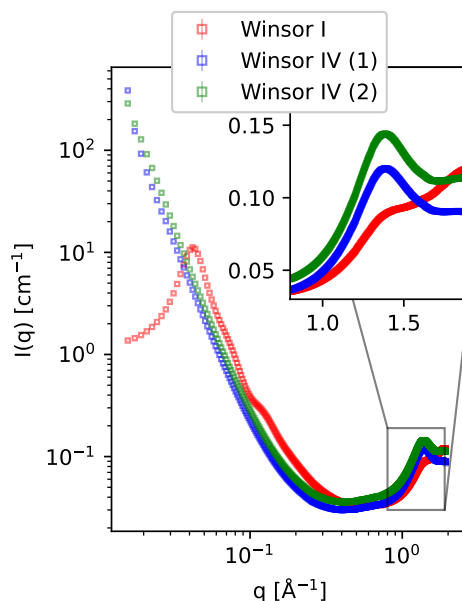


Figure 4.21: WAXS measurements of μ Es of RL and mono-disperse C₁₂E₄ in Winsor I (red) and Winsor IV (blue and green).

To further analyze the existence of domain-like structures, WAXS experiments were performed. Figure 4.21 displays the scattering curves of the Winsor I and IV phases. The scattering curves are similar to the SAXS and SANS scattering curves in the low q region as seen in the Figures 4.17 and 4.20. The curves exhibit a maximum at 1.45 \AA^{-1} which is more pronounced for the Winsor IV μ Es. This peak corresponds to a distance of 4.3 \AA which is hence a characteristic distance within the system. This distance could be a domain size or it could indicate intermolecular C $\cdot \cdot$ C or C $\cdot \cdot$ O interactions [267, 268]. The differences between the intensity of the peak at 1.45 \AA^{-1} in Winsor I and IV might be due to the different curvatures of the amphiphilic film, which are close to zero for Winsor IV.

The experimental and simulation results dealing with the structure of the μ E RL/C₁₂E₄/n-decane/water will next be discussed regarding the bulk structure, i.e. mainly the structuring of the oil and water domains, and the structure of the amphiphilic film, i.e. mainly the structuring of the interface.

4.4.2 Bulk Structure

Optical appearance, conductivity (Figure 4.12) and PGSE-NMR (Figure 4.16) provide evidence for the presence of Winsor I, II, IV or lamellar phases. Winsor I and II are

water or oil continuous media, in which oil or water droplets are dispersed, respectively. PGSE-NMR and SANS data show that the oil droplets in Winsor I have a radius of 10-50 and 55-67 Å (Figure A16 and Table A3 in the Appendix). It should be noted that the size from PGSE-NMR is only an estimate, whereas the SANS data are more reliable. The droplet size 55-67 Å indicates the presence of a μ E which are characterized by emulsion droplets with a radius between 50 and 500 Å [269].

Furthermore, the presence of the bicontinuous phase and lamellar is distinguished by optical appearance between two polarization filters (Figure 4.12 C), scattering and PGSE-NMR (Figure 4.16). PGSE-NMR shows that water and n-decane can move almost freely in the bicontinuous and lamellar phases. One reason is the orientation of the lamellae in the magnetic field (see Pake peak in Figure A15 in the Appendix). The SAXS data suggest that the maximum domain size d is 543 Å, e.g. measured from the water domain through the oil domain to the next water domain. The maximum domain size of μ Es C₁₂E₅/n-decane/water is 652 Å, and the one of C₁₀E₄/n-decane/water 309 Å [109]. Hence, it is difficult to conclude whether RL increases or decreases the domain size. The same applies to the persistence length ξ which is approximately half of the domain size, as reported in the literature [123].

The amphiphilicity factor f_a quantifies the amphiphilic strength of a surfactant system and hence characterizes the structuring of a formed μ E [270]. While $f_a = 1$ describes a disordered structure, $f_a = -1$ stands for an ordered structure [243]. Thus, the value of $f_a = -0.83$ for the μ E RL/C₁₂E₄/n-decane/water suggests a rather ordered structure and a flexible μ E. The value is below the wetting transition of -0.33, resulting in a non-wetting interface of the μ E of RL and C₁₂E₄. This non-wetting characteristic means that the microemulsion phase does not spread at the interface of the excess water and oil phases in Winsor III, but rather that the μ E middle phase forms lenses at the interface [270–272]. The μ E C₁₀E₄/n-decane/water has $f_a = -0.82$ and the one of C₁₂E₅/n-decane/water $f_a = -0.84$ [109]. Hence, the addition of RL to the μ E C₁₂E₄/n-decane/water exerts a negligible effect on the structuring degree of the bulk in μ Es.

4.4.3 Structure of the Amphiphilic Film

The structure of the amphiphilic film at the interface was modeled by MD simulations, SANS contrast variation and WAXS. Contrast variation via SANS indicate that RL is rather inserted into the amphiphilic film compared to C₁₂E₄ (Table 4.8). One reason could be a higher interface activity of RL compared to C₁₂E₄, as it has been shown by neutron reflectometry measurements of mono-RL/RL/C₁₂E₈/LAS systems [25]. This could be due to the monomeric solubility of C₁₂E₄ in n-decane which is ≈ 2.2 wt% [109, 263]. When C₁₂E₄ is solubilized in the bulk oil, less C₁₂E₄ molecules are available to adsorb at the interface. Since only ≈ 0.01 wt% of RL solubilizes in water (cmc), RL is probably enriched in the amphiphilic film.

The RL molecules form a thinner amphiphilic layer compared to the C₁₂E₄ molecules

(Figure 4.18, Figure 4.19 A and Table A3 in the Appendix). Furthermore, RL is rather located closer to the water and C₁₂E₄ closer to the oil, giving in a typical distance of 6 Å along the z-axis (Figure 4.19). Hence, RL and C₁₂E₄ are arranged according to the linker concept, where a more hydrophilic and a more hydrophobic amphiphilic molecule are mixed [206] and which have also been observed for the catanionic species with BSs. This arrangement of RL and C₁₂E₄ may be a reason why the fits of the RL and EO contrasts in the Winsor I scattering data (Table A3 in the Appendix) indicate a shorter chain length of the surfactant molecules than estimated by the Tanford formula.

The interactions between the RL and C₁₂E₄ molecules, both between their hydrophilic and hydrophobic parts, are weaker than the interactions within the same type of molecule, namely RL with RL and C₁₂E₄ with C₁₂E₄. This is particularly due to the strong interactions between the sugar beads of coarse-grained simulations (RL-B1 & RL-B1 curve in Figure 4.19). Therefore, the surfactant molecules interact with themselves rather than with each other, indicating antisnergistic interactions [239]. The affinity of RL to other sugar surfactants through hydrogen bonds has also been reported by Sottmann et al. [199]. One result of the antisnergistic interactions could be the formation of nanodomains which have been observed in the catanionic mixtures with BSs and in dissipative particle simulation [193]. In SANS experiments, the profiles of the film contrasts have an unusual shape, but a suitable fitting model is lacking (Figure 4.20). In addition, a peak corresponding to a distance of 4.3 Å were found in WAXS experiments (Figure 4.21). This peak could also indicate a domain formation, but it could also result from intermolecular C · · · C or C · · · O interactions [267, 268]. Although the formation of domains in membranes by natural lipids such as RL has been extensively discussed, its experimental validation remains challenging [195, 273]. In summary, indications for a nanoscopic phase separation due to carbohydrate interaction were also found at the interface of the RL/C₁₂E₄/n-decane/water μ E besides in the case of the catanionics species with BSs which has been already discussed.

4.5 Adsorption of Rhamnolipid and Ethoxylate

After having studied the phase behavior and structure of μ Es containing RL and ethoxylates, their adsorption to the air/water and oil/water interface will be assessed. Dynamic IFT measurements are a suitable method for monitoring adsorption processes at the interface. Since the adsorption to the air/water interface is the simpler case compared to the oil/water interface, e.g. due to partitioning phenomena, the former case will be assessed first.

4.5.1 Experiments

Adsorption to the Air/Water Interface

DST measurements were firstly performed by maximum bubble pressure whose data could be fitted with the equations according to Ward-Tordai or Rosen model (Equations 2.68 and 2.66) [135, 136]. With the maximum bubble pressure technique, it becomes also possible to analyze short time scales and to obtain numerical characteristics of the systems from different fits of the data.

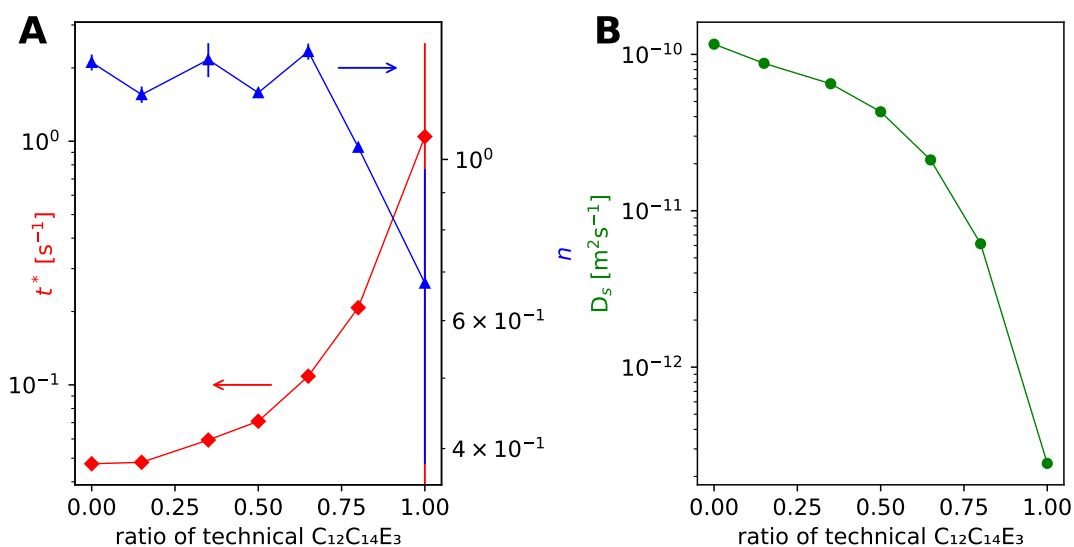


Figure 4.22: Rosen fit parameters t^* and n in A) and the effective diffusion coefficient in B) plotted as a function of the ratio of C₁₂C₁₄E₃ and RL from Table S3 at 22 °C calculated using the Equation 2.68. The raw data are displayed in Figure A19 A in the Appendix. Error bars are derived from the covariance of the nonlinear fit and lines just serve as a guide for the eye.

Figure A19 A in the Appendix shows the effect of the RL-ethoxylate ratio on the DST. At short time scales, the reduction of ST is higher at high ratios of RL. At meso-equilibrium, the ST is lower at low ratios of RL. The DST data was fitted with the Rosen equation (Equation 2.66, Table 4.9, Figure A21 in the Appendix). Looking more closely at the fitted parameters Figure 4.22 A, t^* (which is the time at which half of the total ST reduction has occurred) increases non-linearly with increasing ratio of the ethoxylate, whereas there is no trend in n . Since there is no significant variation in n , the shape of the curves look similar and t^* of the different systems can be compared. Pure RL takes only about 0.047 s to reach half of its total ST reduction, whereas pure technical C₁₂C₁₄E₃ takes about 1.04 s. Hence, the rate of the ST reduction can be accelerated by adding only small amounts of RL to C₁₂C₁₄E₃. This can also be seen if fitting the data with the Ward-Tordai equation

which is an approximation for short adsorption times (Equation 2.68 and Figure A23 in the Appendix). Table 4.9 and Figure 4.22 B show the fitted parameters. Figure 4.22 displays the effective diffusion coefficient D_s as a function of the RL ratio. It is seen that D_s increases non-linearly with an increasing RL content, in accordance with the decrease of t^* .

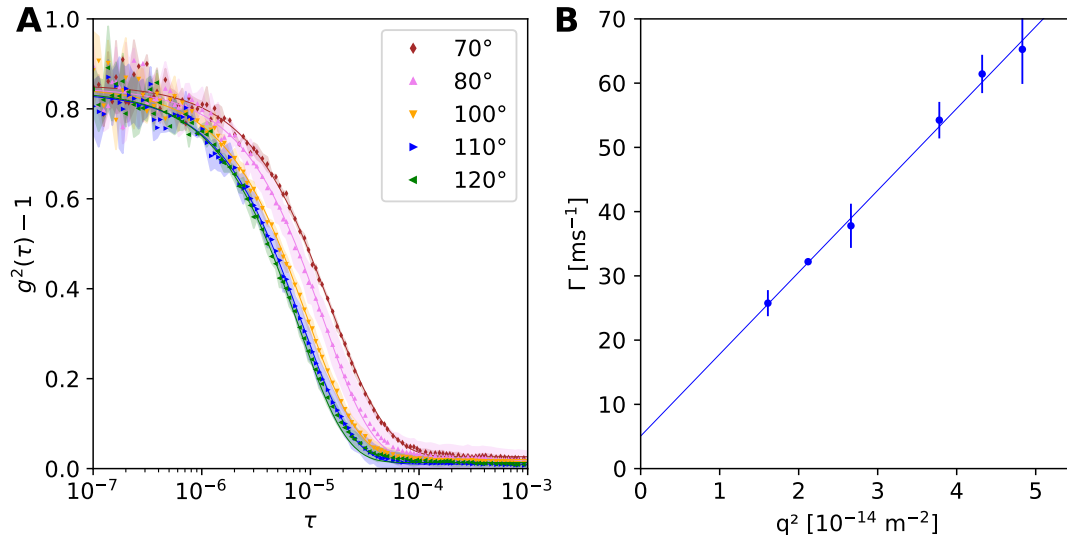


Figure 4.23: Dynamic light scattering measurement of 20 mM RL at different angles, pH 8 and 25 °C. A) displays the autocorrelation functions with the cumulant fit and B) shows the decay rate Γ for different scattering vectors $|\vec{q}| = q$.

In order to evaluate the magnitude of the apparent diffusion coefficient, angle-dependent DLS measurements were performed on RL at 20 mM, which is above the cmc of RL (Figure 4.8). The diffusion measured in DLS is mutual diffusion which occurs due to microscopic fluctuations in temperature and concentration [274]. As shown in Figure 4.23, the RL aggregates show rotational diffusion besides translational diffusion in the probed range of q . The reason is that the Γ vs. q^2 plot follows expected linear behavior with an intercept according to Equation 2.40. The translational diffusion coefficient is about $1.3 \cdot 10^{-10} \text{ m}^2 \text{ s}^{-1}$. Computing the van-der-Waals volume 634.89 \AA^3 of a single di-RL molecule with the software Chemicalize from ChemAxon (October 2022), the diffusion coefficient of RL monomers should be about $11 \cdot 10^{-10} \text{ m}^2 \text{ s}^{-1}$ according to the Stokes-Einstein Equation. With volume of RL 1052 \AA^3 determined by Chen et al., the diffusion coefficient of monomers is $9 \cdot 10^{-10} \text{ m}^2 \text{ s}^{-1}$ [10].

Table 4.9: Dynamic surface tension data fitted with the Rosen and the Ward-Tordai equations. The remaining percentage of the surfactant system is the one of RL. The raw data and corresponding fits are displayed in the Figures A19 and Figure A20 in the Appendix.

	y_m after 11 s	Rosen		Ward-Tordai					apparent D_{app} [m ² s ⁻¹]		R ²	
		t^* [s]	t^*_{err} [s]	n	n_{err}	$R_{1/2}$ [Nm ⁻¹ s ⁻¹]	amount	fit	points	apparent D_{app} [m ² s ⁻¹]	R ²	
RL	0.032	0.047	0.00025	1.36	0.034	1.07E+21	5		5	1.2E-10	1.7E-12	0.98
50% technical C12C4E2	0.026	0.10	0.0033	1.43	0.045	1.06E+07	8		8	2.3E-11	2.1E-13	0.91
15% technical C12C4E3	0.030	0.048	0.00032	1.23	0.032	1.17E+16	5		5	8.8E-11	4.9E-13	0.97
35% technical C12C4E3	0.027	0.059	0.0017	1.37	0.074	2.89E+06	6		6	6.5E-11	3.3E-13	0.94
50% technical C12C4E3	0.026	0.071	0.00073	1.24	0.018	7.03E+02	7		7	4.3E-11	3.0E-34	0.93
65% technical C12C4E3	0.026	0.11	0.0032	1.41	0.036	6.92	9		9	2.1E-11	7.9E-14	0.93
80% technical C12C4E3	0.026	0.21	0.0029	1.04	0.0086	2.90E-02	10		10	6.2E-12	7.6E-14	0.96
100% technical C12C4E3	0.029	1.04	1.48	0.68	0.29	34.12	15		15	2.4E-13	1.5E-15	0.95
50% technical C12C4E4	0.028	0.07	0.0014	1.164	0.034	1.77E+03	6		6	4.8E-11	1.7E-13	0.96
50% pure C12E4	0.029	0.042	0.00017	1.31	0.033	4.67E+05	5		5	7.3E-11	1.8E-12	0.97
50% narrow-range C12C4E3	0.027	0.12	0.0070	1.60	0.082	6.25E+01	10		10	2.1E-11	1.3E-13	0.91
45% pure C12E4, 5% C12E3	0.029	0.047	0.00013	1.28	0.015	4.03E+05	5		5	6.3E-11	4.5E-13	0.99
45% pure C12E4, 5% C12E3	0.030	0.043	0.00010	1.28	0.016	4.03E+07	5		5	6.7E-11	1.7E-13	0.98
40% pure C12E4, 10% C12E5	0.029	0.047	0.00018	1.23	0.020	1.06E+07	5		5	6.2E-11	4.9E-13	0.98
30% pure C12E4, 20% C12E5	0.030	0.042	3.67E-05	1.21	0.0084	1.36E+05	5		5	7.8E-11	7.6E-13	0.95
45% pure C12E4, 5% C12E7	0.030	0.038	2.22E-05	1.16	0.039	6.52E+07	4		4	6.0E-11	3.9E-34	0.94
40% pure C12E4, 10% C12OH	0.027	0.054	0.00055	1.28	0.031	4.43E+11	5		5	5.8E-11	2.0E-13	0.97
30% pure C12E4, 20% C12OH	0.025	0.059	0.0010	1.38	0.046	1.11E+06	7		7	4.4E-11	3.2E-13	0.94

Additionally, the effect of the technical homologue ethoxylates C₁₂C₁₄E₂₋₄ was analyzed (Table 4.9 and Figure A19 B in the Appendix). The initial adsorption of C₁₂C₁₄E₂ is slower than the one of C₁₂C₁₄E₃ and C₁₂C₁₄E₄, seen in the higher ST at short time scales. E.g., the difference of the ST between 50% C₁₂C₁₄E₂ and C₁₂C₁₄E₄ is 5.4 ± 1.0 mN/m at 40 ms. At longer time scales, the ST at meso-equilibrium decreases with lower ethoxylation degree. E.g., the difference of the ST between 50% C₁₂C₁₄E₂ and C₁₂C₁₄E₄ is 1.6 ± 0.3 mN/m at 30 s.

Next, the effect of the mixture of the technical ethoxylate has been studied. Displayed in Figure A19 C in the Appendix, mono-disperse C₁₂E₄ shows a lower ST than the technical variant at short times. However, the narrow-range ethoxylate shows the lowest initial adsorption rate in our experiments.

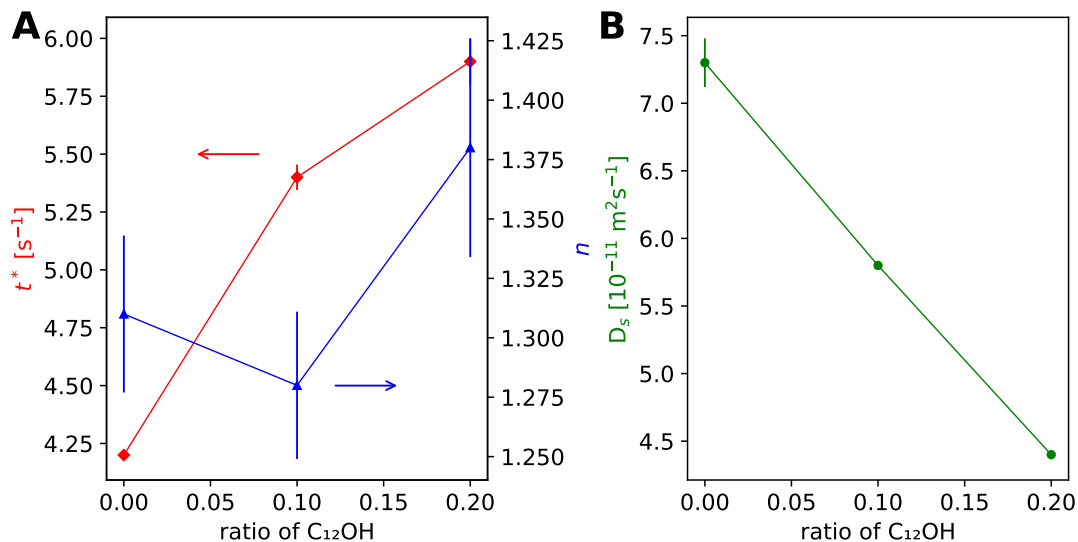


Figure 4.24: Rosen fit parameters t^* and n in A) and effective diffusion coefficient in B) plotted as a function of the ratio of C₁₂OH and C₁₂E₄. The raw data is displayed in Figure A20 A in the Appendix. Error bars are derived from the covariance of the nonlinear fit and lines just serve as a guide for the eye.

To understand the differences of adsorption kinetics between mono-disperse and technical ethoxylates in mixtures with RL, the effects of different components were assessed, beginning with the effect of the fatty alcohol (Table 4.9 and Figure A20 A in the Appendix). A partial replacement of C₁₂E₄ by C₁₂OH results in higher ST at low time scales. Looking at the fit parameters t^* , n and D_s in Figure 4.24, it can be concluded that the adsorption becomes slower with a partial replacement by dodecanol. The ST at meso-equilibrium decreases with partial replacement of C₁₂OH.

Lastly, the effect of the partial replacement of C₁₂E₄ by ethoxylates having a higher or lower ethoxylation degree was analyzed (Table 4.9 and Figures A20 B and C in the Appendix). The effect of the ethoxylation degree on the ST seems to be minor since it is very difficult to see differences. Therefore, no clear effects on the adsorption at the air/water interface can be concluded (Figures A24, A25 and A26 in the Appendix). This is also the case for the technical substances C₁₂C₁₄E_{3,4} (Figure A19 in the Appendix). C₁₂C₁₄E₂ contains a higher amount of C₁₂C₁₄OH which result in the slower adsorption rate. The number of ethoxylation groups does also influence the ST at meso-equilibrium to a minor extend. The ST at meso-equilibrium increases slightly with a higher number of ethoxylation group. Hence, the higher initial ST and lower ST at meso-equilibrium of the technical ethoxylate compared to the mono-disperse one is mainly due to the presence of fatty alcohol in the technical substance.

Adsorption to the Oil/Water Interface

Since applications often involve oil, the adsorption to the oil/water interface was examined. Compared to the air/water interface, monitoring adsorption processes at the oil/water interface are overlaid by other processes as interactions of surfactants with the oil, partitioning effects, and competitive adsorption of the surfactant and the oil at the interface [226].

The IFT of a variety of ethoxylate/RL mixtures at the n-decane/water interface after one minute and one hour are presented in Table 4.10 (raw data in Figure A27 in the Appendix). Whereas pure RL reaches low IFT after a short time, pure C₁₂C₁₄E₃ needs a very long time to lower the IFT to a specific amount. However, C₁₂C₁₄E₃ reaches a relatively low IFT (Figure A27 A in the Appendix). When RL and C₁₂C₁₄E₃ are combined in different mass ratios, the IFT is lower at high levels of RL on short times. In the long term, however, the IFT is lower at high ethoxylate levels (Table 4.10 and Figure A27 B in the Appendix). Next, the effect of the average number of ethoxy groups in technical ethoxylates was analyzed. As the number of ethoxy groups increases, the initial adsorption rate increases on short time scales (Table 4.10 and Figure A27 C in the Appendix).

Furthermore, the differences between mono-disperse ethoxylates and technical ones with a similar average degree of ethoxylation were investigated. At short times, the order of the rate of IFT reduction is broad-range C₁₂C₁₄E_{3,4} > mono-disperse C₁₂E₄ > narrow-range C₁₂C₁₄E₃. At long times, it appears that the IFT of the mono-disperse C₁₂E₄ leads to lower meso-equilibrium IFT (Table 4.10 and Figure A27 D in the Appendix).

In order to understand the differences between technical and mono-disperse ethoxylates in combination with RL, the effect of each component was analyzed and hence, the technical variants were mimicked by well-defined mixtures of mono-disperse species. Therefore, C₁₂E₄ was partially replaced by other components in the 50% C₁₂E₄ and 50% RL mixture (composition of ethoxylates displayed in Figure 3.1).

Table 4.10: Interfacial tension of analyzed samples by spinning drop after 1 min and 1 h. The remaining percentage of the surfactant system is the one of RL. The raw data and corresponding fits are displayed in the Figures A27 and Figure A28 in the Appendix.

system	γ_m after 1 min [mN/m]	γ_m after 1 h [mN/m]
RL	4.2	4.0
50% technical C₁₂C₁₄E₂	5.4	3.8
15% technical C₁₂C₁₄E₃	4.4	3.7
35% technical C₁₂C₁₄E₃	4.7	3.4
50% technical C₁₂C₁₄E₃	5.2	3.1
65% technical C₁₂C₁₄E₃	5.8	3.1
80% technical C₁₂C₁₄E₃	7.3	2.6
100% technical C₁₂C₁₄E₃	3.9	0.066
50% technical C₁₂C₁₄E₄	4.9	3.2
50% pure C₁₂E₄	5.3	2.5
50% narrow-range C₁₂C₁₄E₃	6,4	3,5
45% pure C₁₂E₄, 5% C₁₂E₃	5.0	2.7
45% pure C₁₂E₄, 5% C₁₂E₅	4.9	2.1
40% pure C₁₂E₄, 10% C₁₂E₅	5.0	2.0
30% pure C₁₂E₄, 20% C₁₂E₅	4.9	2.0
45% pure C₁₂E₄, 5% C₁₂E₇	5.5	2.7
40% pure C₁₂E₄, 10% C₁₂OH	5.3	2.9
30% pure C₁₂E₄, 20% C₁₂OH	5.4	3.9

Starting with the effect of fatty alcohol, 10% and 20% C₁₂E₄ were replaced by C₁₂OH. Table 4.10 and Figure A28 A in the Appendix show that C₁₂OH mainly affects the IFT on longer time scales where C₁₂OH increases the IFT.

Next, the effect of different ethoxylation degrees was investigated. Therefore, 10% C₁₂E₄ in 50% RL & 50% C₁₂E₄ mixture were replaced by C₁₂E₅, so that the mixture contained 50% RL & 40% C₁₂E₄ & 10% C₁₂E₅ (Table 4.10 and Figure A28 B. With increasing content of C₁₂E₅, the initial IFT decreases. Thus, lower IFTs are achieved at shorter time scales which is also true for replacing C₁₂E₄ with C₁₂E₇ (Table 4.10 and Figure A28 C). However, when C₁₂E₄ with C₁₂E₃, the initial IFT is lower.

4.5.2 Effect of RL on the Adsorption of Ethoxylates

RL reduces the IFT less effectively than the ethoxylate at both the oil/water and air/water interface. Comparing these results with the literature, Liu et al. found different results by analyzing the dynamic IFT of 1 wt% alcohol polyoxyethylene carboxylate and C₁₂E₃. The combination of the carboxylate and C₁₂E₃ resulted in an overall decrease in IFT for all combinations compared to the pure components [275]. In another study, LAS was also tested with narrow-range C₁₂C₁₄E₃ by Zimoch et al. The addition of LAS to the ethoxylate resulted in similar IFT curves as ours, but LAS had a stronger effect at small additions than the RL [276]. This suggests that the RL acts more like LAS than the carboxylate surfactant, which is surprising since RL contains carboxylate group.

Furthermore, small additions of RL significantly increase the initial adsorption rate of the mixtures with C₁₂C₁₄E₃ at both interfaces. This is unexpected because the ionic surfactant RL may lead to an electrostatic adsorption barrier, which would hinder the adsorption [234]. Therefore, the reason for the faster adsorption with high amounts of RL remains unclear. However, as previously discussed, the RL exhibits only a weak ionic character and has a tendency to form domains. This could result in cooperative adsorption, where the probability of an RL molecule to adsorb next to another RL molecule is enhanced, or the domains might adsorb as a whole. Similar results were reported for a gemini sulfonate surfactant and alkyl polyglycoside [277]. For combinations of sodium dodecylsulfonate & C₁₂E₅, the initial adsorption rate was higher at high ratios of the C₁₂E₅. However, the latter worked at very low surfactant concentrations below the cmc [278].

4.5.3 Type of Diffusion

The apparent diffusion coefficient of RL observed in the DST measurements is $1.4 \cdot 10^{-10} \text{ m}^2 \text{ s}^{-1}$, which is similar to the micellar diffusion coefficient $1.3 \cdot 10^{-10} \text{ m}^2 \text{ s}^{-1}$ in DLS and quite different from the computed diffusion coefficient of monomers $9 \cdot 10^{-10} \text{ m}^2 \text{ s}^{-1}$. Thus, the mutual diffusion flux seems to be mainly dominated by micelles rather than by monomers. This contradicts the standard model of the adsorption process. In this standard model, only monomers adsorb at the interface so that micelles must release monomers or dissolve

in monomers before adsorbing at interfaces [279, 280] . However, other authors already have found indications that micelles adsorb at interfaces (sublayers) by diffusion [281, 282]. Colegate and Bain showed that micelles of C₁₄E₈ adsorb to the air/water interface, that this stops when small amounts of cationic surfactants are added, and that it starts again when small amounts of electrolyte are added. The authors estimated and concluded that the micellar adsorption only occurs in the absence of an electrostatic barrier at the interface [281]. Considering the plots in Figure A23 and A24, our DST data does not show the presence of an electrostatic barrier since the data can be fitted with the Ward-Tordai equation (Equation 2.68) if the Ward Tordai model is applicable. This would imply that the addition of RL does not result in an electrostatic barrier, so that the RL rather acts as a nonionic surfactant which has already been reported in literature and discussed before [11, 283] . However, a consistent model for the adsorption at interfaces of micellar solutions is still lacking and it is unknown whether micelles adsorb at interfaces or if micelles dissociate very close to interfaces [284].

4.5.4 Effect of Ethoxylation Degree

As the number of ethoxy groups increases, the initial adsorption rate increases on short time scales. This was also found by Liu et al. with nonylphenol polyethylene oxide sulfonates [285]. Catanoiu et al. measured the partition coefficients of different ethoxylates and found that the partitioning coefficient of mono-dispersed ethoxylates into the oil decreases with an increasing number of ethoxy groups [286]. Hence, one possible explanation for slow adsorption kinetics of low ethoxylated surfactants is that they may partition into the oil without adsorbing at the interface. Another point is that micellar kinetics may play a role. Hydrophobic ethoxylates have longer relaxation times, resulting in a slower release of monomers, which can diffuse faster than micelles due to their size [287]. Furthermore, the cmcs of the substances must be taken into account. It has been found that the cmc increases with the ethoxylation degree (Table 3.1). A higher cmc means a higher concentration of the fast monomers.

4.5.5 Effect of Technical Ethoxylates

Mixtures of RL and technical ethoxylates showed a faster adsorption at short times and higher IFTs in equilibrium at the oil/water interface than mixtures of RL and pure ethoxylates, while the opposite is true for the air/water interface. When studying the effect of each component of the technical ethoxylates on the adsorption kinetics, C₁₂OH was found to increase the IFT at the oil/water interface and decrease the ST at the air/water interface at long times (Tables 4.10 and 4.9 and Figures A28 A and 4.24 A in the Appendix). In fact, the higher initial ST and lower ST at meso-equilibrium of the technical ethoxylate compared to the mono-disperse one is mainly due to the presence of fatty alcohol in the technical substance. One explanation is that C₁₂OH partitions in the

oil due to its hydrophobicity which reduces the amount of surface-active components available at the interface which leads to a less effective reduction of IFT at the oil/water interface. As this is not possible for a water/air surface, the very surface-active C₁₂OH lowers the ST on a long time scale. Staples et al. demonstrated the preferential adsorption of particularly C₁₂OH in SDS/C₁₂E₅ and C₁₂E₈/C₁₂E₅ mixtures by neutron reflectometry [288], while Samanta and Gosh showed that butanol and hexanol decreased the ST of Tween-surfactants [289]. The partitioning appears to be a rather slow process, as deviations of the IFT curves with and without alcohol can only be distinguished on longer time scales. This shows that partitioning effects must be considered as this has been recently demonstrated by Acosta and Natali in case of phase behavior studies of ethoxylates with different ethoxylation degrees [102]. The slow adsorption kinetics of C₁₂OH may also be due to the decrease of the cmc in presence of long-chained alcohol [290]. Moreover, Patist et al. showed that 1-dodecanol increased the micellar lifetime of sodium dodecyl sulfate (SDS) [291].

The higher ethoxylated compounds were found to accelerate the adsorption kinetics (Table 4.10 and Figures A28 B and C in the Appendix). One explanation may be that the increasing the degree of ethoxylation results in a high cmc (Table 3.1) which is why a more of monomers are present to adsorb rapidly at the interface. In conclusion, hydrophobic components appear to diffuse more slowly from the bulk to the subsurface or segregate into the oil as a consequence of their lower monomeric concentration, their higher solubility in oil and their slower release from micelles [287]. Therefore, they reduce the IFT less effectively and efficiently than the analyzed hydrophilic components. Overall, the equilibrium setting at the interface can be seen as a superposition of adsorption and partitioning equilibria.

4.5.6 Effect of the Ethoxylate's Polydispersity

Mono-disperse C₁₂E₄ shows a lower ST than the technical variant at short times. Contradictory results have been found by Jeong et al. who analyzed C₁₂E₇ of different polydispersities [292]. They found that the more mono-disperse the C₁₂E₇, the smaller is the effective diffusion coefficient. However, our results can be understood by looking at the micellar relaxation time constant τ_2 which describes a characteristic time for a micelle of a specific surfactant species to form and disintegrate. Patist et al. showed that τ_2 of technical C₁₂E₇ (150 s) is significantly higher than the one of mono-disperse C₁₂E₅ (10 s) and C₁₂E₈ (4 s), presumably due to the high content of fatty alcohol [291]. However, the narrow-range ethoxylate shows the lowest initial adsorption rate in our experiments. This difference could be explained by the composition of the narrow-range ethoxylate displayed in Figure 3.1 C. Due to a higher proportion of the C₁₄, the micelles of C₁₄ may have a longer lifetime τ_2 and the cmc is lower resulting in a lower monomer concentration that can diffuse to the interface. The meso-equilibrium ST is higher, the more mono-disperse the ethoxylate is which is in agreement with the results found by

Dillan at the same concentration [293].

Chapter 5

Conclusion and Outlook

Despite the broad literature of microbial biosurfactants, their structure-property relationship is not clear. One reason is the structural complexity of these biosurfactants, which often contain sugar groups and anionic charges in a gemini- or bola-shaped form. It has been reported that explanations and theories for conventional surfactants are inadequate for microbial biosurfactants [8]. To find new explanations and theories, a physico-chemical deep dive is needed.

This is why the phase behavior of biosurfactants has been the subject of analysis in this thesis. Extensive research has already been conducted into the phase behavior of binary systems of biosurfactants in water [14]. Consequently, the biosurfactants were combined with other surfactants in water and in microemulsions with oil. This motivation is substantiated by the fact that products mostly contain mixtures of surfactants. Hence, the analysis of surfactant mixtures and microemulsions is a powerful tool for understanding the behavior of biosurfactants and it is also important for the potential application of biosurfactants in technical green formulations. Such a study of surfactant mixtures with biosurfactants has not been carried out in a systematic way previously, thus representing a significant gap in the existing literature. To fill this gap, the following methods were employed: pulsed-gradient spin-echo nuclear magnetic resonance (PGSE-NMR), dynamic and electrophoretic light scattering (DLS), small- and wide-angle X-ray scattering (SAXS, WAXS), small-angle neutron scattering (SANS), molecular dynamics simulation (MD), optical observation, conductivity, and polarization microscope for determining the structure and spinning drop, maximum bubble pressure, and Du Noüy ring tensiometry for studying the adsorption behavior.

In order to pursue a systematic approach, the anionic biosurfactants rhamnolipid and sophorolipid were combined with model cationic surfactants on the one hand, and with model nonionic surfactants on the other hand. The cationic surfactants employed in this study are cetyl trimethylammonium bromide (CTAB) and hydroxyethyl lauryldimethylammonium chloride (HELDAC). These cationic surfactants differ in terms of their hydrophilicity and counter ion. In order to provide a model for nonionic surfactants,

ethoxylates were employed, with the hydrophilicity of these systematically varied. One unresolved question in the scientific community is whether the anionic surfactants rhamnolipid and sophorolipid behave rather as an anionic or nonionic surfactant. The experiments conducted demonstrate that rhamnolipid and sophorolipid possess both anionic and nonionic characteristics. For example, the interaction parameter of catanionics with biosurfactants falls between those typical of catanionic and ionic-nonionic surfactant systems. One potential reason for the question of whether these biosurfactants are ionic or nonionic in nature may be attributed to the presence of a second flexible sugar group in biosurfactants, which may act as a shield towards the anionic carboxylic group [18]. Hence, rhamnolipid and sophorolipid do not behave as either ionic or nonionic surfactant, but rather exhibit characteristics of both categories, depending on the measurement technique employed.

Moreover, it was found that the biosurfactants possess a membrane lipid-like character that coexists with their well-known surfactant properties. One illustration of this membrane-like character is presumably a nanoscopic phase separation into more ordered and more disordered domains. The nanoscopic phase separation has initially been observed in molecular dynamics simulations and in contrast matching small-angle neutron scattering for one sample. Nevertheless, further indications were obtained through the utilization of pulsed-gradient spin-echo nuclear magnetic resonance and small-angle and wide-angle X-ray scattering experiments. The nanoscopic phase separation may result from the formation of hydrogen bonds between the sugar groups of the biosurfactants, which lead to a pronounced structure factor in scattering profiles and high correlations of the sugar groups.

The origin of this nanoscopic phase separation may be the antisynnergistic interaction of biosurfactants and other surfactants. The presence of strong carbohydrate interactions between the biosurfactants could result in a preferential interaction of biosurfactants with themselves.

In addition, it can be hypothesized that the sugar groups are responsible for the lack of precipitation and vesicle formation when anionic and cationic surfactants are combined. The hydrophilic nature and bulkiness of the sugar groups of biosurfactants permit the packing parameter to remain within the micellar regime.

For achieving an amphiphilic film with a zero curvature, biosurfactants should be combined with other surfactants that increase the packing parameter and thereby decrease the curvature of the amphiphilic film. Such surfactants may include hydrophobic ethoxylates or cationic surfactants.

Catanionic mixtures with rhamnolipid ratios approaching equimolarity tend to form elliptical micelles. The efficacy of the elliptical micelles in emulsifying oil has also been proven to be superior to that of the spherical micelles. It can be reasonably deduced that the presence of a greater number of surfactant molecules within a single micelle enables the micelle to expand in size upon the uptake of oil. Unlike spherical micelles, there is

no need to incorporate additional surfactant molecules upon swelling. In addition to the elliptical configuration of the rhamnolipid mixtures, the combination of rhamnolipids with other surfactants results in low interfacial tensions with n-decane.

The interfacial tensions of sophorolipid mixtures are higher, the adsorption kinetics are slower, and their efficacy in emulsifying oil is lower. The micelles are spherical in shape, with a diameter that is approximately equivalent to that of a single sophorolipid molecule. This can be attributed to the stretched conformation of the sophorolipid molecule within the micelle, along with its "U"-shaped form at the interface, which is typical of bola-amphiphiles. Furthermore, sophorolipid has been found to be incapable of incorporating oil into its micelles, a property presumably attributable to its bola-like shape, which functions as a bridge between opposite sides of the micelles, thereby impeding their swelling. Consequently, sophorolipids are not well-suited for the purpose of oil removal. At the interface, the biosurfactants were observed to be oriented more towards the aqueous phase, while the second surfactants are oriented towards the oil phase, resulting in a linker-like positioning, which has shown to be favorable for oil removal [206].

As anticipated, the surfactant mixtures demonstrated enhanced surface activity relative to the pure (bio)surfactants. This was evidenced by a reduction in critical micelle concentration and interfacial tension against air and oil, indicative of synergistic effects. The surfactant mixture of rhamnolipid and ethoxylate was observed to facilitate the formation of structured microemulsions with n-decane as the oil at 30 °C. It was determined that the optimal formulation of these microemulsions involved the use of mono-disperse C₁₂E₂, C₁₂E₃ and C₁₂E₄ as ethoxylates. These hydrophobic ethoxylates appear to be essential for reducing the high curvature of the amphiphilic layer formed by the hydrophilic rhamnolipid. The effect of rhamnolipid on the efficiency of ethoxylate/oil/water microemulsions is likely to be minor. In contrast, the effect of rhamnolipid to the adsorption characteristics of ethoxylates was found to be strong, in the way that rhamnolipid increased the adsorption kinetics and also the equilibrium interfacial tension non-linearly with increasing rhamnolipid/ethoxylate ratio. However, the investigated microemulsions comprising rhamnolipid and ethoxylates are, to the best of my knowledge, the most effective microemulsions containing a sugar surfactant including alkyl polyglycoside [45, 50, 247]. A technical ethoxylate with a certain average ethoxylation degree behaves more hydrophilic than a mono-disperse ethoxylate with the same average ethoxylation degree. Hence, the more hydrophilic components, which are high ethoxylated species, exert a dominant effect, resulting in a change in phase behavior and in a reduction in interfacial tension. The reason is presumably a partitioning of the hydrophobic components, which are low ethoxylated species and fatty alcohol, into the oil phase, which is particularly evident when comparing the air/water surface with the oil/water interface. This partitioning of the hydrophobic amphiphilic species made them unavailable at the interface, leading to an increase of the interfacial tension of oil/water. In conclusion, the work represents a significant advancement in our understanding of the class of biosurfactants and the

establishment of a structure-function relationship.

Nevertheless, further research is required to substantiate the nanoscopic phase separation found in this thesis and to understand its practical implications. This has already proven to be a significant challenge for those working in the field of membrane science, particularly in relation to the study of rafts [196, 273]. Nevertheless, contrast matching with neutrons has been demonstrated to be an effective approach. In lieu of small-angle neutron scattering, neutron diffraction experiments may cover a different q -range. Furthermore, acetylated biosurfactants could be employed to examine the influence of hydrogen bonds in conjunction with the nanoscopic phase separation. An additional avenue for exploration is the investigation of other sugar-containing surfactants, such as alkyl polyglycoside, together with conventional surfactants or mixtures of biosurfactants with other secondary surfactants. Furthermore, the nonionic biosurfactant mannosylerythritol lipid could be included in mixtures with ionic surfactants.

To gain further insights into the adsorption and phase behavior of microemulsions, it would be beneficial to determine partitioning coefficients for *n*-decane at 25 or 30 °C. This could contribute to a more comprehensive understanding of the adsorption of surfactant systems containing biosurfactants, as well as the analysis of micelle relaxation times. Furthermore, a consistent explanation why an adsorption barrier is observed for the catanionic mixtures but not for the pure ionic surfactants is lacking; despite the belief that an adsorbed layer of ionic surfactants should exhibit an electrostatic barrier. In addition, the contribution of micelles to the adsorption flux at interfaces remains unclear. This thesis, among others, has demonstrated indications for a micellar contribution to the monomer flux, but a systematic study is lacking.

In conclusion, further investigation of multi-component systems containing biosurfactants is required, given that surfactant mixtures revealed to be more efficient in practical applications. The identification and comprehension of the synergistic effects of biosurfactants with other surfactants, with the objective of establishing a linkage between oil and water [294, 295], will facilitate a social transformation towards circular economy.

Bibliography

- (1) Rockström, J.; Gupta, J.; Qin, D.; Lade, S. J.; Abrams, J. F.; Andersen, L. S.; Armstrong McKay, D. I.; Bai, X.; Bala, G.; Bunn, S. E., et al. *Nature* **2023**, *619*, 102–111.
- (2) Rounce, D. R.; Hock, R.; Maussion, F.; Hugonnet, R.; Kochtitzky, W.; Huss, M.; Berthier, E.; Brinkerhoff, D.; Compagno, L.; Copland, L., et al. *Science* **2023**, *379*, 78–83.
- (3) Hoffmann, H.; Ebert, G. *Angewandte Chemie* **1988**, *100*, 933–944.
- (4) Anastas, P.; Eghbali, N. *Chemical Society Reviews* **2010**, *39*, 301–312.
- (5) Georgiou, G.; Lin, S.-C.; Sharma, M. M. *Nature Biotechnology* **1992**, *10*, 60–65.
- (6) Bjerk, T. R.; Severino, P.; Jain, S.; Marques, C.; Silva, A. M.; Pashirova, T.; Souto, E. B. *Bioengineering* **2021**, *8*, 115–132.
- (7) Li, N.; Shen, H.; Wu, S.; Potanin, A.; Lee, J. *Journal of Surfactants and Detergents* **2024**, *27*, 963–975.
- (8) Baccile, N. *Current Opinion in Colloid & Interface Science* **2023**, 101747.
- (9) Esposito, R.; Speciale, I.; De Castro, C.; D’Errico, G.; Russo Krauss, I. *International Journal of Molecular Sciences* **2023**, *24*, 5395.
- (10) Chen, M.; Penfold, J.; Thomas, R.; Smyth, T.; Perfumo, A.; Marchant, R.; Banat, I.; Stevenson, P.; Parry, A.; Tucker, I., et al. *Langmuir* **2010**, *26*, 18281–18292.
- (11) Chen, M.; Penfold, J.; Thomas, R.; Smyth, T.; Perfumo, A.; Marchant, R.; Banat, I.; Stevenson, P.; Parry, A.; Tucker, I., et al. *Langmuir* **2010**, *26*, 17958–17968.
- (12) Liley, J.; Penfold, J.; Thomas, R.; Tucker, I.; Petkov, J.; Stevenson, P.; Banat, I.; Marchant, R.; Rudden, M.; Terry, A., et al. *Journal of Colloid and Interface Science* **2017**, *487*, 493–503.
- (13) Penfold, J.; Chen, M.; Thomas, R. K.; Dong, C.; Smyth, T. J.; Perfumo, A.; Marchant, R.; Banat, I. M.; Stevenson, P.; Parry, A., et al. *Langmuir* **2011**, *27*, 8867–8877.

- (14) Baccile, N.; Seyrig, C.; Poirier, A.; Alonso-de Castro, S.; Roelants, S. L.; Abel, S. *Green Chemistry* **2021**, *23*, 3842–3944.
- (15) Ishigami, Y.; Osman, M.; Nakahara, H.; Sano, Y.; Ishiguro, R.; Matsumoto, M. *Colloids and Surfaces B: Biointerfaces* **1995**, *4*, 341–348.
- (16) Birnbach, J.; Schmiedel, P.; Karg, M. *Current Opinion in Colloid & Interface Science* **2023**, *68*, 101765.
- (17) Morita, T.; Ishibashi, Y.; Fukuoka, T.; Imura, T.; Sakai, H.; Abe, M.; Kitamoto, D. *Bioscience, Biotechnology, and Biochemistry* **2011**, *75*, 1597–1599.
- (18) Luft, C. M.; Munusamy, E.; Pemberton, J. E.; Schwartz, S. D. *The Journal of Physical Chemistry B* **2020**, *124*, 814–827.
- (19) Palos Pacheco, R.; Kegel, L. L.; Pemberton, J. E. *The Journal of Physical Chemistry B* **2021**, *125*, 13585–13596.
- (20) Saci, F.; Roelants, S. L.; Soetaert, W.; Baccile, N.; Davidson, P. *Langmuir* **2022**, *38*, 8564–8574.
- (21) Dhar, P.; Thornhill, M.; Roelants, S.; Soetaert, W.; Chernyshova, I. V.; Kota, H. R. *Minerals Engineering* **2021**, *174*, 107270.
- (22) Esposito, R.; Ingenito, L.; Cavasso, D.; Siciliano, A.; Alfieri, M. L.; Chiappisi, L.; Fragneto, G.; Ottaviani, M. F.; Guida, M.; Paduano, L., et al. *Journal of Molecular Liquids* **2022**, *367*, 120547.
- (23) Xu, L.; Amin, S. *International Journal of Cosmetic Science* **2019**, *41*, 364–370.
- (24) Liley, J. R.; Thomas, R. K.; Penfold, J.; Tucker, I. M.; Petkov, J. T.; Stevenson, P. S.; Banat, I. M.; Marchant, R.; Rudden, M.; Webster, J. R. *Langmuir* **2017**, *33*, 13027–13039.
- (25) Liley, J.; Penfold, J.; Thomas, R. K.; Tucker, I.; Petkov, J.; Stevenson, P.; Banat, I.; Marchant, R.; Rudden, M.; Webster, J. *Journal of Colloid and Interface Science* **2019**, *534*, 64–71.
- (26) Luft, C. M.; Munusamy, E.; Pemberton, J. E.; Schwartz, S. D. *The Journal of Physical Chemistry B* **2018**, *122*, 3944–3952.
- (27) Rekiel, E.; Zdziennicka, A.; Szymczyk, K.; Jańczuk, B. *Molecules* **2022**, *27*, 3600–3621.
- (28) Rekiel, E.; Zdziennicka, A.; Szymczyk, K.; Jańczuk, B. *Molecules* **2022**, *27*, 4706–4728.
- (29) Esposito, R.; Gallucci, N.; Niccoli, M.; Cavalcanti, L. P.; Krauss, I. R.; Paduano, L.; D'Errico, G. *Colloids and Surfaces A: Physicochemical and Engineering Aspects* **2023**, 131931.

- (30) Mei, Q.-X.; Lai, L.; Li, S.-J.; Mei, P.; Wang, Y.-Q.; Ma, Q.-L.; Liu, Y. *Journal of Molecular Liquids* **2019**, *281*, 506–516.
- (31) Song, D.; Li, Y.; Liang, S.; Wang, J. *Colloids and Surfaces A: Physicochemical and Engineering Aspects* **2013**, *436*, 201–206.
- (32) Chen, M.; Dong, C.; Penfold, J.; Thomas, R. K.; Smyth, T. J.; Perfumo, A.; Marchant, R.; Banat, I. M.; Stevenson, P.; Parry, A., et al. *Langmuir* **2011**, *27*, 8854–8866.
- (33) Nguyen, B. V.; Nagakubo, T.; Toyofuku, M.; Nomura, N.; Utada, A. S. *Langmuir* **2020**, *36*, 6411–6420.
- (34) Bao, Q.; Huang, L.; Xiu, J.; Yi, L.; Ma, Y. *Ecotoxicology and Environmental Safety* **2021**, *212*, 111964.
- (35) Shah, M. U. H.; Moniruzzaman, M.; Sivapragasam, M.; Talukder, M. M. R.; Yusup, S. B.; Goto, M. *Journal of Molecular Liquids* **2019**, *280*, 111–119.
- (36) Onaizi, S. A.; Alsulaimani, M.; Al-Sakkaf, M. K.; Bahadi, S. A.; Mahmoud, M.; Alshami, A. *Journal of Petroleum Science and Engineering* **2021**, *198*, 108173.
- (37) Al-Sakkaf, M. K.; Onaizi, S. A. *Fuel* **2022**, *307*, 121845.
- (38) Munusamy, E.; Luft, C. M.; Pemberton, J. E.; Schwartz, S. D. *The Journal of Physical Chemistry B* **2018**, *122*, 6403–6416.
- (39) Wu, L.-m.; Lai, L.; Lu, Q.; Mei, P.; Wang, Y.-q.; Cheng, L.; Liu, Y. *Colloids and Surfaces B: Biointerfaces* **2019**, *181*, 593–601.
- (40) Nguyen, T. T.; Youssef, N. H.; McInerney, M. J.; Sabatini, D. A. *Water Research* **2008**, *42*, 1735–1743.
- (41) Kariyawasam, T.; Prenzler, P. D.; Howitt, J. A.; Doran, G. S. *Environmental Science and Pollution Research* **2023**, *30*, 21638–21653.
- (42) Al-Kashef, A. S.; Nooman, M. U.; Rashad, M. M.; Hashem, A. H.; Abdelraof, M. *Microbial Cell Factories* **2023**, *22*, 79–94.
- (43) Koh, A.; Gross, R. *Colloids and Surfaces A: Physicochemical and Engineering Aspects* **2016**, *507*, 152–163.
- (44) Wu, J.; Mei, P.; Lai, L. *Journal of Molecular Liquids* **2023**, *371*, 120814.
- (45) Trummer, F.; Lade, O.; Glatter, O.; Sottmann, T.; Stubenrauch, C. *Colloids and Surfaces A: Physicochemical and Engineering Aspects* **2023**, *676*, 132133.
- (46) Xie, Y.-w.; Li, Y.; Ye, R.-q. *Journal of Dispersion Science and Technology* **2005**, *26*, 455–461.
- (47) Ma, Y.-j.; Yuan, X.-z.; Huang, H.-j.; Xiao, Z.-h.; Zeng, G.-m., et al. *Journal of Molecular Liquids* **2015**, *203*, 181–186.

- (48) Al-Ghamdi, A.; Haq, B.; Al-Shehri, D.; Muhammed, N. S.; Mahmoud, M. *Energy Reports* **2022**, *8*, 7800–7813.
- (49) Nguyen, T. T.; Sabatini, D. A. *Journal of Surfactants and Detergents* **2009**, *12*, 109–115.
- (50) Nguyen, T. T.; Edelen, A.; Neighbors, B.; Sabatini, D. A. *Journal of Colloid and Interface Science* **2010**, *348*, 498–504.
- (51) Luo, J.; Yang, B.; Yang, X.; Ji, S.; Guo, Z.; Liu, Y.; Chen, Q.; Zhao, T.; Wang, Y.; Lu, B. *Food Chemistry* **2023**, *413*, 135631.
- (52) Shah, M. U. H.; Reddy, A. V. B.; Yusup, S.; Goto, M.; Moniruzzaman, M. *Environmental Pollution* **2021**, *284*, 117119.
- (53) Kume, G.; Gallotti, M.; Nunes, G. *Journal of Surfactants and Detergents* **2008**, *11*, 1–11.
- (54) Eastoe, J.; Dalton, J.; Rogueda, P.; Sharpe, D.; Dong, J.; Webster, J. R. *Langmuir* **1996**, *12*, 2706–2711.
- (55) Caschera, F.; de la Serna, J. B.; Löffler, P.; Rasmussen, T. E.; Hanczyc, M.; Bagatolli, L.; Monnard, P.-A. *Langmuir* **2011**, *27*, 14078–14090.
- (56) Hao, J.; Liu, W.; Xu, G.; Zheng, L. *Langmuir* **2003**, *19*, 10635–10640.
- (57) Silva, B. F.; Marques, E. F.; Olsson, U.; Pons, R. *Langmuir* **2010**, *26*, 3058–3066.
- (58) Tah, B.; Pal, P.; Mahato, M.; Talapatra, G. *The Journal of Physical Chemistry B* **2011**, *115*, 8493–8499.
- (59) Mal, A.; Bag, S.; Ghosh, S.; Moulik, S. P. *Colloids and Surfaces A: Physicochemical and Engineering Aspects* **2018**, *553*, 633–644.
- (60) Amante, J. C.; Scamehorn, J. F.; Harwell, J. H. *Journal of Colloid and Interface Science* **1991**, *144*, 243–253.
- (61) Shiau, B.-J.; Harwell, J. H.; Scamehorn, J. F. *Journal of Colloid and Interface Science* **1994**, *167*, 332–345.
- (62) Silva, B. F.; Marques, E. F.; Olsson, U. *Soft Matter* **2011**, *7*, 225–236.
- (63) Novak, S.; Morasi Piperčić, S.; Makarić, S.; Primožič, I.; Čurlin, M.; Štefanić, Z.; Domazet Jurašin, D. *The Journal of Physical Chemistry B* **2016**, *120*, 12557–12567.
- (64) Oliveira, I. S.; Silva, S. G.; do Vale, M. L.; Marques, E. F. *Membranes* **2023**, *13*, 178–193.
- (65) Nabi, E.; Drechsler, M.; Gradzielski, M. *Colloid and Polymer Science* **2015**, *293*, 3119–3130.

- (66) Eastoe, J.; Rogueda, P.; Shariatmadari, D.; Heenan, R. *Colloids and Surfaces A: Physicochemical and Engineering Aspects* **1996**, *117*, 215–225.
- (67) Penfold, J.; Thomas, R.; Dong, C.; Tucker, I.; Metcalfe, K.; Golding, S.; Grillo, I. *Langmuir* **2007**, *23*, 10140–10149.
- (68) Grillo, I.; Penfold, J. *Langmuir* **2011**, *27*, 7453–7463.
- (69) Akbaş, H.; Işcan, M.; Sidim, T. *Journal of Surfactants and Detergents* **2000**, *3*, 77–80.
- (70) Goloub, T.; Pugh, R.; Zhmud, B. *Journal of Colloid and Interface Science* **2000**, *229*, 72–81.
- (71) Burauer, S.; Sachert, T.; Sottmann, T.; Strey, R. *Physical Chemistry Chemical Physics* **1999**, *1*, 4299–4306.
- (72) Kahlweit, M.; Strey, R.; Firman, P. *The Journal of Physical Chemistry* **1986**, *90*, 671–677.
- (73) Mousavi, N. S.; Miller, R.; Schneck, E. *Journal of Molecular Liquids* **2023**, *375*, 121314.
- (74) Miller, R.; Fainerman, V.; Möhwald, H. *Journal of Colloid and Interface Science* **2002**, *247*, 193–199.
- (75) Valenzuela, M. Á.; Gárate, M. P.; Olea, A. F. *Colloids and Surfaces A: Physicochemical and Engineering Aspects* **2007**, *307*, 28–34.
- (76) Nasibova, S. M.; Rahimov, R. A.; Muradova, S. A.; Abdullayev, Y. *Materials Chemistry and Physics* **2023**, *296*, 127268.
- (77) Munkajohnpong, P.; Kesornpun, C.; Buttranon, S.; Jaroensuk, J.; Weeranoppanant, N.; Chaiyen, P. *Biofuels, Bioproducts and Biorefining* **2020**, *14*, 986–1009.
- (78) Holmberg, K. *Journal of Colloid and Interface Science* **2004**, *274*, 355–364.
- (79) Schmiedel, P.; von Rybinski, W. *Chemistry and Technology of Surfactants* **2006**, 46–90.
- (80) Israelachvili, J. N.; Mitchell, D. J.; Ninham, B. W. *Journal of the Chemical Society, Faraday Transactions 2: Molecular and Chemical Physics* **1976**, *72*, 1525–1568.
- (81) Dutt, S.; Siril, P. F.; Remita, S. *Rsc Advances* **2017**, *7*, 5733–5750.
- (82) Phillips, J. *Transactions of the Faraday Society* **1955**, *51*, 561–569.
- (83) Sun, Q. *Molecules* **2022**, *27*, 7009–7035.
- (84) Holland, P.; Rubingh, D. *The Journal of Physical Chemistry* **1983**, *87*, 1984–1990.
- (85) Holland, P. M.; Rubingh, D. N. In *Mixed Surfactant Systems*; ACS Publications: 1992; Chapter 1.

- (86) Clint, J. H. *Journal of the Chemical Society, Faraday Transactions 1: Physical Chemistry in Condensed Phases* **1975**, 71, 1327–1334.
- (87) Mańko, D.; Zdziennicka, A.; Jańczuk, B. *Journal of Surfactants and Detergents* **2017**, 20, 411–423.
- (88) Li, Y.; Lai, L.; Mei, P.; Zhang, W.-X.; Li, Y.-H.; Cheng, L.; Wang, Y.-Q.; Liu, Y. *Journal of Molecular Liquids* **2019**, 276, 488–496.
- (89) Liu, J.; Wang, Y.; Li, H. *Molecules* **2020**, 25, 4327–4341.
- (90) Mańko, D.; Zdziennicka, A.; Jańczuk, B. *Journal of Solution Chemistry* **2017**, 46, 1251–1271.
- (91) Song, D.; Liang, S.; Yan, L.; Shang, Y.; Wang, X. *Journal of Environmental Quality* **2016**, 45, 1405–1412.
- (92) Kahlweit, M. *Science* **1988**, 240, 617–621.
- (93) Kahlweit, M.; Strey, R. *Angewandte Chemie International Edition* **1985**, 24, 654–668.
- (94) Kahlweit, M.; Strey, R.; Firman, P.; Haase, D.; Jen, J.; Schomäcker, R. *Langmuir* **1988**, 4, 499–511.
- (95) Sottmann, T.; Strey, R. *Fundamentals of Interface and Colloid Science* **2005**, 5, 1–96.
- (96) Stubenrauch, C. *Current Opinion in Colloid & Interface Science* **2001**, 6, 160–170.
- (97) Kahlweit, M.; Strey, R. *The Journal of Physical Chemistry* **1986**, 90, 5239–5244.
- (98) Kahlweit, M.; Strey, R. *The Journal of Physical Chemistry* **1987**, 91, 1553–1557.
- (99) Kahlweit, M.; Strey, R. *The Journal of Physical Chemistry* **1988**, 92, 1557–1563.
- (100) Schneider, K.; Ott, T. M.; Schweins, R.; Frielinghaus, H.; Lade, O.; Sottmann, T. *Industrial & Engineering Chemistry Research* **2019**, 58, 2583–2595.
- (101) Sottmann, T.; Lade, M.; Stolz, M.; Schomacker, R. *Tenside Surfactants Detergents* **2002**, 39, 20–28.
- (102) Acosta, E.; Natali, S. *Journal of Surfactants and Detergents* **2022**, 25, 79–94.
- (103) Clouchoux, C.; Kudelski, D.; Gholipour, A.; Warfield, S. K.; Viseur, S.; Bouyssi-Kobar, M.; Mari, J.-L.; Evans, A. C.; Du Plessis, A. J.; Limperopoulos, C. *Brain Structure and Function* **2012**, 217, 127–139.
- (104) Helfrich, W. *Zeitschrift für Naturforschung C* **1973**, 28, 693–703.
- (105) Meleard, P.; Gerbeaud, C.; Pott, T.; Fernandez-Puente, L.; Bivas, I.; Mitov, M. D.; Dufourcq, J.; Bothorel, P. *Biophysical Journal* **1997**, 72, 2616–2629.

- (106) Daicic, J.; Olsson, U.; Wennerstroem, H. *Langmuir* **1995**, *11*, 2451–2458.
- (107) Tartaro, G.; Mateos, H.; Schirone, D.; Angelico, R.; Palazzo, G. *Nanomaterials* **2020**, *10*, 1657–1696.
- (108) De Gennes, P.; Taupin, C. *The Journal of Physical Chemistry* **1982**, *86*, 2294–2304.
- (109) Sottmann, T.; Strey, R.; Chen, S.-H. *The Journal of Chemical Physics* **1997**, *106*, 6483–6491.
- (110) Tanner, J. *Review of Scientific Instruments* **1965**, *36*, 1086–1087.
- (111) Stejskal, E. O.; Tanner, J. E. *The Journal of Chemical Physics* **1965**, *42*, 288–292.
- (112) Stejskal, E. O. *The Journal of Chemical Physics* **1965**, *43*, 3597–3603.
- (113) Nilsson, M.; Connell, M. A.; Davis, A. L.; Morris, G. A. *Analytical Chemistry* **2006**, *78*, 3040–3045.
- (114) Eitel, K.; Bryant, G.; Schöpe, H. J. *Langmuir* **2020**, *36*, 10307–10320.
- (115) Siegert, A., *On the Fluctuations in Signals Returned by Many Independently Moving Scatterers*; Radiation Laboratory, Massachusetts Institute of Technology: 1943.
- (116) Frisken, B. J. *Applied Optics* **2001**, *40*, 4087–4091.
- (117) Koppel, D. E. *The Journal of Chemical Physics* **1972**, *57*, 4814–4820.
- (118) Porcar, L.; Hamilton, W. A.; Butler, P. D.; Warr, G. *Langmuir* **2003**, *19*, 10779–10794.
- (119) Kotlarchyk, M.; Chen, S.-H. *The Journal of Chemical Physics* **1983**, *79*, 2461–2469.
- (120) Hayter, J. B.; Penfold, J. *Molecular Physics* **1981**, *42*, 109–118.
- (121) Hansen, J.-P.; Hayter, J. B. *Molecular Physics* **1982**, *46*, 651–656.
- (122) Teubner, M.; Strey, R. *The Journal of Chemical Physics* **1987**, *87*, 3195–3200.
- (123) Endo, H.; Mihailescu, M.; Monkenbusch, M.; Allgaier, J.; Gompper, G.; Richter, D.; Jakobs, B.; Sottmann, T.; Strey, R.; Grillo, I. *The Journal of Chemical Physics* **2001**, *115*, 580–600.
- (124) Schubert, K.-V.; Strey, R. *The Journal of Chemical Physics* **1991**, *95*, 8532–8545.
- (125) Prévost, S.; Gradzielski, M.; Zemb, T. *Advances in Colloid and Interface Science* **2017**, *247*, 374–396.
- (126) Gompper, G.; Endo, H.; Mihailescu, M.; Allgaier, J.; Monkenbusch, M.; Richter, D.; Jakobs, B.; Sottmann, T.; Strey, R. *Europhysics Letters* **2001**, *56*, 683–689.
- (127) Lei, N.; Safinya, C.; Roux, D.; Liang, K. *Physical Review E* **1997**, *56*, 608–612.

- (128) Porod, G. *Kolloid-Zeitschrift* **1951**, 124, 83–114.
- (129) Porod, G. *Kolloid-Zeitschrift* **1952**, 125, 108–122.
- (130) Strey, R.; Winkler, J.; Magid, L. *The Journal of Physical Chemistry* **1991**, 95, 7502–7507.
- (131) Prévost, S.; Gradzielski, M. *Journal of Colloid and Interface Science* **2009**, 337, 472–484.
- (132) He, L.; Garamus, V. M.; Funari, S. S.; Malfois, M.; Willumeit, R.; Niemeyer, B. *The Journal of Physical Chemistry B* **2002**, 106, 7596–7604.
- (133) Princen, H. *Journal of Colloid and Interface Science* **1995**, 169, 241–243.
- (134) Vonnegut, B. *Review of Scientific Instruments* **1942**, 13, 6–9.
- (135) Hua, X. Y.; Rosen, M. J. *Journal of Colloid and Interface Science* **1988**, 124, 652–659.
- (136) Ward, A.; Tordai, L. *The Journal of Chemical Physics* **1946**, 14, 453–461.
- (137) Fainerman, V.; Makievski, A.; Miller, R. *Colloids and Surfaces A: Physicochemical and Engineering Aspects* **1994**, 87, 61–75.
- (138) Zhmud, B.; Tiberg, F.; Kizling, J. *Langmuir* **2000**, 16, 2557–2565.
- (139) Danov, K.; Kralchevsky, P.; Denkov, N.; Ananthapadmanabhan, K.; Lips, A. *Advances in Colloid and Interface Science* **2006**, 119, 1–16.
- (140) Eastoe, J.; Dalton, J. *Advances in Colloid and Interface Science* **2000**, 85, 103–144.
- (141) Fainerman, V.; Mys, V.; Makievski, A.; Petkov, J.; Miller, R. *Journal of Colloid and Interface Science* **2006**, 302, 40–46.
- (142) LUTENSOL SURFACTANTS PRODUCT GUIDE; BASF, 2020.
- (143) Rosen, M. J.; Cohen, A. W.; Dahanayake, M.; Hua, X. Y. *The Journal of Physical Chemistry* **1982**, 86, 541–545.
- (144) Griffin, W. C. *Journal of Cosmetic Science* **1946**, 1, 311–326.
- (145) Tang, Y.; Ma, Q.; Du, Y.; Ren, L.; Van Zyl, L. J.; Long, X. *Separation and Purification Technology* **2020**, 245, 116897.
- (146) Ishigami, Y.; Gama, Y.; Nagahora, H.; Yamaguchi, M.; Nakahara, H.; Kamata, T. *Chemistry Letters* **1987**, 16, 763–766.
- (147) Klemmer, A., *A Guide to Formulation and Application of Low-Surfactant Microemulsions in Cleaning-Processes*; Cuvillier Verlag: 2014.
- (148) Marc; Weinstein, B.; tgwoodcock; Simon, C.; chebee7i; Morgan, W.; Knight, V.; Swanson-Hysell, N.; Evans, M.; jl-bernal; ZGainsforth; Badger, T. G.; SaxonAnglo; Greco, M.; Zuidhof, G. marcharper/python-ternary, version 1.0.6, 2019.

- (149) Van Rossum, G.; Drake Jr, F. L., *Python tutorial*; Centrum voor Wiskunde en Informatica Amsterdam, The Netherlands: 1995.
- (150) Virtanen, P. et al. *Nature Methods* **2020**, *17*, 261–272.
- (151) Johnson Jr, C. S. *Progress in Nuclear Magnetic Resonance Spectroscopy* **1999**, *34*, 203–256.
- (152) Nicolò, M. S.; Cambria, M. G.; Impallomeni, G.; Rizzo, M. G.; Pellicorio, C.; Ballistreri, A.; Guglielmino, S. P. *New Biotechnology* **2017**, *39*, 36–41.
- (153) Cuvier, A.-S.; Berton, J.; Stevens, C. V.; Fadda, G. C.; Babonneau, F.; Van Bogaert, I. N.; Soetaert, W.; Pehau-Arnaudet, G.; Baccile, N. *Soft Matter* **2014**, *10*, 3950–3959.
- (154) Ogunjobi, J. K.; McElroy, C. R.; Clark, J. H.; Thornthwaite, D.; Omoruyi, O. E.; Farmer, T. J. *Green Chemistry* **2021**, *23*, 9906–9915.
- (155) Pan, A.; Sil, P.; Dutta, S.; Das, P. K.; Bhattacharya, S. C.; Rakshit, A. K.; Aswal, V. K.; Moulik, S. P. *The Journal of Physical Chemistry B* **2014**, *118*, 3041–3052.
- (156) Moore, J. W.; Wellek, R. M. *Journal of Chemical and Engineering Data* **1974**, *19*, 136–140.
- (157) Holz, M.; Heil, S. R.; Sacco, A. *Physical Chemistry Chemical Physics* **2000**, *2*, 4740–4742.
- (158) Ambrosone, L.; Costantino, L.; D’errico, G.; Vitagliano, V. *Journal of Colloid and Interface Science* **1997**, *190*, 286–293.
- (159) Fournial, A.-G.; Molinier, V.; Vermeersch, G.; Aubry, J.-M.; Azaroual, N. *Colloids and Surfaces A: Physicochemical and Engineering Aspects* **2008**, *331*, 16–24.
- (160) Jerschow, A.; Müller, N. *Macromolecules* **1998**, *31*, 6573–6578.
- (161) Choe, B.-Y.; Krishna, N. R.; Pritchard, D. G. *Magnetic Resonance in Chemistry* **1992**, *30*, 1025–1026.
- (162) Baccile, N.; Birnbach, J.; Ouret-Campagnet, M.; Ramanujam, R. *Self-assembly study of mixtures of biosurfactants with conventional surfactants [dataset]*; tech. rep., <https://doi.org/10.1515/ESRF-ES-1362353346>; European Synchrotron Radiation Facility, 2026.
- (163) Guinier, A.; Fournet, G.; Walker, C. B.; Yudowitch, K. L., *Small-angle Scattering of X-rays*; Wiley New York: 1955.
- (164) Baccile, N.; Delbeke, E. I.; Brennich, M.; Seyrig, C.; Everaert, J.; Roelants, S. L.; Soetaert, W.; Van Bogaert, I. N.; Van Geem, K. M.; Stevens, C. V. *The Journal of Physical Chemistry B* **2019**, *123*, 3841–3858.

- (165) Gonfa, G.; Bustam, M. A.; Muhammad, N.; Ullah, S. *Journal of Molecular Liquids* **2015**, *211*, 734–741.
- (166) Reiss-Husson, F.; Luzzati, V. *The Journal of Physical Chemistry* **1964**, *68*, 3504–3511.
- (167) Fuglestad, B.; Gupta, K.; Wand, A. J.; Sharp, K. A. *Journal of Colloid and Interface Science* **2019**, *540*, 207–217.
- (168) Neil, C. W.; Hjelm, R. P.; Hawley, M. E.; Watkins, E. B.; Cockreham, C.; Wu, D.; Mao, Y.; Cheshire, M.; Burger, J.; Fischer, T. B., et al. *International Journal of Coal Geology* **2022**, *253*, 103950.
- (169) Montalvo, G.; Valiente, M.; Mortensen, K.; Gradzielski, M. *Journal of Colloid and Interface Science* **2001**, *238*, 251–258.
- (170) Birnbach, J.; Bayer, C.; Garthe, J.; Karg, M.; Optatzi, J. P.; Prevost, S. *Phase behavior of biosurfactants*; tech. rep., DOI: 10.5291/ILL-DATA.9-10-1817; Institut Laue-Langevin (ILL), 2024.
- (171) Dewhurst, C. *Journal of Applied Crystallography* **2023**, *56*, 1595–1609.
- (172) Hamuro, Y. *Journal of the American Society for Mass Spectrometry* **2020**, *32*, 133–151.
- (173) Jaksch, S.; Pipich, V.; Frielinghaus, H. *Journal of Applied Crystallography* **2021**, *54*, 1580–1593.
- (174) Schmiedel, H.; Jörchel, P.; Kiselev, M.; Klose, G. *The Journal of Physical Chemistry B* **2001**, *105*, 111–117.
- (175) Strey, R.; Jonströmer, M. *The Journal of Physical Chemistry* **1992**, *96*, 4537–4542.
- (176) Marrink, S. J.; Risselada, H. J.; Yefimov, S.; Tieleman, D. P.; De Vries, A. H. *The Journal of Physical Chemistry B* **2007**, *111*, 7812–7824.
- (177) Lopez, C.; Rzepiela, A.; de Vries, A.; Dijkhuizen, L.; Huenenberger, P.; Marrink, S. *Journal of Chemical Theory and Computation* **2009**, *5*, 3195–3210.
- (178) Scienomics MAPS, Version 4.4, Paris, France, 2022.
- (179) Gloor, G. J.; Jackson, G.; Blas, F. J.; de Miguel, E. *The Journal of Chemical Physics* **2005**, *123*, 134703.
- (180) *Anionic and non-ionic surface active agents Determination of the critical micellization concentration Method by measuring surface tension with a plate, stirrup or ring*; Standard; International Organization for Standardization, 1979.
- (181) Martínez-Balbuena, L.; Arteaga-Jiménez, A.; Hernández-Zapata, E.; Márquez-Beltrán, C. *Advances in Colloid and Interface Science* **2017**, *247*, 178–184.

- (182) Manet, S.; Cuvier, A.-S.; Valotteau, C.; Fadda, G. C.; Perez, J.; Karakas, E.; Abel, S.; Baccile, N. *The Journal of Physical Chemistry B* **2015**, *119*, 13113–13133.
- (183) Yi, Z.; Dumée, L. F.; Garvey, C. J.; Feng, C.; She, F.; Rookes, J. E.; Mudie, S.; Cahill, D. M.; Kong, L. *Langmuir* **2015**, *31*, 8478–8487.
- (184) Baccile, N.; Poirier, A.; Perez, J.; Pernot, P.; Legriel, P.; Blesken, C. C.; Müller, C.; Blank, L.; Tiso, T. *Langmuir* **2023**, *39*, 9273–9289.
- (185) Nagarajan, R. *Chemical Engineering Communications* **1987**, *55*, 251–273.
- (186) Akamatsu, M.; Saito, K.; Iwase, H.; Ogura, T.; Sakai, K.; Sakai, H. *Langmuir* **2021**, *37*, 10770–10775.
- (187) Wang, C.-A.; Yeh, Y.-Q.; Mou, C.-Y.; Su, C.-J.; Wu, W.-R.; Jeng, U.-S. *Materials Chemistry and Physics* **2022**, *277*, 125435.
- (188) Hollamby, M. J.; Borisova, D.; Brown, P.; Eastoe, J.; Grillo, I.; Shchukin, D. *Langmuir* **2012**, *28*, 4425–4433.
- (189) Zhou, W.; Jiang, L.; Liu, X.; Hu, Y.; Yan, Y. *Colloids and Surfaces A: Physico-chemical and Engineering Aspects* **2022**, *637*, 128259.
- (190) Rodriguez, J.; Clavero, E.; Laria, D. *The Journal of Physical Chemistry B* **2005**, *109*, 24427–24433.
- (191) O'Connor, A. J.; Hatton, T. A.; Bose, A. *Langmuir* **1997**, *13*, 6931–6940.
- (192) Stellner, K. L.; Amante, J. C.; Scamehorn, J. F.; Harwell, J. H. *Journal of Colloid and Interface Science* **1988**, *123*, 186–200.
- (193) Xu, J.; Sun, S.; Wang, Z.; Peng, S.; Hu, S.; Zhang, L. *Physical Chemistry Chemical Physics* **2018**, *20*, 9460–9470.
- (194) Zemb, T.; Dubois, M.; Deme, B.; Gulik-Krzywicki, T. *Science* **1999**, *283*, 816–819.
- (195) Thompson, T.; Tillack, T. W. *Annual Review of Biophysics and Biophysical Chemistry* **1985**, *14*, 361–386.
- (196) Ahmadi, D.; Thompson, K. C.; García Sakai, V.; Schweins, R.; Moulin, M.; Haertlein, M.; Strohmeier, G. A.; Pichler, H.; Forsyth, V. T.; Barlow, D. J., et al. *Frontiers in Physics* **2022**, *10*, 864746.
- (197) Dietrich, C.; Bagatolli, L.; Volovyk, Z.; Thompson, N.; Levi, M.; Jacobson, K.; Gratton, E. *Biophysical Journal* **2001**, *80*, 1417–1428.
- (198) Simons, K.; Ikonen, E. *Nature* **1997**, *387*, 569–572.
- (199) Rondelli, V.; Mollica, L.; Koutsoubas, A.; Nasir, N.; Trapp, M.; Deboever, E.; Brocca, P.; Deleu, M. *Journal of Colloid and Interface Science* **2022**, *616*, 739–748.

- (200) Phaodee, P.; Sabatini, D. A. *Journal of Surfactants and Detergents* **2021**, *24*, 551–562.
- (201) Upadhyaya, A.; Acosta, E.; Scamehorn, J.; Sabatini, D. *Journal of Surfactants and Detergents* **2007**, *10*, 269–277.
- (202) Bergström, M. *Langmuir* **1996**, *12*, 2454–2463.
- (203) Chiappisi, L.; Yalcinkaya, H.; Gopalakrishnan, V. K.; Gradzielski, M.; Zemb, T. *Colloid and Polymer Science* **2015**, *293*, 3131–3143.
- (204) Marsh, D. *Chemistry and Physics of Lipids* **2010**, *163*, 667–677.
- (205) Baccile, N.; Poirier, A.; Le Griel, P.; Pernot, P.; Pala, M.; Roelants, S.; Soetaert, W.; Stevens, C. V. *Colloids and Surfaces A: Physicochemical and Engineering Aspects* **2023**, *679*, 132518.
- (206) Sabatini, D. A.; Acosta, E.; Harwell, J. H. *Current Opinion in Colloid & Interface Science* **2003**, *8*, 316–326.
- (207) Baccile, N.; Pedersen, J. S.; Pehau-Arnaudet, G.; Van Bogaert, I. N. *Soft Matter* **2013**, *9*, 4911–4922.
- (208) Goyal, P.; Dasannacharya, B.; Kelkar, V.; Manohar, C.; Rao, K. S.; Valaulikar, B. *Physica B: Condensed Matter* **1991**, *174*, 196–199.
- (209) Berr, S. *Journal of Physical Chemistry* **1987**, *91*, 4760–4765.
- (210) Yang, J.; Huang, H.; Zheng, J.; Huang, Y.; Xie, H.; Gao, F. *Journal of Molecular Liquids* **2020**, *308*, 112995.
- (211) Chabba, S.; Kumar, S.; Aswal, V. K.; Kang, T. S.; Mahajan, R. K. *Colloids and Surfaces A: Physicochemical and Engineering Aspects* **2015**, *472*, 9–20.
- (212) Cuvier, A.-S.; Babonneau, F.; Berton, J.; Stevens, C. V.; Fadda, G. C.; Péhau-Arnaudet, G.; Le Griel, P.; Prévost, S.; Perez, J.; Baccile, N. *Chemistry—A European Journal* **2015**, *21*, 19265–19277.
- (213) Penfold, J.; Staples, E.; Thompson, L.; Tucker, I.; Hines, J.; Thomas, R.; Lu, J. *Langmuir* **1995**, *11*, 2496–2503.
- (214) Penfold, J.; Staples, E.; Thompson, L.; Tucker, I.; Hines, J.; Thomas, R.; Lu, J.; Warren, N. *The Journal of Physical Chemistry B* **1999**, *103*, 5204–5211.
- (215) Hoffmann, H.; Pössnecker, G. *Langmuir* **1994**, *10*, 381–389.
- (216) Dhar, P.; Havskjold, H.; Thornhill, M.; Roelants, S.; Soetaert, W.; Kota, H. R.; Chernyshova, I. *Journal of Colloid and Interface Science* **2021**, *585*, 386–399.
- (217) Pathania, A. S.; Jana, A. K. *Applied Biochemistry and Biotechnology* **2020**, *191*, 1223–1246.

- (218) Kumar, H.; Katal, A.; Rawat, P. *Journal of Molecular Liquids* **2018**, *249*, 227–232.
- (219) Salem, J. K.; El-Nahhal, I. M.; Hammad, T. M.; Kuhn, S.; Sharekh, S. A.; El-Askalani, M.; Hempelmann, R. *Chemical Physics Letters* **2015**, *636*, 26–30.
- (220) Chen, L.; Xiao, J.-X.; Ruan, K.; Ma, J. *Langmuir* **2002**, *18*, 7250–7252.
- (221) Yu, Z.-J.; Zhao, G.-X. *Journal of Colloid and Interface Science* **1989**, *130*, 414–420.
- (222) Letellier, P.; Mayaffre, A.; Turmine, M. *Journal of Colloid and Interface Science* **2011**, *354*, 248–255.
- (223) Li, G.; Yi, X.; Jiang, J.; Zhang, Y.; Li, Y. *Colloids and Surfaces B: Biointerfaces* **2020**, *195*, 111248.
- (224) Phan, C. M.; Le, T. N.; Yusa, S.-i. *Colloids and Surfaces A: Physicochemical and Engineering Aspects* **2012**, *406*, 24–30.
- (225) Li, S.-J.; Lai, L.; Mei, P.; Li, Y.; Cheng, L.; Ren, Z.-H.; Liu, Y. *Journal of Molecular Liquids* **2018**, *254*, 248–254.
- (226) Fainerman, V.; Aksenenko, E.; Kovalchuk, V.; Mucic, N.; Javadi, A.; Liggieri, L.; Ravera, F.; Loglio, G.; Makievski, A.; Schneck, E., et al. *Advances in Colloid and Interface Science* **2020**, *279*, 102143.
- (227) Karthick, A.; Roy, B.; Chattopadhyay, P. *Journal of Environmental Management* **2019**, *243*, 187–205.
- (228) Banat, I. M.; Makkar, R. S.; Cameotra, S. S. *Applied Microbiology and Biotechnology* **2000**, *53*, 495–508.
- (229) Feng, H.; Hou, J.; Ma, T.; Meng, Z.; Wu, H.; Yang, H.; Kang, W. *Colloids and Surfaces A: Physicochemical and Engineering Aspects* **2018**, *554*, 74–80.
- (230) Rodriguez-Escontrela, I.; Puerto, M. C.; Miller, C. A.; Soto, A. *Journal of Colloid and Interface Science* **2017**, *504*, 404–416.
- (231) Li, Z.; Wu, H.; Hu, Y.; Chen, X.; Yuan, Y.; Luo, Y.; Hou, J.; Bai, B.; Kang, W. *Journal of Molecular Liquids* **2020**, *309*, 113099.
- (232) Li, Z.; Kang, W.; Bai, B.; Wu, H.; Gou, C.; Yuan, Y.; Xu, D.; Lu, Y.; Hou, J. *Energy & Fuels* **2019**, *33*, 8279–8288.
- (233) Wang, G.; Yin, Q.; Shen, J.; Bai, Y.; Ma, X.; Du, Z.; Wang, W. *Journal of Molecular Liquids* **2017**, *234*, 142–148.
- (234) He, Y.; Yazhgur, P.; Salonen, A.; Langevin, D. *Advances in Colloid and Interface Science* **2015**, *222*, 377–384.

- (235) Palazzo, G.; Fiorentino, D.; Colafemmina, G.; Ceglie, A.; Carretti, E.; Dei, L.; Baglioni, P. *Langmuir* **2005**, *21*, 6717–6725.
- (236) Zhang, C.; Jin, Z.; Zeng, B.; Wang, W.; Palui, G.; Mattoussi, H. *The Journal of Physical Chemistry B* **2020**, *124*, 4631–4650.
- (237) Lin, T. L.; Chen, S. H.; Gabriel, N. E.; Roberts, M. F. *Journal of Physical Chemistry* **1990**, *94*, 855–862.
- (238) Kim, J.-S.; Kim, C.-G.; Song, P.-S. *Journal of the Society of Cosmetic Scientists of Korea* **1984**, *10*, 13–23.
- (239) Holland, P. M. *Advances in Colloid and Interface Science* **1986**, *26*, 111–129.
- (240) Zhou, Q.; Rosen, M. J. *Langmuir* **2003**, *19*, 4555–4562.
- (241) Chai, J.; Cui, X.; Zhang, X.; Song, M.; Wang, J.; Lu, J. *Journal of Molecular Liquids* **2018**, *264*, 442–450.
- (242) Mahbub, S.; Molla, M. R.; Saha, M.; Shahriar, I.; Hoque, M. A.; Halim, M. A.; Rub, M. A.; Khan, M. A.; Azum, N. *Journal of Molecular Liquids* **2019**, *283*, 263–275.
- (243) Gradzielski, M.; Duvail, M.; de Molina, P. M.; Simon, M.; Talmon, Y.; Zemb, T. *Chemical Reviews* **2021**, *121*, 5671–5740.
- (244) Oberdisse, J.; Hellweg, T. *Advances in Colloid and Interface Science* **2017**, *247*, 354–362.
- (245) Lade, O.; Beizai, K.; Sottmann, T.; Strey, R. *Langmuir* **2000**, *16*, 4122–4130.
- (246) Salager, J.-L.; Marquez, R.; Rondón, M.; Bullón, J.; Graciaa, A. *ACS Omega* **2023**, *8*, 9040–9057.
- (247) Wellert, S.; Karg, M.; Imhof, H.; Steppin, A.; Altmann, H.-J.; Dolle, M.; Richardt, A.; Tiersch, B.; Koetz, J.; Lapp, A., et al. *Journal of Colloid and Interface Science* **2008**, *325*, 250–258.
- (248) Leng, L.; Yuan, X.; Zeng, G.; Chen, X.; Wang, H.; Li, H.; Fu, L.; Xiao, Z.; Jiang, L.; Lai, C. *Fuel* **2015**, *147*, 76–81.
- (249) Lohateeraparp, P.; Wilairuengsuwan, P.; Saiwan, C.; Sabatini, D. A.; Harwell, J. H. *Journal of Surfactants and Detergents* **2003**, *6*, 15–24.
- (250) Rahman, H. M. A. U.; Afzal, S.; Nazar, M. F.; Alvi, D. A.; Khan, A. M.; Asghar, M. N. *Journal of Molecular Liquids* **2017**, *230*, 15–19.
- (251) Fanun, M. *Journal of Surfactants and Detergents* **2010**, *13*, 321–328.
- (252) Wulff, N., *Microemulsions as stepping stones to greener organic chemistry*; Cuvillier Verlag: 2015.

- (253) Acosta, E. J. *Colloids and Surfaces A: Physicochemical and Engineering Aspects* **2008**, *320*, 193–204.
- (254) Marquez, N.; Anton, R.; Graciaa, A.; Lachaise, J.; Salager, J.-L. *Colloids and Surfaces A: Physicochemical and Engineering Aspects* **1995**, *100*, 225–231.
- (255) Di Meglio, J. M.; Dvolaitzky, M.; Taupin, C. *The Journal of Physical Chemistry* **1985**, *89*, 871–874.
- (256) Binks, B.; Meunier, J.; Abillon, O.; Langevin, D. *Langmuir* **1989**, *5*, 415–421.
- (257) Wormuth, K. R.; Geissler, P. R. *Journal of Colloid and Interface Science* **1991**, *146*, 320–329.
- (258) Frank, C.; Frielinghaus, H.; Allgaier, J.; Prast, H. *Langmuir* **2007**, *23*, 6526–6535.
- (259) Lindman, B.; Kamenka, N.; Kathopoulis, T. M.; Brun, B.; Nilsson, P. G. *The Journal of Physical Chemistry* **1980**, *84*, 2485–2490.
- (260) Pake, G. E. *The Journal of Chemical Physics* **1948**, *16*, 327–336.
- (261) Xu, Y.; Laupheimer, M.; Preisig, N.; Sottmann, T.; Schmidt, C.; Stubenrauch, C. *Langmuir* **2015**, *31*, 8589–8598.
- (262) Müller, S.; Börschig, C.; Gronski, W.; Schmidt, C.; Roux, D. *Langmuir* **1999**, *15*, 7558–7564.
- (263) Qi, L.; Christopher, G. F. *Rheologica Acta* **2022**, *61*, 59–68.
- (264) Lee, L.; Langevin, D.; Strey, R. *Physica A: Statistical Mechanics and its Applications* **1990**, *168*, 210–219.
- (265) Tanford, C., *The hydrophobic effect: formation of micelles and biological membranes*; J. Wiley.: 1980; Vol. 2.
- (266) Bryant, G.; Taylor, M. B.; Darwish, T. A.; Krause-Heuer, A. M.; Kent, B.; Garvey, C. J. *Colloids and Surfaces B: Biointerfaces* **2019**, *177*, 196–203.
- (267) Tomšič, M.; Jamnik, A.; Fritz-Popovski, G.; Glatter, O.; Vlček, L. *The Journal of Physical Chemistry B* **2007**, *111*, 1738–1751.
- (268) Takamuku, T.; Maruyama, H.; Watanabe, K.; Yamaguchi, T. *Journal of Solution Chemistry* **2004**, *33*, 641–660.
- (269) Callender, S. P.; Mathews, J. A.; Kobernyk, K.; Wettig, S. D. *International Journal of Pharmaceutics* **2017**, *526*, 425–442.
- (270) Schubert, K.-V.; Strey, R.; Kline, S.; Kaler, E. *The Journal of Chemical Physics* **1994**, *101*, 5343–5355.
- (271) Widom, B. *Langmuir* **1987**, *3*, 12–17.
- (272) Abillon, O.; Lee, L.; Langevin, D.; Wong, K. *Physica A: Statistical Mechanics and its Applications* **1991**, *172*, 209–218.

- (273) Jacobson, K.; Dietrich, C. *Trends in Cell Biology* **1999**, 9, 87–91.
- (274) Sutherland, E.; Mercer, S. M.; Everist, M.; Leaist, D. G. *Journal of Chemical & Engineering Data* **2009**, 54, 272–278.
- (275) Liu, Z.-Y.; Li, Z.-Q.; Song, X.-W.; Zhang, J.-C.; Zhang, L.; Zhang, L.; Zhao, S. *Fuel* **2014**, 135, 91–98.
- (276) Zimoch, J.; Błaszczak, J.; Szarzyńska, K.; Hrecuch, W.; Szymanowski, J. *Journal of Surfactants and Detergents* **1999**, 2, 473–481.
- (277) Wu, J.; Mei, P.; Wu, J.; Fu, J.-W.; Cheng, L.; Lai, L. *Journal of Molecular Liquids* **2020**, 317, 113907.
- (278) Fainerman, V.; Aksenenko, E.; Petkov, J.; Miller, R. *The Journal of Physical Chemistry B* **2010**, 114, 4503–4508.
- (279) Noskov, B. *Advances in Colloid and Interface Science* **2002**, 95, 237–293.
- (280) Fainerman, V. *Colloids and Surfaces* **1992**, 62, 333–347.
- (281) Colegate, D. M.; Bain, C. D. *Physical Review Letters* **2005**, 95, 198302.
- (282) Song, Q.; Couzis, A.; Somasundaran, P.; Maldarelli, C. *Colloids and Surfaces A: Physicochemical and Engineering Aspects* **2006**, 282, 162–182.
- (283) Chen, M.; Dong, C.; Penfold, J.; Thomas, R. K.; Smyth, T. J.; Perfumo, A.; Marchant, R.; Banat, I. M.; Stevenson, P.; Parry, A., et al. *Langmuir* **2013**, 29, 3912–3923.
- (284) Mysona, J. A.; McCormick, A. V.; Morse, D. C. *Journal of Colloid and Interface Science* **2023**, 638, 855–871.
- (285) Liu, X.; Zhao, Y.; Li, Q.; Jiao, T.; Niu, J. *Journal of Molecular Liquids* **2016**, 216, 185–191.
- (286) Catanoiu, G.; Carey, E.; Patil, S.; Engelskirchen, S.; Stubenrauch, C. *Journal of Colloid and Interface Science* **2011**, 355, 150–156.
- (287) Patist, A.; Oh, S.; Leung, R.; Shah, D. *Colloids and Surfaces A: Physicochemical and Engineering Aspects* **2001**, 176, 3–16.
- (288) Staples, E.; Thompson, L.; Tucker, I.; Penfold, J. *Langmuir* **1994**, 10, 4136–4141.
- (289) Samanta, S.; Ghosh, P. *Chemical Engineering Science* **2011**, 66, 4824–4837.
- (290) Shirahama, K.; Kashiwabara, T. *Journal of Colloid and Interface Science* **1971**, 36, 65–70.
- (291) Patist, A.; Kanicky, J. R.; Shukla, P. K.; Shah, D. O. *Journal of Colloid and Interface Science* **2002**, 245, 1–15.
- (292) Jeong, J.-B.; Kim, J.-Y.; Kim, H.-C.; Kim, J.-D. *Journal of Colloid and Interface Science* **2002**, 250, 496–502.

- (293) Dillan, K. *Journal of the American Oil Chemists' Society* **1985**, 62, 1144–1151.
- (294) Salager, J.-L.; Forgiarini, A.; Marquez, R. *Journal of Surfactants and Detergents* **2019**, 22, 935–972.
- (295) Salager, J.-L.; Marquez, R.; Bullon, J.; Forgiarini, A. *Encyclopedia* **2022**, 2, 778–839.

Appendix

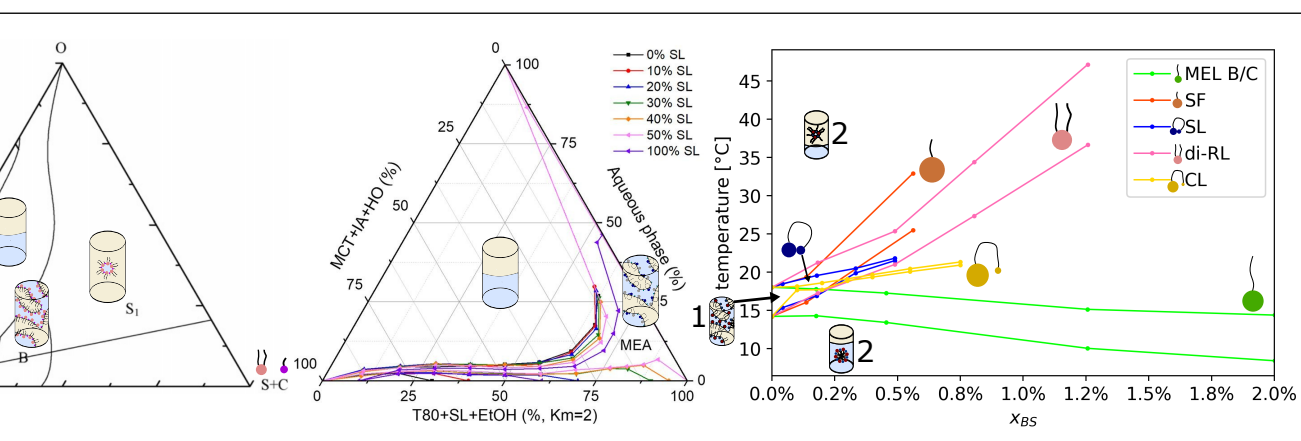


Figure A1: Phase diagram of lactonic SL, polyoxymethylene(20)-sorbitan-monooleate (T80) and ethanol (EtOH) with different contents of l-SL, medium-chain triglycerides (MCT), isoamyl acetate (IA), and hop oil (HO) as oils with MEA being the microemulsion area at 25 °C (left) (reprinted from [16, 51]). Phase boundaries of μ Es depending on the weight concentration of the BS added to the system of C12E4/n-decane/aqueous citrate buffer (0.031/1/1 w/w/w) at pH 8 (right) (reprinted from [16]).

Table A1: Composition of SL by liquid chromatography with electrospray ionisation and mass spectroscopy. The weight percentages were calculated by the signal of oleic acid.

component	weight percentage
C16:0	14.6%
C18:2	30.1%
C18:1	42.5%
C18:0	1.1%
C18:1 1x acetate	7.8%
C18:1 2x acetate	0.4%
C18:2 2x acetate	3.1%
C18:1 2x acetate	0.5%

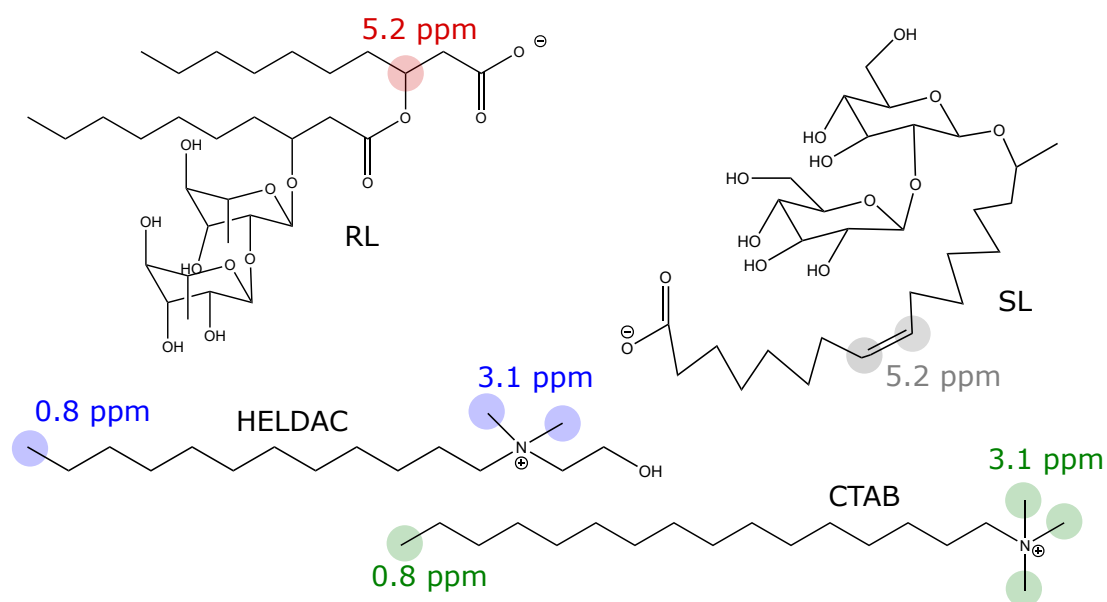


Figure A2: Illustration of the chemical shifts of the studied molecules in NMR spectroscopy.

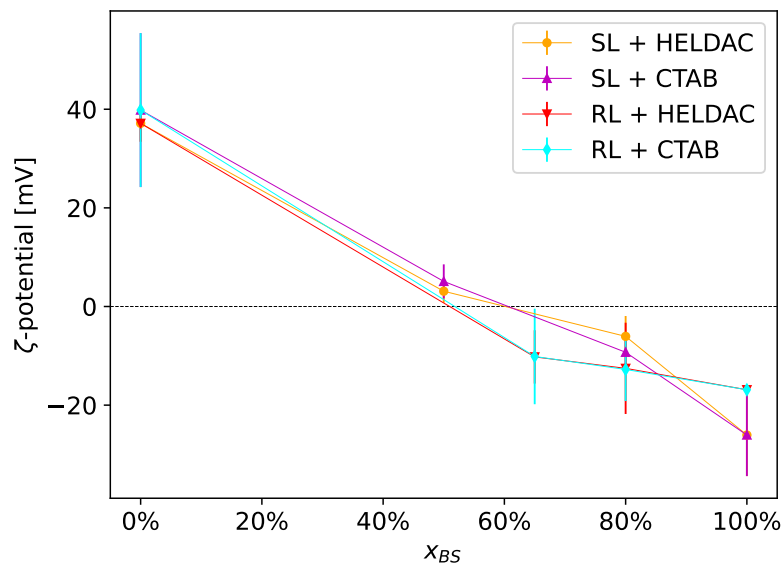


Figure A3: Zeta-potential, ζ , measurements of the catanionic systems as a function of the fraction of the BSs RL and SL in solution, x_{BS} , at 20 mM measured using the Litesizer from Anton Paar Germany GmbH. The error bars describe the standard deviation of at least five measurements.

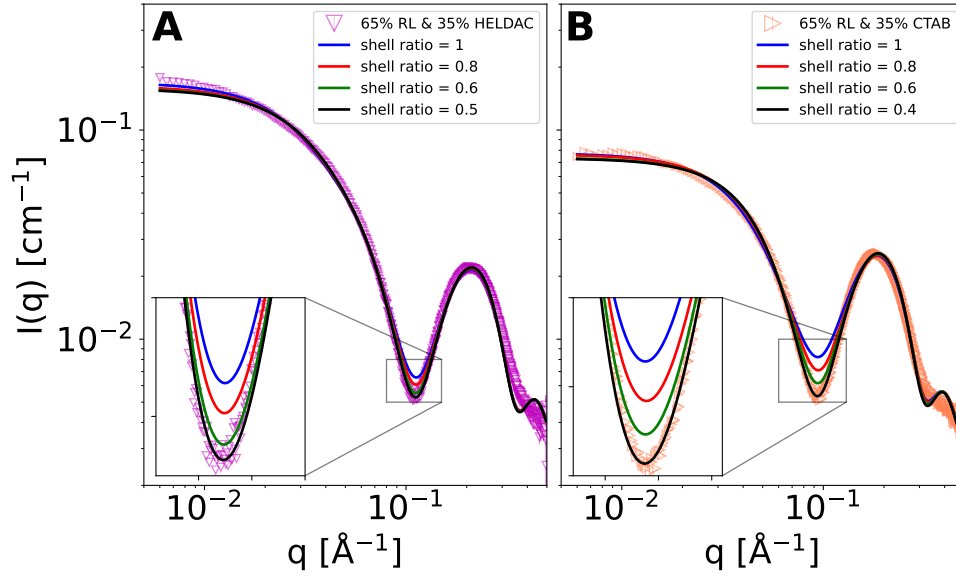


Figure A4: SAXS data of 65% RL & 35% CTAB or HELDAC fitted with the HSA + core-shell ellipsoid model assuming different shell ratios. The different shell ratios correspond to different thicknesses of the hydrophilic headgroups within the aggregate.

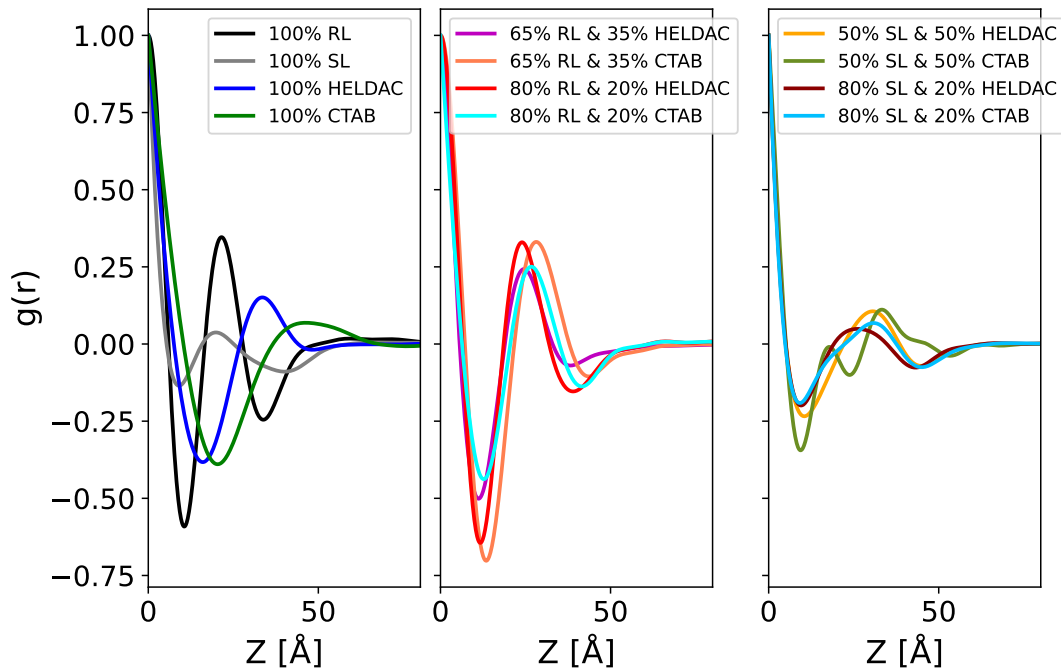


Figure A5: Pair correlation functions of the SAXS profiles in Figure 4.3.

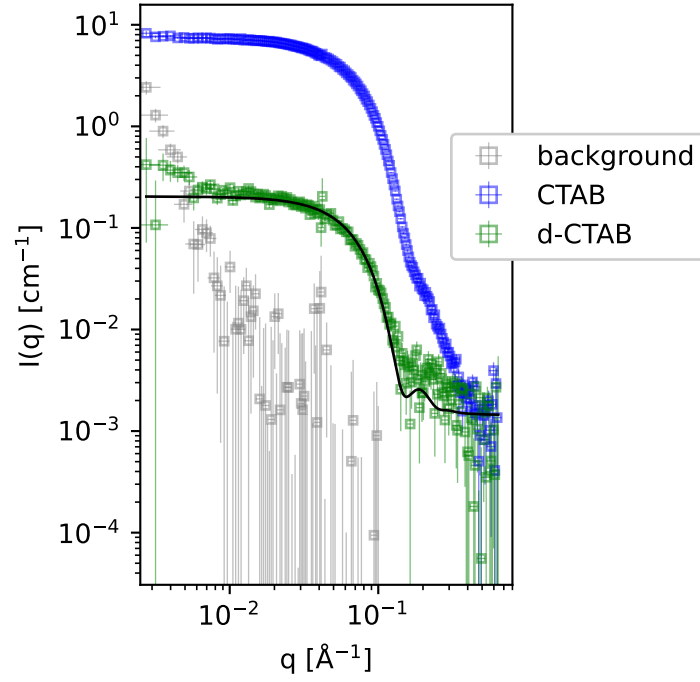


Figure A6: SANS profiles of hydrogenated CTAB (blue markers), deuterated d-CTAB in contrast matched solvent (green markers, $\text{SLD} = 5.86 \cdot 10^{-6} \text{ \AA}^{-2}$) and buffer (grey markers, $\text{SLD} = 5.86 \cdot 10^{-6} \text{ \AA}^{-2}$). The fits (solid lines) show a sphere model with the spheres having a radius of 29 Å and SLD of $6.9 \cdot 10^{-6} \text{ \AA}^{-2}$ while the solvent has a SLD of $5.86 \cdot 10^{-6} \text{ \AA}^{-2}$.

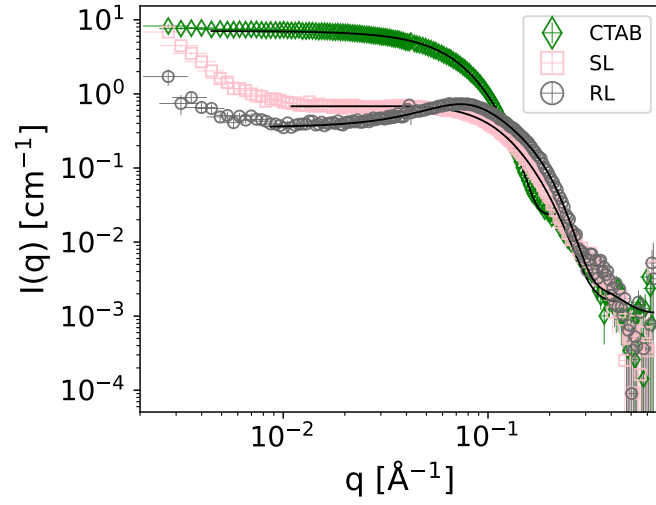


Figure A7: Measured SANS profiles (symbols) and fits (solid lines) of the pure substances CTAB, RL and SL using models of HSA + core-shell ellipsoids.

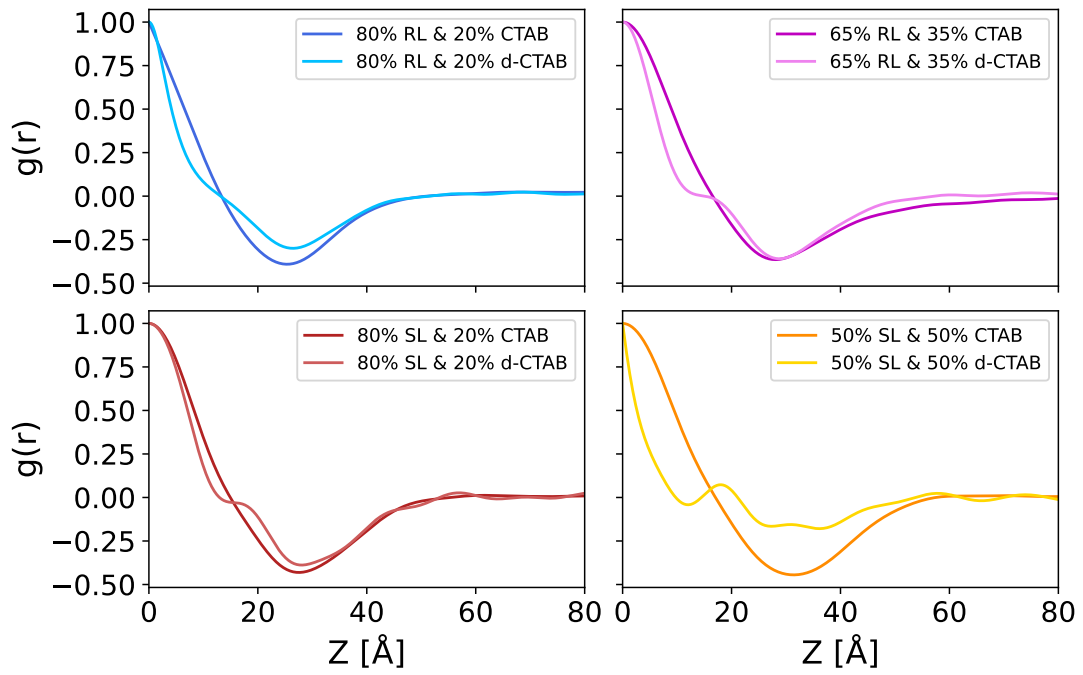


Figure A8: Pair correlation functions of the SANS profiles in Figure 4.4.

Calculation of the micellar composition in the catanionic systems

It is possible to determine the internal composition of the micelles by calculating the invariants of the curves obtained from comparing the total scattering of the samples with h-CTAB and d-CTAB [175]. Matching the SLDs of CTAB and water with d-CTAB, only the BSs remain visible for neutrons and less neutrons are scattered compared to the sample of h-CTAB and RL in which the neutrons get scattered at the RL and the CTAB molecules. The invariants with d-CTAB, however, have to be corrected because d-CTAB and D₂O did not match completely. Hence, the invariant of d-CTAB in D₂O in Figure A6 (adjusted by the actual used amount of d-CTAB used) was subtracted from those of the mixtures of BSs and d-CTAB. For clarity, here is an example: the invariant of d-CTAB in D₂O in Figure A6 is $6.01 \cdot 10^{-6} \text{Å}^{-2}$ and the one of 65% RL & 35% d-CTAB in Figure 4.4 A $5.91 \cdot 10^{-6} \text{Å}^{-2}$. The d-CTAB content of the d-CTAB in D₂O is 1.64v% and of 65% RL & 35% d-CTAB in D₂O is 0.57 v%. The corrected invariant of 65% RL & 35% d-CTAB is then

$$5.91 \cdot 10^{-4} - 6.01 \cdot 10^{-5} \cdot \frac{0.57}{1.64} = 5.70 \cdot 10^{-6} \text{Å}^{-2}. \quad (5.1)$$

The invariants of the different contrasts can then be correlated with a factor

$$f = \frac{\text{Invariant}_{\text{bulk}}}{\text{Invariant}_{\text{film}}}. \quad (5.2)$$

In the case of our example, it is

$$f = \frac{1.33}{5.70} = 2.33. \quad (5.3)$$

This factor also correlates the differences in SLDs (ΔSLDs) of the contrasts

$$f = \frac{\Delta\text{SLD}_{\text{bulk}}^2}{\Delta\text{SLD}_{\text{film}}^2}. \quad (5.4)$$

Therefore, the expected ΔSLD of the film contrast with d-CTAB can be calculated:

$$\Delta\text{SLD}_{\text{film}} = \frac{1}{\sqrt{f}} \cdot \Delta\text{SLD}_{\text{bulk}} = \frac{1}{\sqrt{2.33}} \cdot 5.56 \cdot 10^{-6} \text{Å}^{-2} = 3.64 \cdot 10^{-6} \text{Å}^{-2}. \quad (5.5)$$

By knowing the differences in the ΔSLDs of the pure components in water, the composition can be obtained. Here, 73% RL with a ΔSLD of $5.24 \cdot 10^{-6} \text{Å}^{-2}$ and 27% CTAB with $-0.63 \cdot 10^{-6} \text{Å}^{-2}$ equals the expected ΔSLD of $3.64 \cdot 10^{-6} \text{Å}^{-2}$. This is why it can be assumed that the interface consists of 73% RL and 27% CTAB when the bulk concentration is 65% RL & 35% CTAB. Strey et al. assumed a total error of 0.02 for the volume fraction of each substance [175].

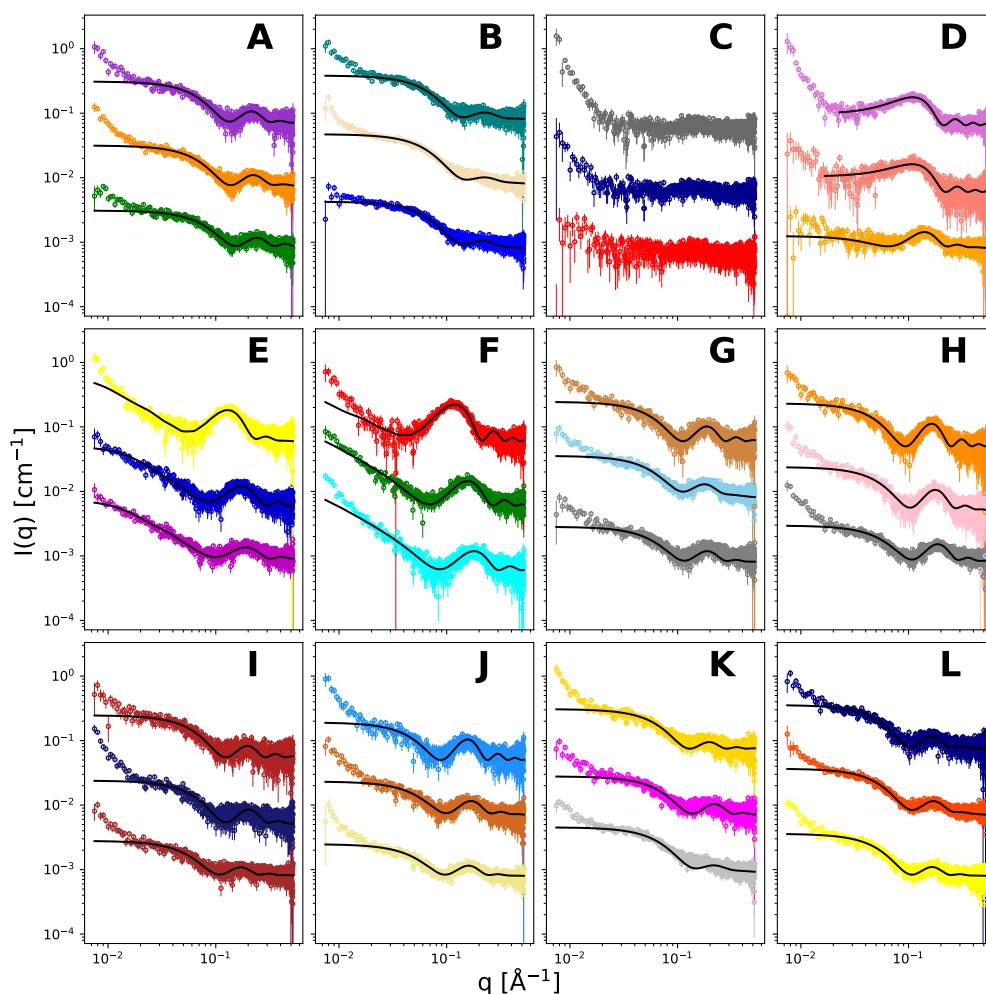


Figure A9: SAXS profiles of the different cationic species with different additions of 0 wt% n-decane at the bottom, 1 wt% n-decane in the middle (shifted by the factor of 10), and 10 wt% n-decane at the top (shifted by the factor of 100). From left top to right bottom the following cationic systems are shown: A) RL, B) SL, C) HELDAC, D) CTAB, E) RL & 35% HELDAC, F) RL & 35% CTAB, G) RL & 20% HELDAC, H) RL & 20% CTAB, I) SL & 50% HELDAC, J) SL & 50% CTAB, K) SL & 20% HELDAC and L) SL & 20% CTAB. The solid black lines display the fit of the profile which parameters are displayed in Figure 4.11. All curves were fitted with the spherical core-shell form factor, except of the RL & 35% HELDAC system which was fitted with a core-shell ellipsoid form factor. The curve of pure HELDAC was not fitted due to the poor contrast.

DLS of Catanionic Systems

DLS measurements were performed to investigate the effect of diffusion on the adsorption and to determine the differences between pure and mixed surfactant systems. Figure A10 A shows the diffusion coefficients obtained from fitting the auto-correlation functions with Equation 2.39. Such an example is shown in Figure A10 B in case of RL & 35% HELDAC. As only one slope is present (indicating one size for all aggregates), the cumulant analysis is appropriate for processing the data. Figure A10 C shows the Γ vs. q^2 -plot, the slope of which corresponds to the average diffusion coefficient of the system. Describing the diffusion coefficients in Figure A10 A, the pure cationic surfactants have a lower diffusion coefficient than the pure anionic BSs. This is due to the smaller size of the aggregates. The diffusion coefficients of the mixture SL & CTAB are linearly between the one of the pure substances. This is expected if the shape of the aggregates remains the same. The diffusion coefficients of the mixture SL & HELDAC also behave linearly, except the diffusion coefficient of 50% SL & 50% HELDAC mixture which is a slightly lower. For the RL & cationic surfactant mixtures, the diffusion coefficients are lower than the expected one. This indicates a change in the aggregate and non-ideal mixing. The respective radii of the diffusion coefficients can be calculated via Stokes-Einstein. For the diffusion coefficients in Figure A10, the radii range between 2 and 5 nm. This size indicates a micellar structure of the aggregates. To study the rotational diffusion, Figure A10 C displays the Γ vs. q^2 -plot of the different surfactant systems. The amount of rotational diffusion can be estimated by looking at the intercept of the plot. All curves show an intercept, except the regression curves of pure RL and its 20% mixture with HELDAC which lie at the origin of the coordinates. Mixtures of 65% RL and 35% HELDAC, 50% SL & 50% HELDAC, 100% CTAB and 100% SL show a large intercept. The existence of an intercept for the other systems means that these systems have a rotational diffusion in addition to their translational one. This presence of rotational diffusion indicates anisotropic structures, e.g. rod-like shaped micelles. This rod-like shape has already been evidenced for 100% CTAB and 100% SL in literature [182, 186–188].

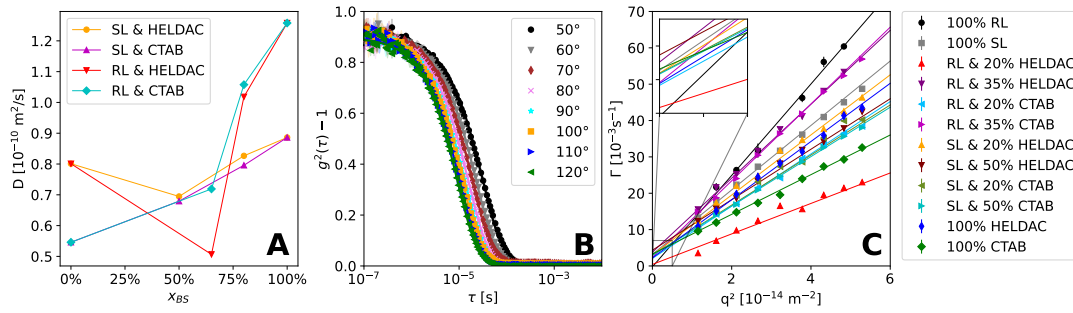


Figure A10: DLS measurements of different cationic surfactant systems at 20 mM and at different angles. A) the average diffusion coefficient D as a function of the fraction of the BS in solution x_{BS} (the lines serve as guide for the eye), B) fitted auto-correlation functions of RL & 35% HELDAC at different angles and C) Γ vs. q^2 -plot for the different surfactant systems.

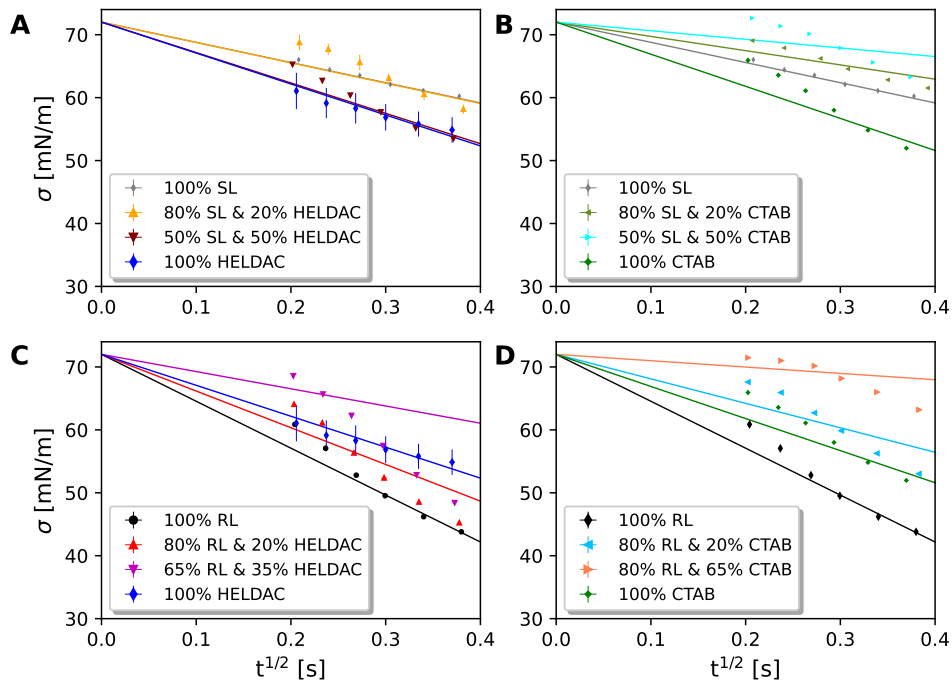


Figure A11: DST, σ , measurements of different cationic systems at 1 g/l by maximum bubble pressure (symbols). The error bar describes the standard deviation of three measurements. The data was fitted with Equation 2.68 (Ward-Tordai Equation, solid lines).

Table A2: Purity of mono-disperse ethoxylates by GC-MS.

substance	C ₁₂ E ₃	C ₁₂ E ₄	C ₁₂ E ₅	C ₁₂ E ₇
1 EO	0.6	0.4		
2 EO	0.5	0.2		
3 EO	0.5	0.1		
4 EO		0.4		
dodecanol	0.6	0.1		0.1
C ₁₂ E ₁	0.4	0.1		0.2
C ₁₂ E ₂	0.5	0.1		0.2
C ₁₂ E ₃	95.6	0.8		0.3
C ₁₂ E ₄		96	<0.1	0.3
C ₁₂ E ₅			99.3	0.3
C ₁₂ E ₆			0.3	2.6
C ₁₂ E ₇			0.1	96.1
others	1.3	1.6	0.3	

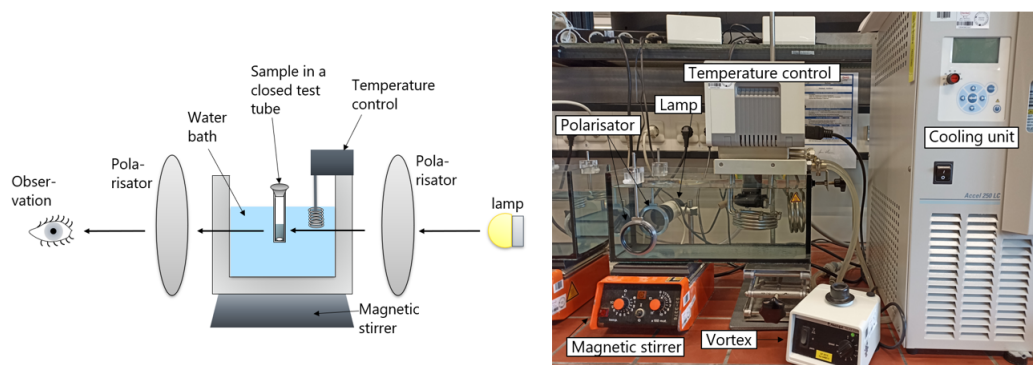


Figure A12: Apparatus for the optical determination of the phase behavior.

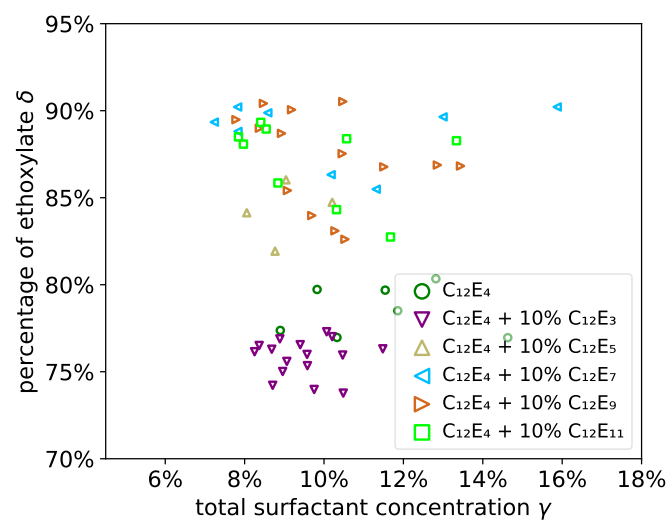


Figure A13: Lamellar phase boundaries of the phase diagram in Figure 4.15.

1H (zg0): 1.18 RL + C12E4 + D2O + n-decane Winsor I
Tregul (BBFO-20181119) =32C => Treal = 30C



Current Data Parameters
NAME 20240104-Paris
EXPNO 301
PROCNO 1

F2 - Acquisition Parameters
Date_ 20240219
Time 16.15 h
INSTRUM spect
PROBHD Z104275_0193 (
PULPROG zg0
TD 16384
SOLVENT D2O
NS 4
DS 0
SWH 6009.615 Hz
FIDRES 0.733596 Hz
AQ 1.3631488 sec
RG 1
DW 83.200 usec
DE 6.50 usec
TE 305.1 K
D1 8.63685131 sec
P1 14.60 usec
TD0 1
ZGPTNS
SFO1 300.1318008 MHz
NUC1 1H
P0 0.50 usec
PLW1 15.00000000 W

F2 - Processing parameters
SI 16384
SF 300.1300000 MHz
WDW EM
SSB 0
LB 0.30 Hz
GB 0
PC 1.00

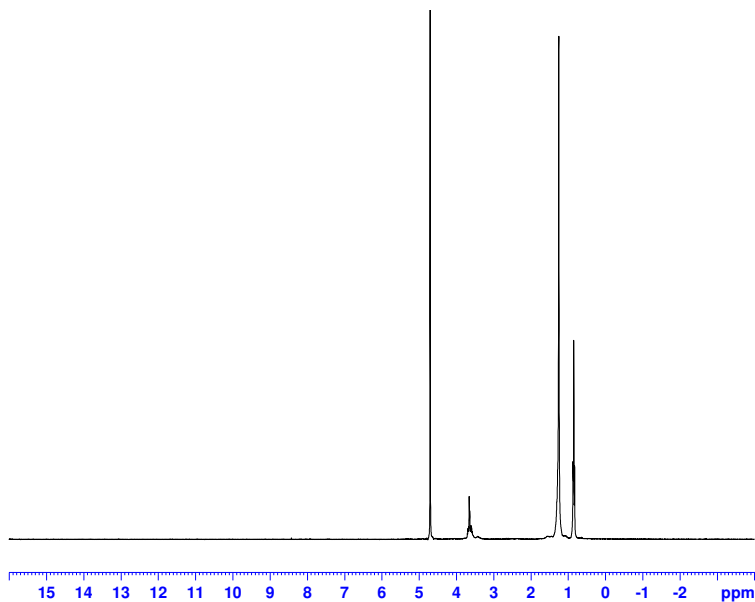


Figure A14: Example of NMR spectrum of a μ E containing RL/C₁₂E₄/n-decane/water. The plot displays the Winsor I phase with the following peaks: 4.7 ppm for water, 3.6 ppm for the C₁₂E₄ and 1.3 ppm and 0.9 ppm for n-decane.

2D (zg0): 1.1 microemulsion RL + C12E4 / D2O / n-decane
Tregul (BBFO-20181119) =32C => Treal = 30C
after shaking



Current Data Parameters
NAME 20240104-Paris
EXPNO 218
PROCNO 1

F2 - Acquisition Parameters
Date_ 20240124
Time 18.11 h
INSTRUM spect
PROBHD Z104275_0193 (4
PULPROG zg0
TD 4096
SOLVENT D2O
NS 64
DS 0
SWH 1842.299 Hz
FIDRES 0.899560 Hz
AQ 1.1116544 sec
RG 10
DW 271.400 usec
DE 10.00 usec
TE 305.2 K
D1 0.88834560 sec
P1 260.00 usec
TD0 1
ZGPGTNS 1
SFO1 46.0719985 MHz
NUC1 2H
P0 10.00 usec
PLW1 3.00000000 W

F2 - Processing parameters
SI 32768
SF 46.0717820 MHz
WDW EM
SSB 0
LB 2.00 Hz
GB 0
PC 1.00

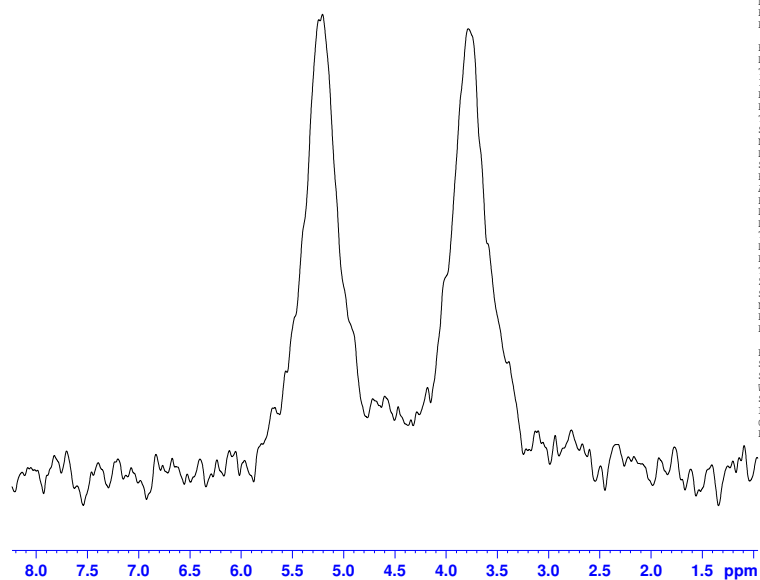


Figure A15: ^2H NMR spectra of a lamellar microemulsion showing quadrupole splitting (Pake peak).

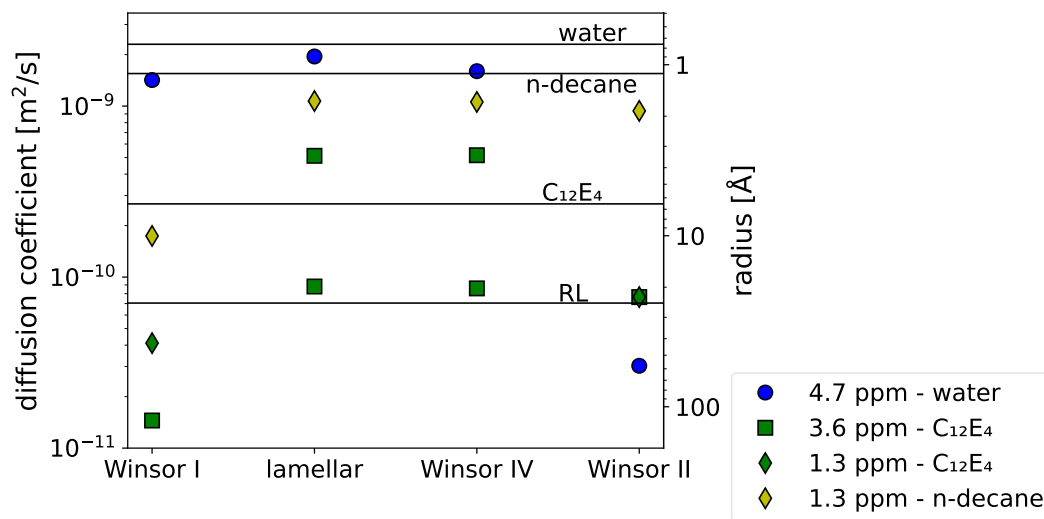


Figure A16: Illustration of Figure 4.16 in log-scale. The lines indicate the diffusion coefficients of free n-decane, water, C_{12}E_4 and RL micelles, respectively. The right axis is an estimate of the size, using the Stokes-Einstein equation and the viscosity of D_2O (Equation 2.41).

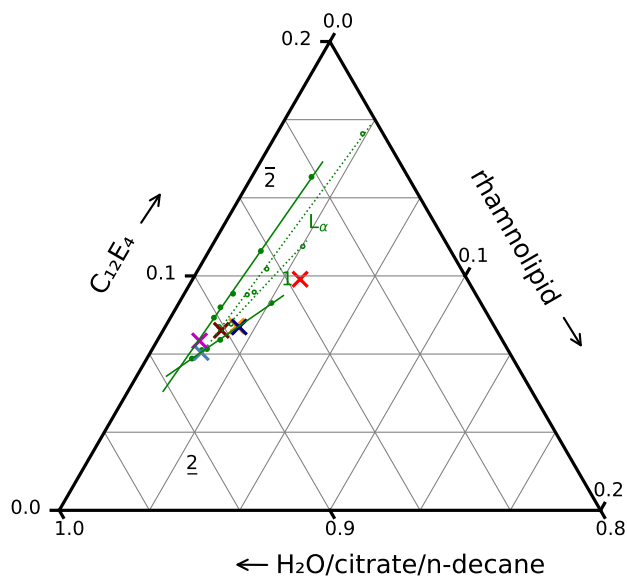


Figure A17: Illustration of the compositions of the analyzed samples by SAXS in Figure 4.17.

Table A3: Fitting parameters of the SANS data of the μE shown in Figure 4.20.

core-shell-shell-sphere model of Winsor I														
contrast	sld _{core} [10 ⁻⁶ Å ⁻²]	sld _{shell 1} [10 ⁻⁶ Å ⁻²]	sld _{shell 2} [10 ⁻⁶ Å ⁻²]	radius		thick-ness		inter- action radius [Å]	Q* [cm ⁻¹ V ⁻³]	err _{Q*} [cm ⁻¹ Å ⁻³]	S/V [V ⁻¹]	err _{S/V} [Å ⁻¹]		
				1 [Å]	2 [Å]	1 [Å]	2 [Å]							
bulk	-0.5	6		58		9	67		0.0154	0.0001	0.03	0.00		
film	6.4	-0.4	6.0	45	11	12	67		0.0074	0.0001	0.25	0.01		
RL	6.4	-0.4	6.4	41	4	11	55		0.0038	0.0001	5.76	0.38		
EO	-0.5	6.1	0.1	40	5	11	55		0.0029	0.0001	1.83	0.17		
Teubner Strey model and Porod decay for diffusive interfaces														
d [Å]	ξ [Å]	t [Å]												
Winsor IV (1)	550	340	4											
Winsor IV (2)	440	230	3											
oblades model of Winsor IV (1)														
contrast	ξ ₁₀ [Å]	ξ ₃ [Å]	d [Å]	σ [Å]	t ₀	d _m	AB	AB _{ratio}	Q* [cm ⁻¹ Å ⁻³]	err _{Q*} [cm ⁻¹ V ⁻³]	S/V [V ⁻¹]	err _{S/V} [Å ⁻¹]		
film	70	250	500	56	9	40	0.15	1.00	0.0061	0.0001	0.39	0.02		
RL	70	250	500	22	6	15	0.00	0.00	0.0018	0.0002	10.41	2.95		
EO	70	250	500	70	13	36	0.01	1.00	0.0039	0.0001	3.61	0.15		
oblades model of Winsor IV (2)														
contrast	ξ ₁₀ [Å]	ξ ₃ [Å]	d [Å]	σ [Å]	t ₀	d _m	AB	AB _{ratio}	Q* [cm ⁻¹ Å ⁻³]	err _{Q*} [cm ⁻¹ Å ⁻³]	S/V [Å ⁻¹]	err _{S/V} [Å ⁻¹]		
film	59	250	500	45	10	40	0.10	1.00	0.0072	0.0001	0.39	0.02		
RL	59	250	500	10	7	9	0.00	0.00	0.0016	0.0002	6.41	2.96		
EO	59	250	500	60	13	36	0.01	1.00	0.0060	0.0003	4.73	0.66		

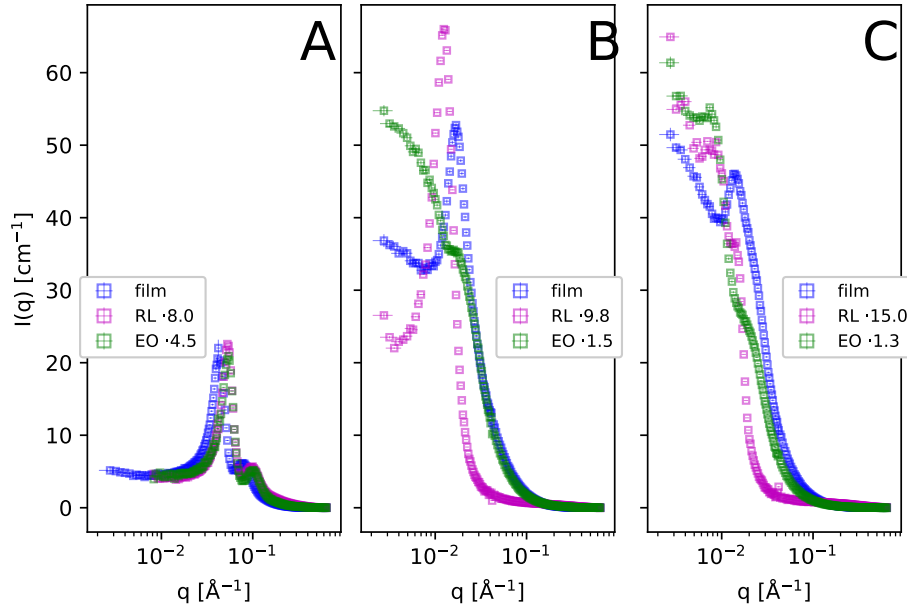


Figure A18: SANS profiles of μE containing RL and mono-disperse C_{12}E_4 in Winsor I A), and Winsor IV B) and C). The contrasts of the individual components were shifted by a certain factor to match the intensities of the film contrast.

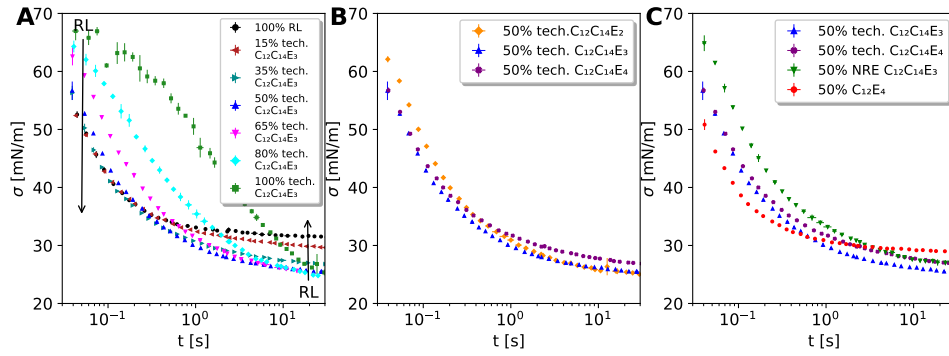


Figure A19: Maximum bubble pressure measurements (ST σ as a function of the bubble lifetime t) of different aqueous surfactant solutions at 1 g/l, pH 8 and 22 °C. A) depicts the ST as a function of time with different ratios of RL and technical $\text{C}_{12}\text{C}_{14}\text{E}_3$, while B) demonstrates the effect of the ethoxylation degree and its width at 50 wt% RL. The error bars show the standard deviation of three replicates.

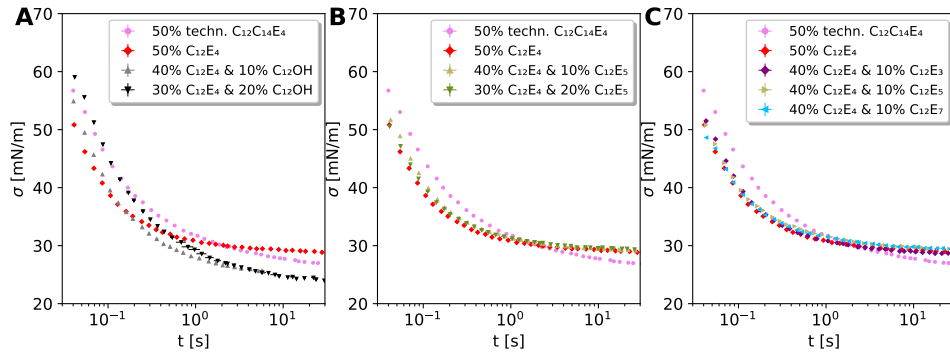


Figure A20: Maximum bubble pressure measurements (ST σ as a function of the bubble lifetime τ) of different aqueous surfactant solutions at 1 g/l, pH 8 and 22 °C. A) depicts the effect of the fatty alcohol, and B) and C) of different ethoxylation degrees with 50 wt% RL. The error bars show the standard deviation of three replicates.

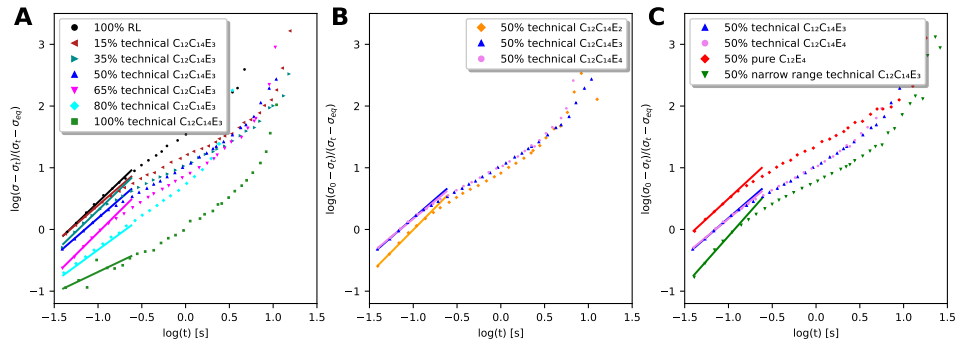


Figure A21: Rosen fit (Equation 2.66) of data of Figure A19 and Table 4.9.

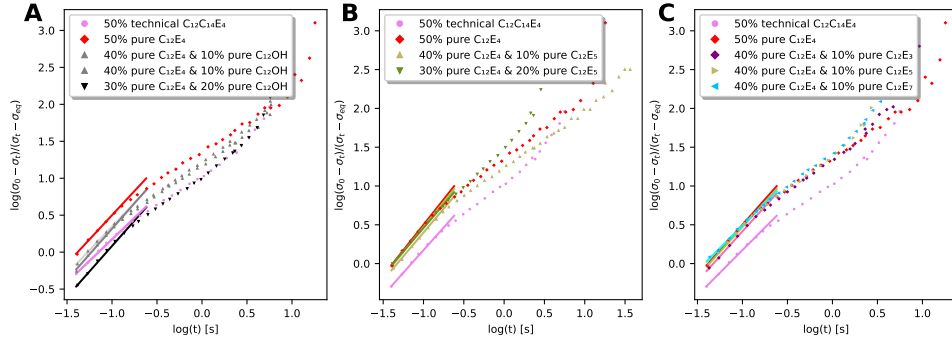


Figure A22: Rosen fit (Equation 2.66) of data of Figure A20 and Table 4.9.

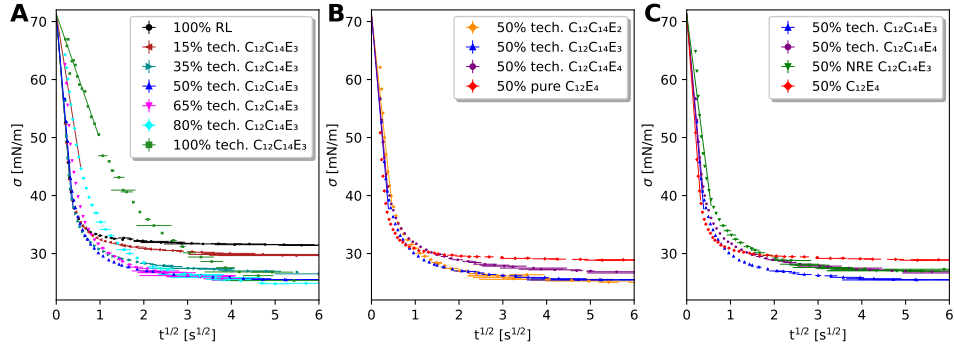


Figure A23: Ward-Tordai fit (Equation 2.68) of data of Figure A19 and Table 4.9.

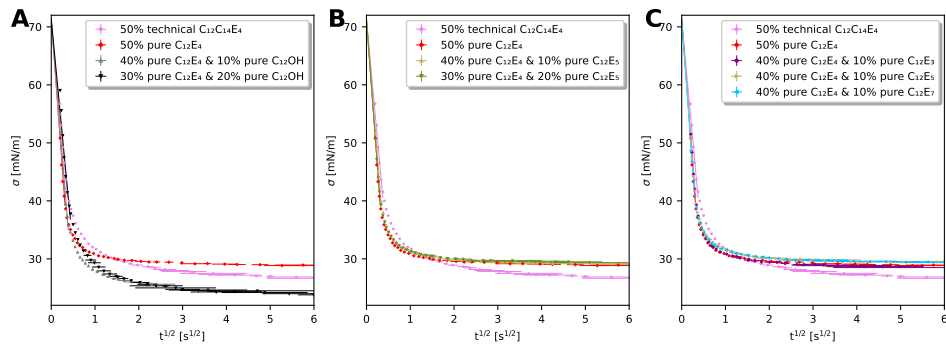


Figure A24: Ward-Tordai fit (Equation 2.68) of data of Figure Figure A20 and Table 4.9.

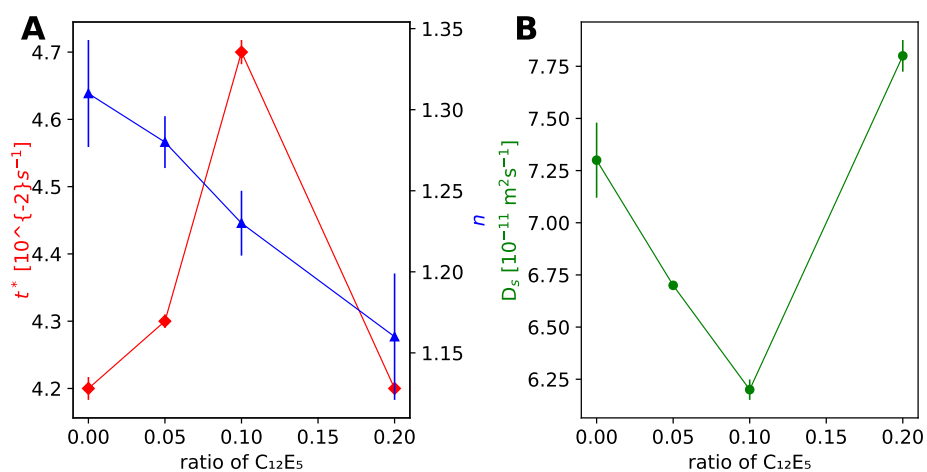


Figure A25: A) Effective diffusion coefficient plotted as a function of the ratio of C₁₂E₅ and C₁₂E₄. B) Constants t^* and n from the Rosen fit. Error bars are derived from the co-variance of the nonlinear fit and lines just serve as a guide for the eye.

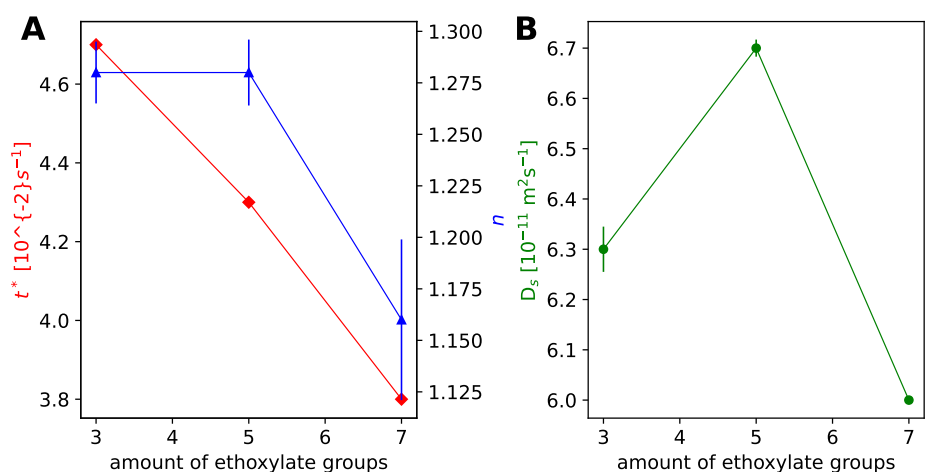


Figure A26: A) Effective diffusion coefficient plotted as a function of the ethoxylate content C₁₂E_x of a 5 wt% ratio C₁₂E_x and C₁₂E₄. B) Constants t^* and n from the Rosen fit. Error bars are derived from the covariance of the nonlinear fit and lines just serve as a guide for the eye.

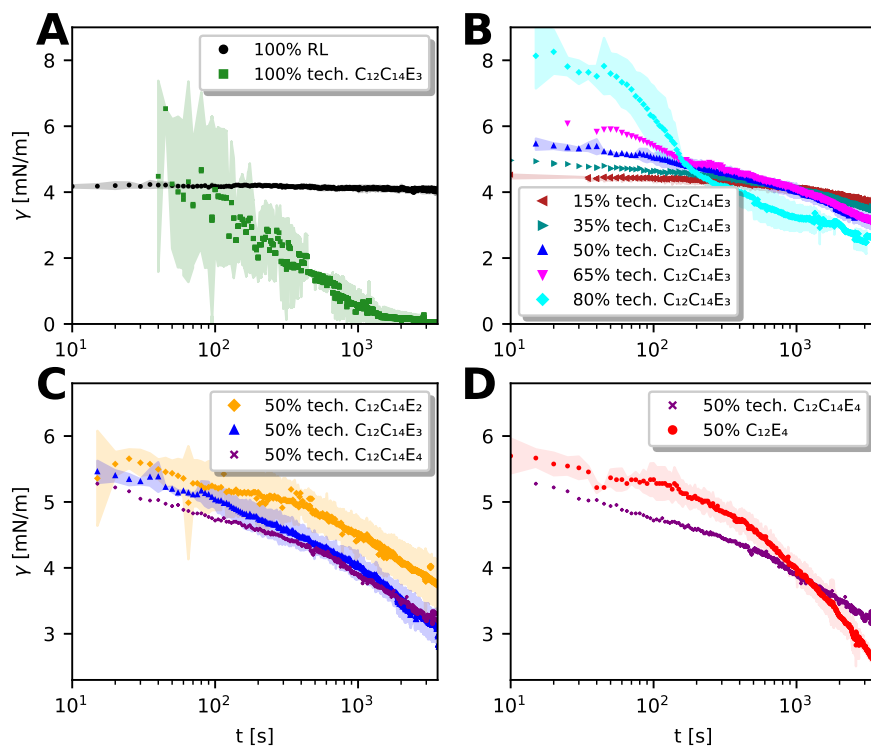


Figure A27: Spinning drop measurements of different aqueous surfactant solutions against n-decane at 1 g/l, pH 8 and 30 °C. A) and B) depict the IFT γ as a function of time t with different ratios of RL and technical C₁₂C₁₄E₃, while C) and D) demonstrate the effect of the ethoxylation degree and its width of distribution at 50 wt% RL each. The shades display the standard deviation of three repetitions.

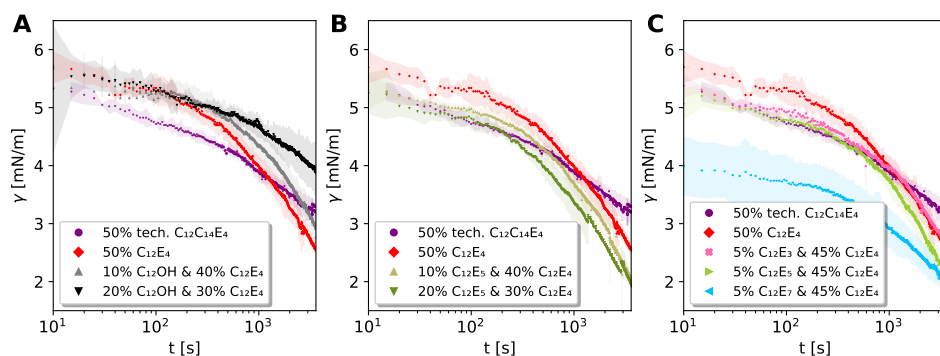


Figure A28: Spinning drop measurements (IFT, γ as a function of time t) of different aqueous surfactant solutions against n-decane at 1 g/l, pH 8 and 30 °C. A) depicts the effect of the fatty alcohol, and B) and C) of different ethoxylation degrees with 50 wt% RL each. The shades display the standard deviation of three repetitions.

